



HAL
open science

Elaboration of laccase T. cross-linked ultraporous aluminas for Remazol Brilliant Blue R removal

Huan Xu

► **To cite this version:**

Huan Xu. Elaboration of laccase T. cross-linked ultraporous aluminas for Remazol Brilliant Blue R removal. Material chemistry. Université Paris-Nord - Paris XIII, 2021. English. NNT : 2021PA131076 . tel-03886067

HAL Id: tel-03886067

<https://theses.hal.science/tel-03886067v1>

Submitted on 6 Dec 2022

HAL is a multi-disciplinary open access archive for the deposit and dissemination of scientific research documents, whether they are published or not. The documents may come from teaching and research institutions in France or abroad, or from public or private research centers.

L'archive ouverte pluridisciplinaire **HAL**, est destinée au dépôt et à la diffusion de documents scientifiques de niveau recherche, publiés ou non, émanant des établissements d'enseignement et de recherche français ou étrangers, des laboratoires publics ou privés.



ECOLE DOCTORALE GALILÉE (ED 146)

LSPM (CNRS)

THÈSE DE DOCTORAT

pour obtenir le grade de

DOCTEUR DE L'UNIVERSITÉ SORBONNE PARIS

NORD

Spécialité: Sciences Matériaux

Présentée et soutenue publiquement par

Huan XU

Titre :

**Elaboration of laccase T. cross-linked ultraporous
aluminas for Remazol Brilliant Blue R removal**

Soutenance publique prévue le 10 Décembre 2021

Thèse soutenue devant le jury composé de :

KESSLER Vadim, Swedish University of Agricultural Sciences	Professeur	Rapporteur
SUBRA-PATERNAULT Pascale, Université Bordeaux	Directrice de Recherche, CNRS	Rapporteur
LEPRINCE-WANG Yamin, Université Gustave Eiffel	Professeur	Examinatrice
ELM'SELMI Abdellatif, École de Biologie Industrielle	Professeur de l'EBI	Co-Directeur de thèse
TRAORE Mamadou, Université Sorbonne Paris Nord	MCF-HDR	Directeur de thèse
AZOUANI Rabah, École de Biologie Industrielle	Professeur de l'EBI-HDR	Invité Co-Encadrant
KANAEV Andrei, Université Sorbonne Paris Nord	Directeur de Recherche, CNRS	Invité
DUFOUR Florence, École de Biologie Industrielle	Directrice de l'EBI	Invité

Abstract

Over the past few decades, enzyme-based green and sustainable chemistry has attracted extensive research attention, which provides a promising alternative to the conventional treatment method of recalcitrant micropollutants. However, enzyme denaturation and stability loss remain critical challenges for its potential applications in industrial wastewater treatment.

In this study, laccase from *Trametes versicolor* (laccase T.) was cross-linked immobilized on ultraporous aluminas (UPA) for an effective biodegradation of Remazol Brilliant Blue R (RBBR). Before accomplishing this, the main challenges were first to determine the candidate material as the supporting carrier, followed by developing an effective method for laccase T. immobilization.

Based on the multiple research work, UPA synthesized via facile oxidation process was applied for direct RBBR adsorption and laccase T. immobilization. The adsorption process depended on the pH value and temperature of the solution. Both film diffusion and intraparticle diffusion contributed to the adsorption kinetics, and chemical reactions also played a significant role during the entire adsorption process.

By sequentially using coupling agent APTES and cross-linker glutaraldehyde, the synthesized biocatalysts showed better immobilization performances. Tolerance to broader pH and temperature ranges, better storage stability, good reusability of the synthesized biocatalysts, and continuous biodegradation kinetics of RBBR highlight the UPA potentials in enzyme immobilization and industrial wastewater treatment, which can broaden our understanding of its practical applications in the environmental field.

Keywords: ultraporous aluminas, laccase T., RBBR, adsorption, biodegradation

Résumé

Au cours des dernières décennies, la recherche sur la chimie verte à base d'enzymes s'est accentuée et offre aujourd'hui une alternative prometteuse à la méthode de traitement conventionnelle des micropolluants récalcitrants. Cependant, la dénaturation des enzymes et la perte de stabilité restent des défis majeurs pour ses applications potentielles dans le traitement des eaux usées industrielles.

Dans cette étude, la laccase de *Trametes versicolor* (laccase T.) a été réticulée et immobilisée par des alumines ultraporeuses (UPA) pour la biodégradation du Remazol Brilliant Blue R (RBBR). Les principaux défis pour atteindre cet objectif ont été d'abord de déterminer le matériau candidat support, puis de développer une méthode efficace pour l'immobilisation de la laccase T..

En s'appuyant sur de multiples travaux de recherche, l'UPA synthétisé par un processus d'oxydation a été utilisé pour l'adsorption directe de RBBR et l'immobilisation de laccase T.. Le processus d'adsorption dépend de la valeur du pH et de la température de la solution. La diffusion intraparticulaire et dans le film ont toutes les deux contribué à la cinétique d'adsorption. Les réactions chimiques ont également joué un rôle important pendant l'ensemble du processus d'adsorption.

En utilisant séquentiellement l'agent de couplage APTES et le glutaraldéhyde réticulant, les biocatalyseurs synthésés ont montré de meilleures performances d'immobilisation. La tolérance à des gammes de pH et de température plus larges, une meilleure stabilité au stockage, une bonne réutilisation des biocatalyseurs synthésés et une cinétique de biodégradation continue du RBBR mettent en évidence les potentiels de l'UPA dans l'immobilisation des enzymes et le traitement des eaux usées industrielles, ce qui peut élargir notre compréhension de ses applications pratiques dans le domaine environnemental.

Mots clés: alumines ultraporeuses, laccase T., RBBR, adsorption, biodégradation

Acknowledgements

First of all, I would like to thank the two lab directors, VREL Dominique (LSPM, Université Sorbonne Paris Nord) and DUFOUR Florence (EBI), for allowing me to conduct my research in laboratories. My acknowledgement to the China Scholarship Council (CSC) for granting my 3-year PhD fellowship, followed by one year of funding resources provided by EBI, which is also gratefully acknowledged.

I would like to express my sincere gratitude to my PhD directors, TRAORE Mamadou from LSPM and ELM'SELMI Abdellatif from EBI as my great mentors. Thank you for providing me with this PhD research subject, guiding me, and supporting me with maximum flexibility and autonomy. This 3-year of PhD career is my fortune in my life.

I would like to thank AZOUANI Rabah, my co-supervisor, for his continuous encouragement and support during these three years' work. Thank you for always showing up in time when I lost faith. I would like to thank KANAIEV Andrei for his valuable advice throughout all my experiments.

I would also like to give my appreciation to BOEUF Guilhem for his help during this 3-year of work at EBI. And my special thank is expressed to JIA Zixian for being a good colleague and a great guide in life.

My gratitude is expressed to my temporary colleagues at LSPM, ANDALOUCI Ahmed, ALLOUCH Amal, SPIRIDIGLIOZZI Hugo, SANCHEZ MENDEZ Miguel, DADI Rania, PASHOVA Katya Bulgaria, and CASTILLO ARVIZU Ken not only for helping me and supporting me through my research but also for being my good friends, our friendship will last for a lifetime. My gratitude to all the staff at LSPM, especially CHALVIGNAC Greg, BRINZA Ovidiu, DUROS Nathalie, OUAZAN Sandrine, I also want to thank you for all the administrative and technical support that you provided. My gratitude is also expressed to BEN ABLA Amina, CHARAABI Saddam, and IMBART Sylvia from EBI for the support on my research.

A big thank to my committee members, KESSLER Vadim, SUBRA-PATERNAULT Pascale, and LEPRINCE-WANG Yamin. Thank you for the valuable comments and suggestions on my work, and also thank you for making my PhD defense such a wonderful and enjoyable moment.

I also want to thank my friends for helping me to enjoy a wonderful life in Paris: WANG Bo, ZHU Kairuo, YU Chuang, FENG Minghao, JIANG Xianwu, SHI Hehuan, HUANG Xian, LIANG Weichao, FENG Shiyuan, PEI Yang, TU Zhengrui, GAO Guohui, XIE Wenjin, GUO Qihao, YANG Yulong, WANG Xianjie, LIU Bo, WANG Wenzhi, GAO Chuan, WEI Baohuan, NI Bin, TANG Chaojun, DUAN Jianan, MA Kailiang, YIN Tiantian, MA Panpan, SUN Chao, YU Haozheng, and LIU Jianhua...

Thank you, Qing, my dear love, for being my wife.

Finally, I thank my family. Without your love and support, I would not have the possibility to make it so far.

Table of contents	
Abstract	I
R ésum é	II
Acknowledgements	III
Table of contents	V
List of figures	IX
List of tables	XIV
Chapter 1: Introduction	1
1.1. Representative and treatment methods of industrial textile effluents	3
1.2. Enzyme immobilization and its market prospects	6
1.3. Oxidoreductases for environmental applications.....	8
1.3.1. Laccase.....	9
1.3.2. Tyrosinases.....	10
1.3.3. Manganese peroxidases	11
1.4. General enzyme immobilization methods	13
1.5. Mesoporous materials for enzyme immobilization.....	15
1.6. Summary and plan of the manuscript	17
1.7. References.....	20
Chapter 2: Experimental methods	29
2.1. Experimental reagents.....	29
2.2. Material syntheses.....	31
2.2.1. Syntheses of UPA monolith, UPA(γ), UPA(θ), and UPA(α) powders	32
2.2.2. Synthesis of APTES silanized UPA powders.....	35
2.2.3. Synthesis of laccase T. cross-linked UPA biocatalysts	35
2.2.3.1. Sequential immobilization	35
2.2.3.2. Glutaraldehyde post-treatment.....	37

2.2.4. Synthesis of laccase T./UPA(γ) powders	37
2.3. Batch experiments.....	38
2.3.1. RBBR adsorption retained by UPA(θ) powders	38
2.3.2. RBBR and laccase T. calibration curves	38
2.3.3. Biocatalyst stability study	41
2.4. Characterizations.....	42
2.5. Law and fitting models	43
2.5.1. Beer-Lambert (Beer's) law	43
2.5.2. Adsorption kinetic models	46
2.5.2.1. Pseudo-first-order	46
2.5.2.2. Pseudo-second-order	46
2.5.3. Rate-limiting step determination.....	46
2.5.3.1. Film diffusion (FD).....	47
2.5.3.2. Intraparticle diffusion (IPD).....	47
2.5.4. Adsorption isotherm models	47
2.5.4.1. Langmuir.....	48
2.5.4.2. Freundlich	49
2.5.4.3. Temkin	49
2.5.4.4. Dubinin-Radushkevich (D.-R.).....	50
2.5.4.5. List of other adsorption isotherm models	51
2.6. Adsorption thermodynamic study	53
2.7. Conclusions.....	53
2.8. References.....	55
Chapter 3: Ultraporous aluminas for highly efficient removal of RBBR.....	62
3.1. Introduction.....	62
3.2. Characterizations.....	63
3.3. Effect of initial pH	71
3.4. Effect of contact time	73

3.5. Effect of dose concentration	74
3.6. Adsorption kinetics	75
3.7. Rate-limiting step determination.....	78
3.8. Effect of temperature	80
3.9. Thermodynamic study	83
3.10. Adsorption mechanisms	84
3.11. Conclusions	88
3.12. References.....	89
Chapter 4: Laccase T. cross-linked immobilized ultraporous aluminas for efficient biodegradation of RBBR	95
4.1. Introduction.....	95
4.2. Characterizations.....	96
4.3. Effect of glutaraldehyde concentration	98
4.4. Disposable bioreactor.....	100
4.5. Effect of immobilization protocol.....	103
4.6. pH and thermal stability.....	104
4.7. Storage and reusability.....	105
4.8. RBBR kinetic study	106
4.9. Modeling kinetics.....	107
4.9.1. Adsorption.....	107
4.9.2. Adsorption and catalysis	109
4.10. Experimental difficulties encountered and troubleshooting	110
4.10.1. 2-propanol and (NH ₄) ₂ SO ₄ induced CLEAs	110
4.10.2. Fresh egg albumin as the protein feeder	113
4.11. Conclusions.....	114
4.12. References.....	116
Chapter 5: Conclusions and perspectives	121
5.1. Conclusions.....	121

5.2. Perspectives.....	124
Appendix A: Nomenclature, greek symbols and subscripts.....	127
Appendix B: List of abbreviations.....	129
Appendix C: Symbols for units.....	131
Appendix D: Article published in Materials.....	133
Appendix E: Article published in Chemical Engineering Transactions.	153

List of figures

Figure 1.1. – Chemical structural diagram, physical and chemical properties of RBBR (Özsoy et al., 2005; Rainert et al., 2021).

Figure 1.2. – The common low-cost adsorbents for the removal of dyes from aqueous solution (Siddiqui et al., 2019).

Figure 1.3. – U.S. industrial enzymes market size, by application, 2016–2027 (USD Billion) (Source: www.grandviewresearch.com).

Figure 1.4. – Cartoon structures of the three-domain laccase from *Bacillus subtilis* (PDB 1GSK) and the homotrimeric two-domain laccase from *Streptomyces coelicolor* (PDB 3CG8). The domain assignments were made using the SWORD partition algorithm (Enguita et al., 2003; Arregui et al., 2019).

Figure 1.5. – Degradation pathways for RBBR degradation by the laccase from (a) *Trametes pubescens* and (b) *Polyporus* sp. S133 (Osma et al., 2010; Hadibarata et al., 2011; Legerska et al., 2016).

Figure 1.6. – Catalytic pathway of phenolic substrate by tyrosinase (Zdarta et al., 2018).

Figure 1.7. – The catalytic cycle of manganese peroxidase (MnP) (Hofrichter, 2002).

Figure 1.8. – Different enzyme immobilization techniques.

Figure 1.9. – Main features of support materials required for effective enzyme immobilization (Zdarta et al., 2018).

Figure 1.10. – Selected examples and the most important properties of support materials used for immobilization of enzymes for environmental application (Zdarta et al., 2018).

Figure 2.1. – (a) Chemical structural diagram of RBBR, (b) 3-D model of RBBR molecule with two negative charges, and (c) visible spectral curves of RBBR before and after adsorption retained by UPA(θ) powders monitoring with time.

Figure 2.2. – Photos of (a) raw aluminium grid, UPA monolith sample after (b) 10 min, (c) 1 h, (d) 2 h, (e) 4 h, (f) 5 h, (g) 6 h, and (h) 16 h of continuous growth process.

Figure 2.3. – Photo of the experimental instrument for the synthesis of UPA monolith.

Figure 2.4. – Photos of (a) raw fragile UPA, under 4 h of isochronous annealing treatment in air at (b) 950 °C (UPA(γ)), (c) 1150 °C (UPA(θ)), and (d) 1350 °C (UPA(α) monolith).

Figure 2.5. – Schematic diagram of UPA silanization by APTES.

Figure 2.6. – Schematic diagram of sequential immobilization protocol for laccase T. immobilization on UPA surfaces.

Figure 2.7. – Effect of reaction time on the residual enzyme activity of laccase T. in the absence and presence of glutaraldehyde with different concentrations (i.e., 0 as the control, 0.25, 0.50, 1.00, 1.50, and 3.00% of v/v).

Figure 2.8. – Schematic diagram of glutaraldehyde post-treatment protocol for laccase T. immobilization on UPA surfaces.

Figure 2.9. – (a) Visible spectral curves of RBBR at different concentrations, (b) calibration curves of RBBR at different wavelengths ($\lambda = 590, 675, \text{ and } 695 \text{ nm}$), (c) visible spectral curves of laccase T. assay by using ABTS as the substrate at different oxidation time ($t = 10, 15, \text{ and } 30 \text{ min}$), and (d) calibration curve of laccase T. assay by using ABTS as the substrate at 5 min of oxidation time ($\lambda = 420 \text{ nm}$).

Figure 2.10. – Technical data of UviLine 9400 UV-Visible spectrophotometer.

Figure 2.11. – Typical visible spectral curve of RBBR (240 mg L^{-1}).

Figure 3.1. – (a) SEM and (b) TEM images of UPA(θ) powders, and elemental mapping of UPA(θ) powders (c) before and (d) after RBBR adsorption.

Figure 3.2. – EDX spectra of UPA(θ) powders (a) before and (b) after RBBR adsorption.

Figure 3.3. – SEM images of UPA(θ) powders (a) before and (b) after RBBR adsorption.

Figure 3.4. – FTIR spectra of UPA(θ) powders before and after RBBR adsorption.

Figure 3.5. – XRD patterns of (a) amorphous UPA, (b) UPA(γ), (c) UPA(θ), and (d) UPA(α) powders.

Figure 3.6. – Nitrogen adsorption-desorption isotherms of (a) UPA(γ), (c) UPA(θ), and (e) UPA(α) powders. Corresponding pore size distributions of (b) UPA(γ), (d) UPA(θ), and (f) UPA(α) powders.

Figure 3.7. – Adsorption isotherm profiles regarding RBBR adsorption capacity with units as (a) mg g^{-1} and (b) mg m^{-2} retained by UPA(γ), UPA(θ), and UPA(α) powders.

Figure 3.8. – Zeta potential values of UPA(γ), UPA(θ), and UPA(α) powders as a function of pH.

Figure 3.9. – (a) Effect of initial pH on RBBR adsorption retained by UPA(θ) powders, (b) zeta potential values of UPA(θ) powders as a function of pH, and (c) pH variation after RBBR adsorption equilibrium retained by UPA(θ) powders.

Figure 3.10. – Adsorption kinetics regarding the (a) adsorption percentage and (b) adsorption capacity of RBBR retained by UPA(θ) powders.

Figure 3.11. – (a) Effect of UPA(θ) dosage on RBBR adsorption kinetics, three-dimensional curved surface simulation based on (b) MATLAB and (c) Origin matrix conversion and gridding.

Figure 3.12. – Tests of the (a) Lagergren pseudo-first-order and (b) pseudo-second-order models on RBBR adsorption retained by UPA(θ) powders.

Figure 3.13. – Tests of the (a) film diffusion (Boyd plot) and (b) intraparticle diffusion (Weber and Morris plot) models on RBBR adsorption retained by UPA(θ) powders.

Figure 3.14. – Adsorption isotherm profiles of RBBR retained by UPA(θ) powders at different temperatures.

Figure 3.15. – Tests of the (a) Langmuir, (b) Freundlich, (c) Temkin, and (d) D.-R. isotherm models on RBBR adsorption retained by UPA(θ) powders. at different temperatures.

Figure 3.16. – Linear plots of (a) $\ln K_d$ versus C_e and (b) $\ln K^0$ versus $1000/T$ for RBBR adsorption retained by UPA(θ) powders.

Figure 3.17. – Possible mechanisms for RBBR adsorption retained by UPA(θ) powders.

Figure 4.1. – (a) FTIR spectra of UPA(γ) powders, APTES silanized UPA(γ) powders, laccase T. cross-linked UPA(γ) biocatalysts, and laccase T., (b) FTIR spectra comparison of UPA(γ) powders and APTES silanized UPA(γ) powders, and (c) FTIR spectra comparison of APTES silanized UPA(γ) powders and laccase T. cross-linked UPA(γ) biocatalysts.

Figure 4.2. – TG curves of UPA(γ) powders, APTES silanized UPA(γ) powders, and laccase T. cross-linked UPA(γ) biocatalysts.

Figure 4.3. – (a) Photos of two parallel experiments regarding ABTS oxidation monitoring: (a) to (b) 0.5 mg, and (c) to (d) 2.0 mg of laccase T. cross-linked UPA(γ) biocatalysts.

Figure 4.4. – (a) Schematic diagram of disposable 2 mL polystyrene column, (b) residual RBBR (C_t / C_0 , %) in the suspension and (c) the corresponding photos of sponge supports inside the polystyrene column after different cycles of dilution.

Figure 4.5. – Photos of the polystyrene column (a) with and (b) without the lower cap to avoid liquid leakage, (c) photo of the sponge support holding laccase T. cross-linked UPA(γ) biocatalysts in the polystyrene column, (d) photos of sponge support surface after RBBR dye biodegradation, and (e) residual RBBR (C_t / C_0 , %) after different time intervals of laccase T. cross-linked UPA(γ) biocatalyst treatment in polystyrene column bioreactor at pH = 5.0.

Figure 4.6. – (a) pH stability and (b) thermal stability profiles of free laccase T., laccase T./UPA(γ), and laccase T. cross-linked UPA(γ) biocatalysts by using ABTS as the substrate.

Figure 4.7. – (a) storage stability and (b) reusability profiles of free laccase T., laccase T./UPA(γ), and laccase T. cross-linked UPA(γ) biocatalysts by using ABTS as the

substrate.

Figure 4.8. – Comparison of UPA(γ) powders and laccase T. cross-linked UPA(γ) biocatalysts on RBBR bioremediation.

Figure 4.9. – RBBR kinetics in the presence of (a) UPA(γ) powders and (b) laccase T. cross-linked UPA(γ) biocatalysts. Solid and dashed lines show the model kinetics.

Figure 4.10. – Preparation of CLEAs with different glutaraldehyde concentrations (Matijošytė et al., 2010).

Figure 4.11. – Photos of CLEAs induced by 2-propanol with different glutaraldehyde concentrations (sequential immobilization protocol).

Figure 4.12. – Photos of CLEAs induced by $(\text{NH}_4)_2\text{SO}_4$ with different glutaraldehyde concentrations (sequential immobilization protocol).

Figure 4.13. – The effect of egg white on the activity of CLEAs-egg (Jiang et al. 2014).

Figure 5.1. – General perspectives of future work regarding RBBR treatment: (a) powders for adsorption, (b) membrane synthesis, (c) membrane for adsorption, (d) laccase T. cross-linking for biodegradation, and (e) laccase T. production by recombination method.

Figure 5.2. – Photos of the synthesized UPA membranes (the surface stickiness and defects occurred with all the membrane samples obviously).

List of tables

Table 1.1. – Standards for the effluent discharged from the textile industry (Paul et al., 1966; Senthil Kumar and Saravanan, 2017).

Table 1.2. – Main immobilization techniques, their characteristics and advantages (Zdarta et al., 2018).

Table 2.1. – Description of the main experimental reagents used in this thesis.

Table 2.2. – List of other adsorption isotherm models.

Table 3.1. – Parameters of RBBR adsorption kinetics fitted by the Lagergren pseudo-first-order and pseudo-second-order models.

Table 3.2. – Parameters of RBBR adsorption kinetics fitted by the film diffusion (Boyd plot) and intraparticle diffusion (Weber and Morris plot) models.

Table 3.3. – Parameters of RBBR adsorption isotherms fitted by the Langmuir, Freundlich, Temkin, and D.-R. isotherm models at different temperatures.

Table 3.4. – Thermodynamic parameters of RBBR adsorption retained by UPA(θ) powders.

Table 3.5. – Comparison of RBBR adsorption capacity retained by UPA materials with other organic, inorganic, or bio-based adsorbents reported in related studies in the literatures.

Table 4.1. – Effect of glutaraldehyde concentration (v/v) on the laccase T. immobilization yield (IY, %), immobilization efficiency (IE, %), and activity recovery (AR, % or mg g^{-1} carrier) of laccase T./UPA (physical adsorption) and laccase T. cross-linked UPA (sequential immobilization) with different UPA polycrystalline phases.

Table 4.2. – Comparison of sequential immobilization, glutaraldehyde post-treatment, and no cross-linking protocols regarding laccase T. immobilization by UPA(γ) powders (0.50% (v/v) of glutaraldehyde concentration).

Chapter 1: Introduction

Color is the main attraction of any fabric, and the art of dyeing is as old as our civilization (Kant, 2012; Saxena and Raja, 2014). Textile dyeing can be dated back to the Neolithic period (also known as the New Stone Age), followed by the serendipitous discovery of the first synthetic dye, mauveine (aniline purple) by William Perkin in 1856 (Lavis, 2017). Moreover, the dyed textile remnants found during archaeological excavations at different places worldwide also provide evidence of dyeing practices in ancient civilizations (Saxena and Raja, 2014).

As the name suggests, natural dyes are mainly derived from natural substances such as plants and herbs, insects, animals, minerals, and other natural resources, among which most natural dyes are safe and harmless (Patel, 2011; Saxena and Raja, 2014; Verma and Gupta, 2017). Different regions of the world had their own natural dyeing traditions, which utilized the local natural resources available in that region. After the invention of synthetic dyes, the consumption and application of natural dyes started to decline substantially, and the tradition of using natural dyes could be preserved only in certain isolated regions or by some environmentally conscious people (Saxena and Raja, 2014).

The worldwide textile industry contributes greatly to the global market economy, and nearly 14% of its total production is contributed by the textile industry (Sahu and Singh, 2019). However, it is also considered as the major fresh water and chemical consumer and it also discharges heavily polluted loaded effluents. At present, $>7 \times 10^5$ tons of dyes are produced worldwide per year, and nearly 10–15% of the total dyes are discharged in the surrounding environment with or without partial treatments, making the dyestuff-related industries responsible for up to 20% of industrial water pollution (Bilal et al., 2017; Routoula and Patwardhan, 2020).

The textile industry involves a wide range of processes to produce different varieties of garments and clothing. Textile effluent contains mainly by-products, residual dye, salts, acid/alkali, auxiliary chemicals, and cleaning solvents, among

which the main source of water pollution in the textile industry is dye pollution (Senthil Kumar and Saravanan, 2017; Sahu and Singh, 2019). For the effluent treatment, the Department of National Environmental Protection from the Central Pollution Control Board determined the permissible limits for the effluent discharged from the textile industry as follows (Table 1.1):

Table 1.1. – Standards for the effluent discharged from the textile industry (Paul et al., 1966; Senthil Kumar and Saravanan, 2017).

	Parameter	Standards
1	pH	5.5–9.0
2	Total suspended solids	100 mg L ⁻¹
3	Biochemical oxygen demand	30 mg L ⁻¹
4	Chemical oxygen demand	250 mg L ⁻¹
5	Total residual chlorine	1 mg L ⁻¹
6	Oil and grease	10 mg L ⁻¹
7	Total chromium	2 mg L ⁻¹
8	Sulphide	2 mg L ⁻¹
9	Phenolic compounds	1 mg L ⁻¹

Currently, the textile wastewater has become a significant causative agent of environmental degradation and human illness. The presence of toxic chemicals (e.g., sulfur, naphthol, nitrates, and acetic acid) and heavy metals (e.g., copper, arsenic, cadmium, and mercury) makes the wastewater highly toxic with high temperature and pH, which makes it extremely damaging. The effluent can prevent sunlight penetration necessary in freshwater for photosynthesis of aquatic flora and fauna (Bharagava and Chandra, 2010; Chandra et al., 2011; Chandra et al., 2012). It also interferes with the oxygen transfer mechanism at the air-water interface, which is the most serious effect of the textile wastewater and thus hinders the self-purification

process of water. When the agricultural fields are irrigated with these effluents, the pores of the soil will be blocked, which results in the loss of soil productivity (Chandra et al. 2009). Therefore, to find the proper treatment methods regarding purifications and remediations of industrial textile effluents is urgent and necessary.

1.1. Representative and treatment methods of industrial textile effluents

The majority of dyes industrially used nowadays are organic compounds with complex and reinforced structures, which normally consist of two major components, i.e., chromophore and auxochrome groups (Moussavi and Mahmoudi, 2009; Gök et al., 2010; Routoula and Patwardhan, 2020). As the representative dye widely exists in industrial textile effluents, Remazol Brilliant Blue R (RBBR) is frequently used as the starting material in the production of polymeric dyes. Moreover, RBBR also represents an important class of toxic and recalcitrant organopollutants (Özsoy et al., 2005; Mechichi et al., 2006; Rainert et al., 2021). Figure 1.1 showed the chemical structural diagram, physical and chemical properties of RBBR, which indicates that RBBR is an anthracene derivative.

Commercial name	Remazol Brilliant Blue Reactive
Generic name	Reactive Blue 19
Abbreviation	RBBR
Functional group	Anthraquinone
C.I. number	61.2
Molecular mass (g/mol)	626.54
λ_{\max} (nm)	590
Manufacturer	DyStar
pH of stock solution	6.20–28 °C
Molecular formula	$C_{22}H_{16}N_2Na_2O_{11}S_3$
Chemical structure	

Figure 1.1. – Chemical structural diagram, physical and chemical properties of RBBR (Özsoy et al., 2005; Rainert et al., 2021).

The persistent structure and poor biodegradability of RBBR and other refractory dyes make the choice of an appropriate dye treatment method challenging (Routoula and Patwardhan, 2020). Generally, the most known and extensively applied methods for the treatment of dyehouse effluents can be classified into the physical (adsorption, membrane filtration, and reverse osmosis), chemical/electrochemical (adsorption, coagulation, flocculation, and advanced oxidation processes), biological (intracellular, and isolated enzymes) methods, and/or emerging combination of several above-mentioned techniques with the purpose of synergistic effects (Cicek et al., 2007; Gök et al., 2010; Madrakian et al., 2013; Hou et al., 2014; Senthil Kumar and Saravanan, 2017; Zdarta et al., 2018; Lassouane et al., 2019).

Physical treatment methods can be applied for the removal of dyes without necessarily changing their chemical structures (Madrakian et al., 2012). Liquid-phase adsorption is one of the most popular methods for the removal of pollutants from wastewater. The proper designation of the adsorption process can produce a high-quality treated effluent. Moreover, activated carbons and zeolites are the representative materials in terms of the physical adsorption process (McIntosh et al., 1947; Thommes et al., 2015).

Chemical treatment methods mainly depend on the chemical interactions of the contaminants from wastewater and the application of chemicals that either aid in the separation of contaminants from wastewater or assist in the neutralization of harmful effects associated with contaminants (Cheremisinoff, 2002; Cicek et al., 2007; Moussavi and Mahmoudi, 2009; Gök et al., 2010; Madrakian et al., 2013; Zhu et al., 2019). For example, Monsef Khoshhesab and Ahmadi (2015) synthesized the NiO nanoparticles by chemical precipitation method and studied its adsorption capacity for RBBR with commercial NiO powders as a comparison. Moussavi and Mahmoudi (2009) synthesized the porous MgO nanoparticle (nano-MgO) by sol-gel method and applied it for both azo and anthraquinone dye removal from industrial wastewaters. In particular, Madrakian et al. (2013) successfully synthesized magnetite-modified

multiwalled carbon nanotubes (MMMCNTs) for the removal of four anionic dyes including RB19, methylthymol blue, congo red, and mordant blue 29.

Compared with the physical and chemical processes, biological treatment is a relatively economical method which can completely change the chemical and physical characteristics of targeted contaminants (Fernando Bautista et al., 2010; Osma et al., 2010; Hou et al., 2014; Lassouane et al., 2019). The removal efficiency of biological treatment is fully based on the ratio between the organic load and biomass present in the treatment tank (Senthil Kumar and Saravanan, 2017). Biological treatment can be classified mainly into two groups: (1) aerobic and (2) anaerobic (Sahu and Singh, 2019). The application of microorganisms in biological treatment is an attractive method and has considerable advantages. However, the application of biological treatment methods is often restricted for the reason of technical constraints. For example, biological treatment requires a large land area and is constrained by sensitivity toward diurnal variation and the toxicity of some chemicals, including less flexibility in design and operation (Siddiqui et al., 2019). Moreover, increasing emphasis is also being placed on biologically mediated chemical reactions, or more generally termed as bioconversion (Sheldon and Woodley, 2018).

Due to the dye potentials for long-range transport, resistance to environmental degradation, ability to bio-magnify and bio-accumulate in the ecosystem, researchers have long recognized the necessity to consider the transition of these organic chemistry-based industries to greener and more sustainable manufacturing processes which can minimize, or preferably avoid, the generation of pollutants and the use of hazardous materials (Sheldon, 2012; Sheldon, 2017; Sheldon and Woodley, 2018). In recent years, low-cost adsorbents including waste materials from industrial and agricultural processes have attracted extensive research attention and are commonly used to remove contaminants from wastewater (Figure 1.2). These waste materials represent the potentially economical alternative adsorbents (Woolard et al., 2002; Tsai et al., 2001):



Figure 1.2. – The common low-cost adsorbents for the removal of dyes from aqueous solution (Siddiqui et al., 2019).

1.2. Enzyme immobilization and its market prospects

Enabled by recent advances in modern biotechnology and protein engineering, bioconversion of persistent organic pollutants (POPs) into non-hazardous or less-hazardous substances has been recognized as a key strategy to control the level of contaminations in water and soil (Sheldon and Woodley, 2018; Zdarta et al., 2018). These biologically mediated chemical reactions can be generally performed under mild conditions by using a biocompatible and biodegradable catalyst which can be derived from renewable resources (Sheldon, 2012; Sheldon and Pelt, 2013; Sheldon, 2017; Sheldon and Woodley, 2018).

The term of immobilized enzymes refers to “enzymes physically confined or localized in a certain defined region of space with retention of their catalytic activities, and which can be used repeatedly and continuously” (Brena et al., 2013, López-Gallego et al., 2013). The enzyme immobilization usually involves a reaction process of binding the enzyme to a prefabricated carrier (supporting substrate), such as an organic resin or silica, or entrapment in a polymeric inorganic or organic matrix formed in the presence of the enzyme (Sheldon, 2017; Zdarta et al., 2018).

Reactions involving multifunctional enzyme molecules characterized by high chemo-, regio-, and stereoselectivity can integrate multiple steps into enzymatic cascade processes, which affords more step-economical routes without the conventional needs for complex functional group activation, protection, and deprotection steps (Sheldon, 2008; Sheldon, 2017). The ultimate goal of enzyme immobilization is to obtain a new kind of biocatalyst which possesses superior operational performances and is more cost-effective than the free enzyme. Binding to the carrier can involve simple adsorption, for example, via hydrophobic or ionic interactions or actual covalent bonding (Cao, 2006). Consequently, enzyme-related methods are more environmentally attractive, more cost-effective, and therefore more sustainable.

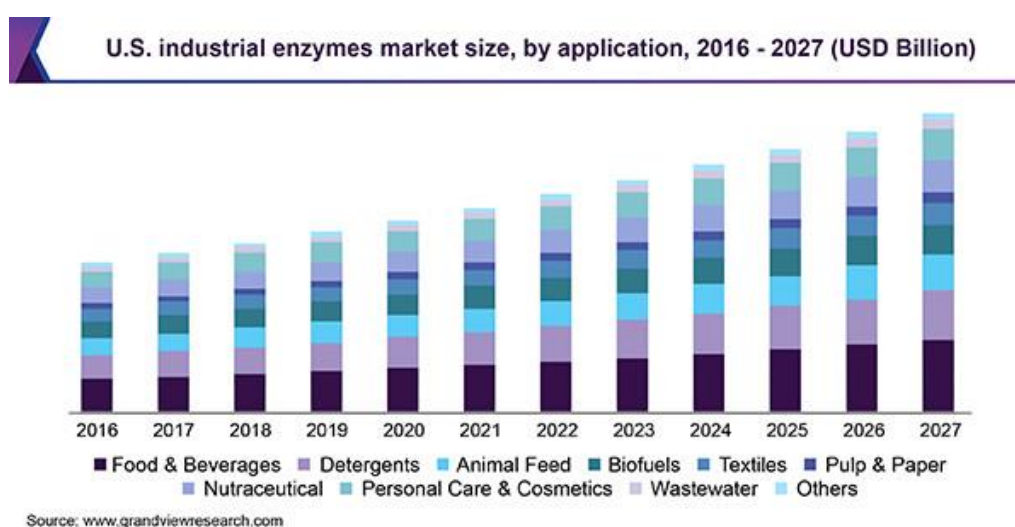


Figure 1.3. – U.S. industrial enzymes market size, by application, 2016–2027 (USD Billion) (Source: www.grandviewresearch.com).

In 2019, the global enzyme market size was valued at USD 9.9 billion and it is expected to grow at a compound annual growth rate (CAGR) of 7.1% from 2020 to 2027 (Figure 1.3). The increasing demand from end-use industries such as food and beverage, biofuel, animal feed, and home cleaning, is projected to drive the market growth over the forecast period. Moreover, the increasing health awareness among consumers also has resulted in the growing consumption of functional food products, which is expected to propel the product demand in the near future (Source: www.grandviewresearch.com).

Notwithstanding all the above-mentioned advantages, the industrial application of enzymes is often hampered by a lack of long-term operational stability and difficult enzyme recovery (Sheldon, 2012; Sheldon and Pelt, 2013; Sheldon, 2017; Sheldon and Woodley, 2018). To expand its commercial viability and sustainability, enzyme immobilization by converting it from a homogeneous catalyst to a heterogeneous catalyst which generally exhibits enhanced stability under both operational and storage conditions than free enzymes has been extensively studied (Osma et al., 2010; Torres-Salas et al., 2011; Hou et al., 2014; Sheldon and Woodley, 2018; Zdarta et al., 2018; Zhang and Sun, 2018; Lassouane et al., 2019).

1.3. Oxidoreductases for environmental applications

Oxidoreductases (EC 1) such as laccases, tyrosinases, manganese, lignin and horseradish peroxidases, and phenoloxidases, are the most frequently enzymes employed for environmental applications (Bilal et al., 2017). These enzymes are being investigated due to their applicability as “green catalysts” in the bioremediation of various dangerous chemicals such as phenols and derivatives, bisphenols, organic dyes or pharmaceuticals (Ba et al., 2014). They have been found to be efficient biocatalysts for remediation of toxic compounds, but the structures, cofactors and mechanisms of action differ for each type of catalyst (Cha et al., 2017; Zdarta et al., 2018).

1.3.1. Laccase

Laccases of various origins such as *Trametes versicolor*, *Trametes vilosa* or *Cerrena unicolor* are the most commonly extracellular enzymes for environmental protection because of their high catalytic activity, availability, and low price (Cha et al., 2017). Laccases constitute a wide group of multi copper oxidase enzymes that contain four copper ions in their structure that exhibit different properties.

Due to their wide substrate specificity and ubiquitous properties, they are able to act on a wide range of phenolic compounds and are increasingly used for bioremediation of environmental pollutants from soils and water (Le et al., 2016; Barrios-Estrada et al., 2018). One of the most well-known bacterial laccases is the outer endospore coat protein CotA from *Bacillus subtilis*, which has three cupredoxin domains (Figure 1.4) (Enguita et al., 2003; Arregui et al., 2019).

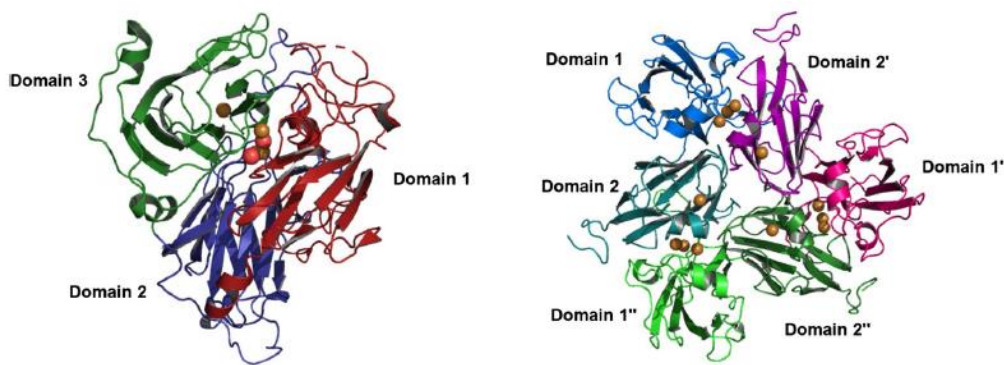


Figure 1.4. – Cartoon structures of the three-domain laccase from *Bacillus subtilis* (PDB 1GSK) and the homotrimeric two-domain laccase from *Streptomyces coelicolor* (PDB 3CG8). The domain assignments were made using the SWORD partition algorithm (Enguita et al., 2003; Arregui et al., 2019).

Most laccases are extracellular proteins with isoelectric points ranging from 3 to 7 for fungal laccases and around 9 for plant laccases. Moreover, differences in optimal pH for both sources of laccases have been found: fungal laccases exhibit maximal catalytic properties at pH between 3.5 and 5, and the laccases from plants have pH optima around pH 7 (Zdarta et al., 2018).

Differences in the temperature optima between various laccases have also been found (Tagger et al., 1998). The examples of the catalytic pathways of conversion of RBBR by laccase from different resources are shown in Figure 1.5 (Osma et al., 2010; Hadibarata et al, 2011; Legerska et al., 2016):

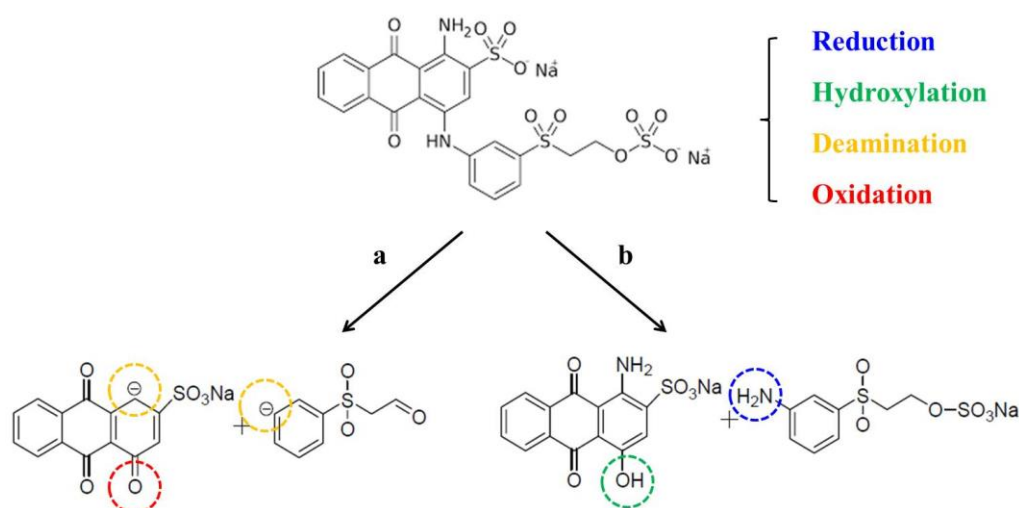


Figure 1.5. – Degradation pathways for RBBR degradation by the laccase from (a) *Trametes pubescens* and (b) *Polyporus* sp. S133 (Osma et al., 2010; Hadibarata et al, 2011; Legerska et al., 2016).

1.3.2. Tyrosinases

Tyrosinases, o-diphenol: oxygen oxidoreductases (EC 1.14.18.1), also contain copper atoms in their active site (Zdarta et al., 2018). Tyrosinases are frequently abundant in nature and are found in plants, fungi, bacteria, insects, and in mammalian tissues (Selinheimo et al., 2007). Tyrosinases differ essentially from laccases in the mechanism of oxidation of phenol and its derivatives. Although tyrosinases also use oxygen as a cofactor, they generate quinones instead of free radicals and water molecules as a by-product (Land et al., 2003).

The mechanism of catalytic action of tyrosinases has been defined as a two-step consecutive reaction of monophenol hydroxylation to corresponding ortho-diphenols and their further oxidation to ortho-quinones by using O₂ molecules in both steps.

Later release of water molecules terminates catalytic oxidation and leads to a polymerization reaction of o-quinones to macromolecular compounds (Figure 1.6) (Shuster and Fishman, 2009):

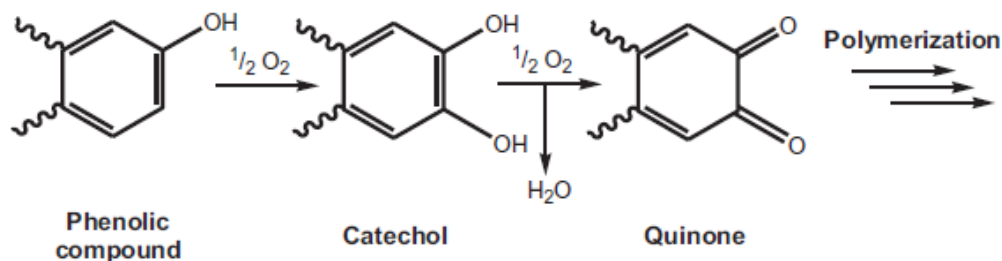


Figure 1.6. – Catalytic pathway of phenolic substrate by tyrosinase (Zdarta et al., 2018).

Due to the fact that tyrosinases can occur in various molecular forms, different intermediates may be formed during catalysis of phenolic compounds (Sanchez-Ferrer et al., 1995). It should be clearly stated that due to their wide specificity, tyrosinases similarly to laccases are able to catalyze transformation of various compounds such as phenol, monophenols and its multisubstituted derivatives, including chloro- and nitrophenols and bisphenols (Faccio et al., 2012). The effect of temperature and pH on the stability and activity of various tyrosinases has been thoroughly studied. A previous study reported pH ranging from 5.5 to 8 as the most suitable for the highest activity of free tyrosinases (Ihekata and Nicell, 2000). Moreover, free tyrosinases exhibit the highest activity at temperatures ranging from 30 to 40 °C, which significantly decreases above 60 °C (Zdarta et al., 2018).

1.3.3. Manganese peroxidases

Manganese peroxidase (EC 1.11.1.13) is another kind of enzyme which belongs to the oxidoreductase group with high biotechnology potential, and it is also known as Mn(II): hydrogen-peroxide oxidoreductase or MnP (Zdarta et al., 2018). These glycosylated heme-containing enzymes can oxidize a wide variety of phenolic compounds, such as dyes and various monomeric and dimeric phenols as well as

oxidize Mn(II) ions to Mn(III) by using hydrogen peroxide (Glenn and Gold, 1986). The catalytic cycle of MnP resembles those of other heme-peroxidases such as horseradish peroxidase (HRP) and lignin peroxidase, and includes the native ferric enzyme as well as the reactive intermediates Compound I and Compound II (Figure 1.7) (Hofrichter, 2002):

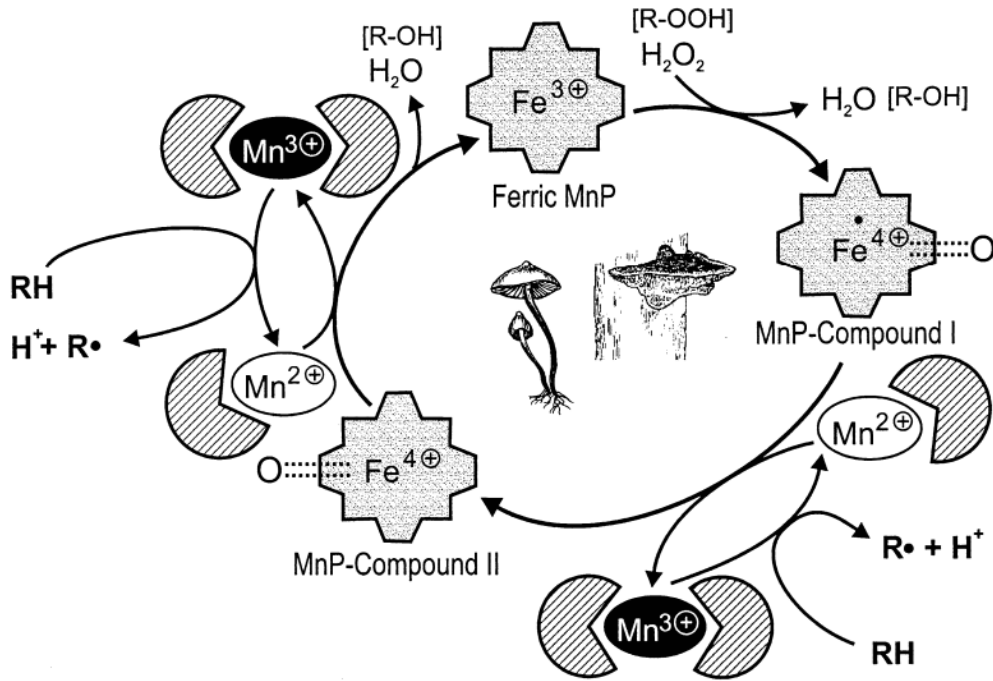


Figure 1.7. – The catalytic cycle of manganese peroxidase (MnP) (Hofrichter, 2002).

MnPs exhibit their maximal activity at Mn(II) concentrations above 100 μM , and calcium cations can enhance their catalytic properties (Glenn and Gold, 1986). Manganese peroxidase was discovered for the first time in *P. chrysosporium*, but in later years the enzyme has also been found in bacteria and other white-rot fungi (Bonnamme and Jeffries, 1990).

The optimum temperature for the highest catalytic activity of manganese peroxidases depends on its source, but in most cases lies the range of 30 to 40 $^{\circ}C$. These enzymes exhibit their highest catalytic properties at slightly acidic pH levels of around 4 (Yehia and Rodriguez-Couto, 2017).

1.4. General enzyme immobilization methods

Methods of enzyme immobilization differ between each other by the types of the created interactions and by type and form of the solid support. In each case, for selection of the immobilization technique, a compromise has been made between retention of high catalytic activity and operational benefits (Guzik et al., 2014; Zdarta et al., 2018). Generally, five main categories are distinguished, namely: (i) covalent bonding, (ii) adsorption (non-covalent), (iii) entrapment, (iv) encapsulation, and (v) cross-linking. Among all the above-mentioned immobilization techniques, cross-linking techniques is usually characterized with strong and stable interactions between enzyme molecules and carrier (supporting substrate) (López-Gallego et al., 2013; Sheldon, 2017; Zdarta et al., 2018). Schematic diagrams, characteristics and advantages of different enzyme immobilization techniques are summarized in Figure 1.8 and Table 1.2, respectively (Zdarta et al., 2018):

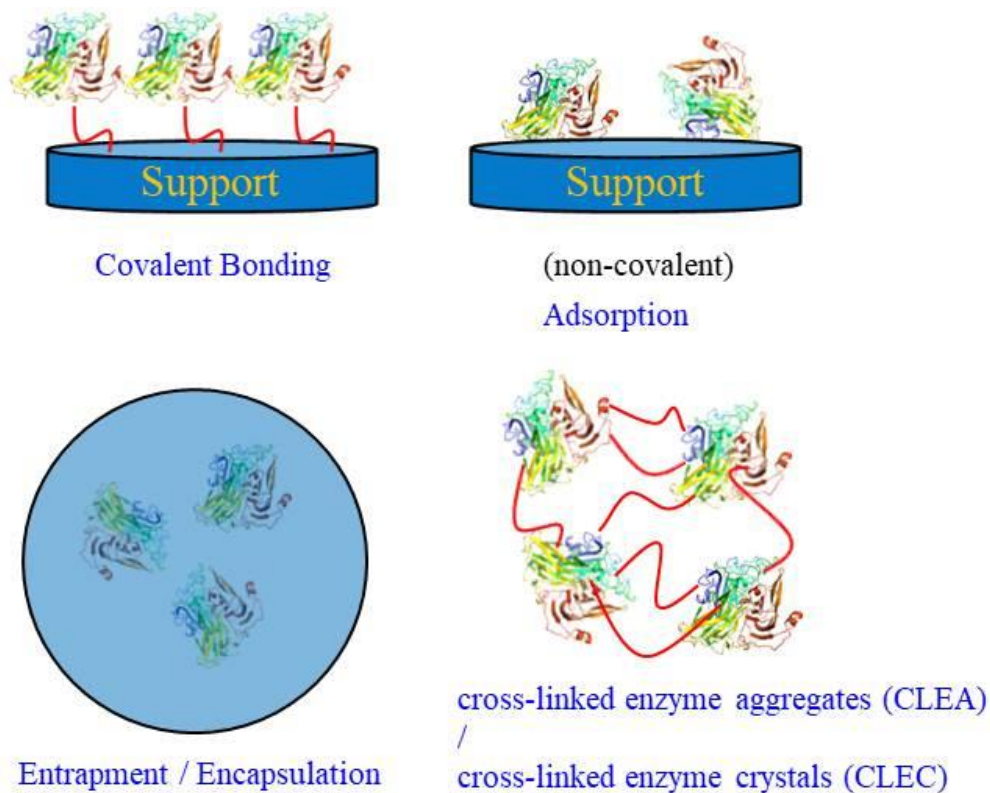


Figure 1.8. – Different enzyme immobilization techniques.

Table 1.2. – Main immobilization techniques, their characteristics and advantages (Zdarta et al., 2018).

Immobilization technique	Main functional groups of the support	Type of interactions	Strength of interactions	Advantages
Non-covalent (adsorption)	–NH ₂ , –SH, –OH, C=O, COOH, epoxy groups	hydrogen bonds, ionic interactions, hydrophobic interactions	weak	no enzyme modification, simple and inexpensive reusability of the support
Covalent binding	–NH ₂ , –SH, –OH, C=O	covalent bonds	strong	strong and stable interactions, multipoint attachment, reducing of enzyme leakage
Encapsulation	–NH ₂ , –OH,	ionic interactions, hydrophobic interactions	weak	no enzyme modification, protection of the enzyme
Entrapment	–NH ₂ , –OH, C=O	ionic interactions, hydrophobic interactions, covalent bonds	weak/strong	no enzyme modification
Cross-linking	C=O, –NH ₂	covalent bonds	strong	no support needed, high strength of interactions

1.5. Mesoporous materials for enzyme immobilization

Mesoporous materials of 2–50 nm pore diameter (IUPAC classified), owing to their numerous advantages including ordered, homogenous pore distributions, regular and tunable pore sizes, high specific surface areas, framework/wall substitutions with various metal oxides, favorable biocompatibility, and low toxicity, have been widely applied in the research field of wastewater treatment, catalyst support, drug delivery, and energy-related aspects, etc. (Li et al., 2018; Zdarta et al., 2018; Qiu et al., 2019). Among all the materials suitable for enzyme immobilization, the main required features for effective enzyme immobilization are summarized in Figure 1.9 (Zdarta et al., 2018):



Figure 1.9. – Main features of support materials required for effective enzyme immobilization (Zdarta et al., 2018).

Besides the size of pores inside the building framework, the compositions of material can vary, including pure organics (e.g., porous polymers), organic/inorganic (e.g., metal-organic frameworks, MOFs), and pure inorganics (e.g., silica, alumina, and titania). The great variety of the possible carriers with regard to shapes, sizes, and forms indicates that enzymes can be immobilized via various protocols. The most important properties of selected examples of supporting materials of different origins, from inorganic through organic to hybrids and composite supports are summarized in Figure 1.10 (Zdarta et al., 2018):

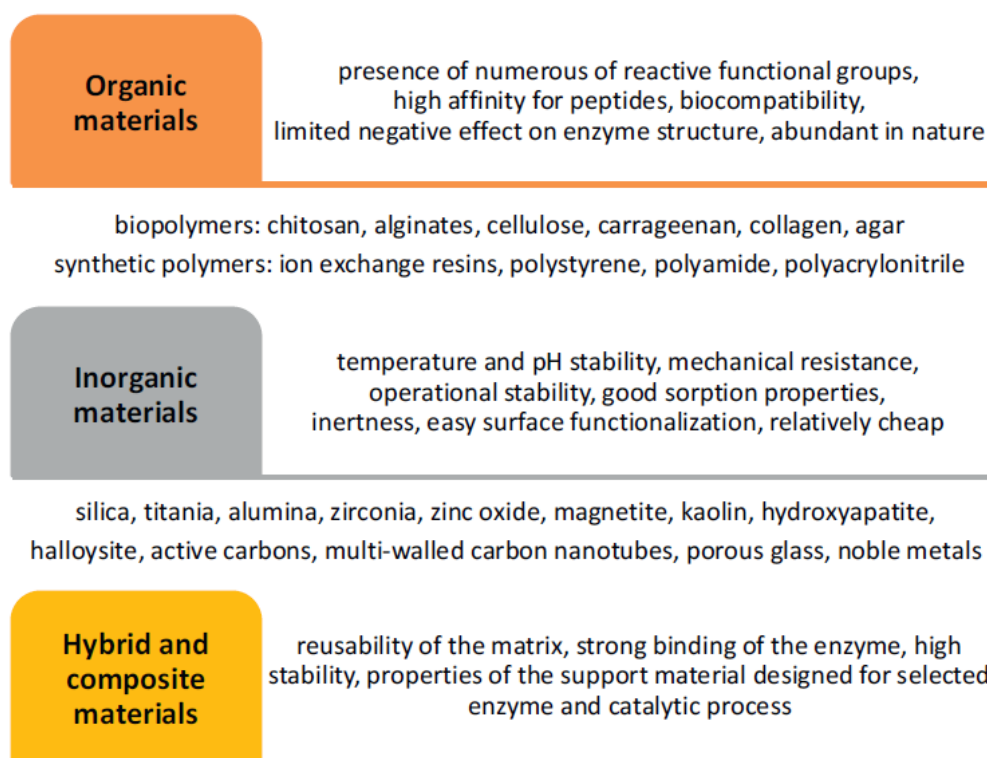


Figure 1.10. – Selected examples and the most important properties of support materials used for immobilization of enzymes for environmental application (Zdarta et al., 2018).

In comparison with the materials of organic origin, broad research interests mainly focus on inorganic materials which can be synthesized relatively cheaply and usually by uncomplicated synthesis procedures (Zdarta et al., 2018; Xu et al., 2021).

The abundant presence of many functional groups, large specific surface area, controllable nanometer size similar to that of enzyme molecules, exceptional mechanical and chemical stabilities may facilitate the versatility of inorganic materials in the case of enzyme immobilization (Brena et al., 2013; Zdarta et al., 2018). Moreover, the presence of many hydroxyl, carbonyl, and carboxyl groups on the surface of the inorganic carriers causes easier enzyme attachment and facilitates support functionalization through the use of surface modifying agents like glutaraldehyde or 3-aminopropyltriethoxysilane (APTES) (Zucca and Sanjust, 2014). For example, Hou et al. (2014) synthesized laccase immobilized TiO₂ nanoparticles and TiO₂ functionalized polyethersulfone (PES) membranes by different approaches, and their biocatalytic performances were compared in terms of laccase activity, loading, activity recovery, stability, and kinetic parameters.

Recently, Beuvy et al. developed a new method for the synthesis of ultraporous alumina (UPA) monolith, which was followed by isochronous annealing treatment in air at different temperatures, anhydrous monolithic UPA with different crystallizations can be accordingly obtained (Beuvy et al., 2004; Beuvy et al., 2005; Vignes et al., 2008; Nguyen, 2016). The versatile applications of UPA materials with regard to photocatalytic, optical, electronic, and arsenic wastewater treatment performances have been extensively studied (Bousslama et al., 2011; Bousslama et al., 2012; Khatim et al., 2014; Chiavola et al., 2016; Tchieda et al., 2016). However, the potential applications of UPA materials in the treatment of industrial textile effluents and enzyme immobilization still need to be studied.

1.6. Summary and plan of the manuscript

In this chapter, current environmental pollution status resulted from industrial textile effluents, different wastewater treatment methods, characteristics and advantages of enzyme immobilization, and the advantages of inorganic materials in terms of enzyme immobilization were briefly introduced.

By taking RBBR as the targeted pollutant, laccase from *Trametes versicolor* (laccase T.) was cross-linked immobilized on ultraporous aluminas (i.e., UPA(γ) and UPA(θ) powders) synthesized via a facile oxidation process. Laccase T. is a monomeric enzyme which can catalyze wide range of reactions, mainly one-electron oxidation of monophenols, diphenols and polyphenols as well as diamines, aromatic amines and related substances such as N-heterocycles and phenothiazines (Zdarta et al., 2018). Glutaraldehyde was employed as the bifunctional cross-linker which primarily bridges free amino groups, usually of lysine residues, on the surface of neighbouring enzyme molecules and/or amino groups from the supporting carrier (Sheldon, 2017; Sheldon, 2018).

Following the Introduction part, Chapter 2 will introduce the experimental methods applied for the material syntheses including UPA monolith, APTES silanized UPA powders, and laccase T. cross-linked UPA biocatalysts. Moreover, batch experiments, characterizations, law and fitting models, and thermodynamic parameter calculations will also be introduced.

Chapter 3 and Chapter 4 will introduce the two main experimental studies conducted during my PhD study, respectively:

Chapter 3: Ultraporous aluminas for highly efficient removal of RBBR

In this study, the experimental factors that affect the material adsorption performances including initial pH, contact time, and temperature were comprehensively studied by batch experiments. Different kinetic and isotherm models were also applied to fit the adsorption equilibrium data.

Chapter 4: Laccase T. cross-linked immobilized ultraporous aluminas for efficient biodegradation of RBBR

In this study, laccase T. was cross-linked immobilized on ultraporous aluminas for an effective biodegradation of RBBR. The effect of glutaraldehyde concentration on laccase T. cross-linking degree, comparison of sequential and glutaraldehyde post-treatment protocols, the biocatalyst stability including pH stability, thermal

stability, storage stability, and reusability, and the continuous biodegradation kinetics of RBBR by the synthesized laccase T. cross-linked UPA biocatalysts were comprehensively studied.

Finally, Chapter 5 will make a conclusion of the obtained results and give some suggestions for future research directions.

The findings of my PhD study highlight the potentials of inorganic materials in enzyme immobilization and industrial wastewater treatment, which can broaden our understanding of their practical applications in the environmental field.

1.7. References

- Arregui, L.; Ayala, M.; Gomez-Gil, X.; Gutierrez-Soto, G.; Hernandez-Luna, C.E.; Herrera de Los Santos, M.; Levin, L.; Rojo-Dominguez, A.; Romero-Martinez, D.; Saparrat, M.C.N.; Trujillo-Roldan, M.A.; Valdez-Cruz, N.A., Laccases: structure, function, and potential application in water bioremediation, *Microbial Cell Factories*, 18 (2019) 1–33.
- Ba, S.; Haroune, L.; Cruz-Morato, C; Jacquet, C; Touahar, I.E.; Bellenger, J.-P.; Legault, C.Y.; Jones, J.P.; Cabana, H., Synthesis and characterization of combined cross-linked laccase and tyrosinase aggregates transforming acetaminophen as a model phenolic compound in wastewaters, *Science of the Total Environment*, 487 (2014) 748–755.
- Barrios-Estrada, C.; Rostro-Alanis, M.J.; Parra, A.L.; Belleville, M.-P.; Sanchez-Marcano, J.; Iqbal, H.M.N.; Parra-Saldivar, R., Potentialities of active membranes with immobilized laccase for Bisphenol A degradation, *International Journal of Biological Macromolecules*, 108 (2018) 837–844.
- Beauvy, M.; Vignes, J.-L.; Michel, D.; Mazerolles, L.; Frappart, C.; Di Costanzo, T., Process for the preparation of monolithic hydrated alumina, amorphous or crystallized alumina, aluminates and composite materials by metal aluminum oxidation or aluminum alloy (in French), European Patent, (CNRS–CEA) (2004) FR2847569.
- Beauvy, M.; Vignes, J.-L.; Michel, D.; Mazerolles, L.; Frappart, C.; Di Costanzo, T., Method for preparing monolithic hydrated aluminas and composite materials (in French and German), European Patent, (CNRS–CEA) (2005) EP1562859.
- Bharagava, R.N.; Chandra, R., Effect of bacteria treated and untreated post-methanated distillery effluent (PMDE) on seed germination, seedling growth and amylase activity in *Phaseolus mungo* L, *Journal of Hazardous Materials*, 180 (2010) 730–734.
- Bilal, M.; Asgher, M.; Parra-Saldivar, R.; Hu, H.-B.; Wang, W.; Zhang, X.-H.; Iqbal,

-
- H.M.N., Immobilized ligninolytic enzymes: An innovative and environmental responsive technology to tackle dye-based industrial pollutants—A review, *Science of the Total Environment*, 576 (2017) 646–659.
- Bonnarme, P.; Jeffries, T.W., Mn(II) regulation of lignin peroxidases and manganese-dependent peroxidases from lignin-degrading white rot fungi, *Applied and Environmental Microbiology*, 56 (1990) 210–217.
- Bousslama, M.; Amamra, M.C.; Brinza, O.; Tieng, S.; Chhor, K.; Abderrabba, M.; Vignes, J.-L.; Kanaev, A., Isolation of titania nanoparticles in monolithic ultraporous alumina: Effect of nanoparticle aggregation on anatase phase stability and photo-catalytic activity, *Applied Catalysis A: General*, 402 (2011) 156–161.
- Bousslama, M.; Amamra, M.C.; Jia, Z.-X.; Ben Amar, M.; Chhor, K.; Brinza, O.; Abderrabba, M.; Vignes, J.-L.; Kanaev, A., Nanoparticulate TiO₂-Al₂O₃ photocatalytic media: Effect of particle size and polymorphism on photocatalytic activity, *ACS Catalysis*, 2 (2012) 1884–1892.
- Brena, B.; González-Pombo, P.; Batista-Viera F., Immobilization of enzymes: A literature survey. In *Immobilization of Enzymes and Cells*, Walker, J.M. (Ed.), Springer, ISBN: 978-1-62703-549-1 (2013) 14–31.
- Cao, L.-Q., Carrier-bound immobilized enzymes: principles, application and design, Wiley-VCH, ISBN: 978-3-527-60766-2 (2006).
- Cha, J.-Y.; Kim, T.-W.; Choi, J.H.; Jang, K.-S.; Khaleda, L.; Kim, W.-Y.; Jeon, J.-R., Fungal laccase-catalyzed oxidation of naturally occurring phenols for enhanced germination and salt tolerance of *Arabidopsis thaliana*: A green route for synthesizing humic-like fertilizers, *Journal of Agricultural and Food Chemistry*, 65 (2017) 1167–1177.
- Chandra, R.; Bharagava, R.N.; Yadav, S.; Mohan, D., Accumulation and distribution of toxic metals in wheat (*Triticum aestivum* L.) and Indian mustard (*Brassica campestris* L.) irrigated with distillery and tannery effluents, *Journal of*

-
- Hazardous Materials, 162 (2009) 1514–1521.
- Chandra, R.; Bharagava, R.N.; Kapley, A.; Purohit, H.J., Bacterial diversity, organic pollutants and their metabolites in two aeration lagoons of common effluent treatment plant during the degradation and detoxification of tannery wastewater, *Bioresource Technology*, 102 (2011) 2333–2341.
- Chandra, R.; Bharagava, R.N.; Kapley, A.; Purohit, H.J., Characterization of *Phargmites cummunis* rhizosphere bacterial communities and metabolic products during the two stage sequential treatment of post methanated distillery effluent by bacteria and wetland plants, *Bioresource Technology*, 103 (2012) 78–86.
- Cheremisinoff, N.P., An overview of water and wastewater treatment. In *Handbook of water and wastewater treatment technologies*, Cheremisinoff, N.P. (Ed.), Butterworth-Heinemann, ISBN: 978-075-067-498-0 (2002) 1–61.
- Chiavola, A.; Tchieda, V.K.; D’Amato, E.; Chianese, A.; Kanaev, A., Synthesis and characterization of nanometric titania coated on granular alumina for arsenic removal, *Chemical Engineering Transactions*, 47 (2016) 331–336.
- Cicek, F.; Özer, D.; Özer, A.; Özer, A., Low cost removal of reactive dyes using wheat bran, *Journal of Hazardous Materials*, 146 (2007) 408–416.
- Enguita, F.J.; Martins, L.O.; Henriques, A.O.; Carrondo, M.A., Crystal structure of a bacterial endospore coat component, *Journal of Biological Chemistry*, 278 (2003) 19416–19425.
- Faccio, G.; Kruus, K.; Saloheimo, M.; Thöny-Meyer, L., Bacterial tyrosinases and their applications, *Process Biochemistry*, 47 (2012) 1749–1760.
- Glenn, J.K.; Akileswaran, L.; Gold, M.H., Mn(II) oxidation is the principal function of the extracellular Mn-peroxidase from *Phanerochaete chrysosporium*, *Archives of Biochemistry and Biophysics*, 251 (1986) 688–696.
- Guzik, U.; Hupert-Kocurek, K.; Wojcieszynska, D., Immobilization as a strategy for improving enzyme properties-application to oxidoreductases, *Molecules*, 19 (2014) 8995–9018.

-
- Gök, Ö.; Özcan, A.S.; Özcan, A., Adsorption behavior of a textile dye of Reactive Blue 19 from aqueous solutions onto modified bentonite, *Applied Surface Science*, 256 (2010) 5439–5443.
- Hadibarata, T.; Yusoff, A.R.M.; Ayu, R., Decolorization and metabolism of anthraquinone-type dye by laccase of white-rot fungi *Polyporus* sp. S133, *Water, Air, & Soil Pollution*, 223 (2011) 933–941.
- Hofrichter, M., Review: lignin conversion by manganese peroxidase (MnP), *Enzyme and Microbial Technology*, 30 (2002) 454–466.
- Hou, J.-W.; Dong, G.-X.; Ye, Y.; Chen, V., Laccase immobilization on titania nanoparticles and titania-functionalized membranes, *Journal of Membrane Science*, 452 (2014) 229–240.
- Ihekata, K.; Nicell, J.A., Characterization of tyrosinase for the treatment of aqueous phenols, *Bioresource Technology*, 74 (2000) 191–199.
- Kant, R., Textile dyeing industry an environmental hazard, *Natural Science*, 4 (2012) 22–26.
- Khatim, O.; Nguyen, T.H.N.; Amamra, M.; Museur, L.; Khodan, A.; Kanaev, A., Synthesis and photoluminescence properties of nanostructured mullite/ α -Al₂O₃, *Acta Materialia*, 71 (2014) 108–116.
- Land, E.J.; Ramsden, C.A.; Riley, P.A., Tyrosinase autoactivation and the chemistry of ortho-quinone amines, *Accounts of Chemical Research*, 2003 (36) 300–308.
- Lassouane, F.; A ĩ-Amar, H.; Amrani, S.; Rodriguez-Couto, S., A promising laccase immobilization approach for Bisphenol A removal from aqueous solutions, *Bioresource Technology*, 271 (2019) 360–367.
- Lavis, L.D., Teaching old dyes new tricks: Biological probes built from fluoresceins and rhodamines, *Annual Review of Biochemistry*, 86 (2017) 825–843.
- Le, T.T.; Murugesan, K.; Lee, C.-S.; Vu, C.H.; Chang, Y.-S.; Jeon, J.-R., Degradation of synthetic pollutants in real wastewater using laccase encapsulated in core–shell magnetic copper alginate beads, *Bioresource Technology*, 216 (2016) 203–

- Legerska, B.; Chmelova, D.; Ondrejovic, M., Degradation of synthetic dyes by laccases – A mini review, *Nova Biotechnological et Chimica*, 15 (2016) 1–15.
- Li, J.; Wang, X.-X.; Zhao, G.-X.; Chen, C.-L.; Chai, Z.-F.; Alsaedi, A.; Hayat, T.; Wang, X.-K., Metal-organic framework-based materials: Superior adsorbents for the capture of toxic and radioactive metal ions, *Chemical Society Reviews*, 47 (2018) 2322–2356.
- López-Gallego, F.; Guisán, J.M.; Betancor, L., Glutaraldehyde-mediated protein immobilization. In *Immobilization of Enzymes and Cells*, Walker, J.M. (Ed.), Springer, ISBN: 978-1-62703-549-1 (2013) 33–41.
- Madrakian, T.; Afkhami, A.; Jalal, N.R.; Ahmadi, M., Kinetic and thermodynamic studies of the adsorption of several anionic dyes from water samples on magnetite-modified multi-walled carbon nanotubes, *Separation and Purification Technology*, 48 (2013) 2638–2648.
- Madrakian, T.; Afkhami, A.; Mahmood-Kashani, H.; Ahmadi, M., Adsorption of some cationic and anionic dyes on magnetite nanoparticles-modified activated carbon from aqueous solutions: Equilibrium and kinetics study, *Journal of the Iranian Chemical Society*, 10 (2012) 481–489.
- Matijošytė, I.; Arends, I.W.C.E.; de Vries, S.; Sheldon, R.A., Preparation and use of cross-linked enzyme aggregates (CLEAs) of laccases, *Journal of Molecular Catalysis B: Enzymatic*, 62 (2010) 142–148.
- McIntosh, R.; Haines, R.S.; Benson, G.C., The effect of physical adsorption on the electrical resistance of activated carbon, *The Journal of Chemical Physics*, 15 (1947) 17–27.
- Mechichi, T.; Mhiri, N.; Sayadi, S., Remazol Brilliant Blue R decolourization by the laccase from *Trametes trogii*, *Chemosphere*, 64 (2006) 998–1005.
- Moussavi, G.; Mahmoudi, M., Removal of azo and anthraquinone reactive dyes from industrial wastewaters using MgO nanoparticles, *Journal of Hazardous Materials*,

168 (2009) 806–812.

Nguyen, T.H.N., Elaboration and modifications of nanofibrous Al₂O₃, Chemical and Process Engineering, Université Sorbonne Paris Cité (2016) PhD thesis.

Osma, J.F.; Toca-Herrera, J.L.; Rodriguez-Couto, S., Transformation pathway of Remazol Brilliant Blue R by immobilised laccase, *Bioresource Technology*, 101 (2010) 8509–8514.

Özsoy, H.D.; Ünyayar, A.; Mazmanci, M.A., Decolourisation of reactive textile dyes Drimarene Blue X3LR and Remazol Brilliant Blue R by *Funalia trogii* ATCC 200800, *Biodegradation*, 16 (2005) 195–204.

Patel, B.H., Natural dyes. In *Handbook of Textile and Industrial Dyeing*, Clark, M. (Ed.), Woodhead Publishing, ISBN: 978-1-84569-695-5 (2011) 395–424.

Paul, R.; Malanker, J.V.; Naik, S.R., Natural dyes: Classification, extraction and fastness properties, *Textile Dyer and Printer*, 29 (1996) 16–24.

Qiu, P.-P.; Ma, B.; Hung, C.-T.; Li, W.; Zhao, D.-Y., Spherical mesoporous materials from single to multilevel architectures, *Accounts of Chemical Research*, 52 (2019) 2928–2938.

Routoula, E.; Patwardhan, S.V., Degradation of anthraquinone dyes from effluents: A review focusing on enzymatic dye degradation with industrial potential, *Environmental Science & Technology*, 54 (2020) 647–664.

Sahu, O.; Singh, N., Significance of bioadsorption process on textile industry wastewater. In *The Impact and Prospects of Green Chemistry for Textile Technology*, Ul-Islam, S.; Butola, B.S. (Ed.), Woodhead Publishing, ISBN 978-0-08102-491-1 (2019) 367–416.

Sanchez-Ferrer, A.; Rodriguez-Lopez, J. N.; Garcia-Canovas, F.; Garcia-Camona, F., Tyrosinase: a comprehensive review of its mechanism, *Biochimica et Biophysica Acta*, 1247 (1995) 1–11.

Saxena, S.; Raja, A.S.M., Natural dyes: Sources, chemistry, application and sustainability issues. In *Roadmap to Sustainable Textiles and Clothing*:

-
- Eco-friendly Raw Materials, Technologies, and Processing Methods*, Muthu, S.S. (Ed.), Springer, ISBN: 978-981-287-065-0 (2014) 37–80.
- Selinheimo, E.; NiEidhin, D.; Steffensen, C.; Nielsen, J.; Lomascolo, A.; Halaouli, S.; Record, E.; O’Beirne, D.; Buchert, J.; Kruus, J., Comparison of the characteristics of fungal and plant tyrosinases, *Journal of Biotechnology*, 130 (2007) 471–480.
- Senthil Kumar, P.; Saravanan, A., Sustainable wastewater treatments in textile sector. In *Sustainable Fibres and Textiles*, Muthu, S.S. (Ed.), Woodhead Publishing, ISBN: 978-0-08-102041-8 (2017) 323–346.
- Sheldon, R.A., Enzyme-catalyzed cascade reactions. In *Multi-Step Enzyme Catalysis: Biotransformations and Chemoenzymatic Synthesis*, Garcia-Junceda, E. (Ed.), Wiley-VCH, ISBN: 978-3-527-31921-3 (2008) 109–135.
- Sheldon, R.A., Fundamentals of green chemistry: Efficiency in reaction design, *Chemical Society Reviews*, 41 (2012) 1437–1451.
- Sheldon, R.A., Cross-linked enzyme aggregates (CLEAs): From concept to industrial biocatalyst. In *Biocatalysis: An Industrial Perspective*, Gonzalo, G.; Mar á, P.D. (Ed.), Royal Society of Chemistry, ISBN: 978-1-78262-619-0 (2017) 363–396.
- Sheldon, R.A.; Pelt, S.V., Enzyme immobilisation in biocatalysis: Why, what and how, *Chemical Society Reviews*, 42 (2013) 6223–6235.
- Sheldon, R.A.; Woodley, J.M., Role of biocatalysis in sustainable chemistry, *Chemical Reviews*, 118 (2018) 801–838.
- Shuster, V.; Fishman, A., Isolation, Cloning and characterization of a tyrosinase with improved activity in organic solvents from *Bacillus megaterium*, *Journal of Molecular Microbiology and Biotechnology*, 17 (2009) 188–200.
- Siddiqui, S.I.; Fatima, B.; Tara, N.; Rathi, G.; Chaudhry, S.A., Recent advances in remediation of synthetic dyes from wastewaters using sustainable and low-cost adsorbents, In *The Impact and Prospects of Green Chemistry for Textile Technology*, Ul-Islam, S.; Butola, B.S. (Ed.), Woodhead Publishing, ISBN

978-0-08102-491-1 (2019) 471–507.

- Tagger, S.; Perissol, C.; Gil, G.; Vogt, G.; Le Petit, J., Phenoloxidases of the white-rot fungus *Marasmius quercophilus* isolated from an evergreen oak litter (*Quercus ilex* L.), *Enzyme and Microbial Technology*, 23 (1998) 372–379.
- Tchieda, V.K.; D’Amato, E.; Chiavola, A.; Parisi, M.; Chianese, A.; Amamra, M.; Kanaev, A., Removal of arsenic by alumina: Effects of material size, additives, and water contaminants, *Clean-Soil Air Water*, 44 (2016) 496–505.
- Thommes, M.; Guillet-Nicolas, R.; Cychosz, K.A., Physical adsorption characterization of mesoporous zeolites. In *Mesoporous Zeolites: Preparation, Characterization and Applications*, Garc á-Mart ínez, J.; Li, K.H. (Ed.), Wiley-VCH, ISBN: 978-9-401-06392-0 (2015) 349–383.
- Torres-Salas, P.; del Monte-Martinez, A.; Cuti ño-Avila, B.; Rodriguez-Colinas, B.; Alcalde, M.; Ballesteros, A.O.; Plou, F.J., Immobilized biocatalysts: Novel approaches and tools for binding enzymes to supports, *Advanced Materials*, 23 (2011) 5275–5282.
- Tsai, W.T.; Chang, C.-Y.; Lin, M.-C.; Chien, S.-F.; Sun, H.-F.; Hsieh, M.F., Adsorption of acid dye onto activated carbon prepared from agricultural waste bagasse by $ZnCl_2$ activation, *Chemosphere*, 45 (2001) 51–58.
- Verma, S.; Gupta, G., Natural dyes and its applications: A brief review, *International Journal of Research and Analytical Reviews*, 4 (2017) 1–4.
- Vignes, J.-L.; Frappart, C.; Di Costanzo, T.; Rouchaud, J.-C.; Mazerolles, L.; Michel, D., Ultraporous monoliths of alumina prepared at room temperature by aluminium oxidation, *Journal of Materials Science*, 43 (2008) 1234–1240.
- Woolard, C.D.; Strong, J.; Erasmus, C.R., Evaluation of the use of modified coal ash as a potential sorbent for organic waste streams. *Applied Geochemistry*, 17 (2002) 1159–1164.
- Xu, H.; Boeuf, G.; Jia, Z.-X.; Zhu, K.-R.; Nikravech, M.; Kanaev, A.; Azouani, R.; Traore, M.; Elm’selmi, A., Solvent-free synthesized monolithic ultraporous

-
- aluminas for highly efficient removal of Remazol Brilliant Blue R: Equilibrium, kinetic, and thermodynamic studies, *Materials*, 14 (2021) 1–19.
- Yehia, R.S.; Rodriguez-Couto, S., Discoloration of the azo dye Congo Red by manganese-dependent peroxidase from *Pleurotus sajor caju*, *Applied Biochemistry and Microbiology*, 53 (2017) 222–229.
- Zdarta, J.; Meyer, A.S.; Jesionowski, T.; Pinelo, M., A general overview of support materials for enzyme immobilization: Characteristics, properties, practical utility, *Catalysts*, 8 (2018) 1–27.
- Zdarta, J.; Meyer, A.S.; Jesionowski, T.; Pinelo, M., Developments in support materials for immobilization of oxidoreductases: A comprehensive review, *Advances in Colloid and Interface Science*, 258 (2018) 1–20.
- Zhang, L.-Q.; Sun, Y., Poly(carboxybetaine methacrylate)-grafted silica nanoparticle: A novel carrier for enzyme immobilization, *Biochemical Engineering Journal*, 132 (2018) 122–129.
- Zhu, K.-R.; Xu, H.; Chen, C.-L.; Ren, X.-M.; Alsaedi, A.; Hayat, T., Encapsulation of Fe⁰-dominated Fe₃O₄/Fe⁰/Fe₃C nanoparticles into carbonized polydopamine nanospheres for catalytic degradation of tetracycline via persulfate activation, *Chemical Engineering Journal*, 372 (2019) 304–311.
- Zucca, P.; Sanjust, E., Inorganic materials as supports for covalent enzyme immobilization: methods and mechanisms molecules, *Molecules*, 19 (2014) 14139–14194.

Chapter 2: Experimental methods

In this chapter, several parts including experimental reagents, material syntheses, batch experiments, characterization techniques, Beer-Lambert law, kinetic models, isotherm models, and thermodynamic parameter calculations will be introduced in detail.

2.1. Experimental reagents

The name (molecular formula, if applicable), CAS number, and supplier of the main experimental reagents are listed in Table 2.1 as follows. In terms of the full name of some abbreviations, please switch to the section “Appendix B: List of abbreviations”. All the experimental reagents used in this thesis were of the analytical grade and used as received directly without further purification. Milli-Q water (Millipore Corp., Burlington, MA, USA) with a specific resistivity of $18.2 \text{ M}\Omega \cdot \text{cm}^{-1}$ at $25 \text{ }^\circ\text{C}$ was used to prepare solutions throughout the experiments.

Table 2.1. – Description of the main experimental reagents used in this thesis.

Name (molecular formula)	CAS number	Supplier
ABTS ^a (HPLC)	30931-67-0	Sigma-Aldrich, Inc.
acetic acid (CH ₃ COOH)	64-19-7	Sigma-Aldrich, Inc.
acetone	67-64-1	Sigma-Aldrich, Inc.
ammonium sulfate ((NH ₄) ₂ SO ₄)	7783-20-2	Sigma-Aldrich, Inc.
APTES ^a (99%)	919-30-2	Sigma-Aldrich, Inc.
disodium hydrogen phosphate (Na ₂ HPO ₄ · 2H ₂ O)	10028-24-7	Sigma-Aldrich, Inc.
fresh egg albumin	ND ^b	Supermarch éLiDL, France

glutaraldehyde (GA, 25% of v/v)	111-30-8	Sigma-Aldrich, Inc.
hydrochloric acid (HCl)	7647-01-0	Sigma-Aldrich, Inc.
isopropanol	67-63-0	Sigma-Aldrich, Inc.
laccase T. ^a ($\geq 0.5 \text{ U} \cdot \text{mg}^{-1}$)	80498-15-3	Sigma-Aldrich, Inc.
mercury(II) nitrate monohydrate ($\text{Hg}(\text{NO}_3)_2 \cdot \text{H}_2\text{O}$, $\geq 98.5\%$)	7783-34-8	Sigma-Aldrich, Inc.
phosphoric acid (H_3PO_4)	7664-38-2	Sigma-Aldrich, Inc.
RBBR ^a (also called RB19)	2580-78-1	Sigma-Aldrich, Inc.
silver nitrate (AgNO_3 , $\geq 99.0\%$)	7761-88-8	Sigma-Aldrich, Inc.
sodium acetate (CH_3COONa)	127-09-3	Sigma-Aldrich, Inc.
sodium hydroxide (NaOH)	1310-73-2	Sigma-Aldrich, Inc.
Tris hydrochloride (Tris-HCl, ultra pure)	1185-53-1	Sigma-Aldrich, Inc.

^a Abbreviation, full name can be found in the section “Appendix B: List of abbreviations”.

^b ND: No data.

Figures 2.1a and 2.1b showed the physicochemical characteristics of RBBR and its molecular compositions (wt%) including C (42.17%), H (2.57%), N (4.47%), Na (7.34%), O (28.09%), and S (15.35%) (Özsoy et al., 2005). Figure 2.1c showed the visible spectral curves of RBBR before and after adsorption retained by UPA(θ) powders monitoring with time.

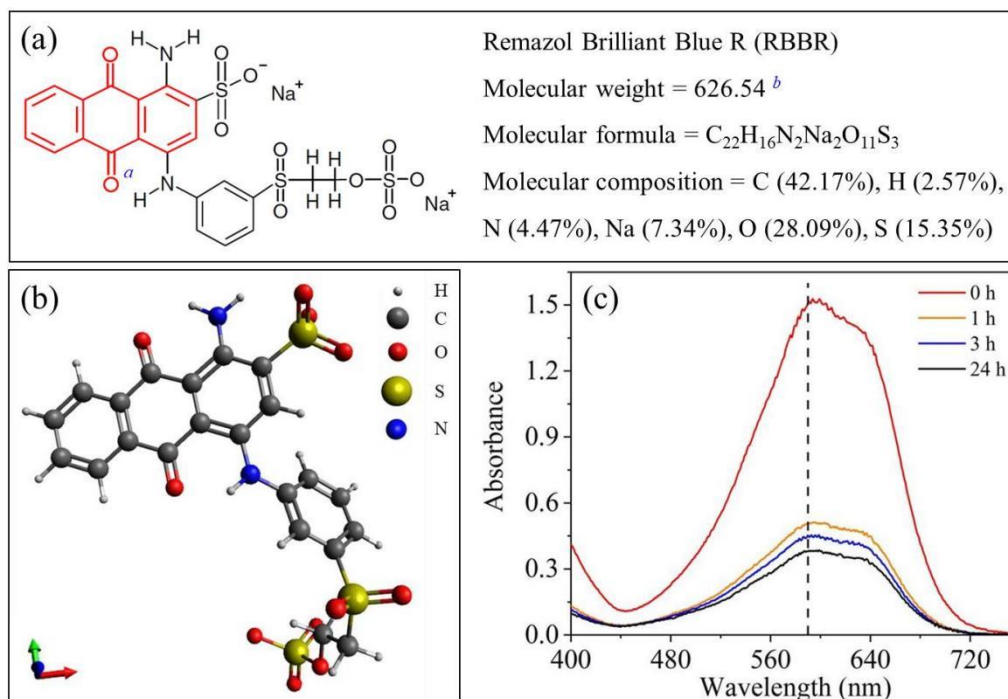


Figure 2.1. – (a) Chemical structural diagram of RBBR, (b) 3-D model of RBBR molecule with two negative charges, and (c) visible spectral curves of RBBR before and after adsorption retained by UPA(θ) powders monitoring with time.

^a Highlighted: Chemical structure of the anthracene-based anthraquinone group which consists of three fused benzene rings with two carbonyl groups on the central ring.

^b Molecular weight in nonionized form.

2.2. Material syntheses

The raw laminated metallic aluminium plate (100×100 mm, 1.0 mm of thickness, 99.99% of purity) and disposable 2 mL polystyrene column were supplied by Goodfellow Cambridge Ltd. (Huntingdon, UK) and ThermoFisher Scientific Inc. (Waltham, MA, USA), respectively.

2.2.1. Syntheses of UPA monolith, UPA(γ), UPA(θ), and UPA(α) powders

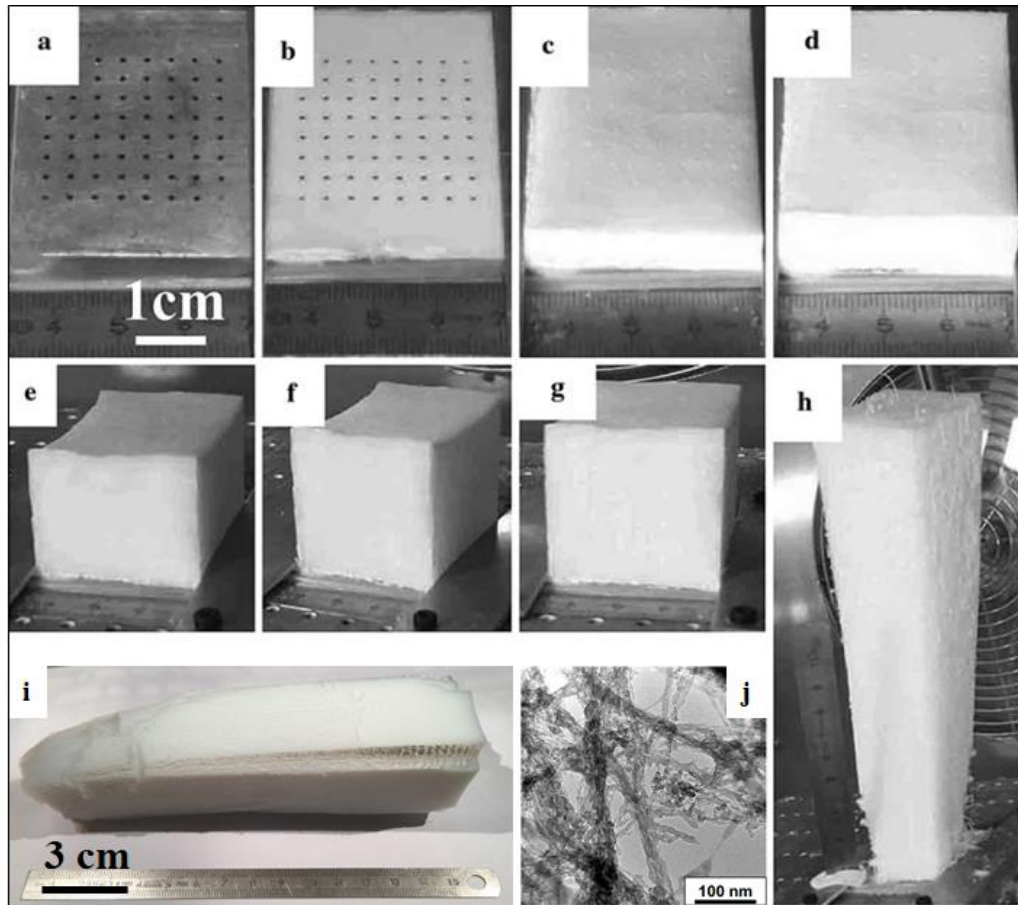


Figure 2.2. – Photos of (a) raw aluminium grid, UPA monolith sample after (b) 10 min, (c) 1 h, (d) 2 h, (e) 4 h, (f) 5 h, (g) 6 h, and (h) 16 h of continuous growth process. $T = 20\text{ }^{\circ}\text{C}$, RH (relative humidity) = 70%, $C[\text{Hg}(\text{NO}_3)_2] = 0.05\text{ mol L}^{-1}$, $C[\text{AgNO}_3] = 0.01\text{ mol L}^{-1}$ (Vignes et al., 2008; Nguyen, 2016). (i) Photo and (j) TEM image of UPA monolith sample (Khodan et al., 2018).

The UPA monolith samples were synthesized via a facile oxidation process according to the previous studies (Figure 2.2) (Vignes et al., 2008; Bouslama et al., 2012; Khatim et al., 2014; Nguyen, 2016; Khodan et al., 2018). Briefly, high purity but fragile UPA monolith samples were obtained with a growth rate of $\sim 1\text{ cm h}^{-1}$ at room temperature in a humid atmosphere (70–80% RH) by the oxidation of metallic aluminium plates through a liquid layer of mercury-silver amalgam (Figure 2.3) (Vignes et al., 2008).



Figure 2.3. – Photo of the experimental instrument for the synthesis of UPA monolith.

According to Vignes et al. (2008), complete and approximately half oxidation of aluminium plate can be obtained by using plates with 99.999% and 99.99% of purity, respectively. Anhydrous monolithic UPA can be obtained from fragile UPA, converting to amorphous UPA, polycrystalline UPA(γ), UPA(θ), and UPA(α) monolith under 4 h of isochronous annealing treatment in air at < 870, 950, 1150, and 1350 °C, respectively (Figure 2.4) (Vignes et al., 2008; Bouslama et al., 2011; Bouslama et al., 2012; Nguyen, 2016; Khodan et al., 2018). After rigorous grinding process, the UPA powders with different polycrystalline phases (i.e., γ , θ , and α) can be accordingly obtained. Compared with UPA(γ) ($201.7 \text{ m}^2 \text{ g}^{-1}$) and UPA(θ) ($93.4 \text{ m}^2 \text{ g}^{-1}$) monoliths, UPA(α) monolith possesses the minimal specific surface area ($5.7 \text{ m}^2 \text{ g}^{-1}$) for laccase T. immobilization but the highest mechanical stability to be ground into powders (Xu et al., 2021). Therefore, except where otherwise specified, in the following studies regarding laccase T. immobilization (Chapter 4), the term of UPA mainly refers to UPA materials in γ and θ polycrystalline phases.

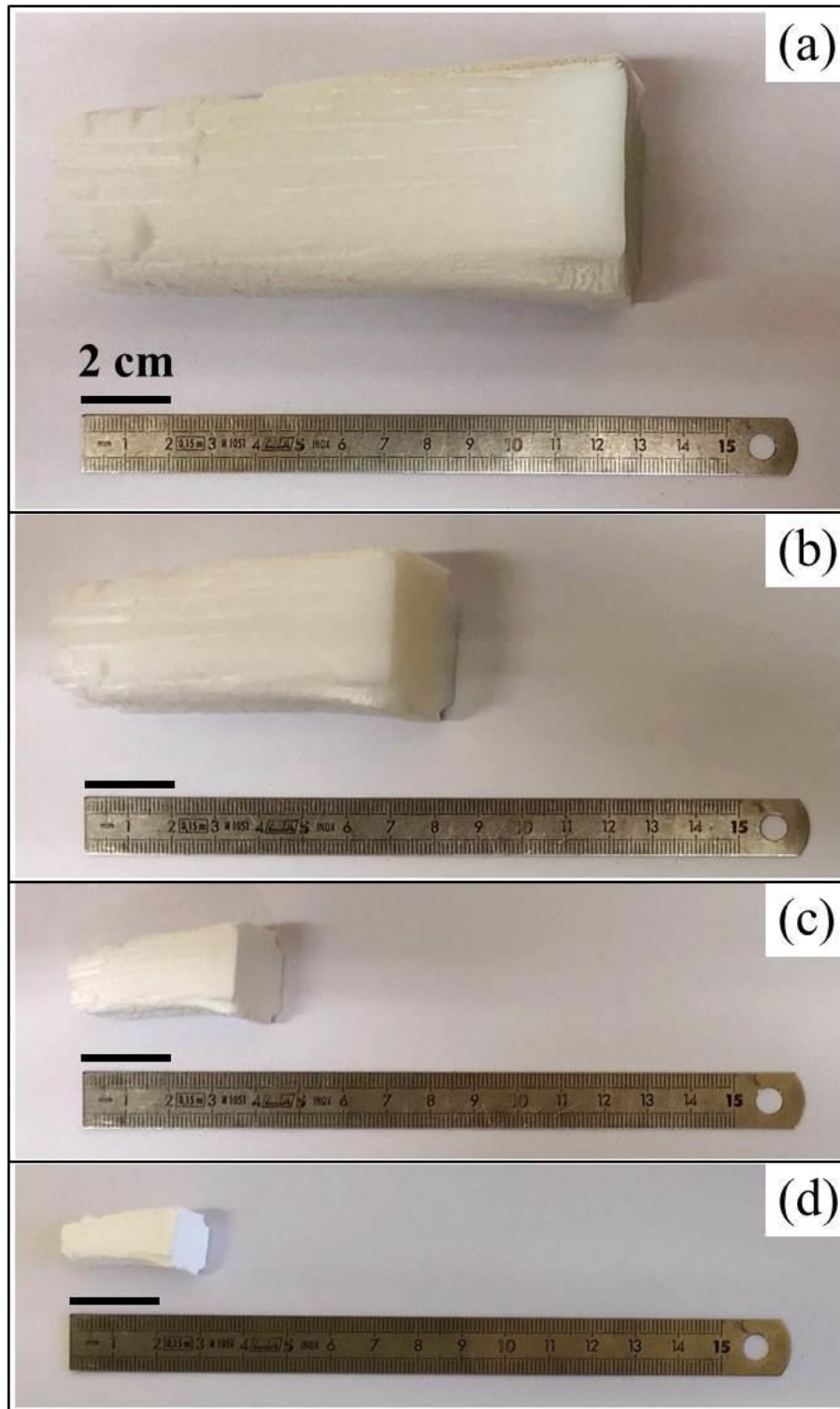


Figure 2.4. – Photos of (a) raw fragile UPA, under 4 h of isochronous annealing treatment in air at (b) 950 °C (UPA(γ)), (c) 1150 °C (UPA(θ)), and (d) 1350 °C (UPA(α) monolith).

2.2.2. Synthesis of APTES silanized UPA powders

In terms of glutaraldehyde cross-linking process, aminosilane coupling APTES is one of the most frequently used organosilane agents for preparing amino group terminated compounds as the anchor points for aldehyde groups (Landoulsi et al., 2011; Hou et al., 2014). Prior to the immobilization procedure, UPA powders were silanized with 2.5% (v/v) APTES in acetone at 45 °C and 100 rpm for 24 h, followed by washing the obtained powders with phosphate buffer for three times to remove any residual organics (Figure 2.5).

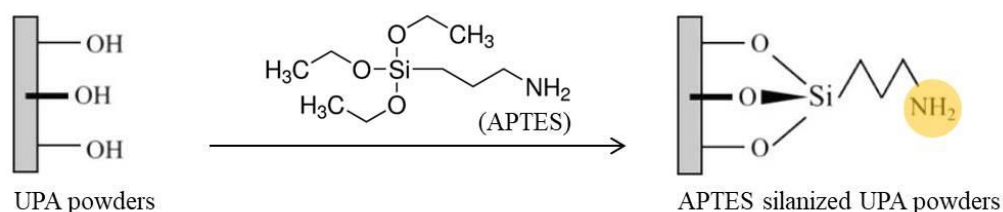


Figure 2.5. – Schematic diagram of UPA silanization by APTES.

2.2.3. Synthesis of laccase T. cross-linked UPA biocatalysts

2.2.3.1. Sequential immobilization

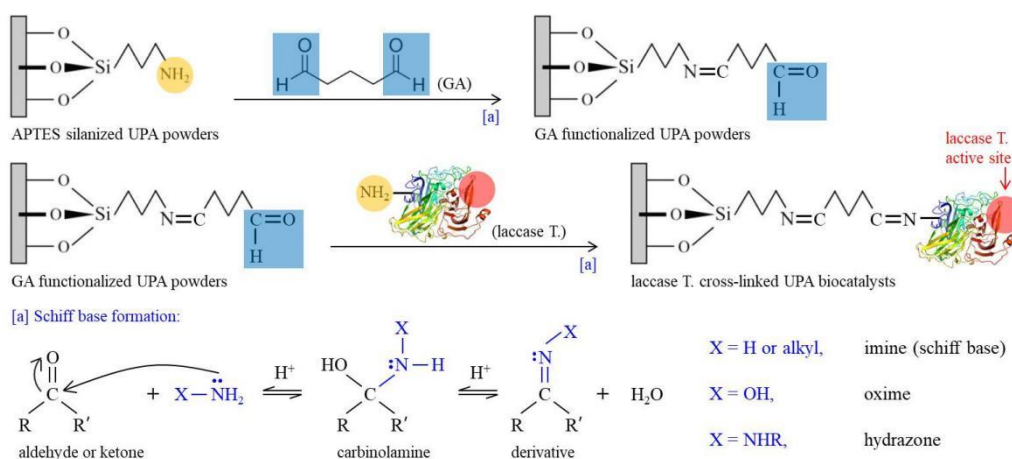


Figure 2.6. – Schematic diagram of sequential immobilization protocol for laccase T. immobilization on UPA surfaces.

In this process, a given amount of APTES silanized UPA powders were dispersed in glutaraldehyde solution with different concentrations (i.e., 0.25, 0.50, 1.00, 1.50, and 3.00% of v/v) under neutral conditions. The mixture was kept under stirring at 20 °C and 100 rpm for 6 h, followed by the washing procedure as mentioned above to remove unreacted glutaraldehyde molecules. After glutaraldehyde functionalization, the obtained powders were suspended in laccase T. solution, resulting in Schiff base formation and subsequent cross-linking of laccase T. with glutaraldehyde functionalized UPA powders (Figure 2.6).

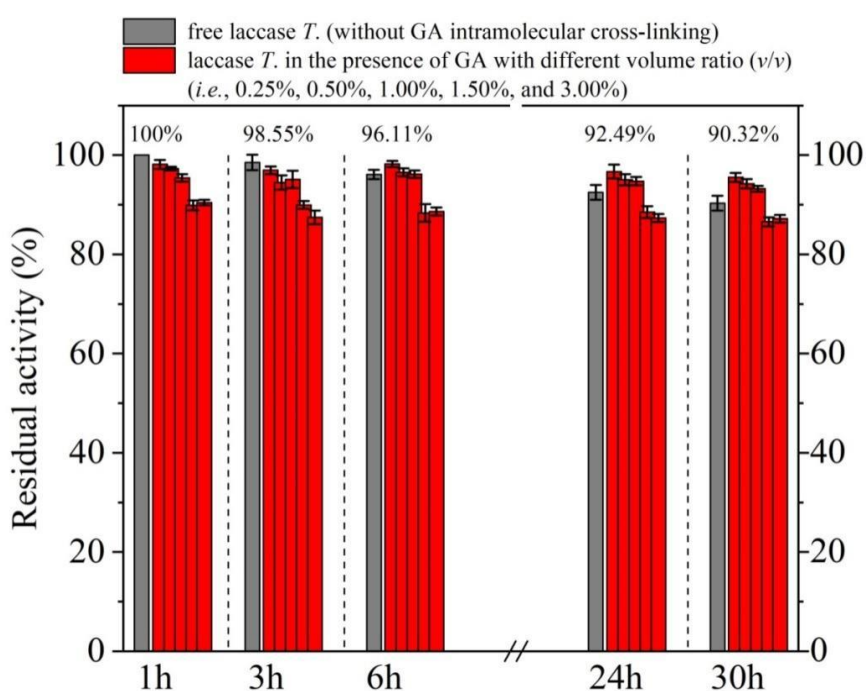


Figure 2.7. – Effect of reaction time on the residual enzyme activity of laccase T. in the absence and presence of glutaraldehyde with different concentrations (i.e., 0 as the control, 0.25, 0.50, 1.00, 1.50, and 3.00% of v/v).

According to Matijošytė et al. (2010), the minimal cross-linking time for laccase T. should not be shorter than 19 h, and higher specific activity of laccase T. can be observed at room temperature. Furthermore, cross-linking time had negligible effect on the activity loss of free laccase T. in the presence of glutaraldehyde (Figure 2.7). Consequently, in order to obtain complete cross-linking equilibrium, the mixture was kept under stirring at 20 °C and 100 rpm for 24 h.

2.2.3.2. Glutaraldehyde post-treatment

Unlike the sequential immobilization protocol, the APTES silanized UPA powders were firstly suspended in laccase T. solution without glutaraldehyde functionalization step, and the mixture was kept under stirring at 20 °C and 100 rpm for 24 h. Then the powders were separated by centrifugation (4000 rpm, 5 min) and dispersed in glutaraldehyde solution at 20 °C and 100 rpm for 6 h with glutaraldehyde concentration which led to the highest activity recovery of laccase T. by using ABTS as the substrate (Figure 2.8).

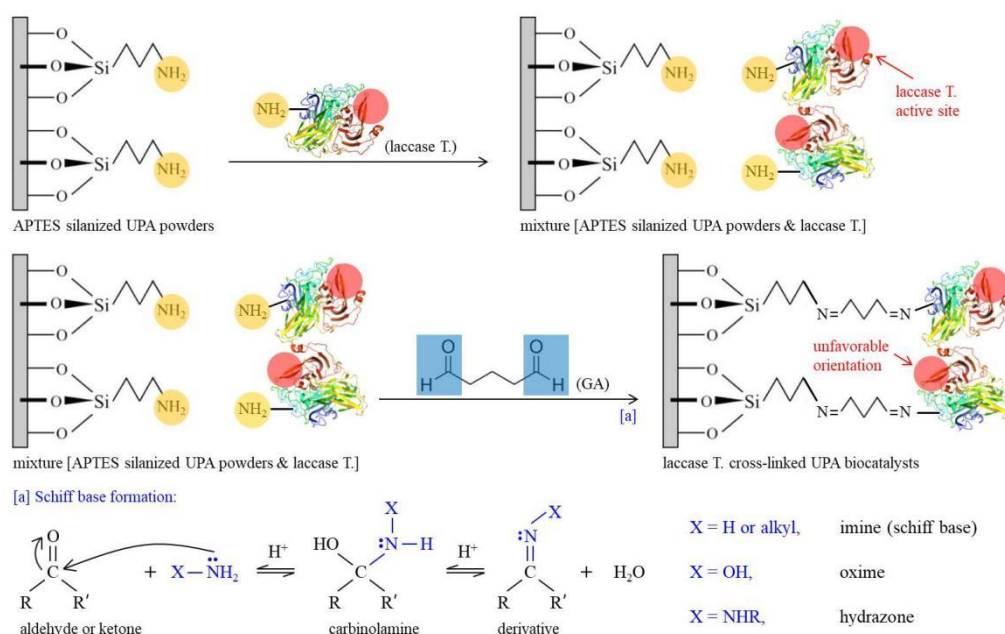


Figure 2.8. – Schematic diagram of glutaraldehyde post-treatment protocol for laccase T. immobilization on UPA surfaces.

2.2.4. Synthesis of laccase T./UPA(γ) powders

For comparison purpose, the laccase T. entrapped UPA(γ) powders by non-covalent bonding (laccase T./UPA(γ)) were synthesized by following similar protocol as mentioned above without either UPA silanization or cross-linking operation of laccase T. by using glutaraldehyde.

2.3. Batch experiments

2.3.1. RBBR adsorption retained by UPA(θ) powders

Except for the study of adsorption isotherms, the adsorption process of RBBR retained by UPA(θ) powders was carried out by batch experiments at $T = 310\text{ K}$ ($37\text{ }^\circ\text{C}$). In order to achieve homogeneous dispersion, the certain amount of UPA(θ) powders was taken immediately to prepare suspension and shaken for 1 min on the multifunctional vortex oscillator before the corresponding experiment. Appropriate volumes of RBBR (10 g L^{-1}) and sodium acetate (400 mmol L^{-1}) stock solutions were added into Eppendorf tube to achieve the desired concentrations of different components. After adding the above components and controlling the final volume of suspension in the Eppendorf tube, the initial concentrations of RBBR and sodium acetate were 800 mg L^{-1} and 100 mmol L^{-1} , respectively. For the study of adsorption isotherms at $T = 295\text{ K}$ ($22\text{ }^\circ\text{C}$), 310 K ($37\text{ }^\circ\text{C}$), and 333 K ($60\text{ }^\circ\text{C}$), the suspensions were placed in the Infors HT Minitron Incubator Shaker at determined temperature for continuous shaking. After the suspensions were shaken for certain time interval, the solid and liquid phases were separated by centrifugation at 8000 rpm for 5 min.

2.3.2. RBBR and laccase T. calibration curves

Figure 2.9 showed the calibration curves of RBBR and laccase T. stoichiometrically determined by the spectrophotometry method. The RBBR concentration in supernatant (C_t , mg L^{-1}) was determined at the wavelength of 590 nm (Figure 2.9b). The laccase T. catalytic activity was determined by using ABTS as the substrate at the wavelength of 420 nm (Figure 2.9d). ABTS was commonly selected as the specific substrate of choice because of its higher affinity to free and immobilized laccase T. than phenol-based substrates (e.g., 2,6-dimethoxyphenol (DMP), 3 times more sensitive) and other assay substrates (e.g., dihydroxyphenylalanine (DOPA), dimethylaminoborane (DMAB), and syringaldazine, over 40 times more sensitive) (Hou et al., 2014).

In order to compare sequential immobilization and glutaraldehyde post-treatment protocols regarding laccase T. immobilization by UPA with different polycrystalline phases, three parameters in terms of enzyme immobilization including immobilization yield (IY, %, immobilized activity divided by total starting activity), immobilization efficiency (IE, %, obtained activity in biocatalyst divided by immobilized activity), and activity recovery (AR, % or mg g^{-1} carrier, obtained activity in biocatalyst divided by total starting activity) were determined (Sheldon and Pelt, 2013).

For example: A given kind of enzyme is immobilized on a supporting carrier. 1 gram of supporting carrier is incubated in the enzyme solution containing a total of 100 units of enzyme activity. After 24 hours the supporting carrier is filtered and washed. Total enzyme activity left in the enzyme suspension and wash water is 20 units. The washed supporting carrier is assayed for activity and the total activity of the supporting carrier is found to be 40 units. In this case the IY (%), IE (%), and AR (%) would be 80%, 50%, and 40%, respectively (Sheldon and Pelt, 2013). Moreover, the AR (%) mathematically equals to the value of IY (%) multiplied by the IE (%).

The adsorption percentage (%), adsorption capacity at equilibrium (q_e , mg g^{-1}), and the distribution coefficient (K_d) were obtained as follows, respectively:

$$\text{Adsorption (\%)} = \frac{C_0 - C_e}{C_0} \times 100\% \quad (2.1)$$

$$q_e = \frac{C_0 - C_e}{m} \times V \quad (2.2)$$

$$K_d = \frac{C_0 - C_e}{C_e} \times \frac{V}{m} = \frac{q_e}{C_e} \quad (2.3)$$

where C_0 (mg L^{-1}) is the initial adsorbate concentration in suspension, C_e (mg L^{-1}) is the adsorbate concentration in supernatant at equilibrium, V (L) is the volume of suspension, and m (g) is the mass of adsorbent. All of the experimental data were the averages of triplicate determinations and displayed in the form of average value \pm standard deviation (S.D.).

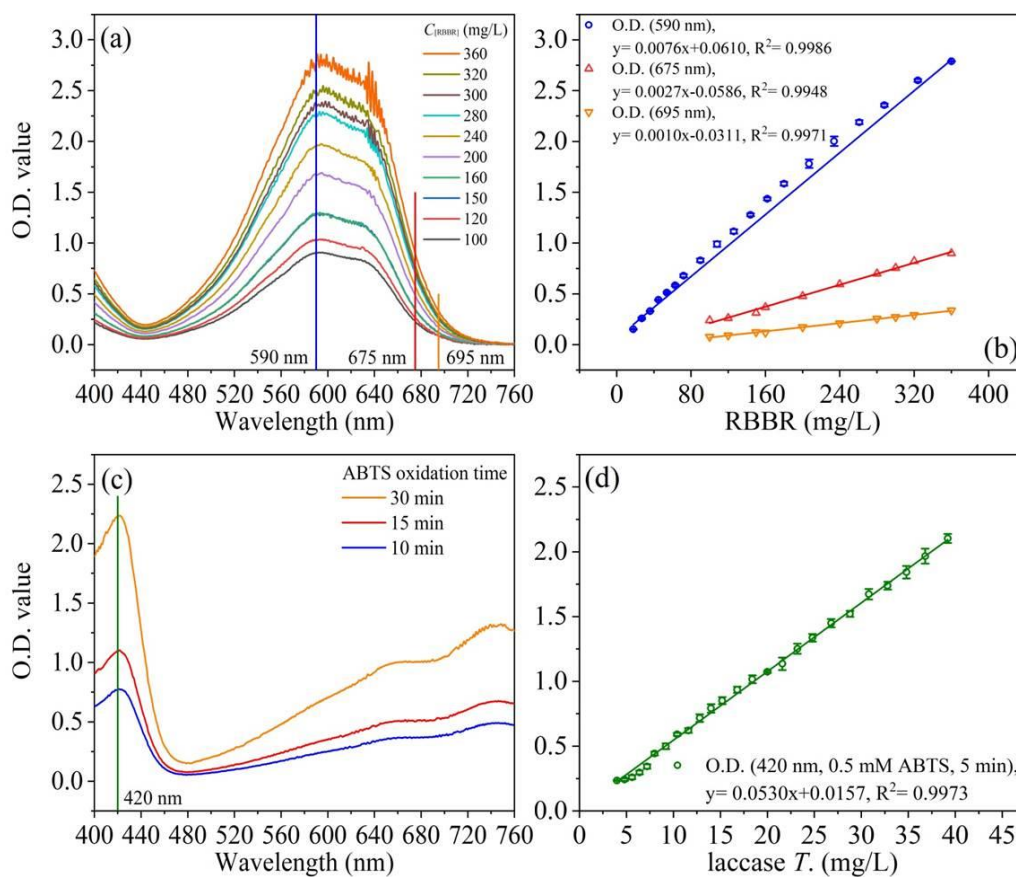


Figure 2.9. – (a) Visible spectral curves of RBBR at different concentrations, (b) calibration curves of RBBR at different wavelengths ($\lambda = 590, 675,$ and 695 nm), (c) visible spectral curves of laccase T. assay by using ABTS as the substrate at different oxidation time ($t = 10, 15,$ and 30 min), and (d) calibration curve of laccase T. assay by using ABTS as the substrate at 5 min of oxidation time ($\lambda = 420$ nm).

As shown in Figure 2.9b, except for the wavelength of 590 nm, the linear relationships between optical density value and RBBR concentration can also be obtained at higher spectral positions (i.e., $\lambda = 675$ and 695 nm). Therefore, for the determination of high RBBR concentration which may exceed the detection limit of the visible spectrophotometer applied, a higher spectral position for measurement (e.g., 675 and 695 nm) other than one more step dilution operation at 590 nm of absorbance peak can also be applicable.

In Figure 2.9c, obviously the optical density value regarding ABTS oxidation by laccase T. kept increasing as the oxidation time increased. Generally, the oxidation of colourless ABTS can undergo a fast one-electron transfer process, and the reaction product $\text{ABTS}^{\bullet+}$ is a stable green coloured radical (Pinkernell et al., 2000). According to Fernando Bautista et al. (2010), laccase T. possesses higher oxidation capacity because it can catalyze the four 1-electron oxidations of electron-rich compounds with the simultaneous 4-electron reduction of molecular dioxygen to water. Therefore, in terms of laccase T. calibration curve, the ABTS oxidation time was fixed at 5 min, in which the corresponding determination coefficient (R^2) of linear equation fitting and relative error bar of triplicate measurements were 0.9973 and below 5%, respectively (Figure 2.9d). In addition, it is also suggested to separately measure the corresponding optical density value rather than unify the measurements altogether.

2.3.3. Biocatalyst stability study

The experimental factors that can affect the biocatalyst stability including pH, temperature, storage time and reusability were studied. The pH stability was determined by incubating free and immobilized laccase T. at different pH values (3.5–9.0) at 20 °C for 45 min, and the residual enzyme activity of free and immobilized laccase T. was accordingly measured as mentioned above. The buffers used were sodium acetate (3.5–5.5, 100 mM), phosphate (6.0–7.5, 100 mM), and Tris-HCl (8.0–9.0, 100 mM). The thermal stability was determined by incubating free and immobilized laccase T. at different temperatures (20–85 °C) at optimal pH (i.e., pH = 5.0, sodium acetate buffer) for 45 min. In terms of the storage stability, free and immobilized laccase T. were kept refrigerated at 4 °C, and the residual enzyme activity was measured until 49 days. The reusability of immobilized laccase T. was determined by measuring the residual enzyme activity through 10 consecutive batches. After each cycle, the powders were recovered by centrifugation at 4000 rpm for 5 min, and washed with phosphate buffer for three times.

2.4. Characterizations

The UPA(θ) powders before and after RBBR adsorption were characterized by using scanning electron microscopy (SEM, Zeiss Supra 40 VP, Carl Zeiss, Jena, Germany) and transmission electron microscopy (TEM, JEOL 2011, JEOL Ltd., Tokyo, Japan) techniques. The material compositions of UPA(θ) powders before and after RBBR adsorption were analyzed by elemental mapping with energy-dispersive X-ray (EDX) spectroscopy (SEM S440, LEICA, Germany).

The powder X-ray diffraction (XRD) patterns of amorphous UPA, UPA(γ), UPA(θ), and UPA(α) powders were carried out by using an Inel Equinox 1000 X-ray diffractometer (Inel, Celje, Slovenia) with Co K α radiation source ($\lambda = 1.7902 \text{ \AA}$), and the analysis was performed at 2θ diffraction angles from 25° to 85° ($2^\circ/\text{min}$).

The Brunauer-Emmett-Teller (BET) specific surface area and pore size distribution of UPA(γ), UPA(θ), and UPA(α) powders were studied by nitrogen adsorption-desorption measurement with outgassing at 200°C for 12 h. The mass of UPA(γ), UPA(θ), and UPA(α) powders and the corresponding range of points (P/P_0) used for the BET measurements were 0.0602 (0.0052–0.9888), 0.0586 (0.0100–0.9898), and 0.4335 g (0.0063–0.9948 pressure), respectively.

The Fourier transform infrared (FTIR) spectra of the obtained samples were recorded by using a PerkinElmer Spectrum 100 system spectrometer (PerkinElmer, Waltham, MA, USA) in pressed KBr pellets (Sigma-Aldrich, St. Louis, MO, USA, 99%, analytical reagent) and in the $400\text{--}4000 \text{ cm}^{-1}$ region.

The thermogravimetric (TG) curves were recorded by a NETZSCH TG 209F1 Libra instrument under the nitrogen atmosphere by heating the samples from 30 to 800°C at a heating rate of $15^\circ\text{C min}^{-1}$.

The zeta potential values of UPA(γ), UPA(θ), and UPA(α) powders as a function of pH were measured by a Nano ZS90 Zetasizer (Malvern Instruments Ltd., Malvern, UK). The desired pH values of suspensions were adjusted by adding negligible volumes of $0.1\text{--}0.01 \text{ mol L}^{-1}$ HCl ($2.0\text{--}3.5$), CH_3COOH ($3.5\text{--}7.0$) or NaOH solution.

2.5. Law and fitting models

2.5.1. Beer-Lambert (Beer's) law

The Beer-Lambert law, also known as Beer's law, relates to the attenuation of light to the properties of the material through which the light is travelling. In 1760, Johann Heinrich Lambert stated in his *Photometria* that the loss of light intensity when it propagates in a medium is directly proportional to intensity and path length (Lambert, 1760). Much later, August Beer discovered another attenuation relation in 1852 that the transmittance of a solution remains constant if the product of concentration and path length stays constant (Beer, 1852).

The modern derivation of the Beer-Lambert law combines these two laws and correlates the absorbance, which is the negative decadic logarithm of the transmittance, to both the concentrations of the attenuating species and the thickness of the material sample. Nowadays, the Beer-Lambert law is commonly applied to chemical analysis measurements and used in understanding attenuation in physical optics, for photons, neutrons, or rarefied gases.

A common and practical expression of the Beer-Lambert law relates the optical attenuation of a physical material containing a single attenuating species of uniform concentration to the optical path length through the sample and absorptivity of the species (Swinehart et al., 1962):

$$A = \varepsilon \times l \times c \quad (2.4)$$

where A is the absorbance, ε is the molar attenuation coefficient or absorptivity of the attenuating species, l (cm) is the optical path length, c (g L^{-1} or mol L^{-1}) is the concentration of the attenuating species.

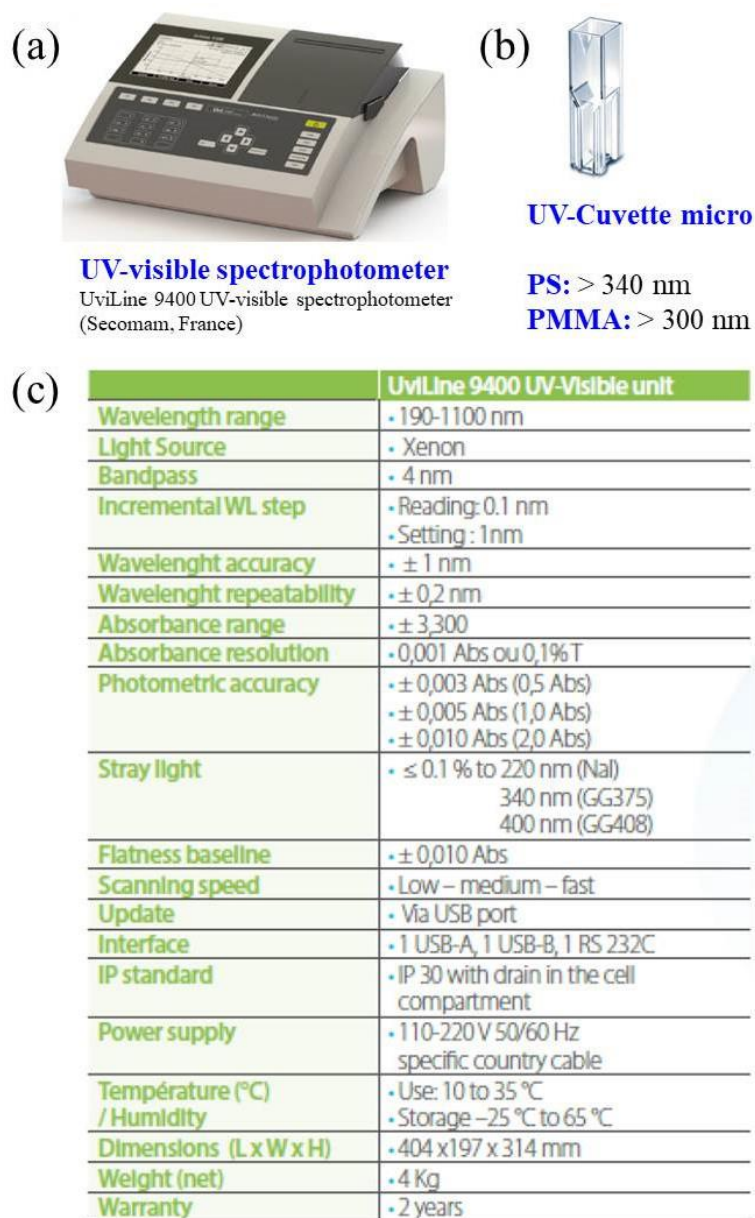


Figure 2.10. – Technical data of UviLine 9400 UV-Visible spectrophotometer.

Figure 2.10 introduced the measurement characteristics of the UviLine 9400 UV-Visible spectrophotometer applied to the RBBR and laccase T. calibration curves. The UV-cuvettes micro made from polystyrene (PS) and polymethyl methacrylate (PMMA) can be applied for determinations above 340 and above 300 nm, respectively (Figure 2.10b). These disposable cuvettes are available in macro and semi-micro sizes to accommodate most sample volumes, and also are compatible with most spectrophotometers and photometers.

As shown in Figure 2.10c, the absorbance range of the visible spectrophotometer applied is 3.300 with 0.001 as the absorbance resolution. Moreover, the photometric accuracy (absorbance accuracy) is 0.003 Abs. Therefore, the applicability of the visible spectrophotometer should always be considered before the determination of the calibration curves.

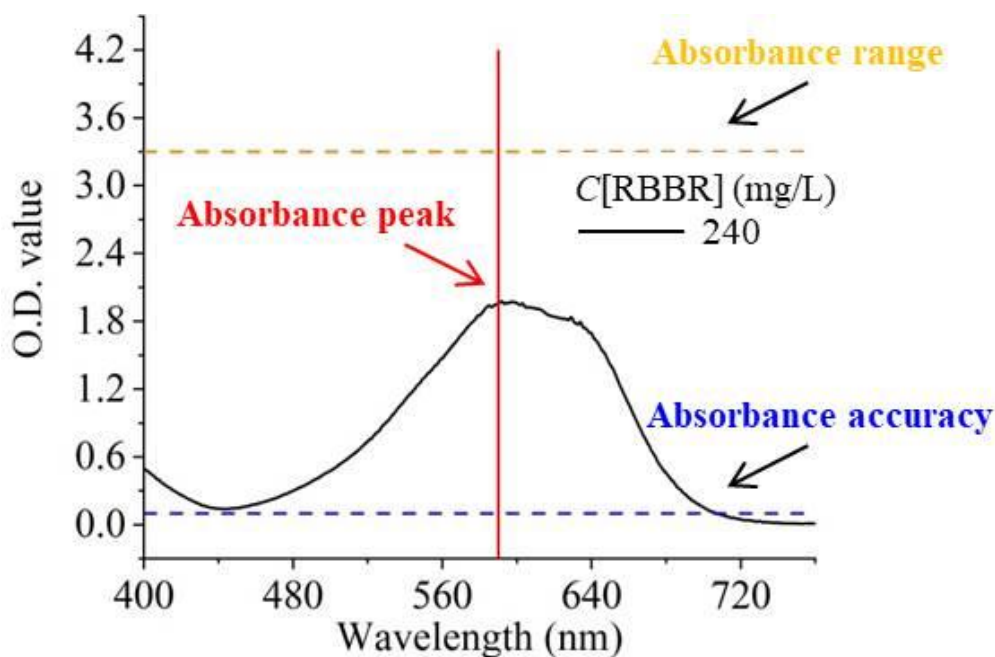


Figure 2.11. – Typical visible spectral curve of RBBR (240 mg L^{-1}).

Figure 2.11 showed a typical visible spectral curve of RBBR with a concentration of 240 mg L^{-1} , several parameters including absorbance peak, absorbance range, and absorbance accuracy were also shown in this figure. As mentioned above, to avoid exceeding the detection limit of the visible spectrophotometer applied, the spectral position other than the absorbance peak (e.g., $\lambda = 590 \text{ nm}$ for RBBR) can also be applicable for the measurement of RBBR in high concentration (Figure 2.9b).

2.5.2. Adsorption kinetic models

In this part, the adsorption kinetic models in linear form including the Lagergren pseudo-first-order model and pseudo-second-order model applied for the kinetic data fittings will be introduced in detail.

2.5.2.1. Pseudo-first-order

The Lagergren pseudo-first-order model in linear form can be found as follows (Ho and Mckay, 1998; Ho and Mckay, 1999):

$$\ln(Q_m - Q_t) = \ln Q_m - k't \quad (2.5)$$

where Q_t and Q_m (mg g^{-1}) refer to the adsorption capacity at time t (h) and at equilibrium obtained from the kinetic model. k' (h^{-1}) is the pseudp-first-order adsorption rate constant obtained from the kinetic model.

2.5.2.2. Pseudo-second-order

The pseudo-second-order model in linear form can be found as follows (Ho and Mckay, 1998; Ho and Mckay, 1999):

$$\frac{t}{Q_t} = \frac{1}{k''Q_m^2} + \frac{t}{Q_m} \quad (2.6)$$

where k'' ($\text{g mg}^{-1} \text{h}^{-1}$) is the pseudp-second-order adsorption rate constant obtained from the kinetic model.

2.5.3. Rate-limiting step determination

In order to identify the bottleneck (slowest) step of the adsorption process, in this part both the first-curved and second-linear adsorption parts of the kinetic data were fitted by the film diffusion (Boyd plot) and intraparticle diffusion (Weber and Morris plot) models (Boyd et al., 1947; Weber and Morris, 1963; Ho et al., 2000). The corresponding models in linear form applied for rate-limiting step determination will be introduced in detail.

2.5.3.1. Film diffusion (FD)

The film diffusion model in linear form can be found as follows (Boyd et al., 1947; Ho et al., 2000):

$$\ln\left(1 - \frac{Q_t}{Q_m}\right) = -k_{FD}t \quad (2.7)$$

where Q_t/Q_m is the fractional attainment of equilibrium. k_{FD} (min^{-1}) is the FD diffusion rate constant obtained from the diffusion model.

2.5.3.2. Intraparticle diffusion (IPD)

The intraparticle diffusion model in linear form can be found as follows (Weber and Morris, 1963):

$$Q_t = k_{IPD}t^{0.5} + C_{IPD} \quad (2.8)$$

where k_{IPD} ($\text{mg g}^{-1} \text{min}^{-0.5}$) is the IPD diffusion rate constant obtained from the diffusion model. C_{IPD} is proportional to the boundary layer, which provides information about boundary layer thickness, i.e., the larger value of C_{IPD} , the greater of boundary layer effect on the adsorption process (Weber and Morris, 1963; Fan et al., 2016).

If the intraparticle diffusion, often the rate controlling step, plays the dominant role in adsorption process, it should be well fitted by the relationship between Q_t and the square root of time ($t^{0.5}$) (Albadarin et al., 2012; Álvarez-Torrellas et al., 2016; Fan et al., 2016). However, if the kinetic data exhibit multi-linear plots, then two or more steps may be involved in the adsorption process (Fan et al., 2016).

2.5.4. Adsorption isotherm models

In this part, the adsorption isotherm models in linear form including the Langmuir, Freundlich, Temkin, and the Dubinin-Radushkevich (D.-R.) isotherm models applied for the isotherm data fittings will be introduced in detail, and several other isotherm models can also be found in the following part.

2.5.4.1. Langmuir

Based on the assumption that the monolayer adsorption can only occur at a finite number of definite localized sites with no lateral interaction and steric hindrance between the adsorbed molecules, even on adjacent sites, the Langmuir isotherm model is widely used for the fitting of the homogeneous adsorption (Langmuir, 1916; Langmuir, 1917; Langmuir, 1918).

This empirical model is graphically characterized by a plateau and an equilibrium saturation point where once a molecule occupies a site, no further adsorption can take place (Foo and Hameed, 2010). The Langmuir model in linear form can be found as follows (Langmuir, 1916; Langmuir, 1917; Langmuir, 1918):

$$\frac{C_e}{q_e} = \frac{1}{K_L q_{e, \max}} + \frac{C_e}{q_{e, \max}} \quad (2.9)$$

where $q_{e, \max}$ (mg g^{-1}) is the maximum adsorption capacity obtained from the isotherm models, and K_L (L mg^{-1}) is the constant of the Langmuir isotherm model related to the adsorption energy.

The essential characteristics of the Langmuir model can be expressed in terms of a dimensionless constant, commonly known as separation factor or equilibrium parameter (R_L), which is defined by the following equation (Hall et al., 1966; Webber and Chakravorti, 1974):

$$R_L = \frac{1}{1 + K_L C_0} \quad (2.10)$$

According to Hall et al. (1966), the magnitude of R_L indicates the adsorption process in nature to be either unfavorable ($R_L > 1$), linear ($R_L = 1$), favorable ($0 < R_L < 1$) or irreversible ($R_L = 0$).

2.5.4.2. Freundlich

Unlike the Langmuir model, the Freundlich isotherm model is an empirical model widely applied in heterogeneous systems (e.g., organic compounds, highly interactive species on activated carbon and molecular sieves), which describes the nonideal and reversible adsorption with no restrictions to the formation of monolayer (Freundlich, 1906). The Freundlich model in linear form can be found as follows (Freundlich, 1906):

$$\log q_e = \log K_F + \frac{1}{n} \log C_e \quad (2.11)$$

where K_F ($\text{mg}^{(1-1/n)} \text{L}^{1/n} \text{g}^{-1}$) and $1/n$ are the constants of the Freundlich isotherm model indicating the adsorption capacity and adsorption intensity, respectively. The magnitude of $1/n$ ranges between 0 and 1, indicating the surface heterogeneity, which becomes more heterogeneous as its value approaches zero (Haghseresht and Lu, 1998; Cicek et al., 2007; Foo and Hameed, 2010). Meanwhile, $1/n > 1$ indicates a cooperative adsorption (Foo and Hameed, 2010).

2.5.4.3. Temkin

The Temkin isotherm model, which contains a factor that explicitly takes account of the adsorbent-adsorbate interactions, was firstly introduced describing the adsorption of hydrogen onto platinum electrodes in acidic solutions (Temkin and Pyzhev, 1940). By ignoring the extremely low and large value of concentrations, this model assumes that the heat of adsorption (function of temperature) of all the molecules in the layer would decrease linearly rather than logarithmically with coverage (Kim et al., 2004; Foo and Hameed, 2010). Compared with its less applicability to the more complex adsorption systems, especially the liquid phase adsorption isotherms, the Temkin model can be well applied for predicting the gas phase equilibrium. The Temkin model in linear form can be found as follows (Temkin and Pyzhev, 1940):

$$q_e = B \ln K_T + B \ln C_e \quad (2.12)$$

where $B = RT/b_T$ ($J \text{ mol}^{-1}$) and K_T ($L \text{ g}^{-1}$) are the constant and equilibrium binding constant of the Temkin isotherm model, respectively.

2.5.4.4. Dubinin-Radushkevich (D.-R.)

The D.-R. isotherm model is an empirical model generally applied to express the adsorption mechanism with a Gaussian energy distribution onto a heterogeneous surface (Dubinin and Radushkevich, 1947). This model has often successfully fitted high solute activities and the intermediate range of concentrations data well. The D.-R. model in linear form can be found as follows (Dubinin and Radushkevich, 1947):

$$\ln q_e = \ln q_{e, \max} - \beta \varepsilon^2 \quad (2.13)$$

$$\varepsilon = RT \ln\left(1 + \frac{1}{C_e}\right) \quad (2.14)$$

where β ($\text{mol}^2 \text{ kJ}^{-2}$) is the constant of the D.-R. isotherm model, ε is the constant of the D.-R. isotherm model related to the Polanyi potential, R ($8.3145 \text{ J mol}^{-1} \text{ K}^{-1}$) is the universal gas constant, and T (K) is the absolute temperature in Kelvin.

E (kJ mol^{-1}) is defined as the free energy change required to transfer 1 mol of adsorbate from infinity in solution to the solid surface (Fan et al., 2016). This relationship can be described as follows (Hobson, 1969):

$$E = \frac{1}{\sqrt{2\beta}} \quad (2.15)$$

If the value of E is in the range of 8–16 kJ mol^{-1} , the adsorption process is governed by an ion-exchange mechanism, while in the case of $E < 8 \text{ kJ mol}^{-1}$, the adsorption process may be affected by physical forces. On the other hand, the adsorption process may be dominated by particle diffusion if the value of E is greater than 16 kJ mol^{-1} (Özcan et al., 2006; Patel and Vashi, 2014).

2.5.4.5. List of other adsorption isotherm models

For interests, several other two- and three-parameter isotherm models in linear form applied for the isotherm data fittings can also be found in Table 2.2 as follows (Foo and Hameed, 2010):

Table 2.2. – List of other adsorption isotherm models.

Isotherm model	Linear form	Plot	Reference	Equation
Two-parameter				
Flory-Huggins	$\log\left(\frac{\theta}{C_0}\right) = \log(K_{FH}) + n_{FH}\log(1 - \theta)$	$\log\left(\frac{\theta}{C_0}\right)$ vs $\log(1 - \theta)$	(Horsfall and Spiff, 2005)	(2.16)
Three-parameter				
Sips	$\beta_S \ln C_e = -\ln\left(\frac{K_S}{q_e}\right) + \ln(a_S)$	$\ln\left(\frac{K_S}{q_e}\right)$ vs $\ln C_e$	(Sips, 1948)	(2.17)
Toth	$\ln\left(\frac{q_e}{K_T}\right) = \ln C_e - \frac{1}{t} \ln(a_T + C_e)$	$\ln\left(\frac{q_e}{K_T}\right)$ vs $\ln C_e$	(Toth, 1971)	(2.18)
Redlich-Peterson	$\ln\left(K_R \frac{C_e}{q_e} - 1\right) = g \ln C_e + \ln(a_R)$	$\ln\left(K_R \frac{C_e}{q_e} - 1\right)$ vs $\ln C_e$	(Redlich and Peterson, 1959)	(2.19)

Flory-Huggins isotherm model, which occasionally deriving the degree of surface coverage characteristics of adsorbate onto adsorbent, can express the feasibility and spontaneous nature of an adsorption process (Horsfall and Spiff, 2005). In this respect, θ is the degree of surface coverage, where K_{FH} and n_{FH} are the indications of its equilibrium constant and model exponent. Its equilibrium constant, K_{FH} that used for the calculation of spontaneity free Gibbs energy, is related to the Equation 2.20 listed as follows (Vijayaraghavan et al., 2006):

$$\Delta G^0 = -RT \ln K_{FH} \quad (2.20)$$

Sips isotherm model is a combined form of Langmuir and Freundlich expressions deduced for predicting the heterogeneous adsorption systems and circumventing the limitation of the rising adsorbate concentration associated with the Freundlich isotherm model (Sips, 1948; Gunay et al., 2007). At low adsorbate concentrations, it reduces to the Freundlich isotherm; while at high concentrations, it predicts a monolayer adsorption capacity characteristic of the Langmuir isotherm. As a general rule, the equation parameters are governed mainly by the operating conditions such as the alteration of pH, temperature, and concentration (Pérez-Marín et al., 2007).

Toth isotherm model is another empirical equation developed to improve Langmuir isotherm fittings (experimental data), and useful in describing heterogeneous adsorption systems, which satisfying both low and high-end boundaries of the concentration (Toth, 1971; Vijayaraghavan et al., 2006). Its correlation presupposes an asymmetrical quasi-Gaussian energy distribution, with most of its sites has adsorption energy lower than the peak (maximum) or mean value (Ho et al., 2002).

Redlich-Peterson isotherm is a hybrid isotherm featuring both Langmuir and Freundlich isotherms, which incorporate three parameters into an empirical equation (Redlich and Peterson, 1959; Prasad and Srivastava, 2009). This model has a linear

dependence on concentration in the numerator and an exponential function in the denominator to represent adsorption equilibrium over a wide concentration range, that can be applied either in homogeneous or heterogeneous systems due to its versatility (Ng et al., 2002; Gimbert et al., 2008).

2.6. Adsorption thermodynamic study

In order to identify whether the adsorption process was endothermic or exothermic, spontaneous or not, the thermodynamic parameters including standard Gibbs free energy (ΔG^0 , kJ mol⁻¹), standard enthalpy change (ΔH^0 , kJ mol⁻¹), and standard entropy change (ΔS^0 , J mol⁻¹ K⁻¹) were obtained from the following equations, respectively:

$$\Delta G^0 = -RT \ln K^0 \quad (2.21)$$

$$\ln K^0 = \frac{\Delta S^0}{R} - \frac{\Delta H^0}{RT} \quad (2.22)$$

where $\ln K^0$ (K^0 , the standard distribution coefficient) can be obtained by plotting $\ln K_d$ versus C_e and extrapolating C_e to zero. The slope and intercept of the plot of $\ln K_0$ versus $1000/T$ correspond to $-\Delta H_0/1000R$ and $\Delta S_0/R$, respectively.

2.7. Conclusions

In this chapter, several parts including experimental reagents, material syntheses, batch experiments, characterization techniques, Beer-Lambert law, kinetic models, isotherm models, and thermodynamic parameter calculations were introduced in detail.

In terms of material syntheses, several materials were introduced including UPA monoliths, APTES silanized UPA powders, laccase T. cross-linked UPA biocatalysts based on sequential immobilization and glutaraldehyde post-treatment protocols. For the comparison of these two laccase T. immobilization protocols, please switch to the “Effect of immobilization protocol” section (Section 4.5).

Compared with UPA materials in γ and θ polycrystalline phases, the minimal specific surface area, the minimal amount of functional groups on the surfaces, and the lowest zeta potential values of UPA(α) powders may limit its applicability for either RBBR removal or laccase T. immobilization which will be discussed in the following chapters.

2.8. References

- Albadarin, A.B.; Mangwandi, C.; Al-Muhtaseb, A.H.; Walker, G.M.; Allen, S.J.; Ahmad, M.N.M., Kinetic and thermodynamics of chromium ions adsorption onto low-cost dolomite adsorbent, *Chemical Engineering Journal*, 179 (2012) 193–202.
- Álvarez-Torrellas, S.; Ribeiro, R.S.; Gomes, H.T.; Ovejero, G.; García, J., Removal of antibiotic compounds by adsorption using glycerol-based carbon materials, *Chemical Engineering Journal*, 296 (2016) 277–288.
- Beer A., Determination of the absorption of red light in colored liquids (in German), *Annalen der Physik und Chemie*, 162 (1852) 78–88.
- Bousslama, M.; Amamra, M.C.; Brinza, O.; Tieng, S.; Chhor, K.; Abderrabba, M.; Vignes, J.-L.; Kanaev, A., Isolation of titania nanoparticles in monolithic ultraporous alumina: Effect of nanoparticle aggregation on anatase phase stability and photocatalytic activity, *Applied Catalysis A: General*, 402 (2011) 156–161.
- Bousslama, M.; Amamra, M.C.; Jia, Z.-X.; Ben Amar, M.; Chhor, K.; Brinza, O.; Abderrabba, M.; Vignes, J.-L.; Kanaev, A., Nanoparticulate $\text{TiO}_2\text{-Al}_2\text{O}_3$ photocatalytic media: Effect of particle size and polymorphism on photocatalytic activity, *ACS Catalysis*, 2 (2012) 1884–1892.
- Boyd, G.E.; Adamson, A.W.; Myers, L.S.J., The exchange adsorption of ions from aqueous solutions by organic zeolites. II. Kinetics, *Journal of the American Chemical Society*, 69 (1947) 2836–2848.
- Cicek, F.; Özer, D.; Özer, A.; Özer, A., Low cost removal of reactive dyes using wheat bran, *Journal of Hazardous Materials*, 146 (2007) 408–416.
- Dubin, M.M.; Radushkevich, L.V., The equation of the characteristic curve of the activated charcoal, *Proceedings of the USSR Academy of Sciences*, 55 (1947) 331–337.
- Fan, H.-T.; Sun, W.; Jiang, B.; Wang, Q.-J.; Li, D.-W.; Huang, C.-C.; Wang, K.-J.;

-
- Zhang, Z.-G.; Li, W.-X., Adsorption of antimony(III) from aqueous solution by mercapto-functionalized silica-supported organic-inorganic hybrid sorbent: Mechanism insights, *Chemical Engineering Journal*, 286 (2016) 128–138.
- Foo, K.Y.; Hameed, B.H., Insights into the modeling of adsorption isotherm systems, *Chemical Engineering Journal*, 156 (2010) 2–10.
- Freundlich, H.M.F., Over the adsorption in solution (in German), *Journal of Physical Chemistry*, 57 (1906) 385–471.
- Gimbert, F.; Morin-Crini, N.; Renault, F.; Badot, P.M.; Crini, G., Adsorption isotherm models for dye removal by cationized starch-based material in a single component system: Error analysis, *Journal of Hazardous Materials*, 157 (2008) 34–46.
- Gunay, A.; Arslankaya, E.; Tosun, I., Lead removal from aqueous solution by natural and pretreated clinoptilolite: adsorption equilibrium and kinetics, *Journal of Hazardous Materials*, 146 (2007) 362–371.
- Haghseresht, F.; Lu, G.-Q., Adsorption characteristics of phenolic compounds onto coal-reject-derived adsorbents, *Energy & Fuels*, 12 (1998) 1100–1107.
- Hall, K.R.; Eagleton, L.C.; Acrivos, A.; Vermeulen, T., Pore- and solid-diffusion kinetics in fixed-bed adsorption under constant-pattern conditions, *Industrial & Engineering Chemistry Fundamentals*, 5 (1966) 212–223.
- Ho, Y.S.; McKay, G., A comparison of chemisorption kinetic models applied to pollutant removal on various sorbents, *Process Safety and Environmental Protection*, 76 (1998) 332–340.
- Ho, Y.S.; McKay, G., Pseudo-second order model for sorption processes, *Process Biochemistry*, 34 (1999) 451–465.
- Ho, Y.S.; Ng, J.C.Y.; McKay, G., Kinetics of pollutant sorption by biosorbents: Review, *Separation and Purification Methods*, 29 (2000) 189–232.
- Ho, Y.S.; Porter, J.F.; McKay, G., Equilibrium isotherm studies for the sorption of divalent metal ions onto peat: copper, nickel and lead single component systems,

-
- Water, Air, & Soil Pollution, 141 (2002) 1–33.
- Hobson, J.P., Physical adsorption isotherms extending from ultrahigh vacuum to vapor pressure, *Journal of Physical Chemistry*, 73 (1969) 2720–2727.
- Horsfall, M.; Spiff, A.I., Equilibrium sorption study of Al^{3+} , Co^{2+} and Ag^+ in aqueous solutions by fluted pumpkin (*Telfairia occidentalis* HOOK f) waste biomass, *Acta Chimica Slovenica*, 52 (2005) 174–181.
- Hou, J.-W.; Dong, G.-X.; Ye, Y.; Chen, V., Laccase immobilization on titania nanoparticles and titania-functionalized membranes, *Journal of Membrane Science*, 452 (2014) 229–240.
- Khatim, O.; Nguyen, T.H.N.; Amamra, M.; Museur, L.; Khodan, A.; Kanaev, A., Synthesis and photoluminescence properties of nanostructured mullite/ α - Al_2O_3 , *Acta Materialia*, 71 (2014) 108–116.
- Khodan, A.; Nguyen, T.H.N.; Esaulkov, M.; Kiselev, M.R.; Amamra, M.; Vignes, J.-L.; Kanaev, A., Porous monoliths consisting of aluminum oxyhydroxide nanofibrils: 3D structure, chemical composition, and phase transformations in the temperature range 25–1700 °C, *Journal of Nanoparticle Research*, 20 (2018) 1–11.
- Kim, Y.; Kim, C.; Choi, I.; Rengraj, S.; Yi, J., Arsenic removal using mesoporous alumina prepared via a templating method, *Environmental Science & Technology*, 38 (2004) 924–931.
- Lambert, J.H., *Photometria sive de mensura et gradibus luminis, colorum et umbrae* (Photometry, or, On the measure and gradations of light intensity, colors, and shade), Augsburg: Eberhardt Klett.
- Landoulsi, J.; Genet, M.J.; El Kirat, K.; Richard, C.; Pulvin, S.; Rouxhet, P.G., Silanization with APTES for controlling the interactions between stainless steel and biocomponents: Reality vs Expectation. In *Biomaterials – Physics and Chemistry*, Pignatello, R. (Ed.), InTech, ISBN 978-953-307-418-4 (2011) 109–138.

-
- Langmuir, I., The constitution and fundamental properties of solids and liquids. Part I. Solids, *Journal of the American Chemical Society*, 38 (1916) 2221–2295.
- Langmuir, I., The constitution and fundamental properties of solids and liquids. Part II. Liquids, *Journal of the American Chemical Society*, 39 (1917) 1848–1906.
- Langmuir, I., The adsorption of gases on plane surfaces of glass, mica and platinum, *Journal of the American Chemical Society*, 40 (1918) 1361–1403.
- Matijošytė, I.; Arends, I.W.C.E.; de Vries, S.; Sheldon, R.A., Preparation and use of cross-linked enzyme aggregates (CLEAs) of laccases, *Journal of Molecular Catalysis B: Enzymatic*, 62 (2010) 142–148.
- Ng, J.C.Y.; Cheung, W.H.; McKay, G., Equilibrium studies of the sorption of Cu(II) ions onto chitosan, *Journal of Colloid and Interface Science*, 255 (2002) 64–74.
- Nguyen, T.H.N., Elaboration and modifications of nanofibrous Al₂O₃, *Chemical and Process Engineering*, Université Sorbonne Paris Cité (2016) PhD thesis.
- Özcan, A.; Öncü, E.M.; Özcan, A.S., Kinetics, isotherm and thermodynamic studies of adsorption of Acid Blue 193 from aqueous solutions onto natural sepiolite, *Colloids and Surfaces A: Physicochemical and Engineering Aspects*, 277 (2006) 90–97.
- Özsoy, H.D.; Ünyayar, A.; Mazmanci, M.A., Decolourisation of reactive textile dyes Drimarene Blue X3LR and Remazol Brilliant Blue R by *Funalia trogii* ATCC 200800, *Biodegradation*, 16 (2005) 195–204.
- Patel, H.; Vashi, R.T., Wastewater treatment by physical-chemical technologies. In *Wastewater Engineering: Advanced Wastewater Treatment Systems*, Aziz, H.A.; Mojiri, A. (Ed.), IJSR, ISSN: 2322-4657 (2014) 5–48.
- Pérez-Marín, A.B.; Meseguer Zapata, V.; Ortuño, J.F.; Aguilar, M.; Sáez, J.; Lloréns, M., Removal of cadmium from aqueous solutions by adsorption onto orange waste, *Journal of Hazardous Materials*, 139 (2007) 122–131.
- Pinkernell, U.; Nowack, B.; Gallard, H.; von Gunten, U., Methods for the photometric determination of reactive bromine and chlorine species with ABTS, *Water*

-
- Research, 34 (2000) 4343–4350.
- Prasad, R.K.; Srivastava, S.N., Sorption of distillery spent wash onto fly ash: Kinetics and mass transfer studies, *Chemical Engineering Journal*, 146 (1) (2009) 90–97.
- Redlich, O.; Peterson, D.L., A useful adsorption isotherm, *Journal of Physical Chemistry*, 63 (1959) 1024–1026.
- Sheldon, R.A.; Pelt, S.V., Enzyme immobilisation in biocatalysis: Why, what and how, *Chemical Society Reviews*, 42 (2013) 6223–6235.
- Sips, R., Combined form of Langmuir and Freundlich equations, *Journal of Chemical Physics*, 16 (1948) 490–495.
- Swinehart, D.F., The Beer-Lambert law, *Journal of Chemical Education*, 39 (1962) 1–3.
- Temkin, M.I.; Pyzhev, V.P., Kinetics of ammonia synthesis on promoted iron catalyst, *Acta Physicochimica USSR*, 12 (1940) 327–356.
- Toth, J., State equations of the solid gas interface layer, *Acta Chimica Academiae Scientiarum Hungaricae*, 69 (1971) 311–317.
- Vignes, J.-L.; Frappart, C.; Di Costanzo, T.; Rouchaud, J.-C.; Mazerolles, L.; Michel, D., Ultraporous monoliths of alumina prepared at room temperature by aluminium oxidation, *Journal of Materials Science*, 43 (2008) 1234–1240.
- Vijayaraghavan, K.; Padmesh, T.V.N.; Palanivelu, K.; Velan, M., Biosorption of nickel(II) ions onto *Sargassum wightii*: application of two-parameter and three parameter isotherm models, *Journal of Hazardous Materials*, 133 (2006) 304–308.
- Weber, W.J.; Morris, J.C., Kinetics of adsorption of carbon from solutions, *Journal of the Sanitary Engineering Division*, 89 (1963) 31–63.
- Webber, T.W.; Chakkravorti, R.K., Pore and solid diffusion models for fixed-bed adsorbers, *AIChE Journal*, 20 (1974) 228–238.
- Xu, H.; Boeuf, G.; Jia, Z.-X.; Zhu, K.-R.; Nikravec, M.; Kanaev, A.; Azouani, R.; Traore, M.; Elm'selmi, A., Solvent-free synthesized monolithic ultraporous

aluminas for highly efficient removal of Remazol Brilliant Blue R: Equilibrium, kinetic, and thermodynamic studies, *Materials*, 14 (2021) 1–19.

Chapter 3: Ultraporous aluminas for highly efficient removal of RBBR

3.1. Introduction

This chapter aims to investigate the adsorption characteristics of UPA materials towards RBBR. The UPA monoliths were grown via facile oxidation process, followed by isochronous annealing treatment in air at different temperatures, through which γ , θ , and α phase polycrystalline fibrous grains of UPA can be accordingly obtained. The experimental factors that affect the material adsorption performances including initial pH, contact time, and temperature were comprehensively studied by batch experiments. The RBBR adsorption isotherms of UPA(γ) and UPA(θ) powders were found almost identical, while UPA(α) powders showed low effectiveness. To obtain the desirable mechanical stability of the UPA monolith with considerable RBBR adsorption capacity, UPA(θ) powders were further studied.

The UPA(θ) powders exhibited maximum RBBR adsorption at pH 2 due to the positively charged surface under acidic conditions. Compared with the Lagergren pseudo-first-order model, the pseudo-second-order model was found to explain the adsorption kinetics better. Despite the film diffusion dominating the adsorption process, the contributions of the intraparticle diffusion and chemical reactions were also found significant. The adsorption equilibrium data at different temperatures were fitted by the Langmuir, Freundlich, Temkin, and D.-R. isotherm models. The Langmuir model was found the most effective in the description of equilibrium data, and the maximum RBBR adsorption capacity retained by UPA(θ) powders was 122.55 mg g^{-1} at 295 K (22 °C). Thermodynamic parameters (ΔG^0 , ΔH^0 , and ΔS^0) indicated the adsorption process was spontaneous and exothermic in nature.

3.2. Characterizations

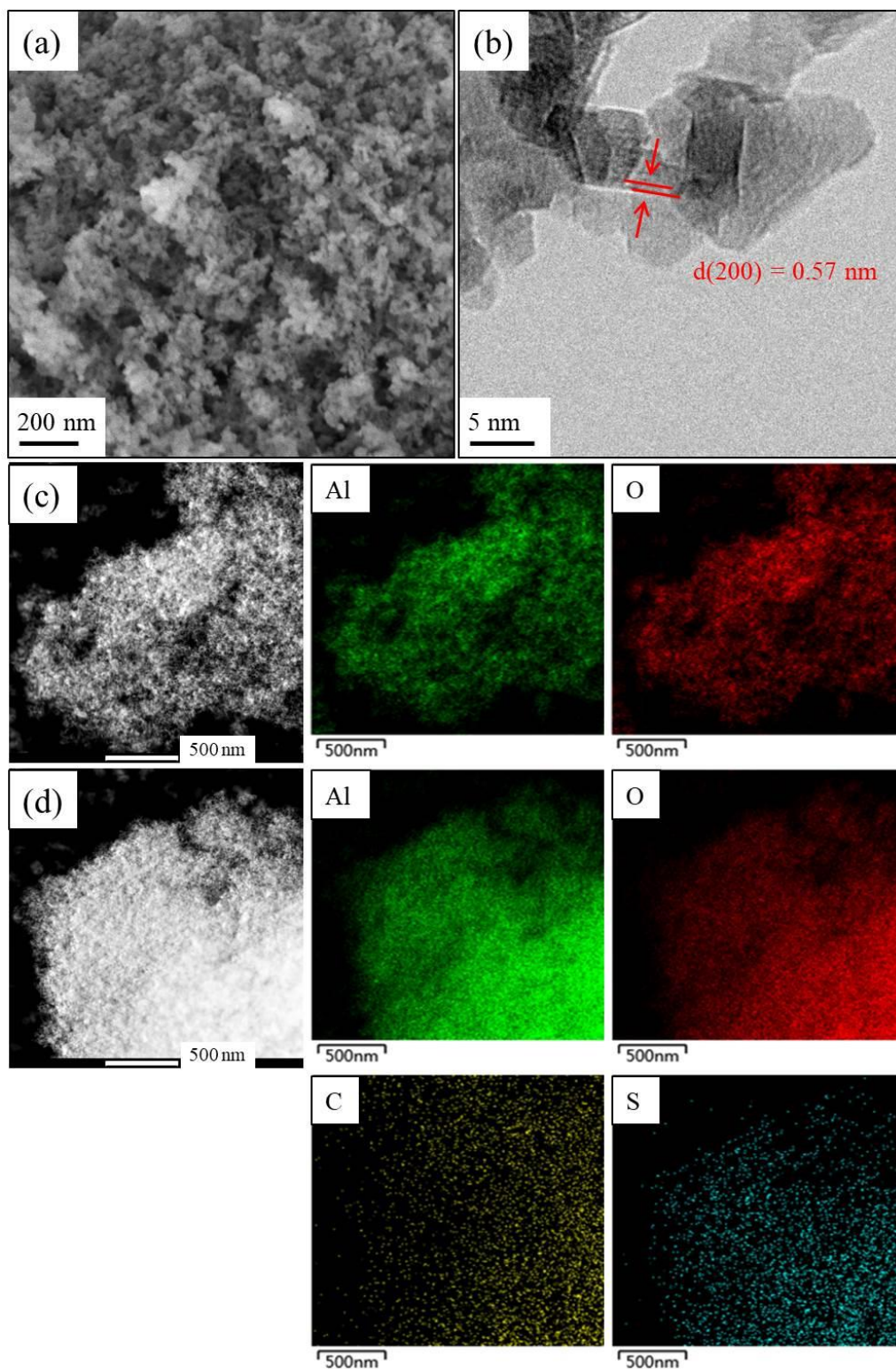


Figure 3.1. – (a) SEM and (b) TEM images of UPA(θ) powders, and elemental mapping of UPA(θ) powders (c) before and (d) after RBBR adsorption.

Figures 3.1a and 3.1b showed the SEM and TEM images of UPA(θ) powders, which evidenced the ultraporous morphology of obtained samples. The TEM image at high magnification revealed the clear lattice fringe with a d-spacing of 0.57 nm, which corresponds to the (200) plane of theta-alumina (JCPDS 23-1009) (Figure 3.1b) (Souza Santos et al., 2000).

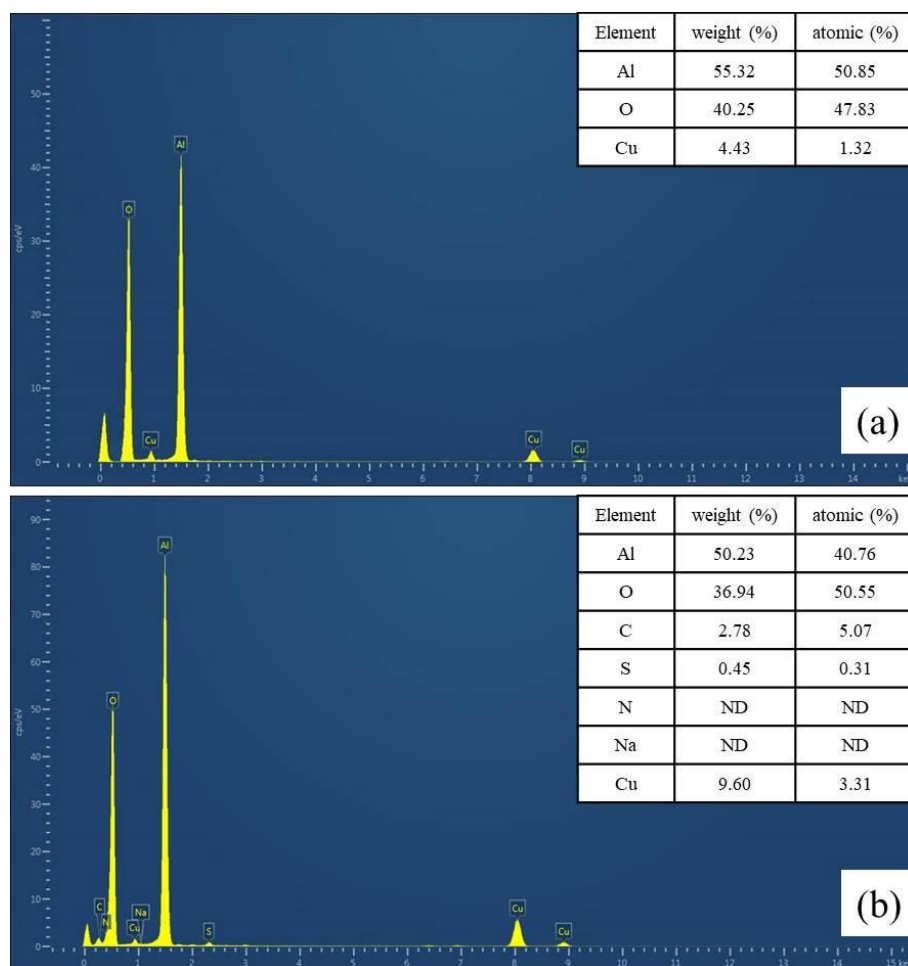


Figure 3.2. – EDX spectra of UPA(θ) powders (a) before and (b) after RBBR adsorption.

The EDX spectra of UPA(θ) powders before RBBR adsorption showed that there was no residual mercury or silver element retained on the surface of synthesized UPA(θ) samples (Figure 3.2a). After RBBR adsorption, the weak element signals of carbon (5.07%) and sulfur (0.31%) in EDX spectra confirmed the presence of RBBR retained on UPA(θ) surfaces (Figure 3.2b).

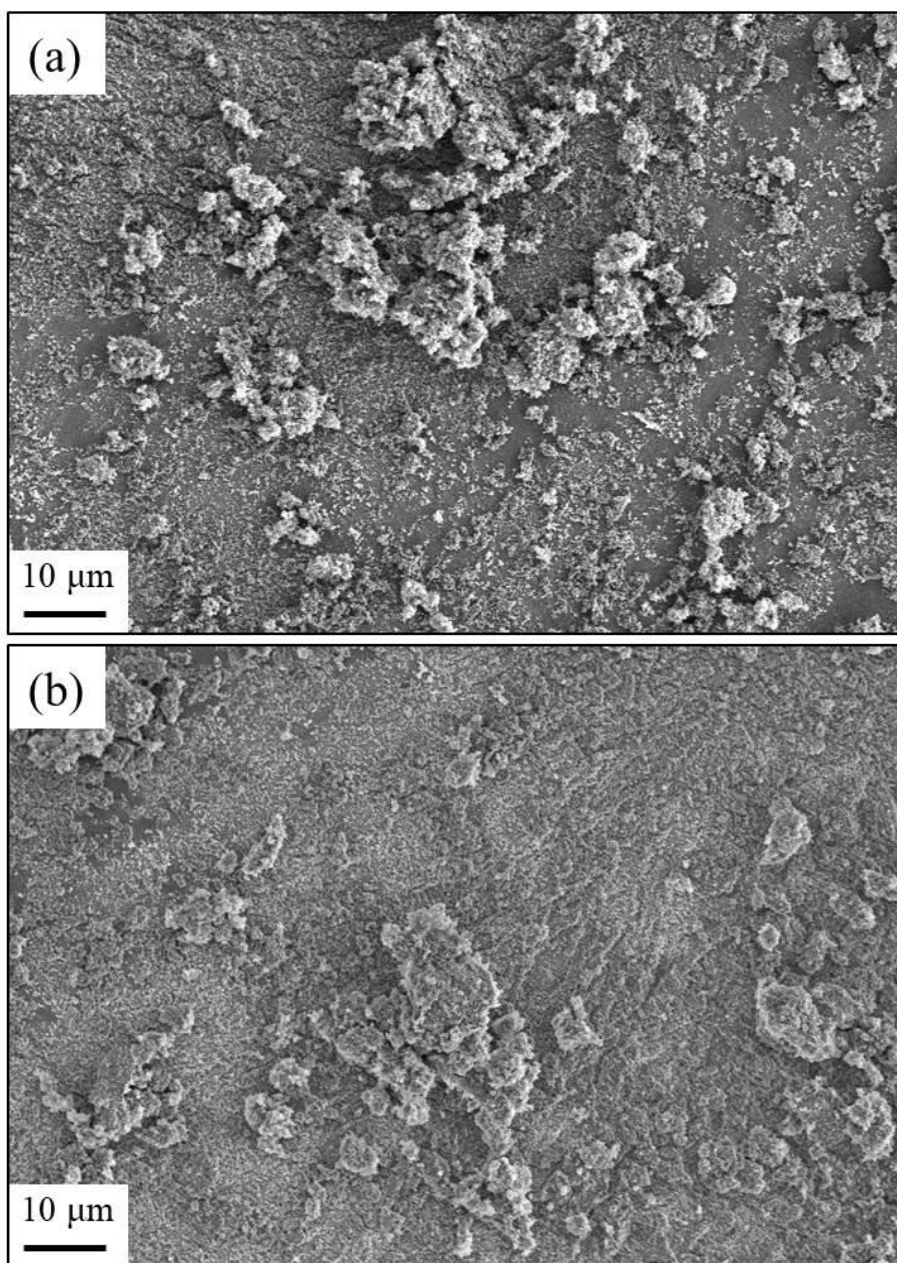


Figure 3.3. – SEM images of UPA(θ) powders (a) before and (b) after RBBR adsorption.

Figure 3.3 showed the SEM images of UPA(θ) powders before and after RBBR adsorption, and the UPA(θ) border became smoother after RBBR adsorption. Moreover, the corresponding TEM elemental mappings in Figures 3.1c and 3.1d clearly confirmed the uniform distribution of RBBR retained on the UPA(θ) surfaces.

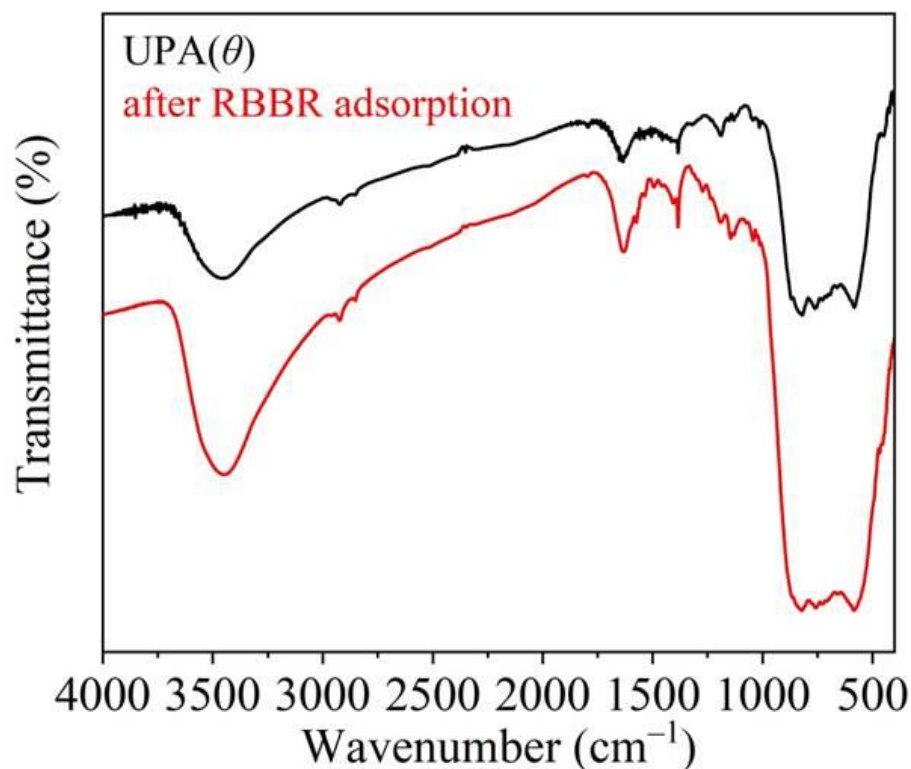


Figure 3.4. – FTIR spectra of UPA(θ) powders before and after RBBR adsorption.

In Figure 3.4, the broad absorption band in the range of 3400–3500 cm^{-1} was assigned to the –OH stretching vibrations of alumina (Al-Rubayee et al., 2016). After RBBR adsorption, the broader absorption band in this range indicated the presence of carboxyl and amino groups of RBBR distributed on the UPA(θ) surfaces (Figure 2.2a).

Figure 3.5 showed the XRD patterns of amorphous UPA, UPA(γ), UPA(θ), and UPA(α) powders. As shown in Figure 3.5a, negligible absorption peaks can be observed in the XRD pattern of amorphous UPA. Based on the calculation from Bragg equation ($2d\sin\theta = n\lambda$, $n = 1, 2, 3$, etc.), the typical XRD patterns at different 2θ positions correspond to the planes of UPA(γ), UPA(θ) and UPA(α) powders.

For example, as shown in Figure 3.5b, the two typical XRD patterns at $2\theta = 53.42^\circ$ ($d = 1.99$ nm) and $2\theta = 79.40^\circ$ ($d = 0.14$ nm) correspond to the (400) and (440) planes of gamma-alumina, respectively (JCPDS 29-0063) (Souza Santos et al., 2000).

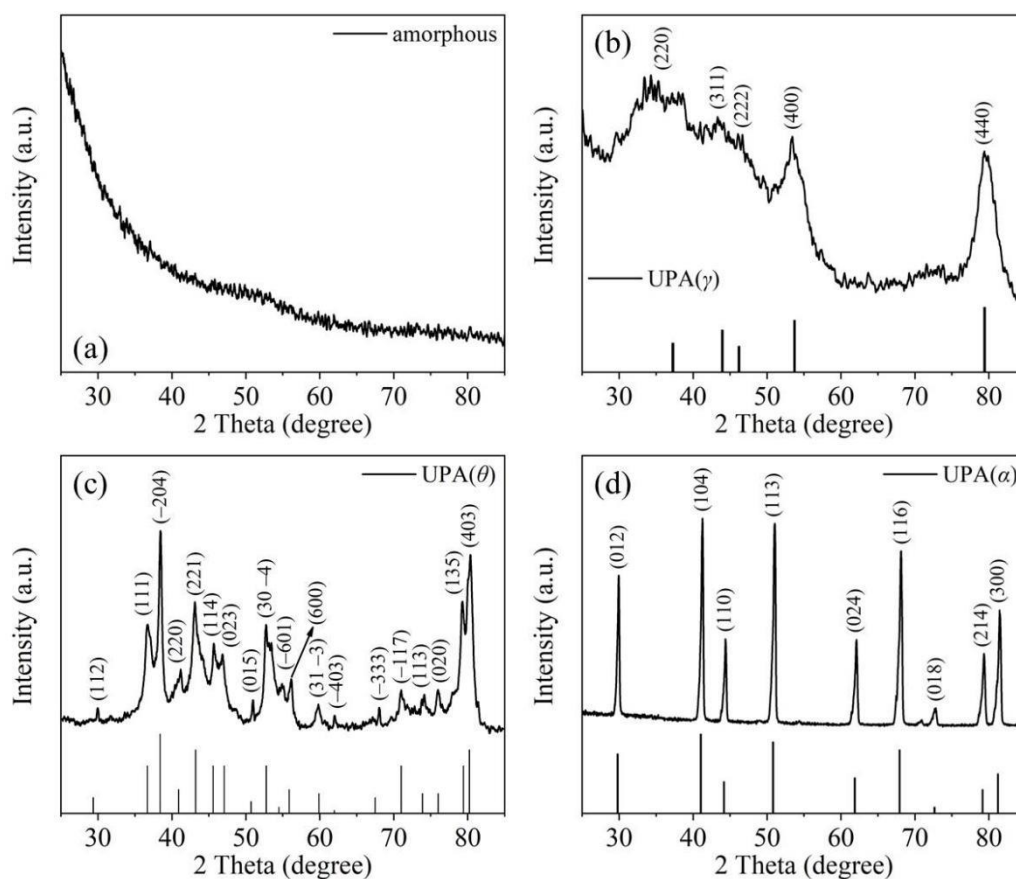


Figure 3.5. – XRD patterns of (a) amorphous UPA, (b) UPA(γ), (c) UPA(θ), and (d) UPA(α) powders.

In Figure 3.5c, the typical XRD patterns at $2\theta = 36.64^\circ$ ($d = 0.28$ nm), 38.46° ($d = 0.27$ nm), and 80.32° ($d = 0.14$ nm) correspond to the (111), (-204), and (403) planes of theta-alumina, respectively, (JCPDS 35-0121, 11-0517, and 23-1009) (Souza Santos et al., 2000). In Figure 3.5d, the typical XRD patterns at $2\theta = 41.26^\circ$ ($d = 0.25$ nm), $2\theta = 51.03^\circ$ ($d = 0.21$ nm), $2\theta = 68.16^\circ$ ($d = 0.16$ nm), and $2\theta = 81.45^\circ$ ($d = 0.14$ nm) correspond to the (104), (113), (116), and (300) planes of alpha-alumina, respectively (JCPDS 10-0173) (Souza Santos et al., 2000).

The mechanical stability of the UPA materials increased with the increasing calcination temperature at the expense of the specific surface area, which decreased from $300 \text{ m}^2 \text{ g}^{-1}$ (raw fragile UPA) to $201.7 \text{ m}^2 \text{ g}^{-1}$ of UPA(γ), $93.4 \text{ m}^2 \text{ g}^{-1}$ of UPA(θ), and $5.7 \text{ m}^2 \text{ g}^{-1}$ of UPA(α) monoliths (Figure 3.6). The nitrogen adsorption-desorption isotherm curve of UPA materials followed the typical characteristics of type IV

isotherm and H3 hysteresis (IUPAC), which indicates the mesoporous property of UPA materials (Figures 3.6a, 3.6c and 3.6e) (Sing et al., 1985; Storck et al., 1998). Moreover, the average pore diameters of UPA(γ), UPA(θ), and UPA(α) powders were 15.3, 35.1 and 67.6 nm (Gaussian curve in the pore diameter ranges from 0 to 150 nm, 0 to 150 nm, and 0 to 225 nm), respectively. And the most data of pore size distribution located in the mesoporous range (Figures 3.6b, 3.6d and 3.6f).

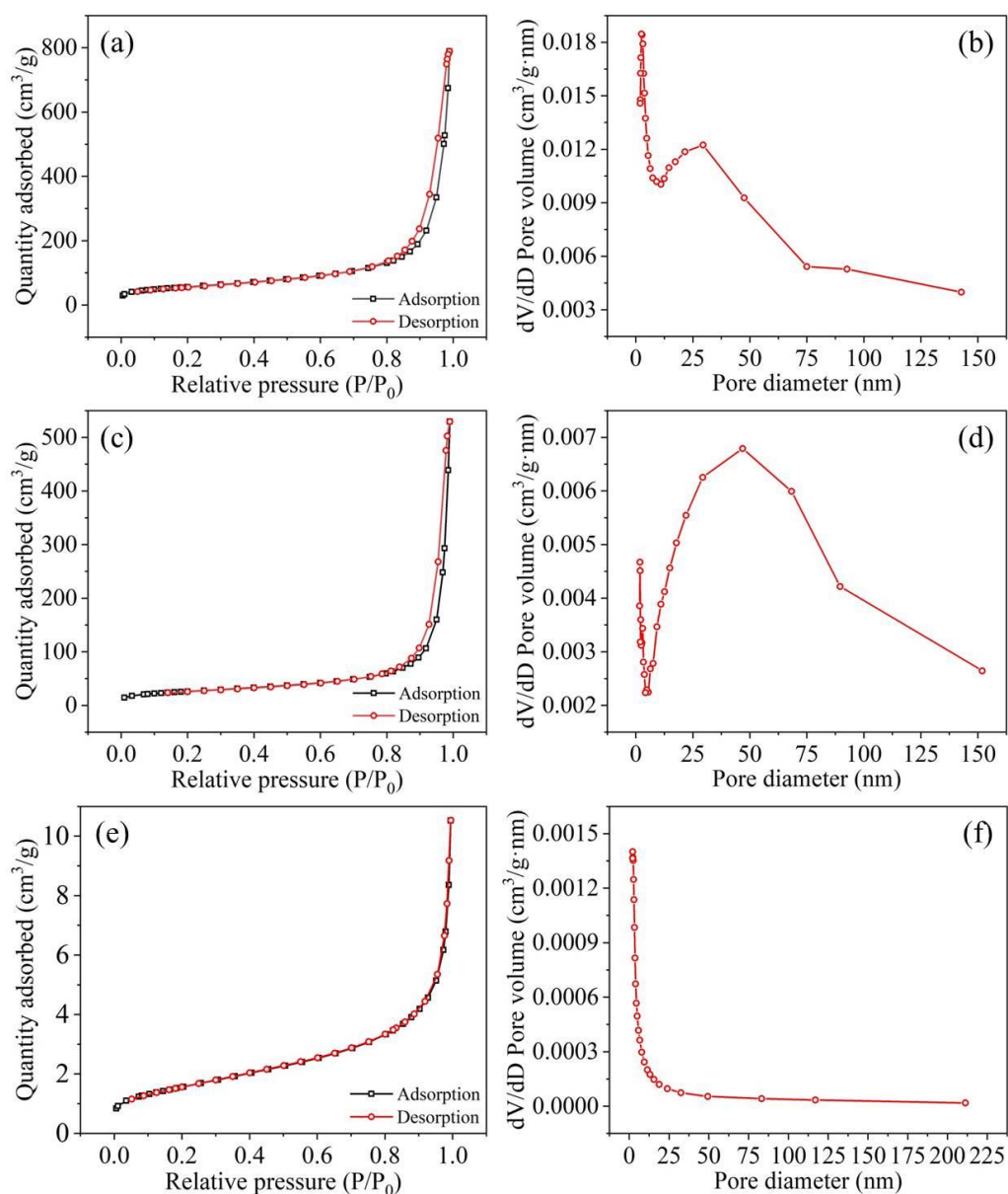


Figure 3.6. – Nitrogen adsorption-desorption isotherms of (a) UPA(γ), (c) UPA(θ), and (e) UPA(α) powders. Corresponding pore size distributions of (b) UPA(γ), (d) UPA(θ), and (f) UPA(α) powders.

Figure 3.7 showed the adsorption isotherm profiles regarding RBBR adsorption capacity with units as mg g^{-1} and mg m^{-2} retained by UPA(γ), UPA(θ), and UPA(α) powders, respectively. These results showed that the RBBR adsorption capacity was proportional to the UPA specific surface area and attained approximately 1.1 mg m^{-2} regardless of its polycrystalline phase (Figure 3.7b).

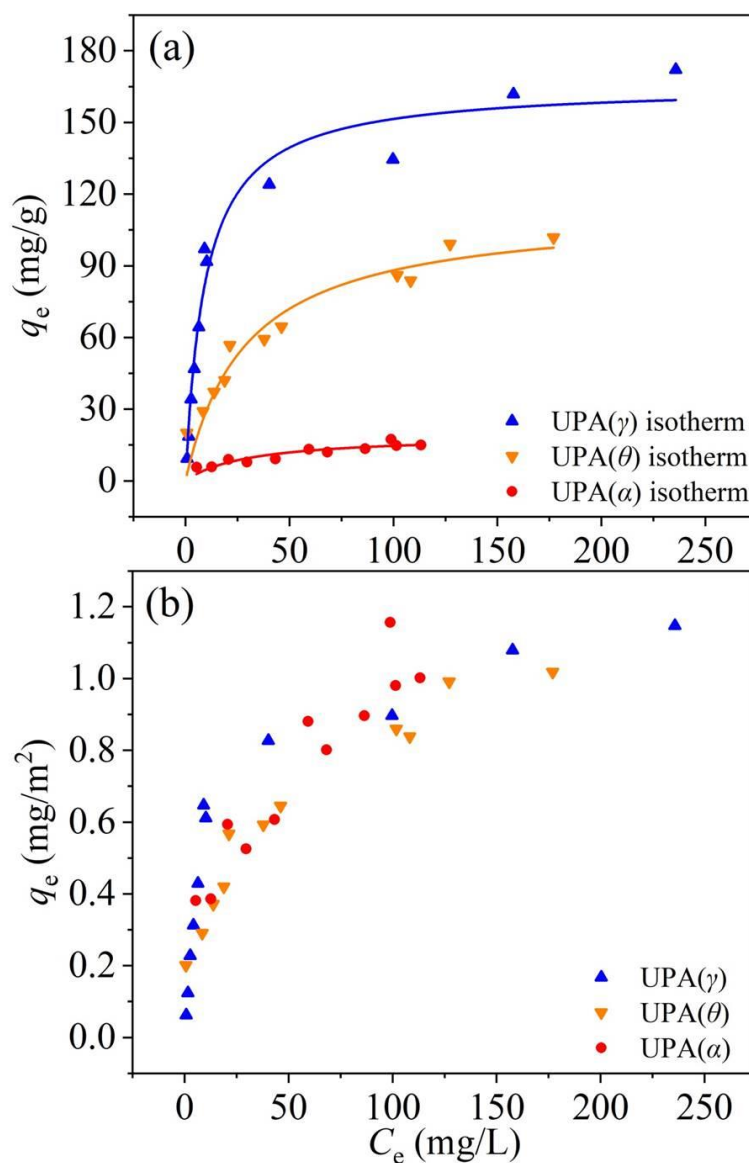


Figure 3.7. – Adsorption isotherm profiles regarding RBBR adsorption capacity with units as (a) mg g^{-1} and (b) mg m^{-2} retained by UPA(γ), UPA(θ), and UPA(α) powders. $m/V[\text{UPA}(\gamma)] = 5.56 \text{ g}\cdot\text{L}^{-1}$, $m/V[\text{UPA}(\theta)] = 5.56 \text{ g}\cdot\text{L}^{-1}$, $m/V[\text{UPA}(\alpha)] = 8.33 \text{ g}\cdot\text{L}^{-1}$, initial $\text{pH} = 4.0 \pm 0.1$, $I = 100 \text{ mmol L}^{-1}$ sodium acetate, $T = 310 \text{ K}$ ($37 \text{ }^\circ\text{C}$), stirring speed = 150 rpm, and equilibrium time = 24 h.

Therefore, to obtain the desirable mechanical stability of UPA monolith with considerable RBBR adsorption capacity, in the following studies, UPA(θ) monolith was employed to achieve more homogeneous adsorbent dispersion after a rigorous grinding process.

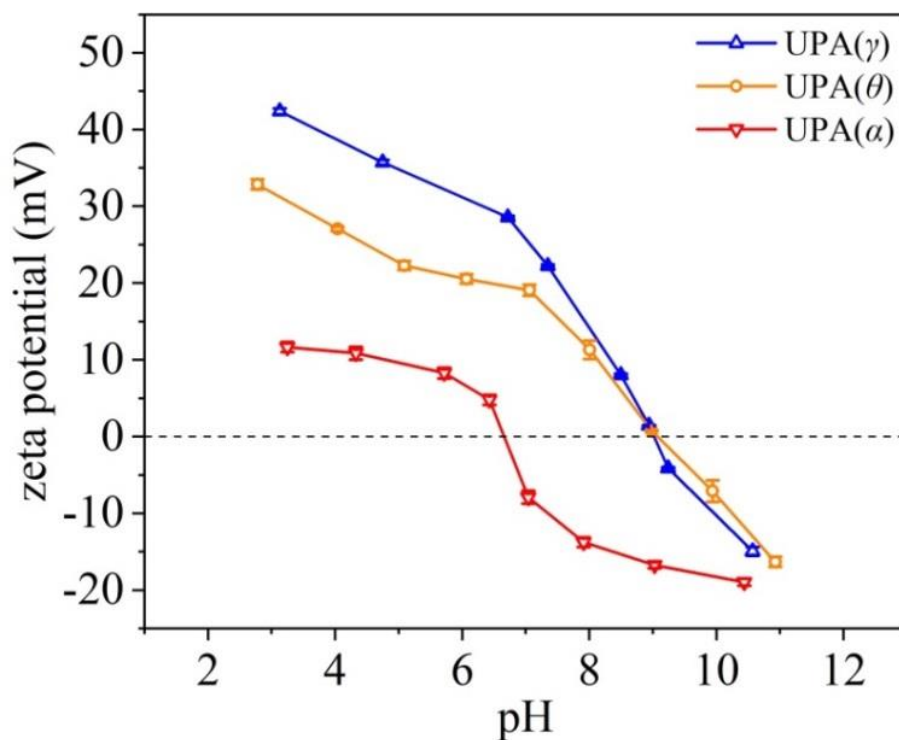


Figure 3.8. – Zeta potential values of UPA(γ), UPA(θ), and UPA(α) powders as a function of pH. $m/V[UPA] = 4.44 \text{ g L}^{-1}$, and $I = 100 \text{ mmol L}^{-1}$ sodium acetate.

As shown in Figure 3.8, UPA(γ) and UPA(θ) powders possessed similar pH of zero point of charge (pHzpc) values (i.e., pHzpc = 9.0), while the pHzpc value of UPA(α) powders decreased obviously (i.e., pHzpc = 6.7). Moreover, under acidic conditions which is less than the corresponding pHzpc values., the zeta potential values of UPA(α) powders were less than those of UPA(γ) and UPA(θ) powders. At low pH values, the electrostatic attraction between the protonated (positively charged) functional groups on UPA surfaces should significantly contribute to RBBR adsorption, while these gradually deprotonated (negatively charged) functional groups may become less favorable for the adsorption process.

Based on the above-mentioned discussions, compared with UPA materials in γ and θ polycrystalline phases, UPA(α) powders possess the minimal specific surface area, the minimal amount of functional groups on the surfaces, and the lowest zeta potential values, which may limit its applicability for either RBBR removal or laccase T. immobilization.

3.3. Effect of initial pH

The effect of initial pH on RBBR adsorption retained by UPA(θ) powders was studied in the pH range from 2.0 to 11.0 (Figure 3.9):

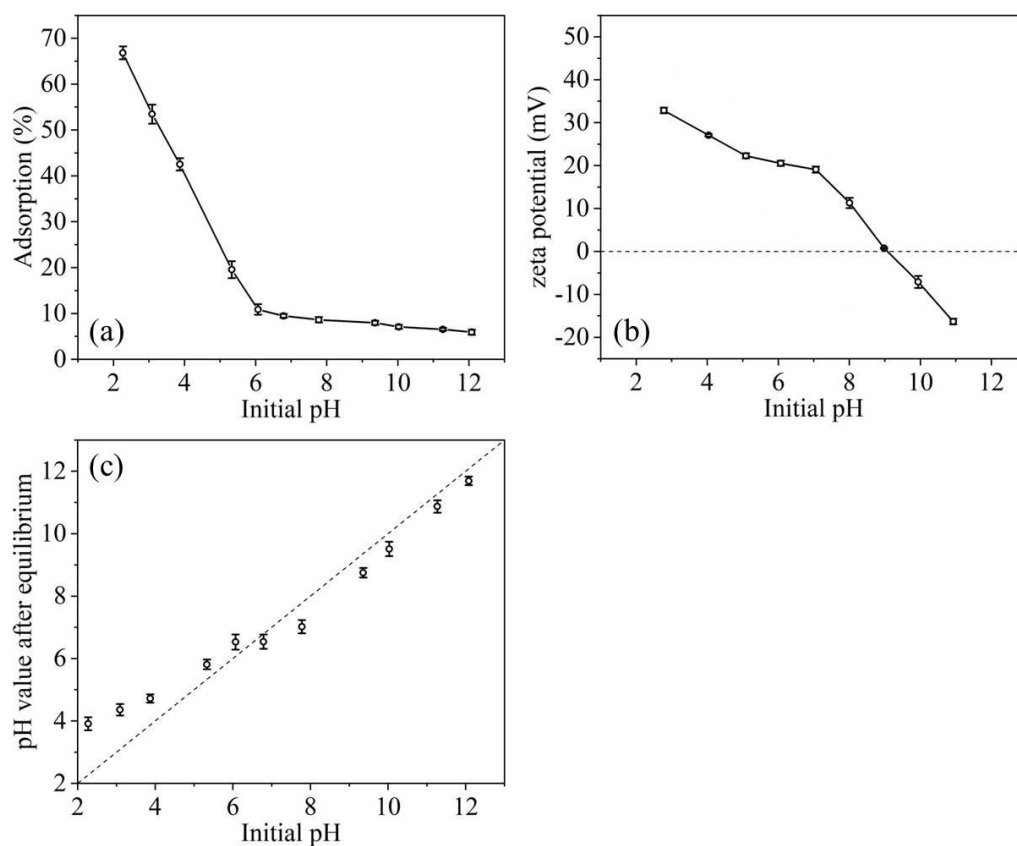


Figure 3.9. – (a) Effect of initial pH on RBBR adsorption retained by UPA(θ) powders, (b) zeta potential values of UPA(θ) powders as a function of pH, and (c) pH variation after RBBR adsorption equilibrium retained by UPA(θ) powders. $C[\text{RBBR}]_{\text{initial}} = 800 \text{ mg L}^{-1}$, $m/V[\text{UPA}(\theta)] = 4.44 \text{ g}\cdot\text{L}^{-1}$, $I = 100 \text{ mmol L}^{-1}$ sodium acetate, $T = 310 \text{ K}$ ($37 \text{ }^\circ\text{C}$), stirring speed = 150 rpm, and equilibrium time = 24 h.

As shown in Figure 3.9a, the RBBR adsorption retained by UPA(θ) powders strongly decreased with increasing pH (up to pH = 6) and then slowly decreased in the following pH range. According to Figures 3.8 and 3.9b, the pHzpc value of UPA(θ) powders approximately equaled to 9.0, and the increasing solution pH values after RBBR adsorption equilibrium indicated the significant consumption of hydrogen ions under acidic conditions (Figure 3.9c).

At low pH values, the electrostatic attraction between the protonated (positively charged) functional groups on UPA(θ) surfaces and RBBR species resulted in the high adsorption percentage of RBBR (O'Mahony et al., 2002; Iqbal and Saeed, 2007; Moussavi and Mahmoudi, 2009). As the pH value increased, these gradually deprotonated (negatively charged) functional groups became less favorable for the adsorption process, and consequently, the affinity of UPA(θ) powders toward the negatively charged RBBR species (e.g., $-\text{SO}_3^-$, sulfonate groups) decreased (Figure 3.9b). Moreover, at high pH values, the formation of excessed OH^- ions under alkaline conditions and subsequent competition with the RBBR species for the finite reaction sites on UPA(θ) surfaces may also lead to the low RBBR adsorption percentage (Moussavi and Mahmoudi, 2009).

According to the previous studies, similar results have also been reported by applying other kinds of adsorbents for RBBR removal (O'Mahony et al., 2002; Taty-Costodes et al., 2003; Iqbal and Saeed, 2007; Gök et al., 2010; Shanehsaz et al., 2015). For example, Gök et al. (2010) found that the adsorption of RBBR onto 1,6-diamino hexane modified bentonite (DAH-bentonite) was strongly pH dependent, with the optimum pH = 1.5.

Therefore, the low adsorption percentage of RBBR under alkaline conditions can be attributed to the electrostatic repulsion between the negatively charged UPA(θ) surfaces and the anionic RBBR species, which became the essential factor in controlling the adsorption process.

3.4. Effect of contact time

In order to determine the adsorption mechanism, the kinetic studies of an adsorption process are significant from the points of following perspectives (Taty-Costodes et al., 2003): (1) The kinetic data can be used in determining the time required to achieve adsorption equilibrium; (2) The adsorption rate constants determined from the kinetic studies can be used to deduce predictive models for batch experiments; (3) These kinetic studies can be used in understanding the effects of variables on the adsorption of solutes.

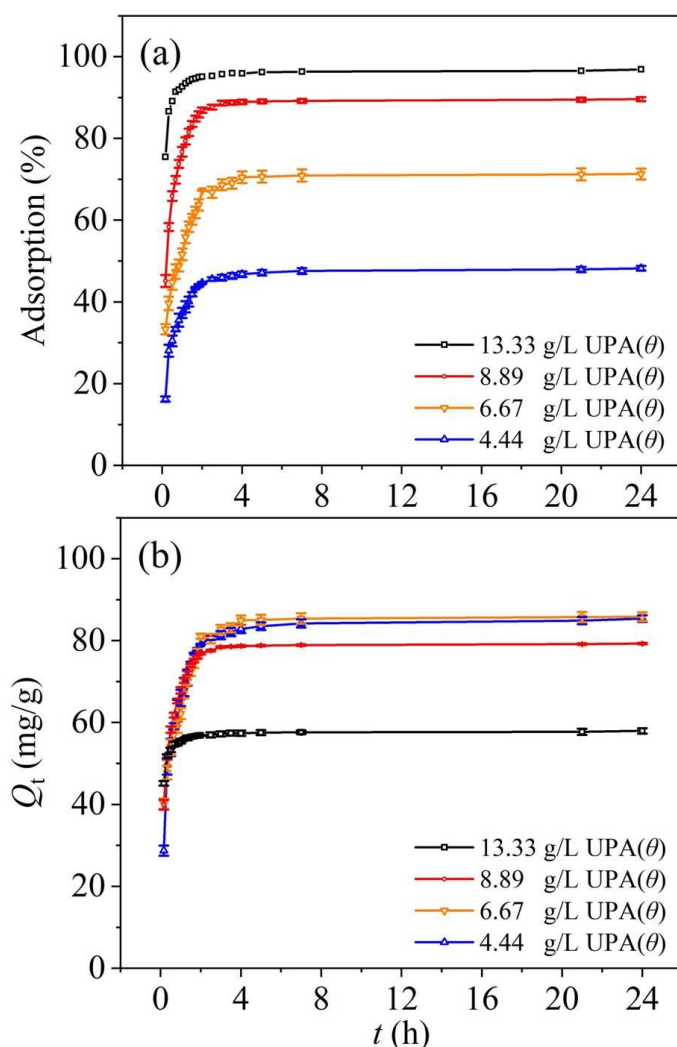


Figure 3.10. – Adsorption kinetics regarding the (a) adsorption percentage and (b) adsorption capacity of RBBR retained by UPA(θ) powders. $C[\text{RBBR}]_{\text{initial}} = 800 \text{ mg L}^{-1}$, initial $\text{pH} = 4.0 \pm 0.1$, $I = 100 \text{ mmol L}^{-1}$ sodium acetate, $T = 310 \text{ K}$ ($37 \text{ }^\circ\text{C}$), stirring speed = 150 rpm, and terminal equilibrium time = 24 h.

The kinetic data regarding the adsorption percentage and adsorption capacity of RBBR retained by UPA(θ) powders were shown in Figures 3.10a and 3.10b, respectively. The RBBR adsorption increased rapidly in the first 4 h and then maintained at a high level until the adsorption process achieved equilibrium.

Figures 3.10a and 3.10b also showed that in the initial step, the adsorption process achieved equilibrium much more rapidly at high adsorbent dosage. In Figure 3.10b, the decrease of Q_t value of RBBR adsorption may result from the increasing UPA(θ) dosage on which more vacant reaction sites became available. In general, the RBBR adsorption process was rapid and 4 h was enough to achieve the entire adsorption equilibrium.

3.5. Effect of dose concentration

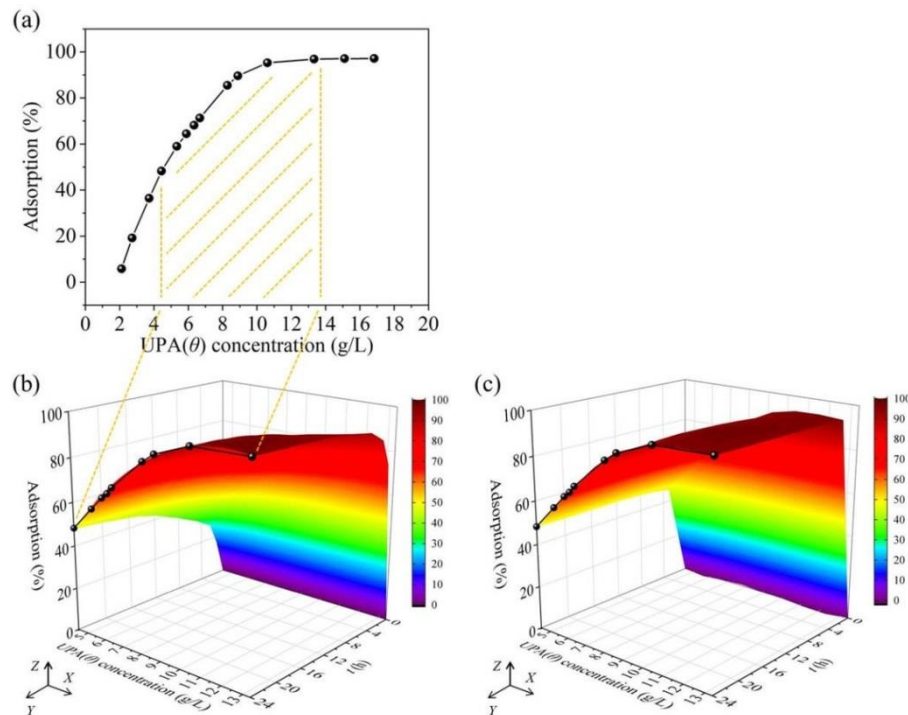


Figure 3.11. – (a) Effect of UPA(θ) dosage on RBBR adsorption kinetics, three-dimensional curved surface simulation based on (b) MATLAB and (c) Origin matrix conversion and gridding. $C[\text{RBBR}]_{\text{initial}} = 800 \text{ mg L}^{-1}$, initial pH = 4.0 ± 0.1 , $I = 100 \text{ mmol L}^{-1}$ sodium acetate, $T = 310 \text{ K}$ ($37 \text{ }^\circ\text{C}$), stirring speed = 150 rpm, and terminal equilibrium time = 24 h.

The effect of UPA(θ) dosage on RBBR adsorption kinetics was shown in Figure 3.11a. This increase can be attributed to the more functional groups on UPA(θ) surfaces and the increase in more vacant reaction sites available for RBBR adsorption. Based on the profiles of kinetic data (Figure 3.11a), the three-dimensional curved surface simulation based on MATLAB and Origin matrix conversion and gridding were shown in Figures 3.11b and 3.11c, respectively (XZ side, i.e., “UPA(θ) dosage (g L^{-1})–Adsorption (%)” side in Figures 3.11b and 3.11c).

Compared with MATLAB-based simulation, the three-dimensional curved surface derived from Origin-based direct worksheet conversion to matrix showed less smoothness. As discussed above, the increasing UPA(θ) dosage may result in more vacant reaction sites available on the adsorbent surfaces for RBBR adsorption. This positive relationship explained the Γ line type of kinetic data on the XZ side of Figures 3.11b and 3.11c at 24 h of equilibrium time (black line highlighted).

The RBBR adsorption increased with increasing UPA(θ) dosage and exceeded 96% when UPA(θ) dosage attained more than $10 \text{ g}\cdot\text{L}^{-1}$. As long as sufficient reaction sites were provided, the RBBR adsorption was independent of UPA(θ) dosage. All the above discussions indicated that the UPA(θ) dosage played an important role in the adsorption process; however, the economic issues usually should be taken into consideration in the actual adsorbent applications. Therefore, in order to obtain suitable dye treatment, one should determine the appropriate UPA(θ) dosage according to the initial concentration of dye effluents (Gök et al., 2010; Moussavi and Mahmoudi, 2009; Monsef Khoshhesab and Souhani, 2018; Monsef Khoshhesab and Modaresnia, 2019).

3.6. Adsorption kinetics

The overall adsorption rate and migration process of the solutes at solid–liquid interface are controlled by the adsorbent surface characteristics and solute diffusion rate within the microporous structure of adsorbents (Plazinski et al., 2013;

Álvarez-Torrellas et al., 2016). Therefore, utilization of a suitable kinetic model can provide useful information in determining the underlying mechanisms during the entire adsorption process.

The fitting results of the Lagergren pseudo-first-order and pseudo-second-order models were shown in Figures 3.12a and 3.12b, respectively, and the fitting parameters were listed in Table 3.1 as follows:

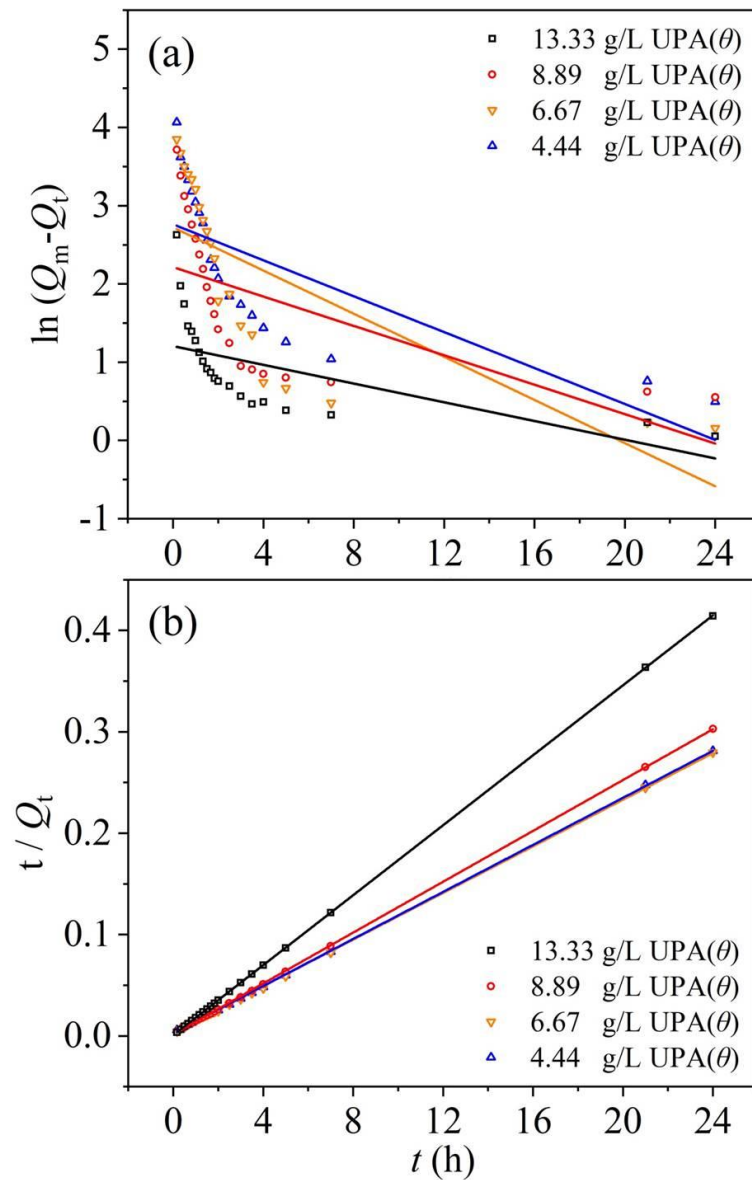


Figure 3.12. – Tests of the (a) Lagergren pseudo-first-order and (b) pseudo-second-order models on RBBR adsorption retained by UPA(θ) powders.

Table 3.1. – Parameters of RBBR adsorption kinetics fitted by the Lagergren pseudo-first-order and pseudo-second-order models. ^a

Kinetic Models	UPA(θ) dose (g L^{-1})			
	4.44	6.67	8.89	13.33
Lagergren pseudo-first-order				
k' (h^{-1})	0.12	0.14	0.09	0.06
Q_{mc} (mg g^{-1}) ^a	15.84	15.24	9.17	3.34
R^2	0.521	0.511	0.336	0.332
Pseudo-second-order				
k'' ($\text{g mg}^{-1} \text{h}^{-1}$)	0.05	0.05	0.10	0.42
Q_{mc} (mg g^{-1}) ^a	86.21	86.96	79.75	57.80
R^2	0.999	0.999	0.999	0.999
Q_{me} (mg g^{-1}) ^b	87.39	87.93	81.12	59.99

^a Q_{mc} (mg g^{-1}) is the calculated adsorption capacity at equilibrium obtained from the kinetic models.

^b Q_{me} (mg g^{-1}) is the experimental adsorption capacity at equilibrium.

As shown in Table 3.1, the low determination coefficients (R^2) obtained from the Lagergren pseudo-first-order model showed that between the kinetic data and this model, there was no significant correlation. On the other hand, the pseudo-second-order model fitted the kinetic data better, and the calculated adsorption capacities at equilibrium (Q_{mc}) were closer to the experimental ones (Q_{me}). Therefore, the adsorption process followed the pseudo-second-order model based on the assumption that the rate-limiting step may be chemical adsorption or chemisorption involving valence forces through sharing or exchanging electrons between the adsorbent and adsorbate, which provides the best correlation of the kinetic data (Ho and Mckay, 1999; Ijagbemi et al., 2009).

3.7. Rate-limiting step determination

Generally, the adsorption kinetics of solutes retained by porous materials is controlled by different steps (Ijagbemi et al., 2009; Monsef Khoshhesab and Modaresnia, 2019): (1) Solutes transfer from the aqueous phase to the more external adsorbent surface, crossing the boundary film bordering the solid adsorbent particles (film diffusion step); (2) Internal diffusion of solutes transferring from the adsorbent surface to the intraparticle active sites (particle diffusion step); (3) Sequestration on the active sites via adsorption, complexation, or intraparticle precipitation phenomena.

One or more of the above-mentioned steps may affect the mechanisms governing the adsorption process. The fitting results of the film diffusion and intraparticle diffusion models were shown in Figures 3.13a and 3.13b, respectively, and the fitting parameters were listed in Table 3.2 as follows.

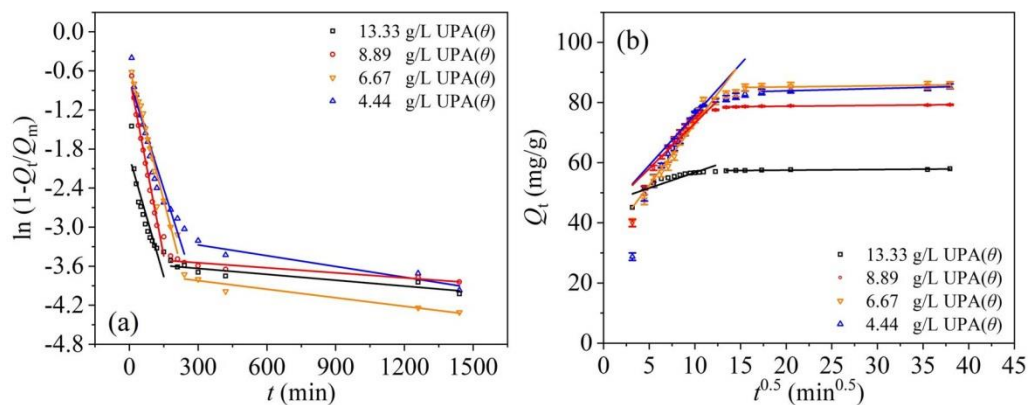


Figure 3.13. – Tests of the (a) film diffusion (Boyd plot) and (b) intraparticle diffusion (Weber and Morris plot) models on RBBR adsorption retained by UPA(θ) powders.

The nonlinear distribution of points with two distinct regions observed in Figure 3.13b indicated that intraparticle/pore diffusion may participate in the adsorption process but was not the single rate-limiting step (Ijagbemi et al., 2009). The deviation of intercepts of Weber and Morris plot (C_{IPD} , Figure 3.13b) may be due to the difference in the rate of mass transfer in the initial and final stages of the adsorption process (Srivastava et al., 2006; Fan et al., 2016).

For the RBBR adsorption retained by UPA(θ) powders, the initial curved region of the plot was attributed to the film diffusion, and the subsequent linear region was attributed to the intraparticle diffusion and chemical reactions (Taty-Costodes et al., 2003; Ijagbemi et al., 2009).

Table 3.2. – Parameters of RBBR adsorption kinetics fitted by the film diffusion (Boyd plot) and intraparticle diffusion (Weber and Morris plot) models.

Diffusion models	First-Curved Adsorption Part				Second-Linear Adsorption Part			
	4.44	6.67	8.89	13.33	4.44	6.67	8.89	13.33
Film diffusion								
k_{FD} (min^{-1})	0.011	0.014	0.018	0.012	0.0006	0.0004	0.0003	0.0003
Intercept on Y axis ^a	-0.746	-0.556	-0.690	-1.922	-3.108	-3.691	-3.471	-3.545
R^2	0.911	0.956	0.976	0.807	0.885	0.909	0.866	0.826
Intraparticle diffusion								
k_{IPD} ($\text{mg g}^{-1} \text{min}^{-0.5}$)	3.363	4.054	3.012	1.039	0.077	0.037	0.028	0.022
C_{IPD}	42.309	32.299	43.003	46.347	82.332	84.429	78.199	57.072
R^2	0.708	0.904	0.873	0.704	0.899	0.916	0.875	0.838

^a A linear plot of $-\ln(1-Q_t/Q_m)$ versus t with zero intercept indicates that the kinetics of the adsorption process is controlled by diffusion through the liquid surrounding the solid adsorbent particles.

3.8. Effect of temperature

Adsorption isotherm curves can describe the phenomenon governing the retention or mobility of a substance from the aqueous porous media or aquatic environments to a solid phase at a given temperature and pH (Allen et al., 2004; Limousin et al., 2007; Mbugua et al., 2017).

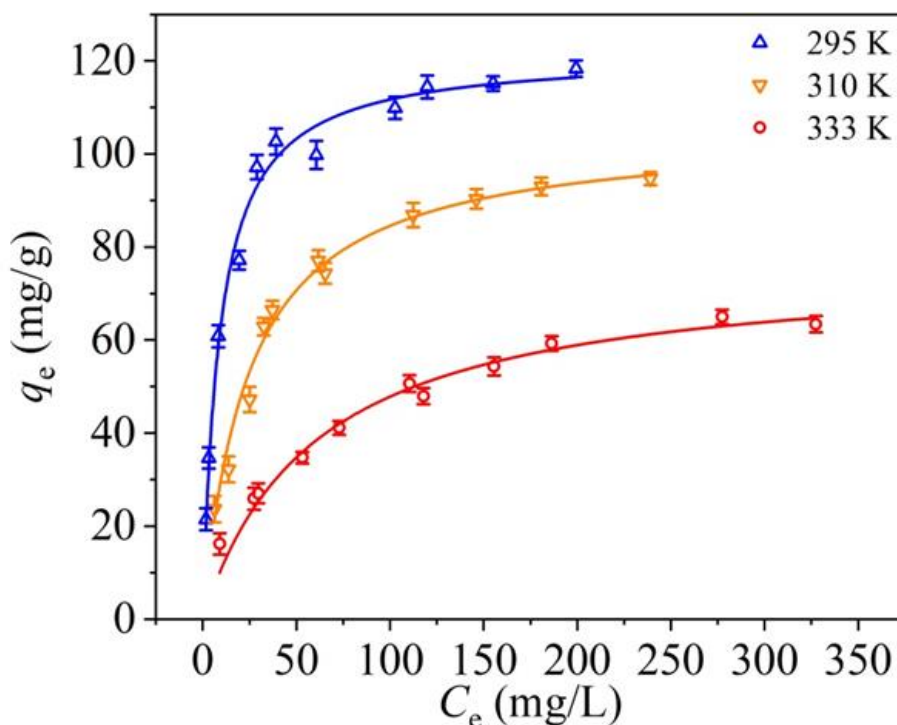


Figure 3.14. – Adsorption isotherm profiles of RBBR retained by UPA(θ) powders at different temperatures. $m/V[\text{UPA}(\theta)] = 5.56 \text{ g}\cdot\text{L}^{-1}$, initial $\text{pH} = 4.0 \pm 0.1$, $I = 100 \text{ mmol L}^{-1}$ sodium acetate, stirring speed = 150 rpm, and equilibrium time = 24 h.

As shown in Figure 3.14, the RBBR adsorption capacity of UPA(θ) powders decreased with increasing temperature, which indicated that the adsorption reaction may be exothermic, and low temperature may favor the adsorption process.

The fitting results of the Langmuir, Freundlich, Temkin, and D.-R. isotherm models were shown in Figure 3.15, and the fitting parameters were listed in Table 3.3 as follows:

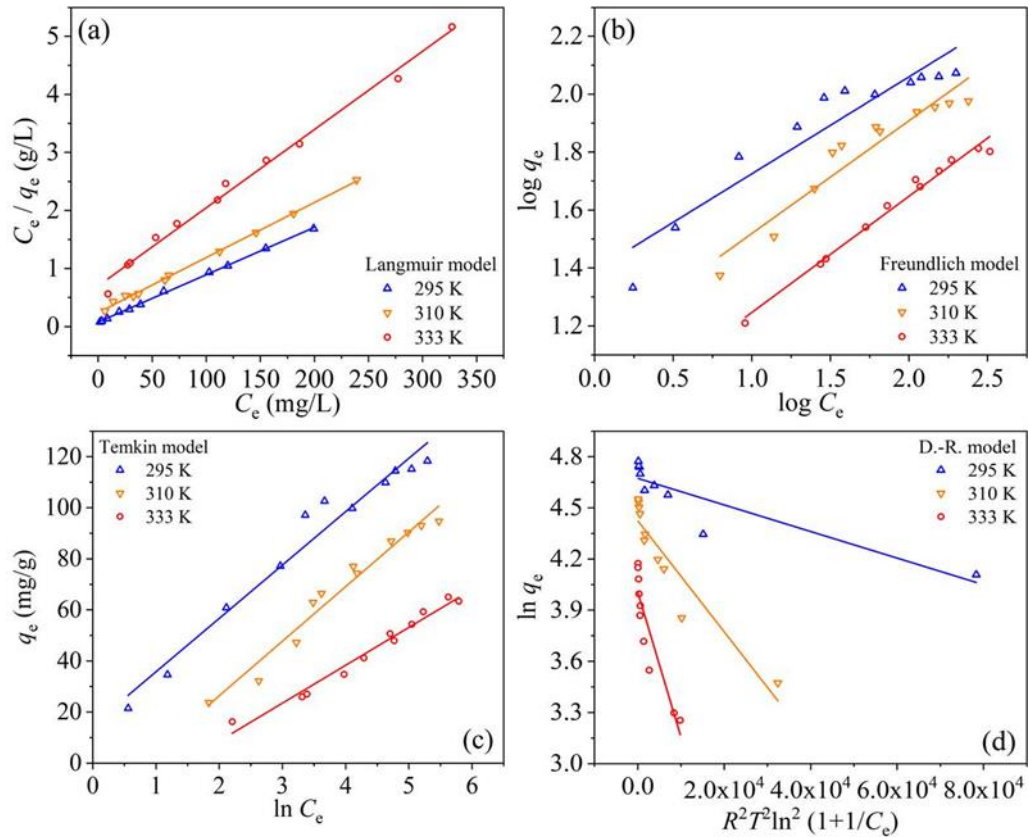


Figure 3.15. – Tests of the (a) Langmuir, (b) Freundlich, (c) Temkin, and (d) D.-R. isotherm models on RBBR adsorption retained by UPA(θ) powders. at different temperatures.

The Langmuir model fitted the adsorption equilibrium data better than the other three models (i.e., Langmuir > Temkin \approx Freundlich > D.-R. model), which indicates the presence of RBBR monolayer coverage on UPA(θ) surfaces (Table 3.3) (Langmuir, 1916; Langmuir, 1917; Langmuir, 1918). Based on the Langmuir model, the $q_{e,max}$ values of RBBR retained by UPA(θ) powders were 122.55, 105.49, and 74.18 mg g^{-1} for 295 K (22 °C), 310 K (37 °C), and 333 K (60 °C), respectively. These results were consistent with the equilibrium q_e values obtained from the adsorption equilibrium study (Figure 3.14), which also indicates that low temperature may favor the adsorption process. Moreover, all the R_L values fell in the range of 0–1, which indicates that the adsorption process was favorable, and RBBR tended to remain the bonding on UPA(θ) surfaces (Table 3.3) (Hall et al., 1966).

Table 3.3. – Parameters of RBBR adsorption isotherms fitted by the Langmuir, Freundlich, Temkin, and D.-R. isotherm models at different temperatures.

Isotherm models	295 K	310 K	333 K
Langmuir			
$q_{e,max}$ (mg g ⁻¹)	122.55	105.49	74.18
K_L (L mg ⁻¹)	0.11	0.04	0.02
R^2	0.999	0.998	0.991
R_L	0.01–0.08	0.03–0.19	0.06–0.28
Freundlich			
K_F (mg ^(1-1/n) L ^{1/n} g ⁻¹)	24.55	13.46	6.99
1/n	0.34	0.39	0.40
R^2	0.880	0.903	0.982
Temkin			
B (J mol ⁻¹)	20.89	21.38	14.82
K_T (L g ⁻¹)	2.04	0.46	0.24
R^2	0.960	0.961	0.973
D.-R.			
$q_{e,max}$ (mg g ⁻¹)	107.04	83.50	54.98
β (mol ² kJ ⁻²)	7.80×10^{-6}	3.26×10^{-5}	8.50×10^{-5}
E (kJ mol ⁻¹)	358.17	175.22	108.49
R^2	0.784	0.866	0.823

The obtained R^2 values from the Temkin model were slightly greater than those of the Freundlich model, and the equilibrium binding constants (K_T) at high temperatures were less than that at room temperature. In the Freundlich model, all the values of 1/n at different temperatures were less than 1, which indicates the surface heterogeneity of UPA(θ) powders during the adsorption process (Haghseresht and Lu, 1998; Cicek et al., 2007; Foo and Hameed, 2010).

Among the isotherm models applied in this study, the obtained R^2 values from the D.-R. model were the lowest among the considered isotherm models, and the $q_{e,max}$ values were much less than the equilibrium q_e values obtained from the adsorption isotherms (Figure 3.14). Consequently, the model analysis indicated the low applicability of the D.-R. model on the adsorption process.

3.9. Thermodynamic study

The thermodynamic parameters can define whether the RBBR adsorption retained by UPA(θ) powders was endothermic or exothermic, spontaneous or not (Anayurt et al., 2009; Aziz et al., 2009). The linear plots of $\ln K_d$ versus C_e and $\ln K^0$ versus $1000/T$ were shown in Figures 3.16a and 3.16b, respectively. The obtained thermodynamic parameters were listed in Table 3.4 as follows:

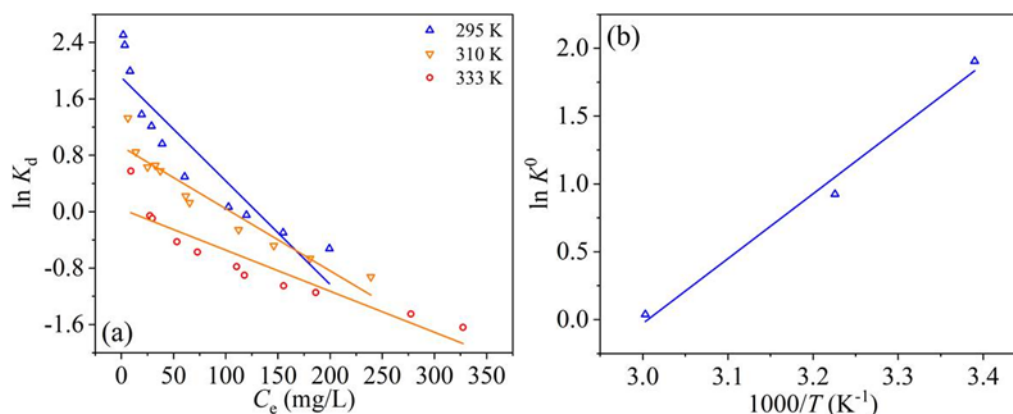


Figure 3.16. – Linear plots of (a) $\ln K_d$ versus C_e and (b) $\ln K^0$ versus $1000/T$ for RBBR adsorption retained by UPA(θ) powders.

Table 3.4. – Thermodynamic parameters of RBBR adsorption retained by UPA(θ) powders.

T (K)	ΔG^0 (kJ mol ⁻¹)	ΔH^0 (kJ mol ⁻¹)	ΔS^0 (J mol ⁻¹ K ⁻¹)
295	-4.67		
310	-2.38	-39.71	-119.37
333	-0.11		

The obtained negative ΔG^0 values indicated that the RBBR adsorption process was thermodynamically favorable and spontaneous (Table 3.4). The increase of ΔG^0 value with increasing temperature indicated that low temperature favored the adsorption process.

The negative ΔH^0 value confirmed the exothermicity of the adsorption process. Moreover, the magnitude order of ΔH^0 value can indicate the type of adsorption process to be either physical (2.1–20.9 kJ mol⁻¹) or chemisorption (80–200 kJ mol⁻¹) (Saha and Chowdhury, 2011). Consequently, the RBBR adsorption retained by UPA(θ) powders can be attributed to a combined physic-chemical adsorption in nature.

The magnitude of ΔS^0 value can be used to describe the randomness at the solid-liquid interface during the adsorption process. According to the previous studies (Anayurt et al., 2009; Aziz et al., 2009; Saha and Chowdhury, 2011), the negative value of ΔS^0 reflected that the adsorption process involves an associative mechanism, and no significant change occurred in the internal structures of the adsorbent during the adsorption process, while the positive ΔS^0 value reflected the affinity of the adsorbent to adsorbate species involving the dissociative mechanism. For the RBBR adsorption retained by UPA(θ) powders, the negative value of ΔS^0 indicated that the adsorption process was enthalpy driven, accompanying a decreased disorder that occurred at the solid-liquid interface.

3.10. Adsorption mechanisms

Film diffusion, intraparticle diffusion, electrostatic attraction, surface complexation, and hydrogen bonding could be considered as the major interactions in the adsorption mechanisms for the removal of RBBR retained by UPA(θ) powders (Figure 3.17). The ultraporous nature of the UPA(θ) powders induced the adsorption of RBBR molecules by film and intraparticle diffusion mechanisms. The hydroxyl functional groups distributed on the UPA(θ) surface tended to form complexes with RBBR molecules by several mechanisms including electrostatic interaction and surface complexation, especially under acidic conditions. Moreover, hydrogen bonding between the hydroxyl functional groups (hydrogen bond donors) and nitrogen and/or oxygen centers in RBBR molecules (hydrogen bond acceptors) may also have some influences on the adsorption process.

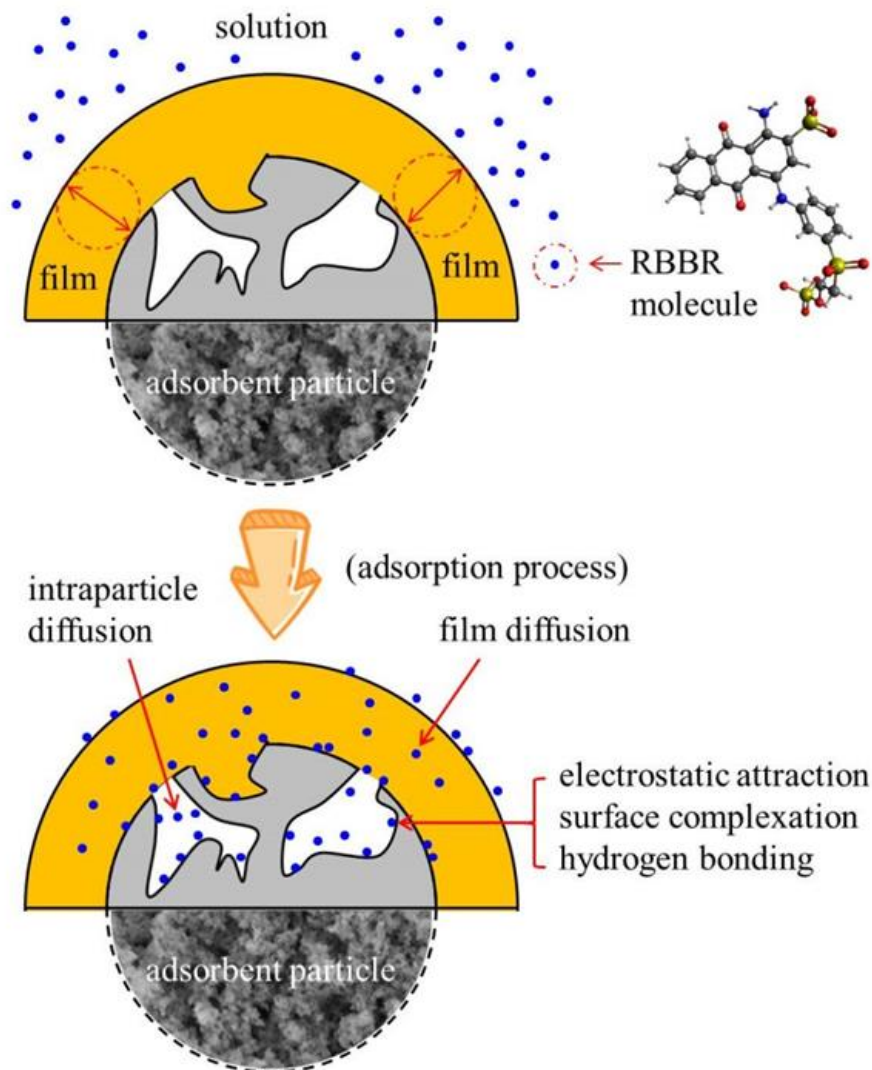


Figure 3.17. – Possible mechanisms for RBBR adsorption retained by UPA(θ) powders.

Compared with the other organic, inorganic, or bio-based adsorbents reported in related studies in the literature, UPA(θ) and UPA(γ) powders possess several advantages for large-scale applications including nontoxicity, facile synthesis, and higher RBBR adsorption capacity (Table 3.5). Therefore, UPA materials have high potentials as alternative adsorbents for the practical treatment of dye effluents.

Table 3.5. – Comparison of RBBR adsorption capacity retained by UPA materials with other organic, inorganic, or bio-based adsorbents reported in related studies in the literatures.

Adsorbents	Experimental conditions ^a	$q_{e,max}$ (mg g ⁻¹) ^b	Reference
Mazandaran wood waste (WW)	pH = 1.72, T = ND	4.75	(Azizi et al., 2012)
ZnO nanoparticles (ZnO NPs)	pH = 3.0, T = 298 K	38.02	(Monsef Khoshhesab and Souhani, 2018)
Commercial NiO	pH = ND, T = 298 K	38.62	(Monsef Khoshhesab and Ahmadi, 2015)
NiO nanoparticles	pH = ND, T = 298 K	98.83	(Monsef Khoshhesab and Ahmadi, 2015)
Magnetite/GO (MGO) nanocomposite	pH = 3.0, T = 298 K	62.50	(Ayazi et al., 2016)
Magnetite nanoparticles (MNPs)	pH = ND, T = 298 K	74.40	(Monsef Khoshhesab and Modaresnia, 2019)
Free fungal biomass (FFB)	pH = 2.0, T = 303 K	80.91	(Iqbal and Saeed, 2007)
Loofa sponge-immobilized fungal biomass (LSIFB)	pH = 2.0, T = 303 K	98.90	(Iqbal and Saeed, 2007)
Magnetite-modified MWCNTs (MMMCNTs)	pH = 4.0, T = 298 K	88.80	(Madrakian et al., 2013)
Rhizopus arrhizus biomass	pH = 2.0, T = 298 K	90.00	(O'Mahony et al., 2002)
Carboxylated MWCNTs	pH = ND, T = 298 K	95.24	(Hu et al., 2017)
Wheat bran	pH = 1.5, T = 293 K	97.10	(Cicek et al., 2007)

Magnetite nanoparticles-modified AC (MMAC)	pH = 4.0, T = 298 K	104.60	(Madrakian et al., 2012)
Polypyrrole-coated Fe ₃ O ₄ (Ppy@Fe ₃ O ₄ MNPs)	pH = 3.0, T = 298 K	112.36	(Shanehsaz et al., 2015)
Ultraporous alumina(α) (UPA(α))	pH = 4.0, T = 295 K	17.42	This study
Ultraporous alumina(θ) (UPA(θ))	pH = 4.0, T = 295 K	122.55	This study
Ultraporous alumina(γ) (UPA(γ))	pH = 4.0, T = 295 K	212.31	This study
Modified polyethyleneimine (LMW-PEI)	pH = 10.0, T = 298 K	121.00	(Liao et al., 2006)
Modified bentonite (DAH-bentonite)	pH = 1.5, T = 293 K	134.71	(Gök et al., 2010)
MgO nanoparticles (Nano-MgO)	pH = 8.0, T = 298 K	166.70	(Moussavi and Mahmoudi, 2009)

^a ND: No data.

^b Adsorption capacity uniformly converted into mg g⁻¹ (typical unit).

3.11. Conclusions

In this chapter, UPA materials were synthesized as new effective adsorbents for RBBR removal from aqueous solutions. The experimental factors that affect the material adsorption performances including initial pH, contact time, and temperature were comprehensively studied by batch experiments. Different kinetic and isotherm models were applied to fit the adsorption equilibrium data. The thermodynamic study and the adsorption mechanisms including film diffusion, intraparticle diffusion, electrostatic attraction, surface complexation, and hydrogen bonding were further discussed.

The adsorption process was pH- and temperature-dependent, and the maximum RBBR adsorption capacity retained by UPA(θ) powders was 122.55 mg g⁻¹ at 295 K (22 °C). Both film diffusion and intraparticle diffusion contributed to the adsorption kinetics, and chemical reactions also played a significant role during the entire adsorption process. The pseudo-second-order model and the Langmuir isotherm model were found to best describe the experimental data (i.e., pseudo-second-order > Lagergren pseudo-first-order model; and Langmuir > Temkin \approx Freundlich > D.-R. isotherm model). Moreover, the thermodynamic parameters (ΔG^0 , ΔH^0 , and ΔS^0) indicated that the adsorption process was spontaneous and exothermic in nature. Compared with the other adsorbents reported in related studies in the literature, UPA(θ) and UPA(γ) powders possess several advantages for large-scale applications including nontoxicity, facile synthesis, and higher RBBR adsorption capacity. The findings of this study highlight the UPA potentials in wastewater treatment, which can broaden our understanding and its practical applications in the environmental field.

3.12. References

- Al-Rubayee, W.T.; Abdul-Rasheed, O.F.; Ali, N.M., Preparation of a modified nanoalumina sorbent for the removal of alizarin yellow R and methylene blue dyes from aqueous solutions, *Journal of Chemistry*, 2016 (2016) 1–12.
- Allen, S.J.; Mckay, G.; Porter, J.F., Adsorption isotherm models for basic dye adsorption by peat in single and binary component systems, *Journal of Colloid and Interface Science*, 280 (2004) 322–333.
- Anayurt, R.A.; Sari, A.; Tuzen, M., Equilibrium, thermodynamic and kinetic studies on biosorption of Pb(II) and Cd(II) from aqueous solution by macrofungus (*Lactarius scrobiculatus*) biomass, *Chemical Engineering Journal*, 151 (2009) 255–261.
- Ayazi, Z.; Khoshhesab, Z.M.; Norouzi, S., Modeling and optimizing of adsorption removal of Reactive Blue 19 on the magnetite/graphene oxide nanocomposite via response surface methodology, *Desalination and Water Treatment*, 57 (2016) 25301–25316.
- Azizi, A.; Alavi Moghaddam, M.R.; Arami, M., Applications of wood waste for removal of reactive blue 19 from aqueous solutions: Optimization through response surface methodology, *Environmental Engineering and Management Journal*, 11 (2012) 795–804.
- Aziz, A.; Ouali, M.S.; Elandaloussi, E.H.; De Menorval, L.C.; Lindheimer, M., Chemically modified olive stone: A low-cost sorbent for heavy metals and basic dyes removal from aqueous solutions, *Journal of Hazardous Materials*, 163 (2009) 441–447.
- Álvarez-Torrellas, S.; Ribeiro, R.S.; Gomes, H.T.; Ovejero, G.; Garc á, J., Removal of antibiotic compounds by adsorption using glycerol-based carbon materials, *Chemical Engineering Journal*, 296 (2016) 277–288.
- Cicek, F.; Özer, D.; Özer, A.; Özer, A., Low cost removal of reactive dyes using wheat bran, *Journal of Hazardous Materials*, 146 (2007) 408–416.

-
- Dubinin, M.M.; Radushkevich, L.V., The equation of the characteristic curve of the activated charcoal, *Proceedings of the USSR Academy of Sciences*, 55 (1947) 331–337.
- Fan, H.-T.; Sun, W.; Jiang, B.; Wang, Q.-J.; Li, D.-W.; Huang, C.-C.; Wang, K.-J.; Zhang, Z.-G.; Li, W.-X., Adsorption of antimony(III) from aqueous solution by mercapto-functionalized silica-supported organic-inorganic hybrid sorbent: Mechanism insights, *Chemical Engineering Journal*, 286 (2016) 128–138.
- Foo, K.Y.; Hameed, B.H., Insights into the modeling of adsorption isotherm systems, *Chemical Engineering Journal*, 156 (2010) 2–10.
- Freundlich, H.M.F., Over the adsorption in solution (in German), *Journal of Physical Chemistry*, 57 (1906) 385–471.
- Gök, Ö.; Özcan, A.S.; Özcan, A., Adsorption behavior of a textile dye of Reactive Blue 19 from aqueous solutions onto modified bentonite, *Applied Surface Science*, 256 (2010) 5439–5443.
- Haghsersht, F.; Lu, G.-Q., Adsorption characteristics of phenolic compounds onto coal-reject-derived adsorbents, *Energy & Fuels*, 12 (1998) 1100–1107.
- Hall, K.R.; Eagleton, L.C.; Acrivos, A.; Vermeulen, T., Pore- and solid-diffusion kinetics in fixed-bed adsorption under constant-pattern conditions, *Industrial & Engineering Chemistry Fundamentals*, 5 (1966) 212–223.
- Ho, Y.S.; McKay, G., Pseudo-second order model for sorption processes, *Process Biochemistry*, 34 (1999) 451–465.
- Hu, C.-W.; Hu, N.-T.; Li, X.-L.; Shen, H.-L.; Zhao, Y.-J., Adsorption of remazol brilliant blue R by carboxylated multi-walled carbon nanotubes, *Desalination and Water Treatment*, 62 (2017) 282–289.
- Ijagbemi, C.O.; Baek, M.H.; Kim, D.S., Montmorillonite surface properties and sorption characteristics for heavy metal removal from aqueous solutions, *Journal of Hazardous Materials*, 166 (2009) 538–546.
- Iqbal, M.; Saeed, A., Biosorption of reactive dye by loofa sponge-immobilized fungal

-
- biomass of *Phanerochaete chrysosporium*, *Process Biochemistry*, 42 (2007) 1160–1164.
- Mbugua, J.K.; Guto, P.M.; Madadi, V.O.; Kamau, G.N., Modeling of experimental adsorption isotherm data for chlorothalonil by Nairobi River sediment, *Modern Chemistry & Applications*, 5 (2017) 259–268.
- Langmuir, I., The constitution and fundamental properties of solids and liquids. Part I. Solids, *Journal of the American Chemical Society*, 38 (1916) 2221–2295.
- Langmuir, I., The constitution and fundamental properties of solids and liquids. Part II. Liquids, *Journal of the American Chemical Society*, 39 (1917) 1848–1906.
- Langmuir, I., The adsorption of gases on plane surfaces of glass, mica and platinum, *Journal of the American Chemical Society*, 40 (1918) 1361–1403.
- Liao, M.-H.; Chen, W.-C.; Lai, W.-C., Magnetic nanoparticles assisted low-molecular weight polyethyleneimine for fast and effective removal of reactive blue 19, *Fresenius Environmental Bulletin*, 15 (2006) 609–613.
- Limousin, G.; Gaudet, J.P.; Charlet, L.; Szenknect, S.; Barthes, V.; Krimissa, M., Sorption isotherms: A review on physical bases, modeling and measurement, *Applied Geochemistry*, 22 (2007) 249–275.
- Madrakian, T.; Afkhami, A.; Jalal, N.R.; Ahmadi, M., Kinetic and thermodynamic studies of the adsorption of several anionic dyes from water samples on magnetite-modified multi-walled carbon nanotubes, *Separation and Purification Technology*, 48 (2013) 2638–2648.
- Madrakian, T.; Afkhami, A.; Mahmood-Kashani, H.; Ahmadi, M., Adsorption of some cationic and anionic dyes on magnetite nanoparticles-modified activated carbon from aqueous solutions: Equilibrium and kinetics study, *Journal of the Iranian Chemical Society*, 10 (2012) 481–489.
- Monsef Khoshhesab, Z.; Ahmadi, M., Removal of reactive blue 19 from aqueous solutions using NiO nanoparticles: Equilibrium and kinetic studies, *Desalination and Water Treatment*, 57 (2015) 20037–20048.

-
- Monsef Khoshhesab, Z.; Modaresnia, N., Adsorption of Acid Black 210 and Remazol Brilliant Blue R onto magnetite nanoparticles, *Inorganic and Nano-Metal Chemistry*, 49 (2019) 231–239.
- Monsef Khoshhesab, Z.; Souhani, S., Adsorptive removal of reactive dyes from aqueous solutions using zinc oxide nanoparticles, *Journal of the Chinese Chemical Society*, 65 (2018) 1482–1490.
- Moussavi, G.; Mahmoudi, M., Removal of azo and anthraquinone reactive dyes from industrial wastewaters using MgO nanoparticles, *Journal of Hazardous Materials*, 168 (2009) 806–812.
- O'Mahony, T.; Guibal, E.; Tobin, J.M., Reactive dye biosorption by *Rhizopus arrhizus* biomass, *Enzyme and Microbial Technology*, 31 (2002) 456–463.
- Plazinski, W.; Dziuba, J.; Rudzinski, W., Modeling of sorption kinetics: The pseudo-second order equation and the sorbate intraparticle diffusivity, *Adsorption* 19 (2013) 1055–1064.
- Saha, P.; Chowdhury, S., Insight into adsorption thermodynamics. In *Thermodynamics*, Mizutani, T. (Ed.), InTech, ISBN 978-953-307-544-0 (2011) 349–364.
- Shanehsaz, M.; Seidi, S.; Ghorbani, Y.; Shoja, S.M.; Rouhani, S., Polypyrrole-coated magnetic nanoparticles as an efficient adsorbent for RB19 synthetic textile dye: Removal and kinetic study, *Spectrochimica Acta Part A*, 149 (2015) 481–486.
- Srivastava, V.C.; Swamy, M.M.; Mall, I.D.; Prasad, B.; Mishra, I.M., Adsorptive removal of phenol by bagasse fly ash and activated carbon: Equilibrium, kinetics and thermodynamics, *Colloids and Surfaces A: Physicochemical and Engineering Aspects*, 272 (2006) 89–104.
- Souza Santos, P.; Souza Santos, H.; Toledo, S.P., Standard transition aluminas. Electron microscopy studies, *Materials Research*, 3 (2000) 104–114.
- Storck, S.; Bretinger, H.; Maier, W.F., Characterization of micro- and mesoporous solids by physisorption methods and pore-size analysis, *Applied Catalysis A: General*, 174 (1998) 137–146.

Taty-Costodes, V.C.; Fauduet, H.; Porte, C.; Delacroix, A., Removal of Cd(II) and Pb(II) ions, from aqueous solutions, by adsorption onto sawdust of *Pinus sylvestris*, *Journal of Hazardous Materials*, 105 (2003) 121–142.

Temkin, M.I.; Pyzhev, V.P., Kinetics of ammonia synthesis on promoted iron catalyst, *Acta Physicochimica USSR*, 12 (1940) 327–356.

Chapter 4: Laccase T. cross-linked immobilized ultraporous aluminas for efficient biodegradation of RBBR

4.1. Introduction

Over the past few decades, enzyme-based green and sustainable chemistry has attracted extensive research attention, which provides a promising alternative for the conventional treatment method of recalcitrant micropollutants. However, enzyme denaturation and stability loss remain critical challenges for its potential applications in industrial wastewater treatment.

In this chapter, laccase T. was cross-linked immobilized on UPA for an effective biodegradation of RBBR. By sequentially using coupling agent APTES and cross-linker glutaraldehyde, the synthesized biocatalysts showed better immobilization performances (about 4-fold to physical adsorption). The glutaraldehyde concentration considerably affected the laccase T. cross-linking degree, while the glutaraldehyde post-treatment protocol showed the highest laccase T. immobilization yield with the lower activity recovery. According to the sequential immobilization protocol, a portable and easy-to-carry bioreactor for RBBR dye biodegradation was designed as the first prototype of an enzymatic bioreactor.

Moreover, the biocatalyst stabilities including pH stability, thermal stability, storage stability, and reusability were also studied. Tolerance to broader pH and temperature ranges, better storage stability, good reusability of the synthesized biocatalysts, and continuous biodegradation kinetics of RBBR highlight the potentials of enzyme-based inorganic materials in industrial wastewater treatment, which can broaden our understanding of their practical applications in the environmental field.

4.2. Characterizations

Figure 4.1a showed the FTIR spectra of UPA(γ) powders, APTES silanized UPA(γ) powders, laccase T. cross-linked UPA(γ) biocatalysts, and laccase T.. According to the FTIR spectrum of UPA(γ) powders, the broad absorption band in the range of 3400–3500 cm^{-1} and weak absorption band at 1642 cm^{-1} were assigned to the –OH and Al–OH stretching vibrations of alumina, respectively (Liu et al., 2012; Al-Rubayee et al., 2016). The symmetric vibrations at 755 and 568 cm^{-1} were assigned to the bending vibrations of Al–O–Al bonds (Al-Rubayee et al., 2016). For the FTIR spectrum of laccase T., the absorption band in the range of 3680–3000 cm^{-1} was assigned to the –OH and –NH stretching vibrations, while the absorption band at 2923 cm^{-1} was assigned to the C–H stretching vibration of the alkane group present in laccase T. molecular structure (Nishida et al., 2012; Samui and Sahu, 2018).

Figure 4.1b showed the FTIR spectra comparison of UPA(γ) powders and APTES silanized UPA(γ) powders. The absorption band at 2933 cm^{-1} was assigned to the C–H stretching vibration of the alkane group (Nishida et al., 2012). The absorption band at 1562 cm^{-1} was assigned to the N–H bending vibration (Hsiao et al., 2016). The absorption band at 750 cm^{-1} was assigned to the Si–C stretching vibration (Mahmoudi et al., 2007, Ivashchenko et al., 2011). Moreover, the double-peak structure between 1050 and 1200 cm^{-1} were assigned to the Si–O–Si stretching vibration (Mahmoudi et al., 2007; Li et al., 2013). After laccase T. immobilization, the FTIR spectra comparison of APTES silanized UPA(γ) powders and laccase T. cross-linked UPA(γ) biocatalysts was shown in Figure 4.1c. The twin peak appeared at 2874 cm^{-1} was assigned to the C–H stretching vibration of the alkane group (Aronson et al., 1987). And the absorption band at 1461 cm^{-1} was assigned to the C–H bending vibration (Nishida et al., 2012).. Moreover, the absorption band at 1658 cm^{-1} was assigned to the C=N stretching vibration, which belongs to the formation of Schiff base between amino groups of APTES silanized UPA(γ) powders and aldehydic groups of glutaraldehyde (Kim et al., 2007; Bashir et al., 2019).

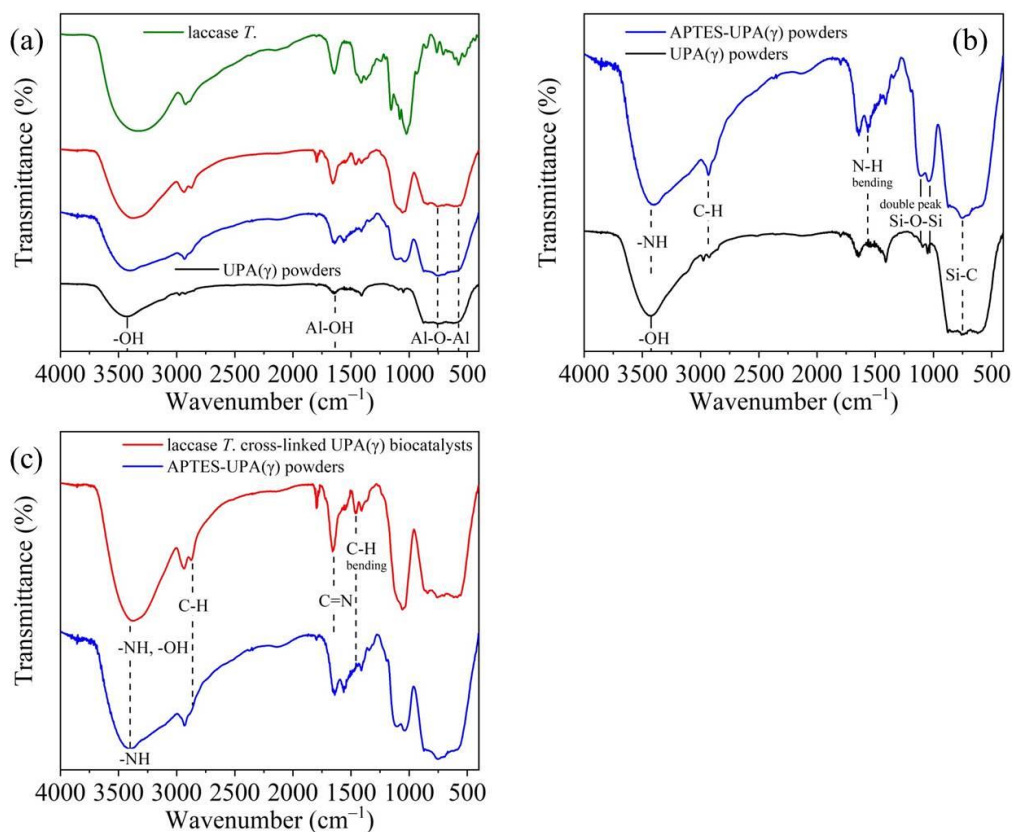


Figure 4.1. – (a) FTIR spectra of UPA(γ) powders, APTES silanized UPA(γ) powders, laccase T. cross-linked UPA(γ) biocatalysts, and laccase T., (b) FTIR spectra comparison of UPA(γ) powders and APTES silanized UPA(γ) powders, and (c) FTIR spectra comparison of APTES silanized UPA(γ) powders and laccase T. cross-linked UPA(γ) biocatalysts.

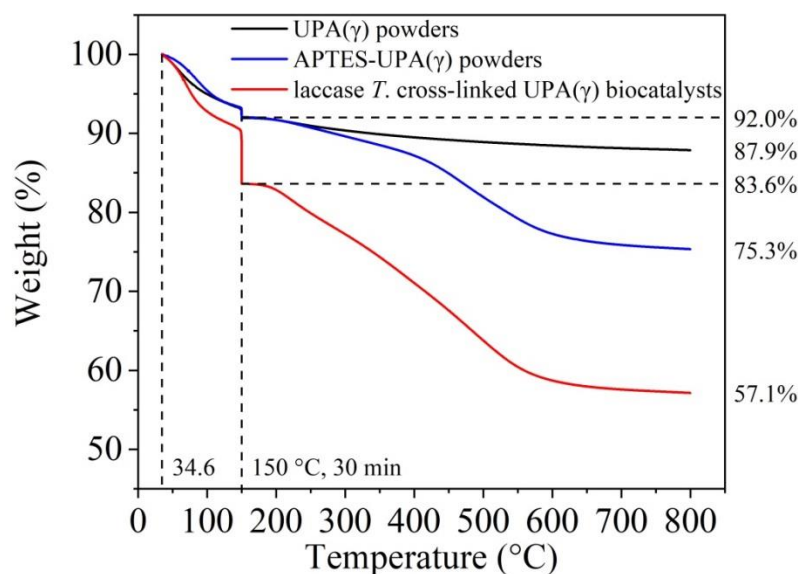


Figure 4.2. – TG curves of UPA(γ) powders, APTES silanized UPA(γ) powders, and laccase T. cross-linked UPA(γ) biocatalysts.

Figure 4.2 showed the TG curves of UPA(γ) powders, APTES silanized UPA(γ) powders, and laccase T. cross-linked UPA(γ) biocatalysts, and the corresponding mass losses occurred from 30 to 800 °C were 12.1, 24.7, and 42.9 wt%, respectively. These mass losses were attributed to the release of adsorbed water, release of structural water related to dehydration, pyrolysis related to methylene, C=N, carboxyl, and amino functional groups of the obtained samples (Zhang et al., 2018; Kaya-Özkipir et al., 2021). All the samples showed slight mass loss around 150 °C, which can be attributed to the release of adsorbed water. Moreover, UPA(γ) powders and APTES silanized UPA(γ) powders showed the same thermal decomposition stage around 150 °C (8.0 wt%), which indicates that only the release of adsorbed water occurred below this temperature. For the UPA(γ) powders, the further mass loss (4.1 wt%) between 150 and 800 °C can be attributed to the release of structural water related to dehydration. For the APTES silanized UPA(γ) powders, 12.6 wt% (150–800 °C) of mass loss can be attributed to the pyrolysis related to methylene. The pyrolysis of methylene and other functional groups resulted in the 26.5 wt% (150–800 °C) mass loss of laccase T. cross-linked UPA(γ) biocatalysts.

4.3. Effect of glutaraldehyde concentration

Glutaraldehyde is generally the cross-linker as it is inexpensive and available in commercial quantities, and the cross-linking of proteins with glutaraldehyde has been designated as generally regarded as safe (GRAS) for use especially in food and beverage processing (Kosseva, 2013; Sheldon, 2017; Sheldon and Woodley, 2018). According to Torres-Salas et al. (2011), predicting and rationalizing the orientation of enzymes which covalently attach to the carrier may affect the activity recovery of biocatalysts. Moreover, the cross-linker ratio to the enzyme is also crucial for enzyme immobilization as the low cross-linker ratio cannot induce sufficient Schiff base formation; while too high excessive cross-linking may lead to the activity loss of enzyme (Hou et al., 2014; Sheldon, 2017; Lassouane et al., 2019).

Compared with the physical adsorption, higher immobilization performances can be observed in terms of the glutaraldehyde cross-linking process, and the highest laccase T. activity recovery can be obtained with the glutaraldehyde concentration of 0.50% (v/v) (Table 4.1). The UPA powders with different polycrystalline phases showed different immobilization performances, while limited immobilization capacity can be found for UPA(α) powders (negligible data not shown).

Table 4.1. – Effect of glutaraldehyde concentration (v/v) on the laccase T. immobilization yield (IY, %), immobilization efficiency (IE, %), and activity recovery (AR, % or mg g⁻¹ carrier) of laccase T./UPA (physical adsorption) and laccase T. cross-linked UPA (sequential immobilization) with different UPA polycrystalline phases.

GA concentration (v/v)	laccase T./UPA(γ)		laccase T. cross-linked UPA(γ)			
	0	0.25%	0.50%	1.00%	1.50%	3.00%
IY (%)	68.8 ± 0.5	88.5 ± 0.5	90.5 ± 0.4	89.7 ± 0.6	87.4 ± 0.7	86.9 ± 0.5
IE (%)	7.3 ± 0.4	16.4 ± 0.6	19.3 ± 0.4	19.2 ± 0.2	16.8 ± 0.5	16.4 ± 0.4
AR (%) ^a	5.0 ± 0.2	14.6 ± 0.3	17.5 ± 0.2	17.2 ± 0.1	14.7 ± 0.3	14.3 ± 0.2
AR (mg g ⁻¹ carrier) ^b	70.0 ± 2.2	203.7 ± 4.3	244.4 ± 2.4	241.3 ± 1.4	205.2 ± 4.2	199.6 ± 2.5

GA concentration (v/v)	laccase T./UPA(θ)		laccase T. cross-linked UPA(θ)			
	0	0.25%	0.50%	1.00%	1.50%	3.00%
IY (%)	44.8 ± 0.7	56.8 ± 0.5	59.3 ± 0.4	58.9 ± 0.6	53.5 ± 0.4	54.0 ± 0.8
IE (%)	6.9 ± 0.2	18.0 ± 0.5	20.8 ± 0.6	20.2 ± 0.3	17.9 ± 0.5	18.3 ± 0.5
AR (%) ^a	3.1 ± 0.2	10.2 ± 0.2	12.3 ± 0.3	11.9 ± 0.2	9.6 ± 0.2	9.9 ± 0.4
AR (mg g ⁻¹ carrier) ^b	43.3 ± 2.3	143.2 ± 3.4	172.7 ± 3.5	166.8 ± 2.9	134.4 ± 2.3	138.4 ± 4.9

^a AR (%) mathematically equals to the value of IY (%) multiplied by the IE (%).

4.4. Disposable bioreactor

Following the sequential immobilization protocol of synthesizing laccase T. cross-linked UPA(γ) biocatalysts with the glutaraldehyde concentration which led to the highest laccase T. activity recovery, two parallel experiments regarding ABTS oxidation by laccase T. cross-linked UPA(γ) biocatalysts were conducted, and the positive results related to the active laccase T. on UPA(γ) surfaces can be observed obviously (Figure 4.3). Moreover, one can see that the green coloured ABTS⁺ radicals were initially diffused from the surface of biocatalysts (Figures 4.3a and 4.3c) (Pinkernell et al., 2000).

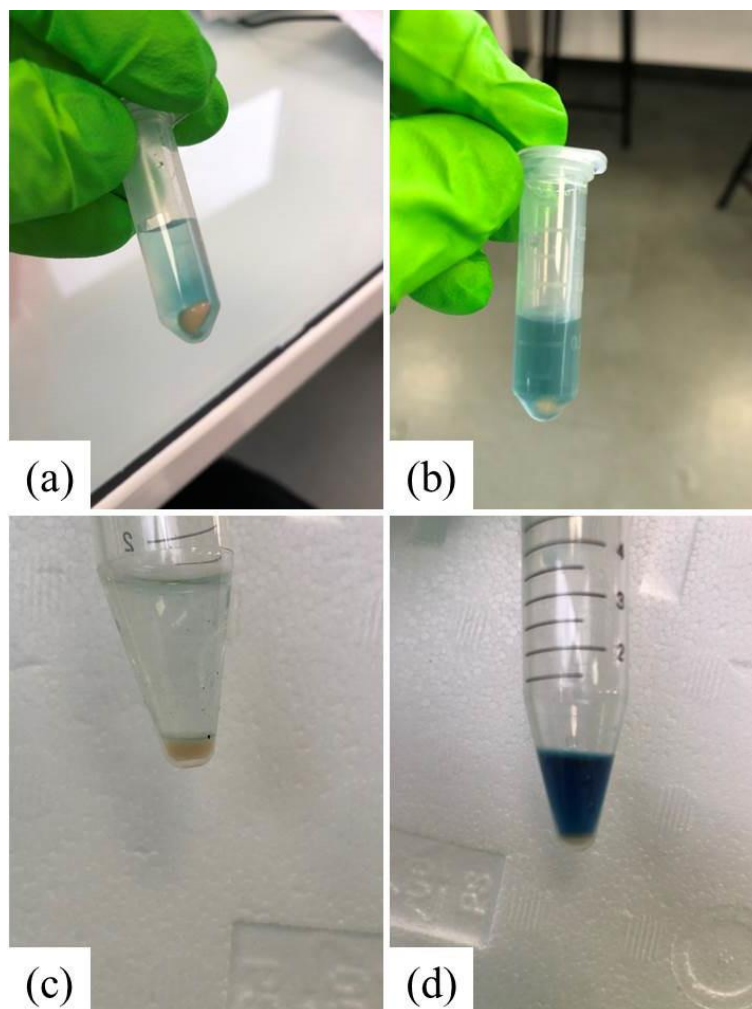


Figure 4.3. – (a) Photos of two parallel experiments regarding ABTS oxidation monitoring: (a) to (b) 0.5 mg, and (c) to (d) 2.0 mg of laccase T. cross-linked UPA(γ) biocatalysts.

Figure 4.4a showed the schematic diagram of a disposable polystyrene column, in which 2 mL of RBBR suspension can be contained and shaken with laccase T. cross-linked UPA(γ) biocatalysts inside after different time intervals. The sponge support inside the polystyrene column played the role of a holder without obvious RBBR dilution after even up to 5 cycles of dilution (Figure 4.4b). In Figure 4.4c, it is worth mentioning that after RBBR dilution, a little amount of RBBR molecules retained but distributed uniformly on the surface of sponge support.

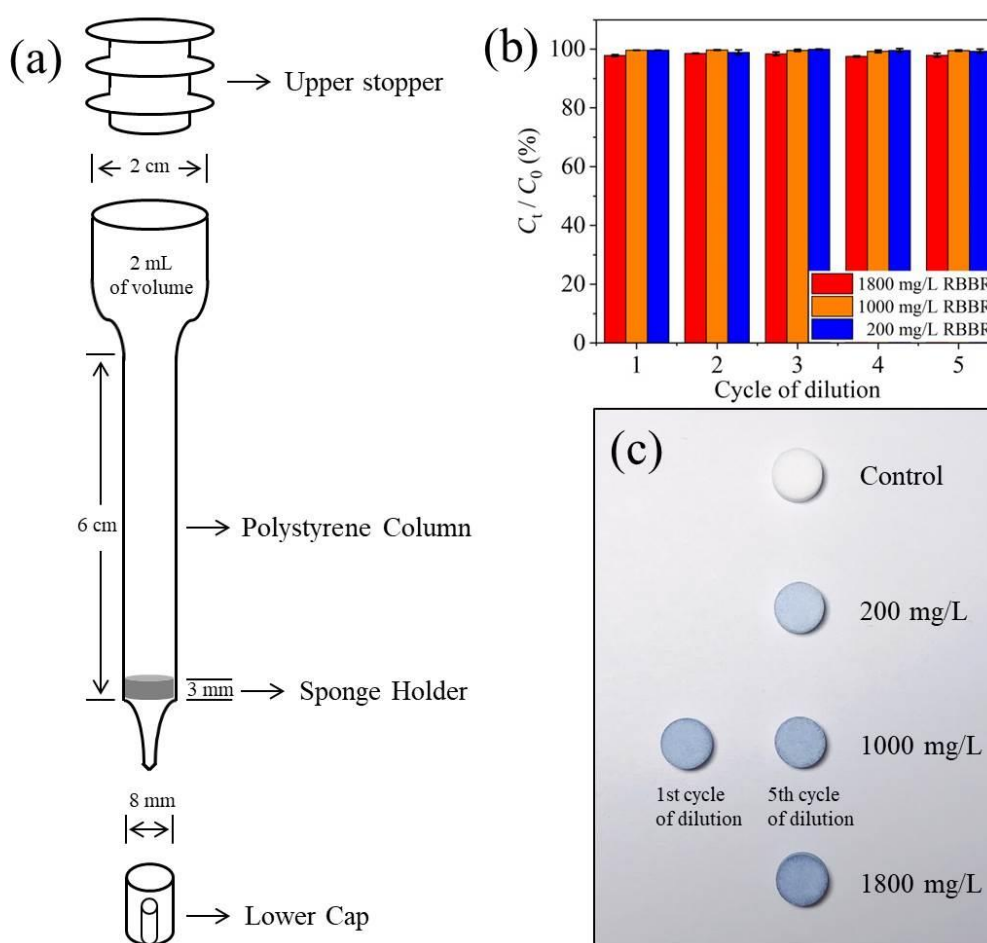


Figure 4.4. – (a) Schematic diagram of disposable 2 mL polystyrene column, (b) residual RBBR (C_t / C_0 , %) in the suspension and (c) the corresponding photos of sponge supports inside the polystyrene column after different cycles of dilution. $C[\text{RBBR}]_{\text{initial}} = 200, 1000, \text{ and } 1800 \text{ mg L}^{-1}$.

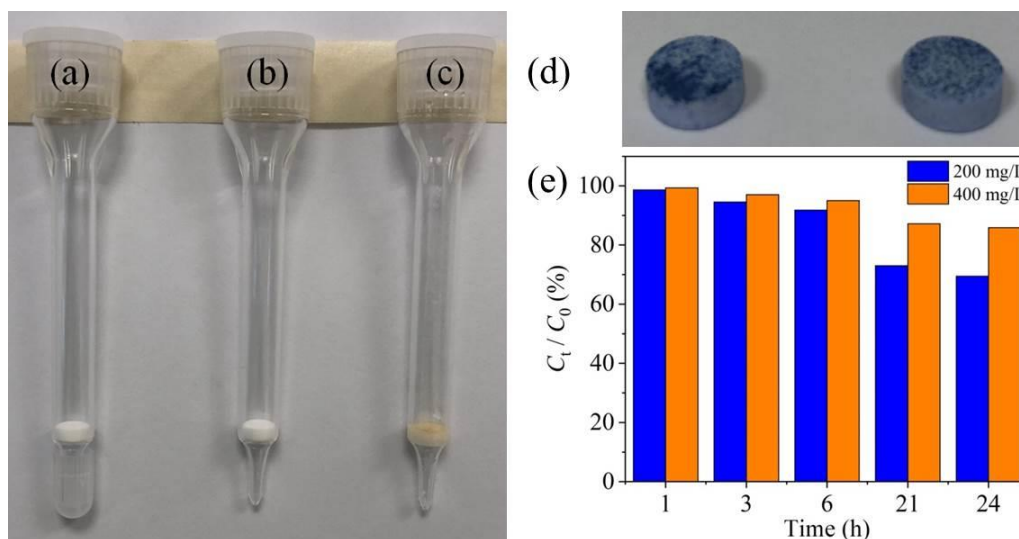


Figure 4.5. – Photos of the polystyrene column (a) with and (b) without the lower cap to avoid liquid leakage, (c) photo of the sponge support holding laccase T. cross-linked UPA(γ) biocatalysts in the polystyrene column, (d) photos of sponge support surface after RBBR dye biodegradation, and (e) residual RBBR (C_t / C_0 , %) after different time intervals of laccase T. cross-linked UPA(γ) biocatalyst treatment in polystyrene column bioreactor at pH = 5.0.

As shown in Figure 4.5d, after the corresponding experiments and excluding the suspension by using the upper stopper of the polystyrene column, the surface of sponge support became coarser, and some blue coloured laccase T. cross-linked UPA(γ) samples distributed non-uniformly on its surface as compared with the results discussed above (Figure 4.4c). By transferring the obtained laccase T. cross-linked UPA(γ) biocatalysts into polystyrene column for RBBR dye biodegradation, approximately 25% and 10% of RBBR with 200 and 400 mg L⁻¹ of initial dye concentrations can be biodegraded with 2 mg of biocatalysts after 24 h of incubation time, respectively (Figure 4.5e).

Therefore, the polystyrene column can be applied as a portable and easy-to-carry bioreactor for RBBR dye biodegradation, which can be used as the first prototype of an enzymatic bioreactor for dye treatment in industrial textile effluents.

4.5. Effect of immobilization protocol

In order to compare different protocols regarding laccase T. immobilization, the glutaraldehyde concentration which led to the highest laccase T. activity recovery was applied, and the comparison results were shown in Table 4.2:

Table 4.2. – Comparison of sequential immobilization, glutaraldehyde post-treatment, and no cross-linking protocols regarding laccase T. immobilization by UPA(γ) powders (0.50% (v/v) of glutaraldehyde concentration).

	Sequential immobilization	glutaraldehyde post-treatment	Physical adsorption
IY (%)	90.5 \pm 0.4	90.8 \pm 0.4	68.8 \pm 0.5
IE (%)	19.3 \pm 0.4	12.9 \pm 0.3	7.3 \pm 0.4
AR (%)	17.5 \pm 0.2	11.7 \pm 0.1	5.0 \pm 0.2
AR (mg g ⁻¹ carrier)	244.4 \pm 2.4	164.3 \pm 1.5	70.0 \pm 2.2

Compared with other protocols, sequential immobilization protocol showed the highest laccase T. activity recovery (about 4-fold to physical adsorption). However, the glutaraldehyde post-treatment protocol showed the highest laccase T. immobilization yield with the lower activity recovery (Table 4.2). By using glutaraldehyde as the cross-linking agent, the strong covalent linkages could be formed not only between the laccase T. and UPA surfaces but also between the laccase T. molecules, resulting in the formation of a stable network structure (Hou et al., 2014; Sheldon, 2017). However, this structure could also change laccase T. conformation and lead to the unfavorable orientation of laccase T. active sites. On the contrary, during the sequential immobilization process, the covalent linkages were mainly formed between laccase T. and UPA surfaces, which could provide higher mobility of the immobilized laccase T. molecules.

Therefore, higher laccase T. activity recovery can be observed with the sequential immobilization protocol, and the laccase cross-linked UPA(γ) biocatalysts synthesized by this protocol were further studied in terms of the biocatalyst stability.

4.6. pH and thermal stability

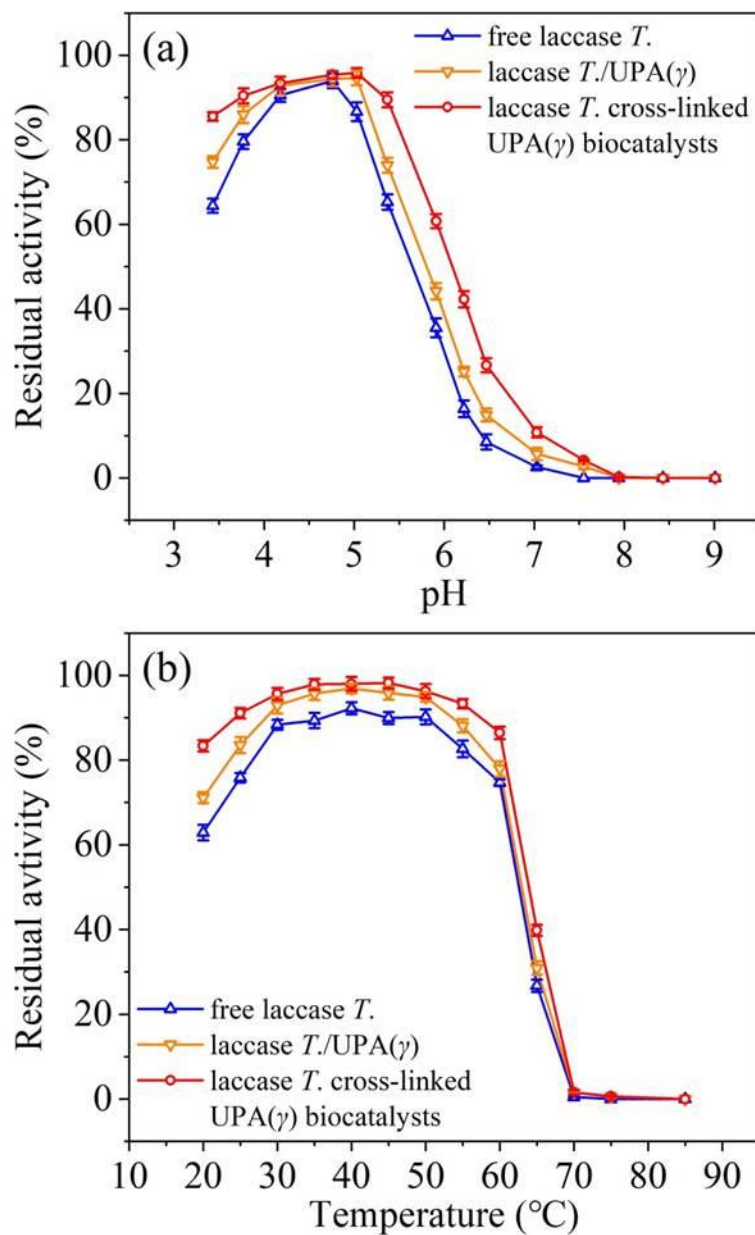


Figure 4.6. – (a) pH stability and (b) thermal stability profiles of free laccase *T.*, laccase *T.*/UPA(γ), and laccase *T.* cross-linked UPA(γ) biocatalysts by using ABTS as the substrate. For pH stability test, the biocatalysts were incubated in the pH range from 3.5 to 9.0 (20 °C, 45 min). For thermal stability test, the biocatalysts were incubated in the temperature range from 20 to 85 °C (pH = 5.0, SA buffer, 45 min). The residual enzyme activity was expressed as a relative percentage as compared with the corresponding initial enzyme activity of immobilized amount which was taken as the control (100%).

The effects of pH and temperature on the activity of free and immobilized laccase T. were shown in Figures 4.6a and 4.6b, respectively. The free laccase T. was affected more adversely by the change of pH than the laccase T. immobilized by physical adsorption and cross-linking protocols (Figure 4.6a). The residual activity of free laccase T. and laccase T./UPA(γ) powders decreased significantly at pH values higher than 5.5, while the residual activity of cross-linked immobilized laccase T. was still higher than 90%. Moreover, the immobilized laccase T. showed higher pH tolerance in both acid and alkaline conditions than the free laccase T. molecules.

Unlike the pH effect, both free and immobilized laccase T. showed broad thermal tolerance in the temperature range from 20 to 85 °C, and the residual activity of free laccase T. decreased more obviously after the 45 min of incubation at pH = 5.0 (Figure 4.6b). A sharp decrease of residual activity of both free and immobilized laccase T. appeared at temperatures higher than 60 °C, and negligible activity can be observed at temperatures higher than 70 °C. Similar results regarding the improved pH and thermal tolerances of immobilized enzymes can also be found in the previous studies (Hou et al., 2014; Zhang and Sun, 2018; Lassouane et al., 2019).

4.7. Storage and reusability

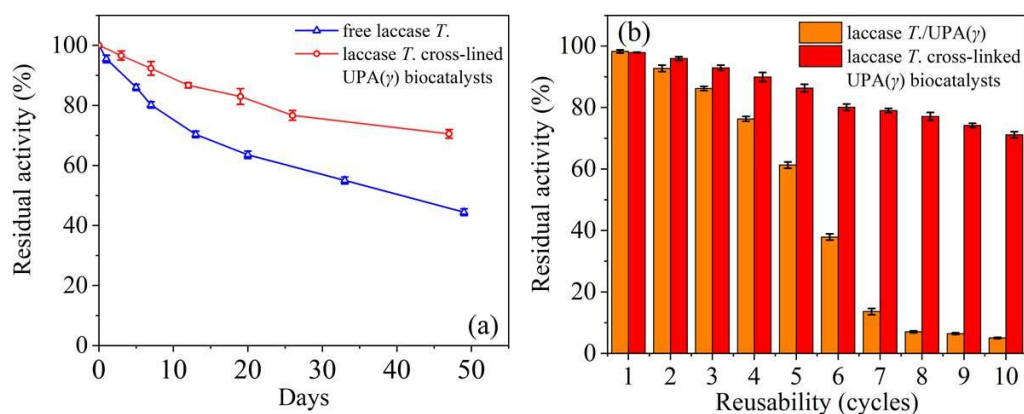


Figure 4.7. – (a) storage stability and (b) reusability profiles of free laccase T., laccase T./UPA(γ), and laccase T. cross-linked UPA(γ) biocatalysts by using ABTS as the substrate. For storage stability test, the biocatalysts were stored in refrigerator at 4 °C until 49 days. For reusability test, the residual enzyme activity of biocatalyst was measured through 10 consecutive batches.

Figures 4.7a and 4.7b showed the storage stability and reusability of free and immobilized laccase T., respectively. After 49 days of storage at 4 °C, the residual activity of free laccase T. and immobilized laccase T. was higher than 40% and 75%, respectively (Figure 4.7a). For the laccase T. immobilized by physical adsorption, drastic drop of activity (nearly 50%) can be observed after 5 cycles (Figure 4.7b). On the other hand, laccase T. immobilized by cross-linking protocol remained 75% of activity after 10 cycles.

4.8. RBBR kinetic study

Figure 4.8 showed the comparison of UPA(γ) powders and laccase T. cross-linked UPA(γ) biocatalysts on RBBR bioremediation. In terms of RBBR adsorption retained by UPA(γ) powders, the amount of RBBR in the suspension decreased rapidly in the first 6 h until the whole process achieved the equilibrium. In the initial step, the adsorption process may result from the vacant reaction sites available on UPA(γ) surfaces, which is consistent with the results discussed in the “Effect of contact time” section (Section 3.4). As long as the whole process achieved the equilibrium, around 25% of RBBR remained in the suspension, waiting for further RBBR treatment.

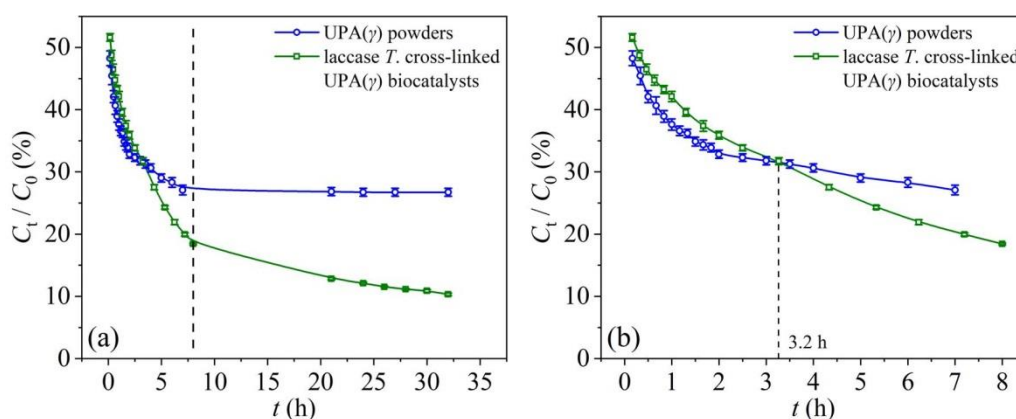


Figure 4.8. – Comparison of UPA(γ) powders and laccase T. cross-linked UPA(γ) biocatalysts on RBBR bioremediation. $C[\text{RBBR}]_{\text{initial}} = 200 \text{ mg L}^{-1}$, $C_{[\text{biocatalyst}]}_{\text{initial}} = 1 \text{ g L}^{-1}$, $\text{pH} = 5.0 \pm 0.1$, $I = 100 \text{ mM}$ sodium acetate, $T = 20 \text{ }^\circ\text{C}$, and stirring speed = 150 rpm.

Unlike the RBBR adsorption retained by UPA(γ) powders, the bioremediation process induced by laccase T. cross-linked UPA(γ) biocatalysts kept continuous RBBR biodegradation even though the initial treatment rate was slightly lower than the adsorption process. After 3.2 hours of the treatment, the amount of RBBR in the suspension of the biodegradation process was less than that of the adsorption process (Figure 4.8b). After 30 hours of the treatment, the amounts of RBBR in the suspensions of the adsorption and biodegradation processes were 25% and 10%, respectively (Figure 4.8a).

4.9. Modeling kinetics

4.9.1. Adsorption

For the adsorption process, we suppose that there are two types of adsorption sites, i.e., a_1 and a_2 , with two adsorption constants k_1 and k_2 , respectively. And the corresponding rate equations are listed as follows:

$$dN/dt = -k_1(a_1 - n_1) - k_2(a_2 - n_2) \quad (4.1)$$

$$dn_1/dt = k_1(a_1 - n_1)(N_0 - n_1 - n_2) \quad (4.2)$$

$$dn_2/dt = k_2(a_2 - n_2)(N_0 - n_1 - n_2) \quad (4.3)$$

where N_0 , n_1 and n_2 are the concentrations of free and adsorbed molecules on a_1 and a_2 sites, respectively. Moreover, we also assume that $k_1 \gg k_2$ and, accordingly, the molecules firstly occupy the a_1 sites, leaving the a_2 sites to be occupied later. Therefore, the Equations 4.2 and 4.3 can be reduced to Equations 4.4 and 4.5, which are listed as follows:

$$dn_1/dt = k_1(a_1 - n_1)(N_0 - n_1) \quad (4.4)$$

$$dn_2/dt = k_2(a_2 - n_2)(N_0 - a_1 - n_2) \quad (4.5)$$

Their solutions are listed as follows:

$$n_1/N_0 = [1 - \exp(-k_1 t(N_0 - a_1))] / [N_0/a_1 - \exp(-k_1 t(N_0 - a_1))] \quad (4.6)$$

$$n_2/(N_0 - a_1) = [1 - \exp(-k_2 t(N_0 - a_1 - a_2))] / [(N_0 - a_1)/a_2 - \exp(-k_2 t(N_0 - a_1 - a_2))] \quad (4.7)$$

The free molecule kinetics can be therefore expressed as follows:

$$\begin{aligned} N/N_0 = 1 - n1/N_0 - n2/N_0 = & [1 - \exp(-k1t(N_0 - a1))] / [N_0/a1 - \exp(-k1t(N_0 - a1))] - \\ & [1 - \exp(-k2t(N_0 - a1 - a2))] / [N_0/a2 - N_0/(N_0 - a1) \exp(-k2t(N_0 - a1 - a2))] \end{aligned} \quad (4.7)$$

By substituting $k1N_0 = a$, $a1/N_0 = b$, $k2N_0 = c$, and $a2/N_0 = d$, the Equation 4.7 can also be expressed as follows:

$$N/N_0 = (1 - e^{-a(1-b)t}) / (b^{-1} - e^{-a(1-b)t}) - (1 - e^{-c(1(b-d)t)}) / (d^{-1} - (1-b)^{-1} e^{-c(1-b-d)t}) \quad (4.8)$$

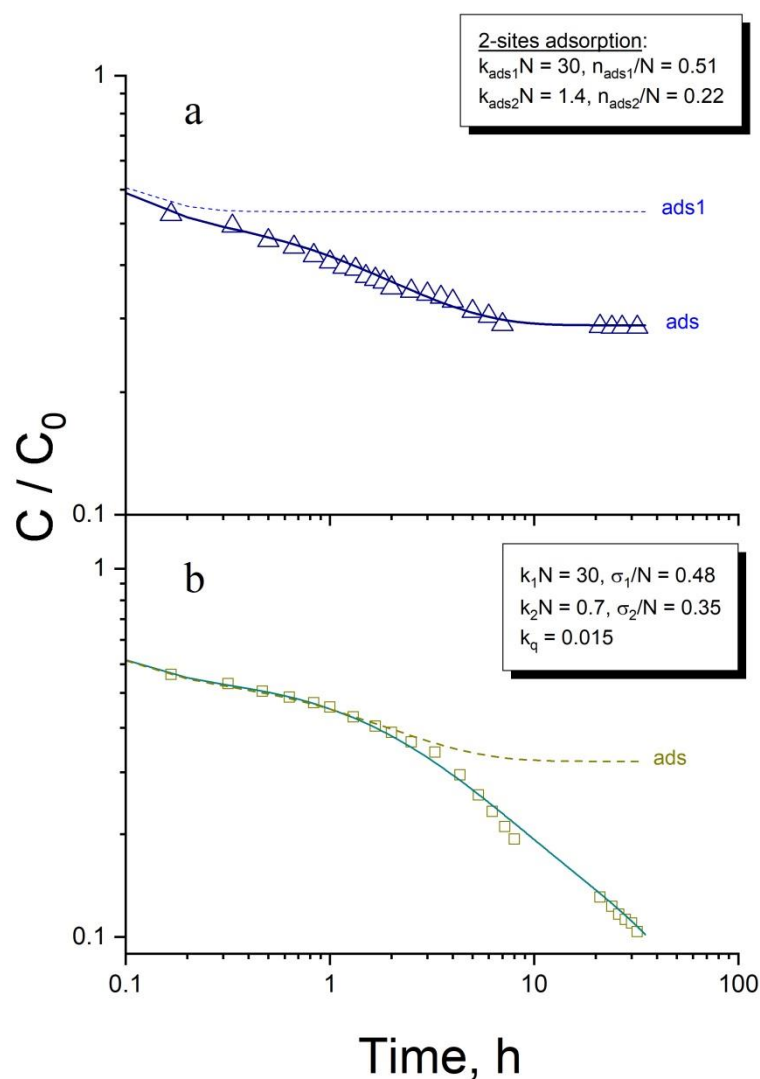


Figure 4.9. – RBBR kinetics in the presence of (a) UPA(γ) powders and (b) laccase T cross-linked UPA(γ) biocatalysts. Solid and dashed lines show the model kinetics.

The fitting of the experimental data by the Equation 4.8 are shown by solid line in Figure 4.9a. The results can be summarized as following:

- 1) The adsorption sites $a1$ with fast kinetics are rapidly filled ($t \leq 0.2h$) with an estimated rate $k1N_0 = 30$, by consuming about 50% of free molecules; this kinetics is shown by dashed line.
- 2) The following (almost total measured) kinetics describes adsorption of RBBR molecules on sites $a2$ with a slower rate $k2N_0 = 1.4$ tending to about 22% for $t > 10h$, when the adsorption process achieved the equilibrium.

4.9.2. Adsorption and catalysis

Since the observed differences in experimental kinetics of RBBR in the presence of UPA(γ) powders and laccase T. cross-linked UPA(γ) biocatalysts appears at relatively long time ($t \geq 2h$), the catalytic kinetics can be simply completed by a slow process of the first order, corresponding to the decomposition of the remaining RBBR molecules in the solution. At the same time, we are unable distinguishing between reactions of free and adsorbed RBBR molecules, since the equilibrium between both populations is expected to establish faster than the decomposition affects one or both populations. Taking into account the Equation 4.8, the, the RBBR kinetics in the presence of laccase T. cross-linked UPA(γ) biocatalysts was expressed as:

$$N/N_0 = [(1 - e^{-a(1-b)t}) / (b^{-1} - e^{-a(1-b)t}) - (1 - e^{-c(1(b-d)t}) / (d^{-1} - (1 - b)^{-1} e^{-c(1-b-d)t})] e^{-k_q N} \quad (4.9)$$

where k_q is the reaction constant.

The fitting of the experimental data with Equation 4.9 is shown by solid line in Figure 4.9b. The results can be summarized as following:

- 1) The adsorption sites $a1$ with fast kinetics survive after laccase T. deposition onto UPA(γ) surfaces and they are rapidly occupied ($t \leq 0.2h$) with rate $k1N_0 = 30$ and by consuming about 50% of free molecules, which is consistent with the results observed in pure UPA adsorption experiments (Figure 4.9a).

-
- 2) The deposition of laccase T. onto UPA(γ) surfaces significantly affects the sites a_2 : adsorption rate decreased $k_2 N_0 = 0.7$ and adsorption capacity increased to 35%.
 - 3) The RBBR decomposition is resolved at $t > 2\text{h}$ with the rate of $k_q = 0.015 \text{ h}^{-1}$.

Based on the above modeling, we can conclude that the adsorbing sites a_1 (fast kinetics) are those lying at the outer surface area of the UPA(γ) grains, and the sites a_2 (slow kinetics) are those belonging to the porous grains structure. Laccase T. significantly modifies the porous structure of UPA: adsorption capacity of the material doubled, and adsorption rate decreased 50%. The modeling also confirms the catalytic activity of the immobilized laccase T..

4.10. Experimental difficulties encountered and troubleshooting

In this part, we will summarize the experiences of failed experiments related to find a suitable solvent for laccase T. immobilization. Indeed, we can obtain the cross linked enzyme aggregates (CLEAs) with the addition of $(\text{NH}_4)_2\text{SO}_4$ or 2-propanol as the background solvent, but we cannot obtain the CLEAs calibration curve with a good linear relationship between optical density value and CLEAs quantity. Finally, we tried to synthesize laccase T. cross-linked UPA(γ) biocatalysts with glutaraldehyde as the cross-linker, and the synthesis methods were introduced in the “Material syntheses” section (Section 2.2).

4.10.1. 2-propanol and $(\text{NH}_4)_2\text{SO}_4$ induced CLEAs

According to Sheldon (2017), the addition of salts, or water miscible organic solvents or non-ionic polymers, to aqueous solutions of proteins can lead to their precipitation as physical aggregates that are held together by non-covalent bonding without perturbation of their tertiary structure. Moreover, cross-linking these physical aggregates, to form what is essentially a cross-linked polymer, would render them permanently insoluble while maintaining their pre-organised superstructure and, hence, their catalytic activity (Sheldon, 2017).

Matijošytė et al. (2010) studied different reagents and confirmed the 2-propanol, dioxane, dimethoxyethane (DME), $(\text{NH}_4)_2\text{SO}_4$, and polyethylene glycol (PEG 3400) as the effective precipitants for laccase T. precipitation at 20 °C (Figure 4.10). Moreover, Yu et al. (2006) also reported that Na_2SO_4 and $(\text{NH}_4)_2\text{SO}_4$ can be chosen as the aggregation agents in the process of CLEAs preparation. Based on this, we decided to use 2-propanol and $(\text{NH}_4)_2\text{SO}_4$ as the representatives as salt and water miscible organic solvent for the preparation of CLEAs, respectively.

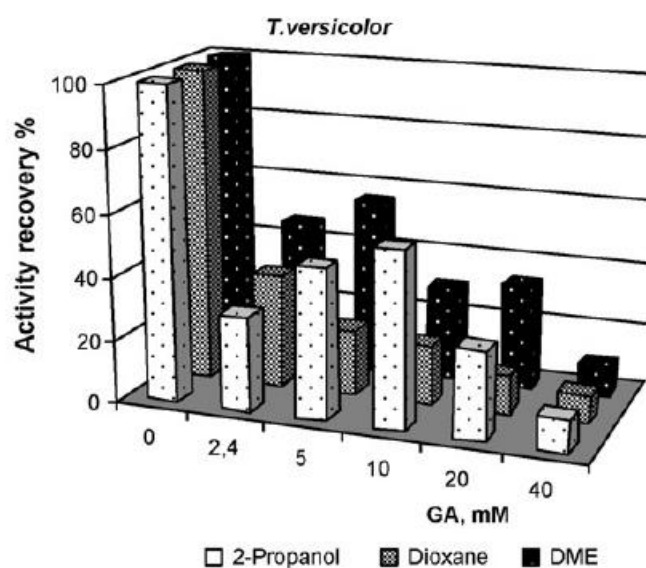


Figure 4.10. – Preparation of CLEAs with different glutaraldehyde concentrations (Matijošytė et al., 2010).

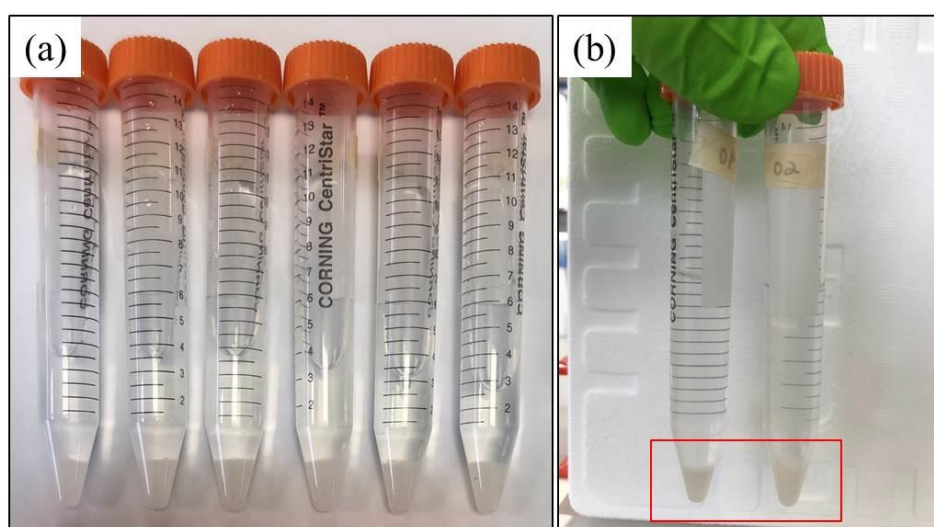


Figure 4.11. – Photos of CLEAs induced by 2-propanol with different glutaraldehyde concentrations (sequential immobilization protocol).

Figure 4.11 showed the photos of CLEAs induced by 2-propanol with different glutaraldehyde concentrations as the cross-linker. Obviously, one can see that the white CLEAs naturally precipitated at the bottom of the centrifuge tube (Figure 4.11b). However, as compared with Figure 2.11d, since the background solvent was 2-propanol for CLEAs preparation, we cannot obtain the CLEAs calibration curve with a good linear relationship between optical density value and CLEAs quantity. Or more specifically, all the optical density values recorded by the UV-Visible spectrophotometer were around zero, and some values were even all negative. Therefore, 2-propanol was not suitable for our experiment to quantitatively determine the amount of laccase T. immobilized by UPA(γ) powders.

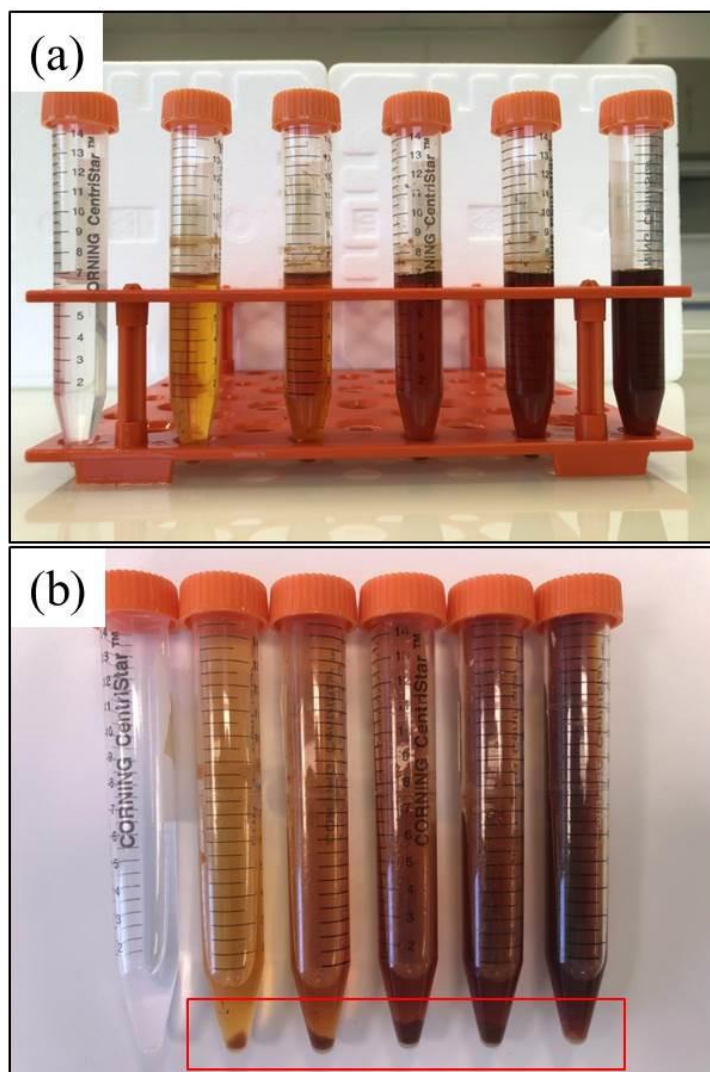


Figure 4.12. – Photos of CLEAs induced by $(\text{NH}_4)_2\text{SO}_4$ with different glutaraldehyde concentrations (sequential immobilization protocol).

The option of $(\text{NH}_4)_2\text{SO}_4$ as the background solvent can also be excluded quickly because the suspension containing CLEAs turned dark brown after the addition of glutaraldehyde (Figure 4.12). Moreover, one can see that from the left to the right, the brown color of the suspension became darker with the increasing concentration of glutaraldehyde (Figure 4.12b). As mentioned above, regarding the ABTS oxidation process, the reaction product $\text{ABTS}^{+\cdot}$ is a stable green coloured radical, which means that the dark brown color of the suspension will strongly interfere with the accuracy of the recorded optical density values (Pinkernell et al., 2000).

Therefore, in terms of laccase T. immobilization on UPA materials, we did not follow the CLEAs preparation procedure and tried to synthesize laccase T. cross-linked UPA(γ) biocatalysts by using milli-Q water and glutaraldehyde as the background solvent and cross-linker, respectively.

4.10.2. Fresh egg albumin as the protein feeder

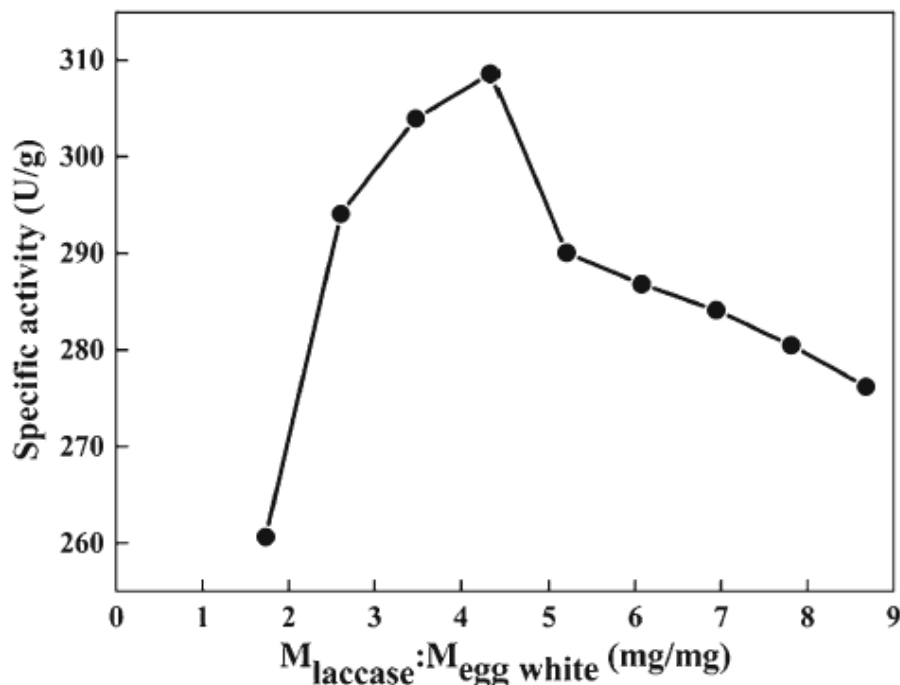


Figure 4.13. – The effect of egg white on the activity of CLEAs-egg (Jiang et al. 2014).

According to some literatures, egg albumin (or egg white), which is rich in lysine amine residues, was also recommended as the protein feeder in the preparation of CLEAs (Kumar et al., 2014; Jiang et al. 2014; Arca-Ramos et al., 2016). The presence of lysozyme in egg albumin can improve enzymes' stability and bacteriolytic activity (Jiang et al. 2014). In terms of the synthesis of laccase T. cross-linked UPA(γ) biocatalysts, we bought fresh eggs from LiDL and drop-wise added the egg albumin into the laccase T. solution. After the addition of glutaraldehyde and shaken for 1 h, we can observe fibrous protein denaturants in the suspension. Therefore, we did not use egg albumin for further synthesis of laccase T. cross-linked UPA(γ) biocatalysts.

4.11. Conclusions

In this chapter, laccase T. was cross-linked immobilized on ultraporous aluminas for an effective biodegradation of RBBR. The effect of glutaraldehyde concentration on laccase T. cross-linking degree, comparison of sequential and glutaraldehyde post-treatment protocols, the biocatalyst stability including pH stability, thermal stability, storage stability, and reusability, and the continuous biodegradation kinetics of RBBR by the synthesized laccase T. cross-linked UPA(γ) biocatalysts were comprehensively studied. Moreover, a portable and easy-to-carry bioreactor for RBBR treatment was designed as the first prototype of an enzymatic bioreactor for dye treatment in industrial textile effluents.

Except for the above-mentioned experiments, some remarks related to the failed experiments were also mentioned to avoid wasting time. Indeed, both 2-propanol and $(\text{NH}_4)_2\text{SO}_4$ were tested as the background solvents for the preparation of cross linked enzyme aggregates (CLEAs, physical aggregates), and the egg albumin were applied as the protein feeder for the cross-linking process. However, we cannot obtain the CLEAs calibration curve with a good linear relationship between optical density value and CLEAs quantity. The fibrous protein denaturants in the suspension were also observed after the addition of egg albumin. From the point of disambiguation, we

described our synthesized biocatalysts as laccase T. cross-linked UPA(γ) biocatalysts rather than CLEAs.

The glutaraldehyde concentration considerably affected the laccase T. cross-linking degree, and the sequential immobilization protocol showed higher laccase T. activity recovery than the glutaraldehyde post-treatment process. Moreover, the synthesized biocatalysts also showed better immobilization performances (about 4-fold to physical adsorption). Based on the sequential immobilization protocol, a portable and easy-to-carry bioreactor for RBBR dye biodegradation was designed as the first prototype of an enzymatic bioreactor. Tolerance to broader pH and temperature ranges, better storage stability, good reusability of the synthesized biocatalysts, and continuous biodegradation kinetics of RBBR highlight the potentials of enzyme-based inorganic materials in industrial wastewater treatment, which can broaden our understanding of their practical applications in the environmental field.

4.12. References

- Arca-Ramos, A.; Kumar, V. V.; Eibes, G.; Moreira, M.T.; Cabana, H., Recyclable cross-linked laccase aggregates coupled to magnetic silica microbeads for elimination of pharmaceuticals from municipal wastewater, *Environmental Science and Pollution Research*, 23 (2016) 8929–8939.
- Aronson, M.T.; Gorte, R.J.; Farneth, W.E., An infrared spectroscopy study of simple alcohols adsorbed on H-ZSM-5, *Journal of Catalysis*, 105 (1987) 455–468.
- Al-Rubayee, W.T.; Abdul-Rasheed, O.F.; Ali, N.M., Preparation of a modified nanoalumina sorbent for the removal of alizarin yellow R and methylene blue dyes from aqueous solutions, *Journal of Chemistry*, 2016 (2016) 1–12.
- Bashir, S.; Teo, Y. Y.; Ramesh, S.; Ramesh, K.; Rizwan, M.; Rizwan, M., Synthesis and characterization of pH-sensitive N-succinyl chitosan hydrogel and its properties for biomedical applications, *Journal of the Chilean Chemical Society*, 64 (2019) 4571–4574.
- Hou, J.-W.; Dong, G.-X.; Ye, Y.; Chen, V., Laccase immobilization on titania nanoparticles and titania-functionalized membranes, *Journal of Membrane Science*, 452 (2014) 229–240.
- Hsiao, P.F.; Peng, S.; Tang, T.-C.; Lin, S.-Y.; Tsai, H.-C., Enhancing the in vivo transdermal delivery of gold nanoparticles using poly(ethylene glycol) and its oleylamine conjugate, *International Journal of Nanomedicine*, 11 (2016) 1867–1878.
- Ivashchenko, L.; Vasin, A.; Ivashchenko, V.; Ushakov, M.; Rusavsky, A., Blue light emission from PECVD deposited nanostructured SiC, *Materials Research Society Symposium Proceedings*, 910 (2011) 1–7.
- Jiang, Y.; Wang, Q.; He, Y.; Zhou, L.; Gao, J., Co-aggregation of laccase and nature egg white: a simple method to prepare stable and recyclable biocatalyst, *Applied Biochemistry and Biotechnology*, 172 (2014) 2496–2506.
- Kaya-Özkiper, K.; Uzun, A.; Soyer-Uzun, S., A novel alkali activated magnesium silicate as an effective and mechanically strong adsorbent for methylene blue removal, *Journal of Hazardous Materials*, In press, DOI:

-
- 10.1016/j.jhazmat.2021.127256.
- Kim, M.; Hwang, S.; Yu, J.-S., Novel ordered nanoporous graphitic C₃N₄ as a support for Pt–Ru anode catalyst in direct methanol fuel cell, *Journal of Materials Chemistry*, 17 (2007) 1656–1659.
- Kosseva, M.R., Use of immobilized biocatalyst for valorization of whey lactose. In *Food Industry Wastes: Assessment and Recuperation of Commodities*, Kosseva, M.R.; Webb, C. (Ed.), Elsevier, ISBN: 978-0-12-391921-2, (2013) 137–156.
- Kumar, V.V.; Sivanesan, S.; Cabana, H., Magnetic cross-linked laccase aggregates – Bioremediation tool for decolorization of distinct classes of recalcitrant dyes, *Science of the Total Environment*, 487 (2014) 830–839.
- Lassouane, F.; A ĩ-Amar, H.; Amrani, S.; Rodriguez-Couto, S., A promising laccase immobilization approach for Bisphenol A removal from aqueous solutions, *Bioresource Technology*, 271 (2019) 360–367.
- Li, S.-Y.; Ma, W.-H.; Zhou, Y.; Chen, X.-H.; Ma, M.-Y.; Xu, Y.-H.; Ding, Z.; Wu, X.-H., 3-aminopropyltriethoxysilanes modified porous silicon as a voltammetric sensor for determination of silver ion, *International Journal of Electrochemical Science*, 8 (2013) 1802–1812.
- Liu, C.-S.; Shih, K.-M.; Gao, Y.-X.; Li, F.-B.; Wei, L., Dechlorinating transformation of propachlor through nucleophilic substitution by dithionite on the surface of alumina, *Journal of Soils and Sediments*, 12 (2012) 724–733.
- Mahmoudi, Be.; Gabouze, N.; Guerbous, L.; Haddadi, M.; Beldjilali, K., Long-time stabilization of porous silicon photoluminescence by surface modification, *Journal of Luminescence*, 2 (2007) 534–540.
- Matijošytė, I.; Arends, I.W.C.E.; de Vries, S.; Sheldon, R.A., Preparation and use of cross-linked enzyme aggregates (CLEAs) of laccases, *Journal of Molecular Catalysis B: Enzymatic*, 62 (2010) 142–148.
- Nishida, J.; Shigeto, S.; Yabumoto, S.; Hamaguchi, H.O., Anharmonic coupling of the CH-stretch and CH-bend vibrations of chloroform as studied by near-infrared electroabsorption spectroscopy, *The Journal of Chemical Physics*, 137 (2012) 1–

9.

- Pinkernell, U.; Nowack, B.; Gallard, H.; von Gunten, U., Methods for the photometric determination of reactive bromine and chlorine species with ABTS, *Water Research*, 34 (2000) 4343–4350.
- Samui, A.; Sahu, S.K., One-pot synthesis of microporous nanoscale metal organic frameworks conjugated with laccase as a promising biocatalyst, *New Journal of Chemistry*, 42 (2018) 4192–4200.
- Sheldon, R.A., Cross-linked enzyme aggregates (CLEAs): From concept to industrial biocatalyst. In *Biocatalysis: An Industrial Perspective*, Gonzalo, G.; Mar á, P.D. (Ed.), Royal Society of Chemistry, ISBN: 978-1-78262-619-0 (2017) 363–396.
- Sheldon, R.A.; Pelt, S.V., Enzyme immobilisation in biocatalysis: Why, what and how, *Chemical Society Reviews*, 42 (2013) 6223–6235.
- Sheldon, R.A.; Woodley, J.M., Role of biocatalysis in sustainable chemistry, *Chemical Reviews*, 118 (2018) 801–838.
- Torres-Salas, P.; del Monte-Martinez, A.; Cuti ño-Avila, B.; Rodriguez-Colinas, B.; Alcalde, M.; Ballesteros, A.O.; Plou, F.J., Immobilized biocatalysts: Novel approaches and tools for binding enzymes to supports, *Advanced Materials*, 23 (2011) 5275–5282.
- Yu, H.W.; Chen, H.; Wang, X.; Yang, Y.Y.; Ching, C.B., Cross-linked enzyme aggregates (CLEAs) with controlled particles: Application to *Candida rugosa* lipase, *Journal of Molecular Catalysis B: Enzymatic*, 43 (2006) 124–127.
- Zhang, L.-Q.; Sun, Y., Poly(carboxybetaine methacrylate)-grafted silica nanoparticle: A novel carrier for enzyme immobilization, *Biochemical Engineering Journal*, 132 (2018) 122–129.
- Zhang, Y.-Z.; Zong, S.-C.; Cheng, C.; Shi, J.-W.; Guo, P.-H.; Guan, X.-J.; Luo, B.; Shen, S.-H.; Guo, L.-J., Rapid high-temperature treatment on graphitic carbon nitride for excellent photocatalytic H₂-evolution performance, *Applied Catalysis B: Environmental*, 233 (2018) 80–87.

Chapter 5: Conclusions and perspectives

5.1. Conclusions

The main objectives of this thesis focused on the laccase T. immobilization on UPA materials by using glutaraldehyde as the cross-linker, and applied the synthesized laccase T. cross-linked UPA biocatalysts for RBBR biodegradation. Following the sequential immobilization protocol, the polystyrene column was applied as a portable and easy-to-carry bioreactor for RBBR treatment, which can be used as the first prototype of an enzymatic bioreactor for dye treatment in industrial textile effluents. To summarize the obtained results, two main experimental studies have been conducted during my PhD study, which was listed as follows:

(1) synthesized ultraporous aluminas for RBBR adsorption,

In this part, UPA materials were synthesized as new effective adsorbents for RBBR removal from aqueous solutions. The experimental factors that affect the material adsorption performances including initial pH, contact time, and temperature were comprehensively studied by batch experiments. Different kinetic and isotherm models were applied to fit the adsorption equilibrium data. The thermodynamic study and the adsorption mechanisms including film diffusion, intraparticle diffusion, electrostatic attraction, surface complexation, and hydrogen bonding were further discussed.

The adsorption process was pH- and temperature-dependent, and the maximum RBBR adsorption capacity retained by UPA(θ) powders was 122.55 mg g^{-1} at 295 K (22 °C). Both film diffusion and intraparticle diffusion contributed to the adsorption kinetics, and chemical reactions also played a significant role during the entire adsorption process. The pseudo-second-order model and the Langmuir isotherm model were found to best describe the experimental data (i.e., pseudo-second-order > Lagergren pseudo-first-order model; and Langmuir > Temkin \approx Freundlich > D.-R. isotherm model).

Moreover, the thermodynamic parameters (ΔG^0 , ΔH^0 , and ΔS^0) indicated that the adsorption process was spontaneous and exothermic in nature. Compared with the other adsorbents reported in related studies in the literature, UPA(θ) and UPA(γ) powders possess several advantages for large-scale applications including nontoxicity, facile synthesis, and higher RBBR adsorption capacity. The findings of this study highlight the UPA potentials in wastewater treatment, which can broaden our understanding and its practical applications in the environmental field.

(2) laccase T. cross-linked UPA biocatalysts for RBBR biodegradation,

In this part, laccase T. was cross-linked immobilized on ultraporous aluminas for an effective biodegradation of RBBR. The effect of glutaraldehyde concentration on laccase T. cross-linking degree, comparison of sequential and glutaraldehyde post-treatment protocols, the biocatalyst stability including pH stability, thermal stability, storage stability, and reusability, and the continuous biodegradation kinetics of RBBR by the synthesized laccase T. cross-linked UPA(γ) biocatalysts were comprehensively studied. Moreover, a portable and easy-to-carry bioreactor for RBBR treatment was designed as the first prototype of an enzymatic bioreactor for dye treatment in industrial textile effluents.

Except for the above-mentioned experiments, some remarks related to the failed experiments were also mentioned to avoid wasting time. Indeed, both 2-propanol and $(\text{NH}_4)_2\text{SO}_4$ were tested as the background solvents for the preparation of cross linked enzyme aggregates (CLEAs, physical aggregates), and the egg albumin were applied as the protein feeder for the cross-linking process. However, we cannot obtain the CLEAs calibration curve with a good linear relationship between optical density value and CLEAs quantity. The fibrous protein denaturants in the suspension were also observed after the addition of egg albumin. From the point of disambiguation, we described our synthesized biocatalysts as laccase T. cross-linked UPA(γ) biocatalysts rather than CLEAs.

The glutaraldehyde concentration considerably affected the laccase T. cross-linking degree, and the sequential immobilization protocol showed higher laccase T. activity recovery than the glutaraldehyde post-treatment process. Moreover, the synthesized biocatalysts also showed better immobilization performances (about 4-fold to physical adsorption). Based on the sequential immobilization protocol, a portable and easy-to-carry bioreactor for RBBR dye biodegradation was designed as the first prototype of an enzymatic bioreactor. Tolerance to broader pH and temperature ranges, better storage stability, good reusability of the synthesized biocatalysts, and continuous biodegradation kinetics of RBBR highlight the potentials of enzyme-based inorganic materials in industrial wastewater treatment, which can broaden our understanding of their practical applications in the environmental field.

5.2. Perspectives

In the context of green and sustainable chemistry, the laccase T. immobilization process can provide a promising alternative for the conventional treatment method of recalcitrant micropollutants. However, there are still some improvements that could be made in the process of industrialization. In future work, several promising perspectives are listed as follows (Figure 5.1):

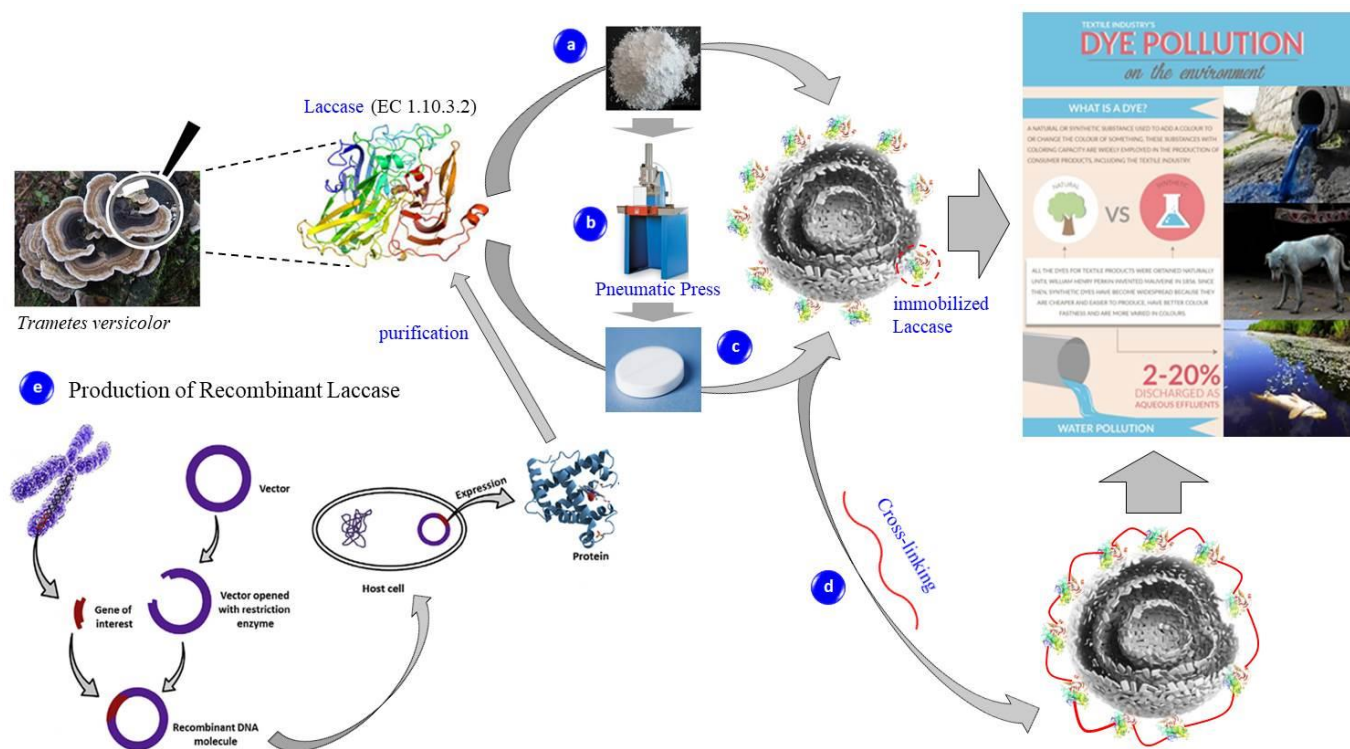


Figure 5.1. – General perspectives of future work regarding RBBR treatment: (a) powders for adsorption, (b) membrane synthesis, (c) membrane for adsorption, (d) laccase T. cross-linking for biodegradation, and (e) laccase T. production by recombination method.

-
- As shown in Figure 5.1b, the UPA membranes can be synthesized by using the pneumatic press at LSPM (EMG industrial press machines).

Actually, we conducted some experiments regarding the synthesis of UPA membranes. For the UPA materials with different polycrystalline phases (γ , θ , and α), surface stickiness and defects occurred all the time. This problem remained unsolved even we applied thermal treatment to remove the adsorbed water inside the UPA materials (200 °C maximum). Unlike UPA materials, the alumina powders provided by Sasol, PURAL SB-1 UHPA for example, did not show problem of either surface stickiness or surface defects, and the alumina membrane can be easily obtained by using the pneumatic press. Therefore, some attempts can be made for UPA membrane synthesis.

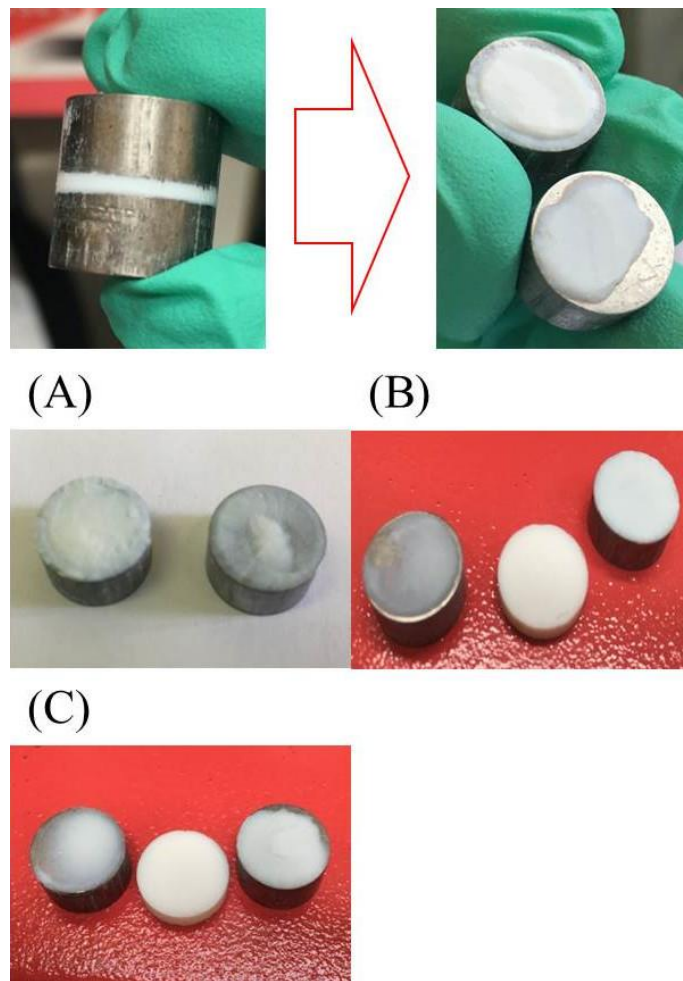


Figure 5.2. – Photos of the synthesized UPA membranes (the surface stickiness and defects occurred with all the membrane samples obviously).

Following the above-mentioned work, a complementary and not negligible point concerns the permittivity of these membranes under applied liquid pressure. Consequently, the measurements of this parameter in connection with the mechanical properties of the membranes have to be conducted.

- As shown in Figure 5.1c, the successfully synthesized UPA membrane can be applied as the filter membrane for the practical treatment of industrial textile effluents.
- As shown in Figure 5.1d, the sequential immobilization protocol regarding laccase T. immobilization can be applied on UPA membranes for the practical treatment of industrial textile effluents.
- As shown in Figure 5.1e, the recombination method can be applied for the production of laccase T., and the above-mentioned experiments can be repeated by replacing the commercial laccase T. with self-synthesized laccase T..

Appendix A: Nomenclature, greek symbols and subscripts.

Nomenclature	
%	the adsorption percentage (dimensionless)
B	the constant of the Temkin isotherm model (J mol^{-1})
C_0	the initial adsorbate concentration in suspension (mg L^{-1})
C_e	the adsorbate concentration in supernatant at equilibrium (mg L^{-1})
C_{IPD}	the constant proportional to the thickness of boundary layer (dimensionless)
E	the free energy change (kJ mol^{-1})
k'	the adsorption rate constant of the Lagergren pseudo-first-order model (h^{-1})
k''	the adsorption rate constant of the pseudo-second-order model ($\text{g mg}^{-1} \text{h}^{-1}$)
k_{FD}	the rate constant of the film diffusion model (min^{-1})
k_{IPD}	the rate constant of the intraparticle diffusion model ($\text{mg g}^{-1} \text{min}^{-0.5}$)
K^0	the standard distribution coefficient (dimensionless)
K_d	the distribution coefficient (dimensionless)
K_F	the constant of the Freundlich isotherm model indicating the adsorption capacity ($\text{mg}^{(1-1/n)} \text{L}^{1/n} \text{g}^{-1}$)
K_L	the constant of the Langmuir isotherm model related to the adsorption energy (L mg^{-1})
K_T	the equilibrium binding constant of the Temkin isotherm model (L g^{-1})
m	the mass of adsorbent (g)
1/n	the constant of the Freundlich isotherm model indicating the adsorption intensity (dimensionless)
q_e	the adsorption capacity at equilibrium (mg g^{-1} , or mg m^{-2})
$q_{e, \max}$	the maximum adsorption capacity obtained from the isotherm models (mg g^{-1})
Q_m and Q_{mc}	the adsorption capacity at equilibrium obtained from the kinetic models (mg g^{-1})
Q_{me}	the experimental adsorption capacity at equilibrium (mg g^{-1})

Q_t	the adsorption capacity (mg g^{-1}) at time t (h, or min)
R	the universal gas constant ($8.3145 \text{ J mol}^{-1} \text{ K}^{-1}$)
R^2	the coefficient of determination (COD, dimensionless)
R_L	the separation factor (dimensionless)
t	the contact time (h, or min)
T	the absolute temperature in Kelvin (K)
V	the volume of suspension (L)
ΔG^0	the standard Gibbs free energy (kJ mol^{-1})
ΔH^0	the standard enthalpy change (kJ mol^{-1})
ΔS^0	the standard entropy change ($\text{J mol}^{-1} \text{ K}^{-1}$)

Greek symbols

α	UPA crystalline phase (1350 °C, and 4 h of isochronous annealing treatment in air)
θ	UPA crystalline phase (1150 °C, and 4 h of isochronous annealing treatment in air)
γ	UPA crystalline phase (950 °C, and 4 h of isochronous annealing treatment in air)
β	the constant of the D.-R. isotherm model ($\text{mol}^2 \text{ kJ}^{-2}$)
ε	the constant of the D.-R. isotherm model related to the Polanyi potential (dimensionless)

Subscripts

0	initial state (i.e., C_0)
e	at equilibrium (i.e., $C_e, q_e, q_{e, \text{max}}$)

Appendix B: List of abbreviations.

Abbreviation	Full name or definition
ABTS	2,2'-azino-bis(3-ethylbenzothiazoline-6-sulfonic acid) diammonium salt
AC	activated carbon
APTES	(3-aminopropyl)triethoxysilane
AR	activity recovery (% or mg g ⁻¹ carrier)
BET	Brunauer-Emmett-Teller
CAGR	compound annual growth rate
CLEAs	cross-linked enzyme aggregates
DAH	1,6-diamino hexane
DMAB	dimethylaminoborane
DMP	2,6-dimethoxyphenol
DOPA	dihydroxyphenylalanine
D.-R.	Dubin-Radushkevich
EDX	energy-dispersive X-ray
FD	film diffusion
FFB	free fungal biomass
FTIR	Fourier-transform infrared spectroscopy
GA	glutaraldehyde
GO	graphene oxide
GRAS	generally regarded as safe
ICDD	International Centre for Diffraction Data
IE	enzyme immobilization efficiency (%)
IPD	intraparticle diffusion
IUPAC	International Union of Pure and Applied Chemistry
IY	enzyme immobilization yield (%)
JCPDS	Joint Committee on Powder Diffraction Standards, changed into ICDD since 1978

laccase T.	laccase from <i>Trametes versicolor</i>
LSIFB	loofa sponge-immobilized fungal biomass
MNP	magnetite nanoparticle
MOF	metal-organic-framework
MWCNT	multi-walled carbon nanotube
O.D.	optical density
PEI	polyethyleneimine
PES	polyethersulfone
pHzpc	pH of zero point of charge
PMMA	polymethyl methacrylate
POP	persistent organic pollutant
Ppy	polypyrrole
PS	polystyrene
RBBR (or RB19)	Remazol Brilliant Blue R, anthraquinone dye
RH	relative humidity
S.D.	standard deviation
SEM	scanning electron microscopy
TEM	transmission electron microscopy
TG	thermogravimetric
UPA	ultraporous nanofibrous alumina
UV-Vis	ultraviolet-visible
WW	wood waste
XRD	X-ray powder diffraction

Appendix C: Symbols for units.

°C	degree Celsius	L	liter
g	Gram	M	mole per liter
h	Hour	m	meter
J	Joule	min	minute
K	kelvin	s	second

Appendix D: Article published in Materials.

Xu, H.; Boeuf, G.; Jia, Z.-X.; Zhu, K.-R.; Nikravech, M.; Kanaev, A.; Azouani, R.; Traore, M.; Elm'selmi, A., Solvent-free synthesized monolithic ultraporous aluminas for highly efficient removal of Remazol Brilliant Blue R: Equilibrium, kinetic, and thermodynamic studies, *Materials*, 14 (2021) 1–19.



Article

Solvent-Free Synthesized Monolithic Ultraporous Aluminas for Highly Efficient Removal of Remazol Brilliant Blue R: Equilibrium, Kinetic, and Thermodynamic Studies

Huan Xu ^{1,2}, Guilhem Boeuf ², Zixian Jia ^{1,*}, Kairuo Zhu ³, Mehrdad Nikravech ¹, Andrei Kanaev ¹, Rabah Azouani ², Mamadou Traore ^{1,*} and Abdellatif Elm'selmi ^{2,*}

¹ Laboratoire des Sciences des Procédés et des Matériaux, CNRS, Université Sorbonne Paris Nord, F-93430 Villetaneuse, France; huan.xu@lspm.cnrs.fr (H.X.); mehrdad.nikravech@lspm.cnrs.fr (M.N.); andrei.kanaev@lspm.cnrs.fr (A.K.)

² EBInnov, École de Biologie Industrielle, F-95000 Cergy, France; g.boeuf@hubebi.com (G.B.); razouani@hubebi.com (R.A.)

³ CAS Key Laboratory of Photovoltaic and Energy Conservation Materials, Institute of Plasma Physics, Chinese Academy of Sciences, P.O. Box 1126, Hefei 230031, China; krzhu@mail.ustc.edu.cn

* Correspondence: zixian.jia@gmail.com (Z.J.); mamadou.traore@lspm.cnrs.fr (M.T.); a.elmselmi@hubebi.com (A.E.); Tel.: +33-01-4940-4052 (M.T.); +33-01-8576-6716 (A.E.)



Citation: Xu, H.; Boeuf, G.; Jia, Z.; Zhu, K.; Nikravech, M.; Kanaev, A.; Azouani, R.; Traore, M.; Elm'selmi, A. Solvent-Free Synthesized Monolithic Ultraporous Aluminas for Highly Efficient Removal of Remazol Brilliant Blue R: Equilibrium, Kinetic, and Thermodynamic Studies. *Materials* **2021**, *14*, 3054. <https://doi.org/10.3390/ma14113054>

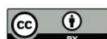
Academic Editor: Aljoša Košak

Received: 20 April 2021

Accepted: 31 May 2021

Published: 3 June 2021

Publisher's Note: MDPI stays neutral with regard to jurisdictional claims in published maps and institutional affiliations.



Copyright: © 2021 by the authors. Licensee MDPI, Basel, Switzerland. This article is an open access article distributed under the terms and conditions of the Creative Commons Attribution (CC BY) license (<https://creativecommons.org/licenses/by/4.0/>).

Abstract: In this study, ultraporous aluminas (UPA) were synthesized as new effective adsorbents for Remazol Brilliant Blue R (RBBR) removal from aqueous solutions. The UPA monoliths were grown via facile oxidation process, followed by isochronous annealing treatment in air at different temperatures, through which γ , θ , and α phase polycrystalline fibrous grains of UPA can be accordingly obtained. The experimental factors that affect the material adsorption performances including initial pH, contact time, and temperature were comprehensively studied by batch experiments. The RBBR adsorption isotherms of UPA(γ) and UPA(θ) powders were found almost identical, while UPA(α) powders showed low effectiveness. To obtain the desirable mechanical stability of the UPA monolith with considerable RBBR adsorption capacity, UPA(θ) powders were further studied. The UPA(θ) powders exhibited maximum RBBR adsorption at pH 2 due to the positively charged surface under acidic conditions. Compared with the Lagergren pseudo-first-order model, the pseudo-second-order model was found to explain the adsorption kinetics better. Despite the film diffusion dominating the adsorption process, the contributions of the intraparticle diffusion and chemical reactions were also found significant. The adsorption equilibrium data at different temperatures were fitted by the Langmuir, Freundlich, Temkin, and Dubinin–Radushkevich (D–R) isotherm models. The Langmuir model was found the most effective in the description of equilibrium data, and the maximum RBBR adsorption capacity retained by UPA(θ) powders was 122.55 mg·g⁻¹ at 295 K. Thermodynamic parameters (ΔG^0 , ΔH^0 , and ΔS^0) indicated the adsorption process was spontaneous and exothermic in nature.

Keywords: ultraporous aluminas; RBBR; kinetic models; diffusion models; isotherm models; thermodynamics

1. Introduction

Throughout history, textile dyeing can be dated back to the Neolithic period (also known as the New Stone Age), followed by the serendipitous discovery of the first synthetic dye, mauveine (aniline purple) by William Perkin in 1856 [1]. Since then, the practice of employing synthetic dyes in the printing and dyeing process of fabrics has been extensively developed worldwide. At present, $>7 \times 10^5$ tons of dyes are produced annually, and nearly 10–15% of the total dyes are discharged in the surrounding environment with or without partial treatments, making the dyestuff-related industries responsible for up to 20% of

industrial water pollution [2,3]. In addition to the textile industry, other kinds of dye-relevant industries (e.g., paper and pulp, plastic, leather, cosmetics, pharmaceuticals, and photography) are also recognized as the most polluting industries. Accompanying the great conveniences brought by dye-based industrial applications, some serious problems are also caused owing to their carcinogenicity, genotoxicity, and/or mutagenicity in nature, which poses numerous threats to the ecological system and living organisms [3–7]. Therefore, proper treatments regarding purifications and remediations of industrial textile effluents are urgent and necessary.

The majority of dyes industrially used nowadays are organic compounds with complex and reinforced structures, which normally consist of two major components, i.e., chromophore and auxochrome groups [2,6,7]. The persistent structure and poor biodegradability of these refractory organics make the choice of an appropriate dye treatment method challenging [2]. Generally, the most known and extensively applied methods for the treatment of dyehouse effluents can be classified into physical (adsorption, membrane filtration, and reverse osmosis), chemical/electrochemical (adsorption, coagulation, flocculation, and advanced oxidation processes), biological (intracellular, and isolated enzymes) methods, and/or emerging combination of several above-mentioned techniques with the purpose of synergistic effects [4–7]. Among the available conventional methods for dye treatment, chemisorption involving chemical reactions between solutes and the functional groups on adsorbent surfaces in aqueous solutions has been confirmed and extensively studied as the most effective process for the treatment of industrial textile effluents [4,6,7].

Mesoporous materials of 2–50 nm pore diameter, owing to their numerous advantages including ordered, homogenous pore distributions, regular and tunable pore sizes, high specific surface areas, framework/wall substitutions with various metal oxides, favorable biocompatibility, and low toxicity, have been widely applied in the research field of wastewater treatment, catalyst support, drug delivery, and energy-related aspects, etc. [8–10]. Besides the size of pores inside the building framework, the compositions of material can vary, including pure organics (e.g., porous polymers), organic/inorganic (e.g., metal–organic frameworks, MOFs), and pure inorganics (e.g., silica, alumina, and titania). The great advantage of inorganic materials, in comparison with other materials, is that they can be synthesized relatively cheaply and usually by simple synthesis procedures [4,6,7,11–13]. For example, Khoshhesab et al. synthesized NiO nanoparticles by chemical precipitation method and studied its adsorption capacity for Remazol Brilliant Blue R (RBBR, also called RB19) with commercial NiO powders as a comparison [13]. Moussavi et al. synthesized porous MgO nanoparticle (nano-MgO) by sol–gel method and applied it for both azo and anthraquinone (AQ) dye removal from industrial wastewaters [7]. In particular, Madrakian et al. successfully synthesized magnetite-modified multiwalled carbon nanotubes (MMM-CNTs) for the removal of four anionic dyes including RB19, Methylthymol blue, Congo red, and Mordant Blue 29 [4]. Recently, Beauvy et al. developed a new method for the synthesis of ultraporous alumina (UPA) monolith, which was followed by isochronous annealing treatment in air at different temperatures, anhydrous monolithic UPA with different crystallizations can be accordingly obtained [11,12,14,15]. The versatile applications of UPA materials with regard to photocatalytic, optical, electronic, and arsenic wastewater treatment performances have been extensively studied [16–20].

In the present study, RBBR was chosen as a representative AQ dye, which widely exists in industrial textile effluents. The UPA powders with different polycrystalline phases (i.e., γ , θ , and α) were synthesized for RBBR removal, and the experimental factors that affect the material adsorption performances were comprehensively studied by batch experiments. The adsorption kinetic models including the Lagergren pseudo-first-order, pseudo-second-order, film diffusion (Boyd plot), and intraparticle diffusion (Weber and Morris plot) models were applied to fit the kinetic data. Additionally, the adsorption equilibrium data at different temperatures were fitted by using the Langmuir, Freundlich, Temkin, and Dubinin–Radushkevich (D–R) isotherm models. The present study provides

an improved understanding of the UPA potentials in wastewater treatment, which can explore its applications in the environmental field.

2. Materials and Methods

2.1. Chemicals and UPA Monolith Synthesis

Figure S1a,b showed the physicochemical characteristics of RBBR and its molecular compositions (wt%) including C (42.17%), H (2.57%), N (4.47%), Na (7.34%), O (28.09%), and S (15.35%) [21]. The chemicals including acetone, $\text{Hg}(\text{NO}_3)_2$, AgNO_3 , sodium acetate, CH_3COOH , and NaOH were purchased from Sigma-Aldrich, Inc. (St. Louis, MO, USA). The raw laminated metallic aluminum plate (100×100 mm, 1.0 mm of thickness, 99.99% of purity) was supplied by Goodfellow Cambridge Ltd. (Huntingdon, UK). All the chemicals used in this study were of analytical grade and used as received directly without further purification. Milli-Q water (Figure S2, Millipore Corp., Burlington, MA, USA) with a specific resistivity of $18.2 \text{ M}\Omega \cdot \text{cm}^{-1}$ at 25°C was used to prepare solutions throughout the experiments.

The UPA monolith samples were synthesized via a facile oxidation process according to the previous studies (Figure S3) [11,12,16,17,22]. Briefly, high purity but fragile UPA monolith samples were obtained with a growth rate of $\sim 1 \text{ cm} \cdot \text{h}^{-1}$ at room temperature in a humid atmosphere (70–80% RH) by the oxidation of metallic aluminum plates through a liquid layer of mercury–silver amalgam (Figure S4) [11]. Anhydrous monolithic UPA can be obtained from fragile UPA, converting to amorphous UPA, polycrystalline UPA(γ), UPA(θ), and UPA(α) monolith under 4 h of an isochronous annealing treatment in air at <870 , 950, 1150, and 1350°C , respectively (Figure S5) [11,12,17,18,22]. The mechanical stability of the UPA materials increased with the increasing calcination temperature at the expense of the specific surface area, which decreased from $300 \text{ m}^2 \cdot \text{g}^{-1}$ (raw fragile UPA) to $202 \text{ m}^2 \cdot \text{g}^{-1}$ of UPA(γ), $93 \text{ m}^2 \cdot \text{g}^{-1}$ of UPA(θ), and $6 \text{ m}^2 \cdot \text{g}^{-1}$ of UPA(α) (Figure S6). Figure S7a,b showed the adsorption isotherm profiles regarding RBBR adsorption capacity with units as $\text{mg} \cdot \text{g}^{-1}$ and $\text{mg} \cdot \text{m}^{-2}$ retained by UPA(γ), UPA(θ), and UPA(α) powders, respectively. These results showed that the RBBR adsorption capacity was proportional to the UPA specific surface area and attained approximately $1.1 \text{ mg} \cdot \text{m}^{-2}$ regardless of its polycrystalline phase. Therefore, to obtain the desirable mechanical stability of UPA monolith with considerable RBBR adsorption capacity, in the following studies, UPA(θ) monolith was employed to achieve more homogeneous adsorbent dispersion after a rigorous grinding process.

2.2. Characterization

The obtained samples were characterized by using scanning electron microscopy (SEM, Zeiss Supra 40 VP, Carl Zeiss, Jena, Germany) and transmission electron microscopy (TEM, JEOL 2011, JEOL Ltd., Tokyo, Japan) techniques. The material compositions before and after RBBR adsorption were analyzed by elemental mapping with energy-dispersive X-ray (EDX) spectroscopy (SEM S440, LEICA, Germany). The Fourier transform infrared (FTIR) spectra of the obtained samples were recorded by using a PerkinElmer Spectrum 100 system spectrometer (PerkinElmer, Waltham, MA, USA) in pressed KBr pellets (Sigma-Aldrich, St. Louis, MO, USA, 99%, analytical reagent) and in the $400\text{--}4000 \text{ cm}^{-1}$ region. The powder X-ray diffraction (XRD) pattern of the obtained samples was carried out by using an Inel Equinox 1000 X-ray diffractometer (Inel, Celje, Slovenia) with $\text{Co K}\alpha$ radiation source ($\lambda = 1.7902 \text{ \AA}$), and the analysis was performed at 2θ diffraction angles from 25° to 85° at a speed of $2^\circ/\text{min}$. The Brunauer–Emmett–Teller (BET) specific surface area and pore size distribution of the obtained samples were studied by nitrogen adsorption–desorption measurement (Belsorp-max, MicrotracBEL, Japan; data analysis: MicroActive for ASAP 2460) with outgassing at 200°C for 12 h. The mass of UPA(γ), UPA(θ), and UPA(α) powders and the corresponding range of points (P/P_0) used for the BET measurements were 0.0602 (0.0052–0.9888), 0.0586 (0.0100–0.9898), and 0.4335 g (0.0063–0.9948 pressure), respectively. The zeta potential values of the obtained samples as a function of pH were measured by a Nano ZS90 Zetasizer (Malvern Instruments Ltd., Malvern, UK). The desired

pH values of suspensions between 2 and 12 were adjusted by adding negligible volumes of 0.1–0.01 mol·L⁻¹ HCl (2.0–3.5), CH₃COOH (3.5–7.0), or NaOH solution.

2.3. Batch Adsorption Studies

The complete experimental details can be found in the Supplementary Materials. The RBBR concentration in the supernatant (C_t , mg·L⁻¹) was determined by spectrophotometry method at the wavelength of 590 nm (Figure S1c,d, UviLine 9400 UV-Visible spectrophotometer, Secomam, France). The adsorption percentage (%), the adsorption capacity at equilibrium (q_e , mg·g⁻¹), and the distribution coefficient (K_d) were obtained from the following equations, respectively:

$$\text{Adsorption (\%)} = \frac{C_0 - C_e}{C_0} \times 100 \quad (1)$$

$$q_e = \frac{C_0 - C_e}{m} \times V \quad (2)$$

$$K_d = \frac{C_0 - C_e}{C_e} \times \frac{V}{m} = \frac{q_e}{C_e} \quad (3)$$

where C_0 (mg·L⁻¹) is the initial adsorbate concentration in suspension, C_e (mg·L⁻¹) is the adsorbate concentration in the supernatant at equilibrium, V (L) is the volume of suspension, and m (g) is the mass of adsorbent. All of the experimental data are the averages of triplicate determinations.

2.4. Data Analysis

2.4.1. Adsorption Kinetic Study

The kinetic data were fitted by the Lagergren pseudo-first-order and pseudo-second-order models by using the following linearized equations, respectively [23,24]:

Lagergren pseudo-first-order model:

$$\ln(Q_m - Q_t) = \ln Q_m - k't \quad (4)$$

pseudo-second-order model:

$$\frac{t}{Q_t} = \frac{1}{k''Q_m^2} + \frac{t}{Q_m} \quad (5)$$

where Q_t and Q_m (mg·g⁻¹) refer to the adsorption capacity at time t (h) and at equilibrium obtained from the kinetic models. k' (h⁻¹) and k'' (g·mg⁻¹·h⁻¹) are the adsorption rate constants obtained from the kinetic models.

2.4.2. Rate-Limiting Step Determination Study

In order to identify the bottleneck (slowest) step of the adsorption process, both the first-curved and second-linear adsorption parts of the kinetic data were fitted by the film diffusion (Boyd plot) and intraparticle diffusion models (Weber and Morris plot) by using the following linearized equations, respectively [25–27]:

Film diffusion model [25,26]:

$$\ln\left(1 - \frac{Q_t}{Q_m}\right) = -k_{FD}t \quad (6)$$

Intraparticle diffusion model [27]:

$$Q_t = k_{IPD}t^{0.5} + C_{IPD} \quad (7)$$

where Q_t/Q_m is the fractional attainment of equilibrium. k_{FD} (min⁻¹) and k_{IPD} (mg·g⁻¹·min^{-0.5}) are the rate constants obtained from the diffusion models. C_{IPD} is proportional to

the boundary layer, which provides information about boundary layer thickness, i.e., the larger value of C_{IPD} , the greater of boundary layer effect on the adsorption process [27,28].

2.4.3. Adsorption Equilibrium Study

To obtain a better understanding of the adsorption mechanisms, the adsorption equilibrium data were fitted by Langmuir, Freundlich, Temkin, and D–R isotherm models [29].

The linearized equation of the Langmuir isotherm model is listed as follows [30–32]:
Langmuir isotherm model:

$$\frac{C_e}{q_e} = \frac{1}{K_L q_{e,max}} + \frac{C_e}{q_{e,max}} \quad (8)$$

where $q_{e,max}$ ($\text{mg}\cdot\text{g}^{-1}$) is the maximum adsorption capacity obtained from the isotherm models, and K_L ($\text{L}\cdot\text{mg}^{-1}$) is the constant of the Langmuir isotherm model related to the adsorption energy. The essential characteristics of the Langmuir model can be expressed in terms of a dimensionless constant, commonly known as separation factor or equilibrium parameter (R_L), which is defined by the following equation [33,34]:

$$R_L = \frac{1}{1 + K_L C_0} \quad (9)$$

According to Hall et al. [33], the magnitude of R_L indicates the adsorption process in nature to be either unfavorable ($R_L > 1$), linear ($R_L = 1$), favorable ($0 < R_L < 1$) or irreversible ($R_L = 0$).

The linearized equation of the Freundlich isotherm model is listed as follows [35]:
Freundlich isotherm model:

$$\log q_e = \log K_F + \frac{1}{n} \log C_e \quad (10)$$

where K_F ($\text{mg}^{(1-1/n)}\cdot\text{L}^{1/n}\cdot\text{g}^{-1}$) and $1/n$ are the Freundlich constants indicating the adsorption capacity and adsorption intensity, respectively. The magnitude of $1/n$ ranges between 0 and 1, indicating the surface heterogeneity, which becomes more heterogeneous as its value approaches zero [5,29,36]. Meanwhile, $1/n > 1$ indicates a cooperative adsorption [29].

The linearized equation of the Temkin isotherm model is listed as follows [37]:
Temkin isotherm model:

$$q_e = B \ln K_T + B \ln C_e \quad (11)$$

where $B = RT/b_T$ ($\text{J}\cdot\text{mol}^{-1}$) and K_T ($\text{L}\cdot\text{g}^{-1}$) are the constant and equilibrium binding constant of the Temkin isotherm model, respectively.

The linearized equation of the D–R isotherm model is listed as follows [38]:
D–R isotherm model:

$$\ln q_e = \ln q_{e,max} - \beta \epsilon^2 \quad (12)$$

$$\epsilon = RT \ln\left(1 + \frac{1}{C_e}\right) \quad (13)$$

where β ($\text{mol}^2\cdot\text{kJ}^{-2}$) is the constant of the D–R isotherm model, ϵ is the constant of the D–R isotherm model related to the Polanyi potential, R ($8.3145 \text{ J}\cdot\text{mol}^{-1}\cdot\text{K}^{-1}$) is the universal gas constant, and T (K) is the absolute temperature in Kelvin. E ($\text{kJ}\cdot\text{mol}^{-1}$) is defined as the free energy change required to transfer 1 mol of adsorbate from infinity in solution to the solid surface [28]. This relationship can be described as follows [39]:

$$E = \frac{1}{\sqrt{2\beta}} \quad (14)$$

The magnitude of E is useful to estimate the mechanism of the adsorption reaction. If the value of E is in the range of $8\text{--}16\text{ kJ}\cdot\text{mol}^{-1}$, the adsorption process is governed by an ion-exchange mechanism, while in the case of $E < 8\text{ kJ}\cdot\text{mol}^{-1}$, the adsorption process may be affected by physical forces. On the other hand, the adsorption process may be dominated by particle diffusion if the value of E is greater than $16\text{ kJ}\cdot\text{mol}^{-1}$ [40,41].

2.4.4. Adsorption Thermodynamic Study

The thermodynamic parameters including standard Gibbs free energy (ΔG^0 , $\text{kJ}\cdot\text{mol}^{-1}$), standard enthalpy change (ΔH^0 , $\text{kJ}\cdot\text{mol}^{-1}$), and standard entropy change (ΔS^0 , $\text{J}\cdot\text{mol}^{-1}\cdot\text{K}^{-1}$) were obtained from the following equations, respectively:

$$\Delta G^0 = -RT \ln K^0 \quad (15)$$

$$\ln K^0 = \frac{\Delta S^0}{R} - \frac{\Delta H^0}{RT} \quad (16)$$

where $\ln K^0$ (K^0 , the standard distribution coefficient) can be obtained by plotting $\ln K_d$ versus C_e and extrapolating C_e to zero. The slope and intercept of the plot of $\ln K^0$ versus $1000/T$ correspond to $-\Delta H^0/1000R$ and $\Delta S^0/R$, respectively.

3. Results and Discussions

3.1. Characterization

Figure 1a,b showed the SEM and TEM images of UPA(θ) powders, which evidenced the ultraporous morphology of obtained samples. The EDX spectra of UPA(θ) powders showed that there were no residual mercury or silver element retained on the surface of obtained samples (Figure S8). As shown in Figure S9, the UPA(θ) border became smoother after RBBR adsorption, and the corresponding TEM elemental mappings in Figure 1c,d clearly confirmed the uniform distribution of RBBR retained on UPA(θ) surfaces.

In Figure 2a, the absorption band in the range of $3400\text{--}3500\text{ cm}^{-1}$ was assigned to the $-\text{OH}$ stretching vibration of UPA(θ) powders, and the broader absorption band in this range indicated the presence of carboxyl and amino groups distributed on the UPA(θ) surface after RBBR adsorption (Figure S1a). Based on the calculation from Bragg equation ($2d\sin\theta = n\lambda$, $n = 1, 2, 3$, etc.) (Figure 2b), the typical XRD patterns at $2\theta = 36.64^\circ$ ($d = 0.28\text{ nm}$), 38.46° ($d = 0.27\text{ nm}$), and 80.32° ($d = 0.14\text{ nm}$) correspond to the (111), (-204), and (403) planes of theta alumina, respectively, (JCPDS 35-0121, 11-0517, and 23-1009) [42]. The nitrogen adsorption-desorption isotherm curve of UPA(θ) powders followed the typical characteristics of type IV isotherm and H3 hysteresis (IUPAC), indicating the mesoporous property of UPA(θ) powders (Figure 2c) [43,44]. Moreover, the specific surface area of UPA(θ) powders was $93\text{ m}^2\cdot\text{g}^{-1}$ with an average pore diameter of 35 nm (Gaussian curve from $0\text{--}150\text{ nm}$), and most data of pore size distribution located in the mesoporous range (Figure 2c). The ultraporous nature of UPA(θ) powders is expected to favor the diffusion-controlled surface reactions, which will be discussed in the following studies.

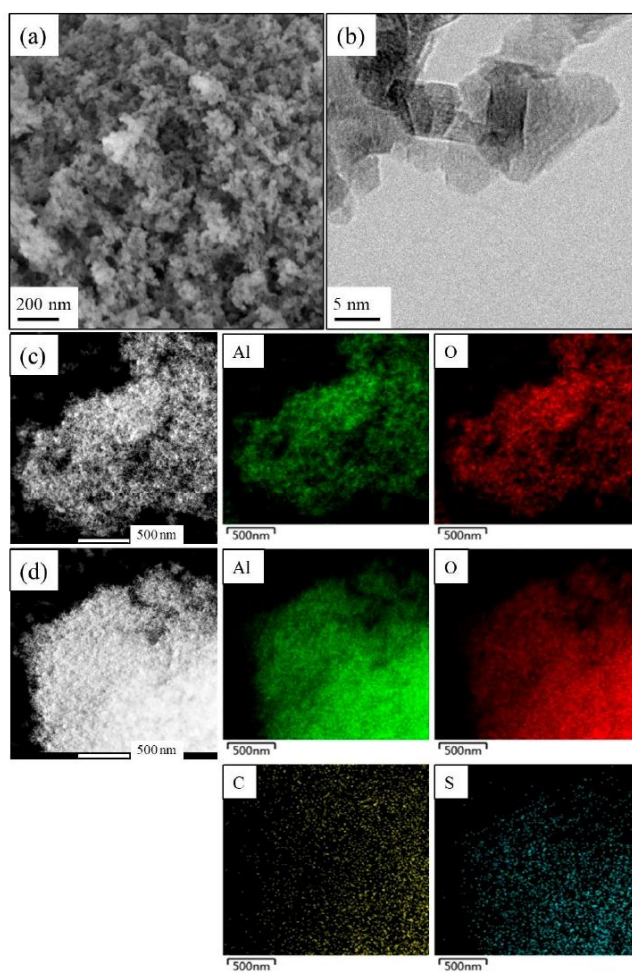


Figure 1. (a) SEM and (b) TEM images of UPA(θ) powders, and elemental mapping of UPA(θ) powders (c) before and (d) after RBBR adsorption.

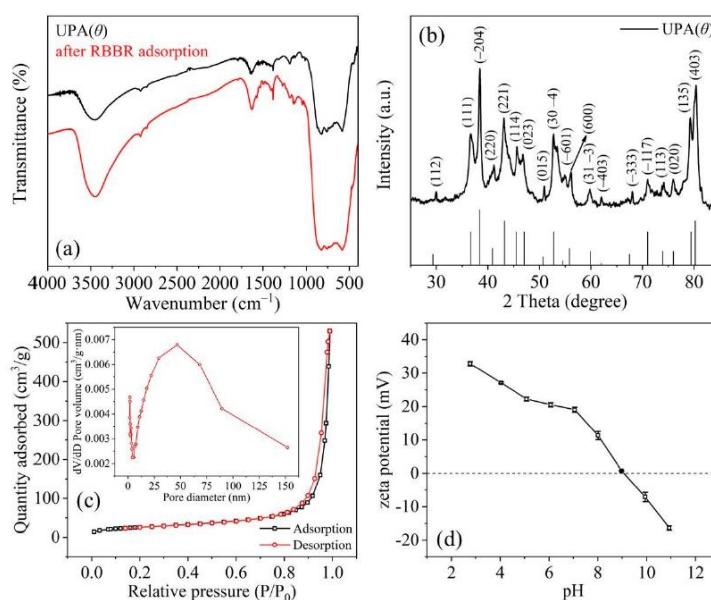


Figure 2. (a) FTIR spectra of UPA(θ) powders before and after RBBR adsorption; (b) XRD pattern and (c) nitrogen adsorption–desorption isotherm of UPA(θ) powders (inset: pore size distribution); (d) zeta potential value of UPA(θ) powders as a function of pH. $m/V_{[UPA(\theta)]} = 4.44 \text{ g}\cdot\text{L}^{-1}$, $I = 100 \text{ mmol}\cdot\text{L}^{-1}$ sodium acetate.

3.2. Initial pH Effect and Adsorption Kinetics

As shown in Figure 3a, the RBBR adsorption retained by UPA(θ) powders strongly decreased with increasing pH (up to pH = 6) and then slowly decreased in the following pH range. According to Figure 2d, the pH_{zpc} value of UPA(θ) powders approximately equaled to 9.0, and the increasing solution pH values after RBBR adsorption equilibrium indicated the significant consumption of hydrogen ions under acidic conditions (Figure S10). At low pH values, the electrostatic attraction between the protonated (positively charged) functional groups on UPA(θ) surfaces and RBBR species resulted in the high adsorption percentage of RBBR [7,45,46]. As the pH value increased, these gradually deprotonated (negatively charged) functional groups became less favorable for the adsorption process, and consequently, the affinity of UPA(θ) powders toward the negatively charged RBBR species (e.g., $-\text{SO}_3^-$, sulfonate groups) decreased (Figure 2d). Moreover, at high pH values, the formation of excess OH^- ions under alkaline conditions and subsequent competition with the RBBR species for the finite reaction sites on UPA(θ) surfaces may also lead to the low RBBR adsorption percentage [7]. According to the previous studies, similar results have also been reported by applying other kinds of adsorbents for RBBR removal [6,45–48]. For example, Gök et al. found that the adsorption of RBBR onto 1,6-diamino hexane modified bentonite (DAH–bentonite) was strongly pH dependent, with the optimum pH = 1.5 [6]. Therefore, the low adsorption percentage of RBBR under alkaline conditions can be attributed to the electrostatic repulsion between the negatively charged UPA(θ) surfaces and the anionic RBBR species, which became the essential factor in controlling the adsorption process.

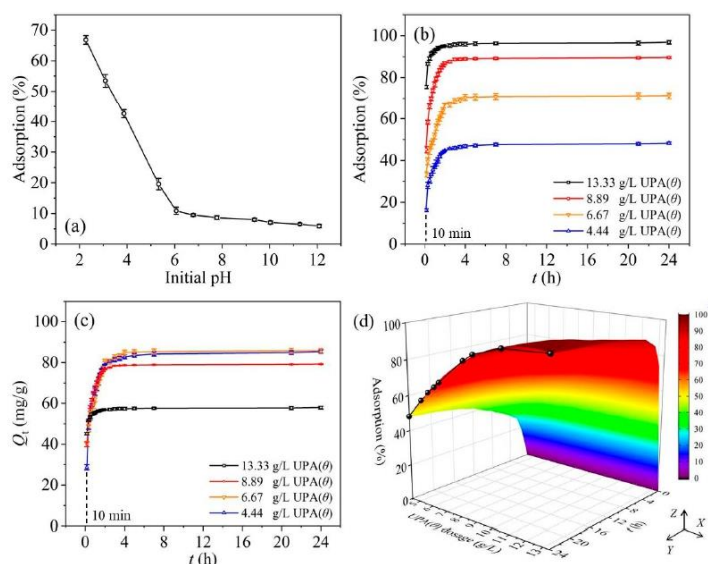


Figure 3. (a) Effect of initial pH on RBBR adsorption, $C_{[RBBR]initial} = 800 \text{ mg}\cdot\text{L}^{-1}$, $m/V_{[UPA(\theta)]} = 4.44 \text{ g}\cdot\text{L}^{-1}$, $I = 100 \text{ mmol}\cdot\text{L}^{-1}$ sodium acetate, $T = 310 \text{ K}$, stirring speed = 150 rpm, and equilibrium time = 24 h. Adsorption kinetics regarding the (b) adsorption percentage and (c) adsorption capacity of RBBR retained by UPA(θ) powders; (d) effect of UPA(θ) dosage on RBBR adsorption kinetics. $C_{[RBBR]initial} = 800 \text{ mg}\cdot\text{L}^{-1}$, initial pH = 4.0 ± 0.1 , $I = 100 \text{ mmol}\cdot\text{L}^{-1}$ sodium acetate, $T = 310 \text{ K}$, stirring speed = 150 rpm, and terminal equilibrium time = 24 h. ^a Three-dimensional curved surface simulation based on MATLAB matrix conversion and gridding.

The kinetic data regarding the adsorption percentage (%) and adsorption capacity (Q_t , $\text{mg}\cdot\text{g}^{-1}$) of RBBR retained by UPA(θ) powders were shown in Figure 3b,c, respectively. The RBBR adsorption increased rapidly in the first 4 h and then maintained a high level until the adsorption process achieved equilibrium. Figure 3b,c also showed that in the initial step, the adsorption process achieved equilibrium much more rapidly at high adsorbent dosage. In Figure 3c, the decrease of Q_t value of RBBR adsorption may result from the increasing UPA(θ) dosage on which more vacant reaction sites became available. In general, the RBBR adsorption process was rapid, and 4 h was enough to achieve the entire adsorption equilibrium. Based on the profiles of kinetic data (Figure 3b), the effect of UPA(θ) dosage on RBBR adsorption kinetics was shown in Figure 3d (XZ side, i.e., “UPA(θ) dosage ($\text{g}\cdot\text{L}^{-1}$)–Adsorption (%)” side). As discussed above, the increasing UPA(θ) dosage may result in more vacant reaction sites available on the adsorbent surfaces for RBBR adsorption. This positive relationship explained the Γ line type of kinetic data on the XZ side of Figure 3d at 24 h of equilibrium time (black line highlighted). The RBBR adsorption increased with increasing UPA(θ) dosage and exceeded 96% when UPA(θ) dosage attained more than $10 \text{ g}\cdot\text{L}^{-1}$. As long as sufficient reaction sites were provided, the RBBR adsorption was independent of UPA(θ) dosage. All the above discussions indicated that the UPA(θ) dosage played an important role in the adsorption process; however, the economic issues usually should be taken into consideration in the actual adsorbent applications. Therefore, in order to obtain suitable dye treatment, one should determine the appropriate UPA(θ) dosage according to the initial concentration of dye effluents [6,7,49,50].

3.3. Adsorption Kinetic and Rate-Limiting Step Determination Studies

The fitting results of the Lagergren pseudo-first-order and pseudo-second-order models were shown in Figure 4a,b, respectively, and the fitting parameters were listed in Table 1.

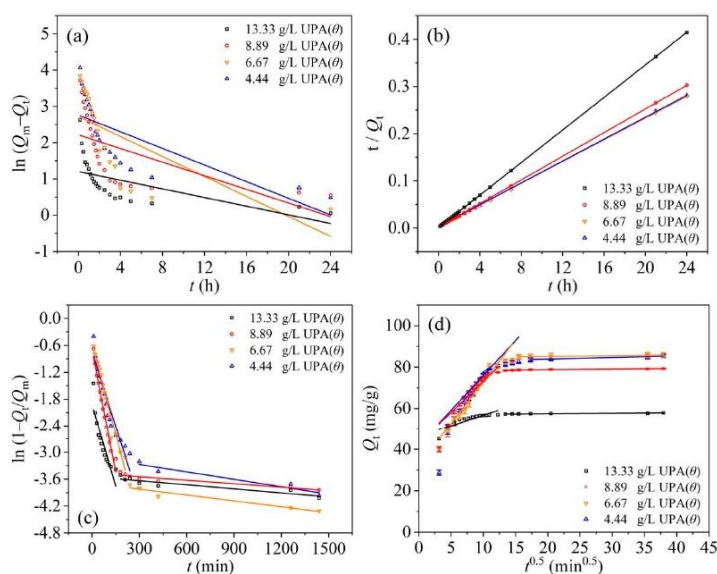


Figure 4. Tests of the (a) Lagergren pseudo-first-order, (b) pseudo-second-order, (c) film diffusion (Boyd plot), and (d) intraparticle diffusion (Weber and Morris plot) models on RBBR adsorption retained by UPA(θ) powders.

Table 1. Parameters of RBBR adsorption kinetics fitted by the Lagergren pseudo-first-order and pseudo-second-order models at T = 310 K.

Kinetic Models	UPA(θ) Dosage (g·L ⁻¹)			
	4.44	6.67	8.89	13.33
Lagergren pseudo-first-order				
k' (h ⁻¹)	0.115	0.138	0.094	0.060
Q_{mc} (mg·g ⁻¹) ^a	15.844	15.243	9.171	3.337
R^2	0.521	0.511	0.336	0.332
Pseudo-second-order				
k'' (g·mg ⁻¹ ·h ⁻¹)	0.049	0.046	0.102	0.422
Q_{mc} (mg·g ⁻¹) ^a	86.207	86.957	79.745	57.803
R^2	0.999	0.999	0.999	0.999
Q_{me} (mg·g ⁻¹) ^b	87.385	87.934	81.116	59.987

^a Q_{mc} (mg·g⁻¹) is the calculated adsorption capacity at equilibrium obtained from the kinetic models. ^b Q_{me} (mg·g⁻¹) is the experimental adsorption capacity at equilibrium.

As shown in Table 1, the low determination coefficients (R^2) obtained from the Lagergren pseudo-first-order model (Equation (4)) showed that between the kinetic data and this model, there was no significant correlation. On the other hand, the pseudo-second-order model (Equation (5)) fitted the kinetic data better, and the calculated adsorption capacities at equilibrium (Q_{mc}) were closer to the experimental ones (Q_{me}). Therefore, the adsorp-

tion process followed the pseudo-second-order model based on the assumption that the rate-limiting step may be chemical adsorption or chemisorption involving valence forces through sharing or exchanging electrons between the adsorbent and adsorbate, which provides the best correlation of the kinetic data [24,51].

Generally, the adsorption kinetics of solutes retained by porous materials is controlled by different steps [50,51]: (i) solutes transfer from the aqueous phase to the more external adsorbent surface, crossing the boundary film bordering the solid adsorbent particles (film diffusion step), (ii) internal diffusion of solutes transferring from the adsorbent surface to the intraparticle active sites (particle diffusion step), and (iii) sequestration on the active sites via adsorption, complexation, or intraparticle precipitation phenomena. One or more of the above-mentioned steps may affect the mechanisms governing the adsorption process. The fitting results of the film diffusion and intraparticle diffusion models were shown in Figure 4c,d, respectively, and the fitting parameters were listed in Table 2.

Table 2. Parameters of RBBR adsorption kinetics fitted by the film diffusion (Boyd plot) and intraparticle diffusion (Weber and Morris plot) models at T = 310 K.

Diffusion Models	First-Curved Adsorption Part				Second-Linear Adsorption Part			
	4.44	6.67	8.89	13.33	4.44	6.67	8.89	13.33
Film diffusion								
k_{FD} (min^{-1})	0.0111	0.0136	0.0184	0.0123	0.0006	0.0004	0.0003	0.0003
Intercept on Y axis ^a	-0.746	-0.556	-0.690	-1.922	-3.108	-3.691	-3.471	-3.545
R^2	0.911	0.956	0.976	0.807	0.885	0.909	0.866	0.826
Intraparticle diffusion								
k_{IPD} ($\text{mg}\cdot\text{g}^{-1}\cdot\text{min}^{-0.5}$)	3.3628	4.0538	3.0117	1.0385	0.0769	0.0374	0.0281	0.0217
C_{IPD}	42.309	32.299	43.003	46.347	82.332	84.429	78.199	57.072
R^2	0.708	0.904	0.873	0.704	0.899	0.916	0.875	0.838

^a A linear plot of $-\ln(1 - Q_t/Q_m)$ versus t with zero intercept indicates that the kinetics of the adsorption process is controlled by diffusion through the liquid surrounding the solid adsorbent particles.

The nonlinear distribution of points with two distinct regions observed in Figure 4d indicated that intraparticle/pore diffusion may participate in the adsorption process but was not the single rate-limiting step [51]. Furthermore, the deviation of intercepts of Weber and Morris plot (C_{IPD} , Figure 4d) may be due to the difference in the rate of mass transfer in the initial and final stages of the adsorption process [28,52]. For the RBBR adsorption retained by UPA(θ) powders, the initial curved region of the plot was attributed to the film diffusion, and the subsequent linear region was attributed to the intraparticle diffusion and chemical reactions [48,51].

3.4. Adsorption Equilibrium Study

As shown in Figure 5, the RBBR adsorption capacity of UPA(θ) powders decreased with increasing temperature, which indicated that the adsorption reaction may be exothermic, and low temperature favored the adsorption process.

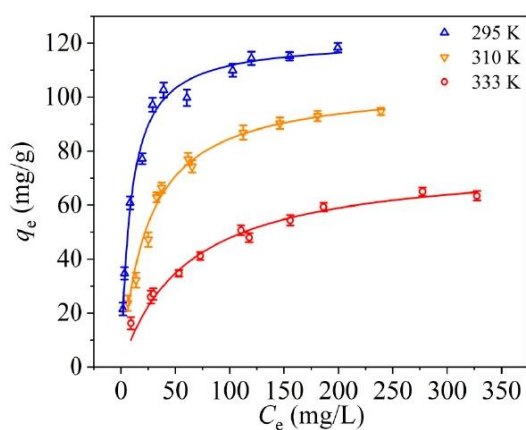


Figure 5. Adsorption isotherm profiles of RBBR retained by UPA(θ) powders at different temperatures. $m/V_{[UPA(\theta)]} = 5.56 \text{ g}\cdot\text{L}^{-1}$, initial pH = 4.0 ± 0.1 , $I = 100 \text{ mmol}\cdot\text{L}^{-1}$ sodium acetate, stirring speed = 150 rpm, and equilibrium time = 24 h.

Based on the assumption that the monolayer adsorption can only occur at a finite number of definite localized sites with no lateral interaction and steric hindrance between the adsorbed molecules, even on adjacent sites, the Langmuir model is widely used for the fitting of the homogeneous adsorption [30–32]. This empirical model is graphically characterized by a plateau and an equilibrium saturation point where once a molecule occupies a site, no further adsorption can take place [29]. Unlike the Langmuir model, the Freundlich model is an empirical model widely applied in heterogeneous systems (e.g., organic compounds, highly interactive species on activated carbon and molecular sieves), which describes the nonideal and reversible adsorption with no restrictions to the formation of monolayer [35]. The Temkin model, which contains a factor that explicitly takes account of the adsorbent–adsorbate interactions, was firstly introduced describing the adsorption of hydrogen onto platinum electrodes in acidic solutions [37]. By ignoring the extremely low and large value of concentrations, this model assumes that the heat of adsorption (function of temperature) of all the molecules in the layer would decrease linearly rather than logarithmically with coverage [29,53]. Compared with its less applicability to the more complex adsorption systems, especially the liquid phase adsorption isotherms, the Temkin model can be well applied for predicting the gas phase equilibrium. The D–R model is an empirical model generally applied to express the adsorption mechanism with a Gaussian energy distribution onto a heterogeneous surface [38]. This model has often successfully fitted high solute activities and the intermediate range of concentrations data well.

The fitting results of the Langmuir, Freundlich, Temkin, and D–R isotherm models were shown in Figure 6, and the fitting parameters were listed in Table 3.

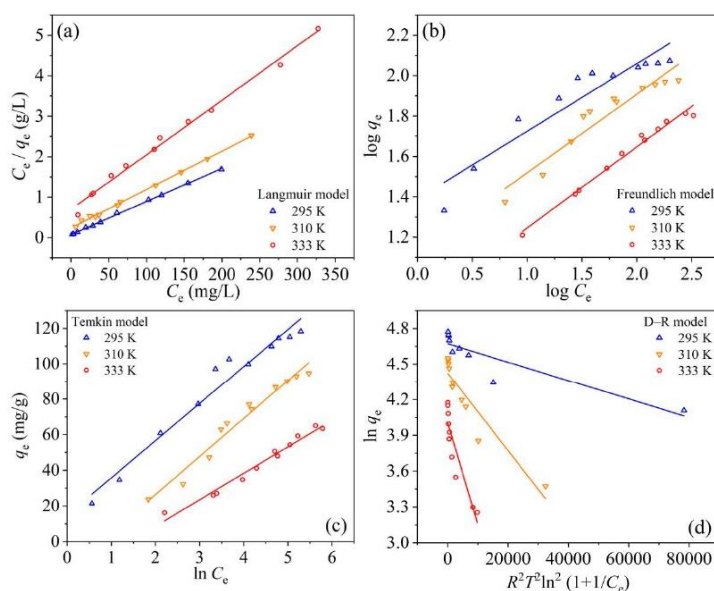


Figure 6. Tests of the (a) Langmuir, (b) Freundlich, (c) Temkin, and (d) D–R isotherm models on RBBR adsorption retained by UPA(θ) powders, at different temperatures.

Table 3. Parameters of RBBR adsorption isotherms fitted by the Langmuir, Freundlich, Temkin, and D–R isotherm models at different temperatures.

Isotherm Models	295 K	310 K	333 K
Langmuir			
$q_{e,max}$ ($mg \cdot g^{-1}$)	122.549	105.485	74.184
K_L ($L \cdot mg^{-1}$)	0.107	0.039	0.019
R^2	0.999	0.998	0.991
R_L	0.011–0.078	0.030–0.188	0.056–0.275
Freundlich			
K_F ($mg^{(1-1/n)} \cdot L^{1/n} \cdot g^{-1}$)	24.548	13.461	6.991
$1/n$	0.335	0.390	0.401
R^2	0.880	0.903	0.982
Temkin			
B ($J \cdot mol^{-1}$)	20.892	21.376	14.824
K_T ($L \cdot g^{-1}$)	2.036	0.464	0.242
R^2	0.960	0.961	0.973
D–R			
$q_{e,max}$ ($mg \cdot g^{-1}$)	107.037	83.502	54.976
β ($mol^2 \cdot kJ^{-2}$)	7.795×10^{-6}	3.257×10^{-5}	8.496×10^{-5}
R^2	0.784	0.866	0.823

Compared the obtained R^2 values from different isotherm models with each other, the Langmuir model fitted the adsorption equilibrium data better than the other three models (i.e., Langmuir > Temkin \approx Freundlich > D–R model), indicating the presence of RBBR monolayer coverage on UPA(θ) surfaces [30–32]. Based on the Langmuir model, the $q_{e,max}$ values of RBBR adsorption retained by UPA(θ) powders were 122.55, 105.49, and

74.18 mg·g⁻¹ for 295, 310, and 333 K, respectively. These results were in good accordance with the equilibrium q_e values obtained from the adsorption equilibrium study (Figure 5), which was consistent with the low-temperature favorable conclusion, as discussed above. The R_L values listed in Table 3 fell in the range of 0–1, indicating that the RBBR adsorption retained by UPA(θ) powders was favorable, and RBBR tended to remain the bonding on UPA(θ) surfaces [33]. The obtained R^2 values from the Temkin model were slightly greater than those of the Freundlich model, and the equilibrium binding constants (K_T) at high temperatures were less than that at room temperature. In the Freundlich model, all the values of $1/n$ at different temperatures were less than 1, indicating the surface heterogeneity of UPA(θ) powders during the adsorption process [5,29,36]. Among the isotherm models applied in this study, the obtained R^2 values from the D–R model were the lowest among the considered isotherm models, and the $q_{e,max}$ values were much less than the equilibrium q_e values obtained from the adsorption isotherms (Figure 5). Consequently, the model analysis indicated the low applicability of the D–R model on the adsorption process. Therefore, the Langmuir isotherm model was found to describe the adsorption equilibrium data best, and the maximum RBBR adsorption capacity retained by UPA(θ) powders was 122.55 mg·g⁻¹ at 295 K.

3.5. Adsorption Thermodynamic Study

The thermodynamic parameters can define whether the RBBR adsorption retained by UPA(θ) powders was endothermic or exothermic, spontaneous or not [54,55]. The linear plots of $\ln K_d$ versus C_e and $\ln K^0$ versus $1000/T$ were shown in Figure 7a,b, respectively. The obtained thermodynamic parameters were listed in Table 4.

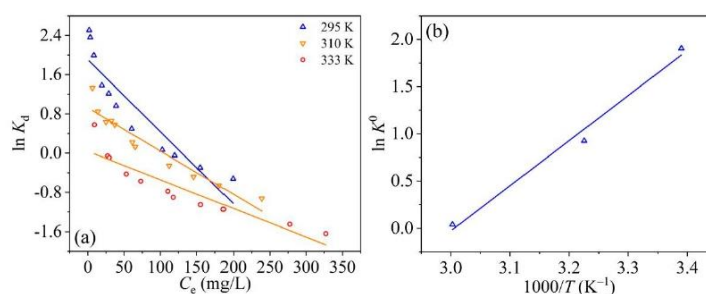


Figure 7. Linear plots of (a) $\ln K_d$ versus C_e and (b) $\ln K^0$ versus $1000/T$ for RBBR adsorption retained by UPA(θ) powders.

Table 4. Thermodynamic parameters of RBBR adsorption retained by UPA(θ) powders.

T (K)	ΔG^0 (kJ·Mol ⁻¹)	ΔH^0 (kJ·Mol ⁻¹)	ΔS^0 (J·Mol ⁻¹ ·K ⁻¹)
295	−4.673		
310	−2.383	−39.711	−119.372
333	−0.107		

In general, the positive ΔG^0 values at all temperatures indicate that the adsorption process requires energy from an external source to convert reactants into products, which is considered thermodynamically unfavorable. In this study, the obtained negative ΔG^0 values indicated that the RBBR adsorption process was thermodynamically favorable and spontaneous. The increase of ΔG^0 value with increasing temperature indicated that low temperature favored the adsorption process. The negative ΔH^0 value confirmed the exothermicity of the adsorption process. Moreover, the magnitude order of ΔH^0 value can indicate the type of adsorption process to be either physical (2.1–20.9 kJ·mol⁻¹) or

chemisorption ($80\text{--}200\text{ kJ}\cdot\text{mol}^{-1}$) [56]. Consequently, the RBBR adsorption retained by UPA(θ) powders can be attributed to a combined physic–chemical adsorption in nature. The magnitude of ΔS^0 value can be used to describe the randomness at the solid–liquid interface during the adsorption process. According to the previous studies [54–56], the negative value of ΔS^0 reflected that the adsorption process involves an associative mechanism, and no significant change occurred in the internal structures of the adsorbent during the adsorption process, while the positive ΔS^0 value reflected the affinity of the adsorbent to adsorbate species involving the dissociative mechanism. For the RBBR adsorption retained by UPA(θ) powders, the negative value of ΔS^0 indicated that the adsorption process was enthalpy driven, accompanying a decreased disorder that occurred at the solid–liquid interface.

3.6. Adsorption Mechanism

Figure 8 showed the possible mechanisms for the adsorption of RBBR retained by UPA(θ) powders. Film diffusion, intraparticle diffusion, electrostatic attraction, surface complexation, and hydrogen bonding could be considered as the major interactions in the adsorption mechanisms for the removal of RBBR retained by UPA(θ) powders. The ultra-porous nature of the UPA(θ) powders induced the adsorption of RBBR molecules by film and intraparticle diffusion mechanisms. The hydroxyl functional groups distributed on the UPA(θ) surface tended to form complexes with RBBR molecules by several mechanisms including electrostatic interaction and surface complexation, especially under acidic conditions. Moreover, hydrogen bonding between the hydroxyl functional groups (hydrogen bond donors) and nitrogen and/or oxygen centers in RBBR molecules (hydrogen bond acceptors) may also have some influences on the adsorption process.

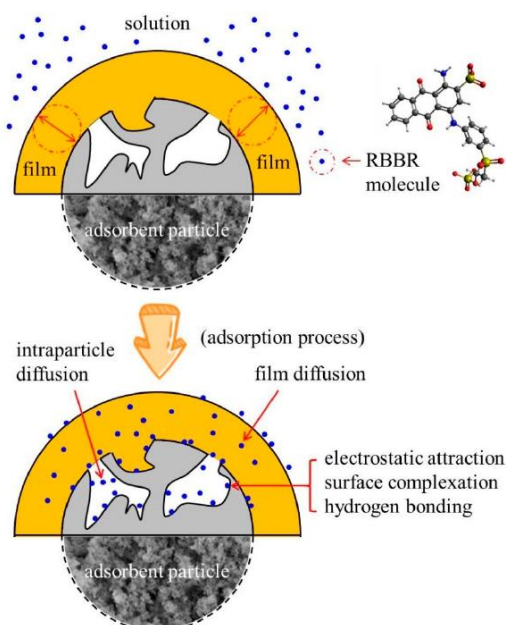


Figure 8. Possible mechanisms for RBBR adsorption retained by UPA(θ) powders.

Compared with the other organic, inorganic, or bio-based adsorbents reported in related studies in the literature (Table 5), UPA(θ) and UPA(γ) powders possess several advantages for large-scale applications including nontoxicity, facile synthesis, and higher RBBR adsorption capacity, compared with referenced adsorbents [4–7,13,45–47,49,50,57–61]. Therefore, UPA materials have high potentials as alternative adsorbents for the practical treatment of dye effluents.

Table 5. Comparison of RBBR adsorption capacity retained by UPA materials with other organic, inorganic, or bio-based adsorbents reported in related studies in the literature.

Adsorbents	Experimental Conditions ^a	$q_{e,max}$ (Mg·g ⁻¹) ^b	Ref.
Mazandaran wood waste (WW)	pH = 1.72, T = ND	4.75	[57]
ZnO nanoparticles (ZnO NPs)	pH = 3.0, T = 298 K	38.02	[49]
Commercial NiO	pH = ND, T = 298 K	38.62	[13]
NiO nanoparticles	pH = ND, T = 298 K	98.83	[13]
Magnetite/GO (MGO) nanocomposite	pH = 3.0, T = 298 K	62.50	[58]
Magnetite nanoparticles (MNPs)	pH = ND, T = 298 K	74.40	[50]
Free fungal biomass (FFB)	pH = 2.0, T = 303 K	80.91	[45]
Loofa sponge-immobilized fungal biomass (LSIFB)	pH = 2.0, T = 303 K	98.90	[45]
Magnetite-modified MWCNTs (MMMCNTs)	pH = 4.0, T = 298 K	88.80	[4]
Rhizopus arrhizus biomass	pH = 2.0, T = 298 K	90.00	[46]
Carboxylated MWCNTs	pH = ND, T = 298 K	95.24	[59]
Wheat bran	pH = 1.5, T = 293 K	97.10	[5]
Magnetite nanoparticles-modified AC (MMAC)	pH = 4.0, T = 298 K	104.60	[60]
Polypyrrole-coated Fe ₃ O ₄ (Ppy@Fe ₃ O ₄ MNPs)	pH = 3.0, T = 298 K	112.36	[47]
Ultraporous alumina(γ) (UPA(α))	pH = 4.0, T = 295 K	17.42	This study
Ultraporous alumina(θ) (UPA(θ))	pH = 4.0, T = 295 K	122.55	This study
Ultraporous alumina(α) (UPA(γ))	pH = 4.0, T = 295 K	212.31	This study
Modified polyethyleneimine (LMW-PEI)	pH = 10.0, T = 298 K	121.00	[61]
Modified bentonite (DAH-bentonite)	pH = 1.5, T = 293 K	134.71	[6]
MgO nanoparticles (Nano-MgO)	pH = 8.0, T = 298 K	166.70	[7]

^a ND: No data. ^b Adsorption capacity uniformly converted into mg·g⁻¹ (typical unit).

4. Conclusions

In this study, UPA materials were synthesized as new effective and low-cost adsorbents for RBBR removal from aqueous solutions. The synthesized materials were characterized using FTIR, XRD, SEM, TEM, and BET. The adsorption process was pH- and temperature dependent, and the maximum RBBR adsorption capacity retained by UPA(θ) powders was 122.55 mg·g⁻¹ at 295 K. Both the film diffusion and intraparticle diffusion contributed to the adsorption kinetics, and chemical reactions also played a significant role during the entire adsorption process. According to the obtained fitting results, the pseudo-second-order model and the Langmuir isotherm model were found to best describe the experimental data (i.e., pseudo-second-order > Lagergren pseudo-first-order model; and Langmuir > Temkin \approx Freundlich > D-R isotherm model). Moreover, the thermodynamic parameters indicated that the adsorption process was spontaneous and exothermic in nature. The findings of this study highlight the UPA potentials in wastewater treatment, which can broaden our understanding and its applications in the environmental field.

Supplementary Materials: The following are available online at <https://www.mdpi.com/article/10.3390/ma14113054/s1>, Table S1: Nomenclature, Greek symbols, and subscripts, Figure S1: Physico-chemical characteristics, molecular compositions, 3-D model and calibration curve of RBBR, Figure S2: Photo of the Milli-Q water system, Figure S3: Photos of raw aluminum grid, UPA monolith sample after different time of continuous growth process, Figure S4: Photo of the experimental instrument for the synthesis of UPA monolith, Figure S5: Photos of raw fragile UPA, under 4 h of isochronous annealing treatment in air at different temperatures, Figure S6: Nitrogen adsorption-desorption isotherms and pore size distributions of UPA(γ), UPA(θ), and UPA(α) powders, Figure S7: Adsorption isotherm profiles regarding RBBR adsorption capacity with units as mg·g⁻¹ and mg·m⁻², Figure S8: EDX spectra of UPA(θ) powders before and after RBBR adsorption, Figure S9: SEM images of UPA(θ) powders before and after RBBR adsorption, Figure S10: The pH variation after RBBR adsorption equilibrium, Figure S11: Zeta potential values of UPA(γ), UPA(θ), and UPA(α) powders as a function of pH, Figure S12: Infrared spectrum of RBBR.

Author Contributions: Conceptualization, H.X.; methodology, H.X. and G.B.; characterization, K.Z.; software, H.X. and K.Z.; formal analysis and investigation, H.X.; resources, M.N. and A.E.; data curation, A.K.; writing—original draft preparation, H.X., Z.J., R.A. and A.K.; writing—review and editing, Z.J., M.T. and A.K.; visualization, H.X.; supervision, Z.J., M.T., R.A. and A.E.; project administration, R.A., M.N. and A.E.; funding acquisition, M.N. and A.E. All authors have read and agreed to the published version of the manuscript.

Funding: This research received no external funding.

Institutional Review Board Statement: Not applicable.

Informed Consent Statement: Not applicable.

Data Availability Statement: The data presented in this study are available from the corresponding authors with reasonable requests.

Acknowledgments: H.X. thanks the China Scholarship Council (CSC) for his PhD fellowship, followed by one year of funding source provided by EBI, which is also gratefully acknowledged. The authors thank Amal Allouch for simulation support of the 3-D model of RBBR molecule, as well as Jianwen Weng for MATLAB-based matrix conversion and gridding.

Conflicts of Interest: The authors declare no conflict of interest.

References

- Lavis, L.D. Teaching old dyes new tricks: Biological probes built from fluoresceins and rhodamines. *Annu. Rev. Biochem.* **2017**, *86*, 825–843. [CrossRef] [PubMed]
- Routoula, E.; Patwardhan, S.V. Degradation of anthraquinone dyes from effluents: A review focusing on enzymatic dye degradation with industrial potential. *Environ. Sci. Technol.* **2020**, *54*, 647–664. [CrossRef] [PubMed]
- Bilal, M.; Asgher, M.; Parra-Saldivar, R.; Hu, H.-B.; Wang, W.; Zhang, X.-H.; Iqbal, H.M.N. Immobilized ligninolytic enzymes: An innovative and environmental responsive technology to tackle dye-based industrial pollutants—A review. *Sci. Total Environ.* **2017**, *576*, 646–659. [CrossRef]
- Madrakian, T.; Afkhami, A.; Jalal, N.R.; Ahmadi, M. Kinetic and thermodynamic studies of the adsorption of several anionic dyes from water samples on magnetite-modified multi-walled carbon nanotubes. *Sep. Purif. Technol.* **2013**, *48*, 2638–2648. [CrossRef]
- Cicek, F.; Özer, D.; Özer, A.; Özer, A. Low cost removal of reactive dyes using wheat bran. *J. Hazard. Mater.* **2007**, *146*, 408–416. [CrossRef]
- Gök, Ö.; Özcan, A.S.; Özcan, A. Adsorption behavior of a textile dye of Reactive Blue 19 from aqueous solutions onto modified bentonite. *Appl. Surf. Sci.* **2010**, *256*, 5439–5443. [CrossRef]
- Moussavi, G.; Mahmoudi, M. Removal of azo and anthraquinone reactive dyes from industrial wastewaters using MgO nanoparticles. *J. Hazard. Mater.* **2009**, *168*, 806–812. [CrossRef]
- Li, J.; Wang, X.-X.; Zhao, G.-X.; Chen, C.-L.; Chai, Z.-F.; Alsaedi, A.; Hayat, T.; Wang, X.-K. Metal-organic framework-based materials: Superior adsorbents for the capture of toxic and radioactive metal ions. *Chem. Soc. Rev.* **2018**, *47*, 2322–2356. [CrossRef] [PubMed]
- Zdarta, J.; Meyer, A.S.; Jesionowski, T.; Pinelo, M. Developments in support materials for immobilization of oxidoreductases: A comprehensive review. *Adv. Colloid Interf. Sci.* **2018**, *258*, 1–20. [CrossRef] [PubMed]
- Qiu, P.-P.; Ma, B.; Hung, C.-T.; Li, W.; Zhao, D.-Y. Spherical mesoporous materials from single to multilevel architectures. *Acc. Chem. Res.* **2019**, *52*, 2928–2938. [CrossRef] [PubMed]
- Vignes, J.-L.; Frappart, C.; Di Costanzo, T.; Rouchaud, J.-C.; Mazerolles, L.; Michel, D. Ultraporous monoliths of alumina prepared at room temperature by aluminium oxidation. *J. Mater. Sci.* **2008**, *43*, 1234–1240. [CrossRef]

12. Nguyen, T.H.N. Elaboration and Modifications of Nanofibrous Al₂O₃. Chemical and Process Engineering. Ph.D. Thesis, Université Sorbonne, Paris, France, 2016.
13. Monsef Khoshhesab, Z.; Ahmadi, M. Removal of reactive blue 19 from aqueous solutions using NiO nanoparticles: Equilibrium and kinetic studies. *Desalination. Water Treat.* **2015**, *57*, 20037–20048. [[CrossRef](#)]
14. Beauvy, M.; Vignes, J.-L.; Michel, D.; Mazerolles, L.; Frappart, C.; Di Costanzo, T. Process for the Preparation of Monolithic Hydrated Alumina, Amorphous or Crystallized Alumina, Aluminates and Composite Materials by Metal Aluminum Oxidation or Aluminum Alloy. European Patent Application FR2847569, 28 May 2004.
15. Beauvy, M.; Vignes, J.-L.; Michel, D.; Mazerolles, L.; Frappart, C.; Di Costanzo, T. Method for Preparing Monolithic Hydrated Aluminas and Composite Materials. European Patent Application EP1562859, 17 August 2005.
16. Khatim, O.; Nguyen, T.H.N.; Amamra, M.; Museur, L.; Khodan, A.; Kanaev, A. Synthesis and photoluminescence properties of nanostructured mullite/ α -Al₂O₃. *Acta Mater.* **2014**, *71*, 108–116. [[CrossRef](#)]
17. Bouslama, M.; Amamra, M.C.; Jia, Z.-X.; Ben Amar, M.; Chhor, K.; Brinza, O.; Abderrabba, M.; Vignes, J.-L.; Kanaev, A. Nanoparticulate TiO₂-Al₂O₃ photocatalytic media: Effect of particle size and polymorphism on photocatalytic activity. *ACS Catal.* **2012**, *2*, 1884–1892. [[CrossRef](#)]
18. Bouslama, M.; Amamra, M.C.; Brinza, O.; Tieng, S.; Chhor, K.; Abderrabba, M.; Vignes, J.-L.; Kanaev, A. Isolation of titania nanoparticles in monolithic ultraporos alumina: Effect of nanoparticle aggregation on anatase phase stability and photocatalytic activity. *Appl. Catal. A* **2011**, *402*, 156–161. [[CrossRef](#)]
19. Tchieda, V.K.; D'Amato, E.; Chiavola, A.; Parisi, M.; Chianese, A.; Amamra, M.; Kanaev, A. Removal of arsenic by alumina: Effects of material size, additives, and water contaminants. *Clean* **2016**, *44*, 496–505. [[CrossRef](#)]
20. Chiavola, A.; Tchieda, V.K.; D'Amato, E.; Chianese, A.; Kanaev, A. Synthesis and characterization of nanometric titania coated on granular alumina for arsenic removal. *Chem. Eng. Trans.* **2016**, *47*, 331–336.
21. Özsoy, H.D.; Ünyayar, A.; Mazmanci, M.A. Decolourisation of reactive textile dyes Drimarene Blue X₃LR and Remazol Brilliant Blue R by *Funalia trogii* ATCC 200800. *Biodegradation* **2005**, *16*, 195–204. [[CrossRef](#)] [[PubMed](#)]
22. Khodan, A.; Nguyen, T.H.N.; Esaulkov, M.; Kiselev, M.R.; Amamra, M.; Vignes, J.-L.; Kanaev, A. Porous monoliths consisting of aluminum oxyhydroxide nanofibrils: 3D structure, chemical composition, and phase transformations in the temperature range 25–1700 °C. *J. Nanopart. Res.* **2018**, *20*, 1–11. [[CrossRef](#)]
23. Ho, Y.S.; McKay, G. A comparison of chemisorption kinetic models applied to pollutant removal on various sorbents. *Process Saf. Environ. Prot.* **1998**, *76*, 332–340. [[CrossRef](#)]
24. Ho, Y.S.; McKay, G. Pseudo-second order model for sorption processes. *Process. Biochem.* **1999**, *34*, 451–465. [[CrossRef](#)]
25. Boyd, G.E.; Adamson, A.W.; Myers, L.S.J. The exchange adsorption of ions from aqueous solutions by organic zeolites. II. Kinetics. *J. Am. Chem. Soc.* **1947**, *69*, 2836–2848. [[CrossRef](#)]
26. Ho, Y.S.; Ng, J.C.Y.; McKay, G. Kinetics of pollutant sorption by biosorbents: Review. *Sep. Pur. Met.* **2000**, *29*, 189–232. [[CrossRef](#)]
27. Weber, W.J.; Morris, J.C. Kinetics of adsorption of carbon from solutions. *J. Sanit. Eng. Div.* **1963**, *89*, 31–63. [[CrossRef](#)]
28. Fan, H.-T.; Sun, W.; Jiang, B.; Wang, Q.-J.; Li, D.-W.; Huang, C.-C.; Wang, K.-J.; Zhang, Z.-G.; Li, W.-X. Adsorption of antimony(III) from aqueous solution by mercapto-functionalized silica-supported organic-inorganic hybrid sorbent: Mechanism insights. *Chem. Eng. J.* **2016**, *286*, 128–138. [[CrossRef](#)]
29. Foo, K.Y.; Hameed, B.H. Insights into the modeling of adsorption isotherm systems. *Chem. Eng. J.* **2010**, *156*, 2–10. [[CrossRef](#)]
30. Langmuir, I. The adsorption of gases on plane surfaces of glass, mica and platinum. *J. Am. Chem. Soc.* **1918**, *40*, 1361–1403. [[CrossRef](#)]
31. Langmuir, I. The constitution and fundamental properties of solids and liquids. Part I. Solids. *J. Am. Chem. Soc.* **1916**, *38*, 2221–2295. [[CrossRef](#)]
32. Langmuir, I. The constitution and fundamental properties of solids and liquids. Part II. Liquids. *J. Am. Chem. Soc.* **1917**, *39*, 1848–1906. [[CrossRef](#)]
33. Hall, K.R.; Eagleton, L.C.; Acrivos, A.; Vermeulen, T. Pore- and solid-diffusion kinetics in fixed-bed adsorption under constant-pattern conditions. *Ind. Eng. Chem. Fundamen.* **1966**, *5*, 212–223. [[CrossRef](#)]
34. Webber, T.W.; Chakkravorti, R.K. Pore and solid diffusion models for fixed-bed adsorbents. *AIChE J.* **1974**, *20*, 228–238. [[CrossRef](#)]
35. Freundlich, H.M.F. Über die adsorption in lösungen (Over the adsorption in solution). *J. Phys. Chem.* **1906**, *57*, 385–471.
36. Haghseresht, F.; Lu, G.-Q. Adsorption characteristics of phenolic compounds onto coal-reject-derived adsorbents. *Energy Fuels* **1998**, *12*, 1100–1107. [[CrossRef](#)]
37. Temkin, M.I.; Pyzhev, V.P. Kinetics of ammonia synthesis on promoted iron catalyst. *Acta Phys. Chim. USSR* **1940**, *12*, 327–356.
38. Dubinin, M.M.; Radushkevich, L.V. The equation of the characteristic curve of the activated charcoal. *Proc. USSR Acad. Sci.* **1947**, *55*, 331–337.
39. Hobson, J.P. Physical adsorption isotherms extending from ultra high vacuum to vapor pressure. *J. Phys. Chem.* **1969**, *73*, 2720–2727. [[CrossRef](#)]
40. Özcan, A.; Öncü, E.M.; Özcan, A.S. Kinetics, isotherm and thermodynamic studies of adsorption of Acid Blue 193 from aqueous solutions onto natural sepiolite. *Colloid. Surf. A* **2006**, *277*, 90–97. [[CrossRef](#)]
41. Patel, H.; Vashi, R.T. Wastewater treatment by physical-chemical technologies. In *Wastewater Engineering: Advanced Wastewater Treatment Systems*; Aziz, H.A., Mojiri, A., Eds.; IJSR Publications: Ahmedabad, India, 2014; pp. 5–48.

42. Souza Santos, P.; Souza Santos, H.; Toledo, S.P. Standard transition aluminas. Electron microscopy studies. *J. Mater. Res.* **2000**, *3*, 104–114. [[CrossRef](#)]
43. Sing, K.S.W.; Everett, D.H.; Haul, R.A.W.; Moscou, L.; Pierotti, R.A.; Rouquérol, J.; Siemieniowska, T. Reporting physisorption data for gas/solid systems with special reference to the determination of surface area and porosity. *Pure Appl. Chem.* **1985**, *57*, 603–619. [[CrossRef](#)]
44. Storck, S.; Bretinger, H.; Maier, W.F. Characterization of micro- and mesoporous solids by physisorption methods and pore-size analysis. *Appl. Catal. A* **1998**, *174*, 137–146. [[CrossRef](#)]
45. Iqbal, M.; Saeed, A. Biosorption of reactive dye by loofa sponge-immobilized fungal biomass of *Phanerochaete chrysosporium*. *Process Biochem.* **2007**, *42*, 1160–1164. [[CrossRef](#)]
46. O'Mahony, T.; Guibal, E.; Tobin, J.M. Reactive dye biosorption by *Rhizopus arrhizus* biomass. *Enzyme Microb. Technol.* **2002**, *31*, 456–463. [[CrossRef](#)]
47. Shanehsaz, M.; Seidi, S.; Ghorbani, Y.; Shoja, S.M.; Rouhani, S. Polypyrrole-coated magnetic nanoparticles as an efficient adsorbent for RB19 synthetic textile dye: Removal and kinetic study. *Spectrochim. Acta A* **2015**, *149*, 481–486. [[CrossRef](#)]
48. Taty-Costodes, V.C.; Fauduet, H.; Porte, C.; Delacroix, A. Removal of Cd(II) and Pb(II) ions, from aqueous solutions, by adsorption onto sawdust of *Pinus sylvestris*. *J. Hazard. Mater.* **2003**, *105*, 121–142. [[CrossRef](#)]
49. Monsef Khoshhesab, Z.; Souhani, S. Adsorptive removal of reactive dyes from aqueous solutions using zinc oxide nanoparticles. *J. Chin. Chem. Soc.* **2018**, *65*, 1482–1490. [[CrossRef](#)]
50. Monsef Khoshhesab, Z.; Modaresnia, N. Adsorption of Acid Black 210 and Remazol Brilliant Blue R onto magnetite nanoparticles. *Inorg. Nano Met. Chem.* **2019**, *49*, 231–239. [[CrossRef](#)]
51. Jjagbemi, C.O.; Baek, M.H.; Kim, D.S. Montmorillonite surface properties and sorption characteristics for heavy metal removal from aqueous solutions. *J. Hazard. Mater.* **2009**, *166*, 538–546. [[CrossRef](#)] [[PubMed](#)]
52. Srivastava, V.C.; Swamy, M.M.; Mall, I.D.; Prasad, B.; Mishra, I.M. Adsorptive removal of phenol by bagasse fly ash and activated carbon: Equilibrium, kinetics and thermodynamics. *Colloid. Surf. A* **2006**, *272*, 89–104. [[CrossRef](#)]
53. Kim, Y.; Kim, C.; Choi, I.; Rengraj, S.; Yi, J. Arsenic removal using mesoporous alumina prepared via a templating method. *Environ. Sci. Technol.* **2004**, *38*, 924–931. [[CrossRef](#)] [[PubMed](#)]
54. Aziz, A.; Ouali, M.S.; Elandaloussi, E.H.; De Menorval, L.C.; Lindheimer, M. Chemically modified olive stone: A low-cost sorbent for heavy metals and basic dyes removal from aqueous solutions. *J. Hazard. Mater.* **2009**, *163*, 441–447. [[CrossRef](#)] [[PubMed](#)]
55. Anayurt, R.A.; Sari, A.; Tuzen, M. Equilibrium, thermodynamic and kinetic studies on biosorption of Pb(II) and Cd(II) from aqueous solution by macrofungus (*Lactarius scrobiculatus*) biomass. *Chem. Eng. J.* **2009**, *151*, 255–261. [[CrossRef](#)]
56. Saha, P.; Chowdhury, S. Insight into adsorption thermodynamics. In *Thermodynamics*; Mizutani, T., Ed.; InTech: London, UK, 2011; pp. 349–364. ISBN 978-953-307-544-0.
57. Azizi, A.; Alavi Moghaddam, M.R.; Arami, M. Applications of wood waste for removal of reactive blue 19 from aqueous solutions: Optimization through response surface methodology. *Environ. Eng. Manag. J.* **2012**, *11*, 795–804.
58. Ayazi, Z.; Khoshhesab, Z.M.; Norouzi, S. Modeling and optimizing of adsorption removal of Reactive Blue 19 on the magnetite/graphene oxide nanocomposite via response surface methodology. *Desalin. Water Treat.* **2016**, *57*, 25301–25316. [[CrossRef](#)]
59. Hu, C.-W.; Hu, N.-T.; Li, X.-L.; Shen, H.-L.; Zhao, Y.-J. Adsorption of remazol brilliant blue R by carboxylated multi-walled carbon nanotubes. *Desalin. Water Treat.* **2017**, *62*, 282–289. [[CrossRef](#)]
60. Madrakian, T.; Afkhami, A.; Mahmood-Kashani, H.; Ahmadi, M. Adsorption of some cationic and anionic dyes on magnetite nanoparticles-modified activated carbon from aqueous solutions: Equilibrium and kinetics study. *J. Iran. Chem. Soc.* **2012**, *10*, 481–489. [[CrossRef](#)]
61. Liao, M.-H.; Chen, W.-C.; Lai, W.-C. Magnetic nanoparticles assisted low-molecular weight polyethyleneimine for fast and effective removal of reactive blue 19. *Fresen. Environ. Bull.* **2006**, *15*, 609–613.

Appendix E: Article published in Chemical Engineering Transactions.

Xu, H.; Boeuf, G.; Jia, Z.-X.; Kanaev, A.; Azouani, R.; Amamra, M.; Elm'selmi, A.; Traore, M., Novel synthesis of oxidoreductase immobilized biocatalyst for effective anthraquinone dye treatment in bioreactor, Chemical Engineering Transactions, 84 (2021) 157–162.

157



VOL. 84, 2021

Guest Editors: Paolo Ciambelli, Luca Di Palma
Copyright © 2021, AIDIC Servizi S.r.l.
ISBN 978-88-95608-82-2; ISSN 2283-9216



DOI: 10.3303/CET2184027

Novel Synthesis of Oxidoreductase Immobilized Biocatalyst for Effective Anthraquinone Dye Treatment in Bioreactor

Huan Xu^a, Guilhem Boeuf^b, Zixian Jia^a, Andrei Kanaev^a, Rabah Azouani^b, Mohamed Amamra^a, Abdellatif Elm'selmi^b, Mamadou Traore^{a,*}

^aLaboratoire des Sciences des Procédés et des Matériaux, CNRS, Université Sorbonne Paris Nord, F-93430, Villetaneuse, France

^bEBInnov, École de Biologie Industrielle, F-95000, Cergy, France
mamadou.traore@lspm.cnrs.fr

Over the past few decades, biotransformations of compounds with complicated and reinforced structures, especially some poorly biodegradable organic pollutants, have attracted extensive research attention. Benefiting from recently developed techniques of protein engineering, oxidoreductase industrial applications such as laccases, tyrosinases, and various oxygenases have been recognized as a promising alternative technique as compared with the conventional treatment processes of industrial textile effluents. However, the lack of long-term operational stability and reusability of the above-mentioned enzymes may limit their further large-scale industrialization. To overcome this, a novel biocatalyst was developed by immobilizing laccase from *Trametes versicolor* onto ultraporous gamma-alumina powders (laccase@UPA(γ)), followed by transferring it into a portable and easy-to-carry bioreactor for Remazol Brilliant Blue R (RBBR) dye biodegradation. The obtained results showed that the treatment capacity of laccase@UPA(γ) towards RBBR reached about 60 mg/g after 24 h of contact time at pH 5. These preliminary results highlight the potentials of bio-based inorganic materials in industrial wastewater treatment, which can broaden our understanding of their practical applications in the environmental field.

1. Introduction

Nowadays, as synthetic dye applications on the printing and dyeing processes of fabrics have been extensively developed worldwide, about 50000 tons of dyes get discharged into the environment every year, and nearly 20% of industrial water pollution results from dyestuff related industries (Bilal et al., 2017; Routoula and Patwardhan, 2020). Among the various dye compounds, Remazol Brilliant Blue R (RBBR) poses a series of environmental problems as its complicated and reinforced anthraquinone structure makes it difficult to be degraded naturally in the environment (Moussavi and Mahmoudi, 2009; Gök et al., 2010). In the meantime, government legislation is becoming stricter than before regarding dye treatment in industrial textile effluents, especially in the more developed countries (Osma et al., 2010). Therefore, in the context of green and sustainable chemistry, proper treatments regarding purifications and remediations of industrial textile effluents are necessary and urgent.

Generally, the most common methods in terms of dye treatment can be classified into physical, chemical/electrochemical, biological methods, and/or emerging combination of several above-mentioned techniques with the purpose of synergistic effects (Cicek et al., 2007; Madrakian et al., 2013). Among these conventional methods, enzyme-based biocatalysis which is widely characterized by high chemo-, regio-, and stereoselectivity has many advantages. Thanks to the recent advances in modern biotechnology and protein engineering, biotransformations of poorly biodegradable dyes into non-hazardous or less-hazardous substances have been recognized as a key strategy to control the level of contaminations in water and soil (Sheldon and Woodley, 2018; Zdarta et al., 2018). Laccase (oxidoreductase, EC 1.30.3.2), which is secreted by white-rot fungi, has received numerous research attention because it only needs molecular oxygen (air) as a co-substrate and can catalyze the oxidation of a great variety of phenolic and non-phenolic compounds

Paper Received: 5 September 2020; Revised: 12 November 2020; Accepted: 23 February 2021

Please cite this article as: Xu H., Boeuf G., Jia Z., Kanaev A., Azouani R., Amamra M., Elm'selmi A., Traore M., 2021, Novel Synthesis of Oxidoreductase Immobilized Biocatalyst for Effective Anthraquinone Dye Treatment in Bioreactor, Chemical Engineering Transactions, 84, 157-162 DOI:10.3303/CET2184027

(Osma et al., 2010; Hou et al., 2014). In addition, laccase applications in the biodegradation of endocrine disrupting chemicals (EDCs) and dye treatments have also been extensively studied in the last decades (Hou et al., 2014; Zdarta et al., 2018). The potential use of enzyme in industrial applications normally requires enzyme immobilization, in which proper selection of supporting carrier (organic origin, inorganic origin, and hybrid materials) is of great importance regarding enhanced enzyme stability against harsh conditions of pH, temperature, and pressure (Torres-Salas et al., 2011; Zdarta et al., 2018). More recently, broad research interests have been focused on inorganic materials which can be obtained relatively cheaply and usually by uncomplicated synthesis procedures. For example, Lassouane et al. (2019) synthesized crude laccase immobilized Ca-alginate beads for Bisphenol A (BPA) degradation from aqueous solutions.

In this study, laccase from *Trametes versicolor* (laccase *T.*) was cross-linked immobilized by ultraporous gamma-alumina powders (UPA(γ)) with glutaraldehyde as the bifunctional cross-linker, and the obtained biocatalyst (laccase@UPA(γ)) was transferred into a disposable 2 mL polystyrene column for RBBR dye biodegradation. The present study highlights the UPA potentials in terms of oxidoreductase immobilization, which can broaden the practical applicability of aluminium materials in industrial wastewater treatment.

2. Experimental procedure

2.1 Materials and chemicals

The raw laminated metallic aluminium plate (100×100 mm, 1.0 mm of thickness, 99.99% of purity) and disposable 2 mL polystyrene column were supplied by Goodfellow Cambridge Ltd. and ThermoFisher Scientific Inc., respectively. The chemicals including acetone, mercury(II) nitrate monohydrate ($\text{Hg}(\text{NO}_3)_2 \cdot \text{H}_2\text{O}$, $\geq 98.5\%$), silver nitrate (AgNO_3 , $\geq 99.0\%$), laccase *T.* ($\geq 0.5 \text{ U} \cdot \text{mg}^{-1}$), RBBR (also called RB19, representative anthraquinone dye), (3-aminopropyl)triethoxysilane (APTES, 99%), glutaraldehyde (25% of *v/v*), 2,2'-azino-bis(3-ethylbenzothiazoline-6-sulfonic acid) diammonium salt (ABTS, HPLC), sodium acetate (CH_3COONa , $\geq 99.0\%$), sodium phosphate dibasic dihydrate ($\text{Na}_2\text{HPO}_4 \cdot 2\text{H}_2\text{O}$, $\geq 99.0\%$, phosphate buffer), glacial acetic acid ($\text{CH}_3\text{CO}_2\text{H}$, $\geq 99.5\%$), and sodium hydroxide (NaOH , $\geq 97.0\%$) were purchased from Sigma-Aldrich, Inc.. All the chemicals used in this study were of analytical grade and used as received directly without further purification. Milli-Q water (Millipore Corp.) with a specific resistivity of $18.2 \text{ M}\Omega \cdot \text{cm}^{-1}$ at 25 °C was used to prepare solutions throughout the experiments.

2.2 UPA(γ) powders and laccase@UPA(γ) biocatalyst syntheses

The UPA(γ) monolith sample was synthesized via facile oxidation process according to the previously reported studies (Vignes et al., 2008; Bouslama et al., 2012; Khodan et al., 2018). Briefly, high purity but fragile UPA monolith sample was obtained with a growth rate of $\sim 1 \text{ cm} \cdot \text{h}^{-1}$ at room temperature in a humid atmosphere (70–80% RH) by the oxidation of metallic aluminium plate through a liquid mercury-silver layer. Anhydrous UPA(γ) monolith can be obtained under 4 h of isochronous annealing treatment in air at 950 °C. After rigorous grinding process, UPA(γ) powders can be accordingly obtained.

Prior to the immobilization procedure, UPA(γ) powders were silanized with 2.5% (*v/v*) APTES in acetone at 45 °C and 100 rpm for 24 h, followed by washing the obtained powders with phosphate buffer for three times to remove any residual organics. Subsequently, a given amount of APTES silanized UPA(γ) powders were dispersed in 0.5% (*v/v*) glutaraldehyde solution under neutral pH conditions. The mixture was kept under stirring at 20 °C and 100 rpm for 6 h, followed by the washing procedure as mentioned above to remove unreacted glutaraldehyde molecules. After glutaraldehyde functionalization, the obtained powders were suspended in laccase *T.* solution at 20 °C and 100 rpm for 24 h, resulting in Schiff base formation and subsequent cross-linking of laccase *T.* with functionalized UPA(γ) powders (laccase@UPA(γ)).

2.3 Characterizations

The obtained samples were characterized by using scanning electron microscopy (SEM, Zeiss Supra 40 VP) and transmission electron microscopy (TEM, JEOL 2011) techniques. The XRD pattern was carried out by using an Inel Equinox 1000 X-ray diffractometer (Inel) with Co K α radiation source ($\lambda = 1.7902 \text{ \AA}$), and the analysis was performed at 2θ diffraction angles from 20° to 95° at a speed of 2°/min. The FTIR spectra were recorded by using a PerkinElmer Spectrum 100 system spectrometer in pressed KBr pellets (Sigma-Aldrich, 99%, analytical reagent) and in the 400–4000 cm^{-1} region.

2.4 Data processing

The concentration of RBBR and laccase *T.* in supernatant (C_t , $\text{mg}\cdot\text{L}^{-1}$) were determined by spectrophotometry method at the wavelength of 590 and 420 nm, respectively (UviLine 9400 UV-Visible spectrophotometer, Secomam). C_0 ($\text{mg}\cdot\text{L}^{-1}$) is the initial concentration of corresponding substances in suspension.

3. Results and discussion

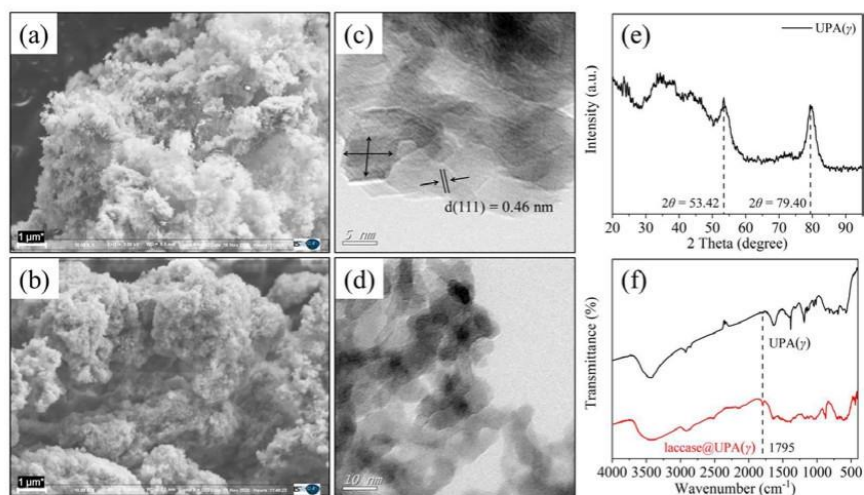


Figure 1: SEM images of (a) UPA(γ) powders and (b) laccase@UPA(γ) biocatalyst, TEM images of (c) UPA(γ) powders and (d) laccase@UPA(γ) biocatalyst, (e) XRD pattern of UPA(γ) powders, and (f) FTIR spectra of UPA(γ) powders and laccase@UPA(γ) biocatalyst.

Figure 1a–1d showed the SEM and TEM images of UPA(γ) powders and laccase@UPA(γ) biocatalyst, which evidences the ultraporous morphology of obtained samples. TEM image at higher magnification (Figure 1c) revealed the clear lattice fringe with a d -spacing of 0.46 nm, which corresponds to the (111) plane of gamma-alumina (JCPDS 10-0425) (Souza Santos et al., 2000). By comparing Figure 1d with Figure 1c, the UPA(γ) border became smoother after laccase *T.* immobilization. Based on the calculation from Bragg equation ($2d\sin\theta = n\lambda$, $n = 1, 2, 3$, etc.) (Figure 1e), the two typical diffraction peaks at $2\theta = 53.42^\circ$ ($d = 1.99 \text{ nm}$) and 79.40° ($d = 0.14 \text{ nm}$) correspond to the (400) and (440) planes of gamma-alumina, respectively (JCPDS 29-0063) (Souza Santos et al., 2000). After laccase *T.* immobilization, the absorption band at 1795 cm^{-1} was assigned to C=O stretching vibration (Figure 1f). Moreover, a broader absorption band in the range of $3400\text{--}3500 \text{ cm}^{-1}$ indicated the presence of carboxyl and amino groups distributed on the UPA(γ) surface after laccase *T.* immobilization. The above-mentioned discussions confirm that laccase *T.* was successfully immobilized on the UPA(γ) surface with glutaraldehyde as the cross-linker.

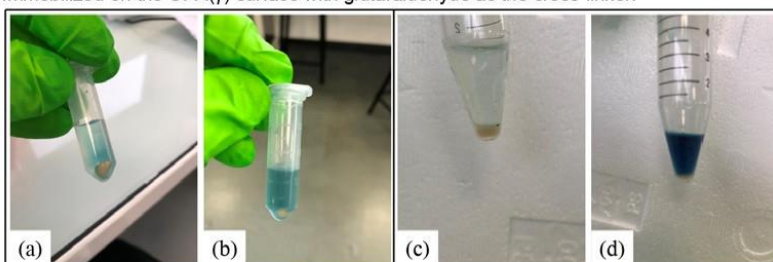


Figure 2: Photos of two parallel experiments regarding ABTS oxidation monitoring: (a) to (b) 0.5 mg, and (c) to (d) 2.0 mg of laccase@UPA(γ) biocatalyst.

In Figure 2, two parallel experiments regarding ABTS oxidation by laccase@UPA(γ) biocatalyst were conducted, and positive results related to active laccase *T.* on UPA(γ) surface can be observed obviously. In Figures 2a and 2c, the green coloured ABTS^{•+} radical was initially diffused from the surface of biocatalyst.

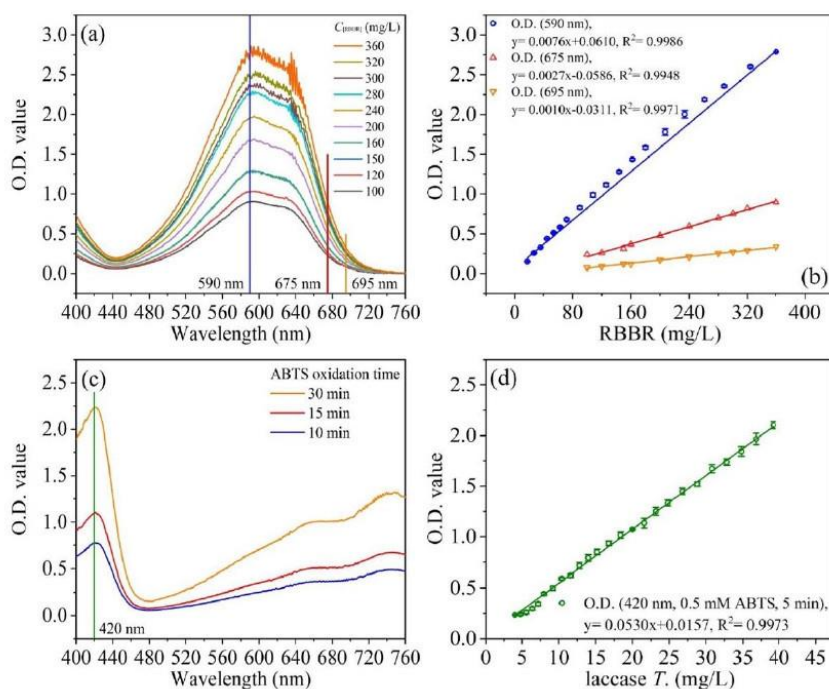


Figure 3: (a) Visible spectral curves of RBBR at different concentrations, (b) working curves of RBBR with optical density (O.D.) values at different wavelengths ($\lambda = 590, 675, \text{ and } 695 \text{ nm}$), (c) visible spectral curves of laccase *T.* assay by using ABTS as the substrate at different oxidation time ($t = 10, 15, \text{ and } 30 \text{ min}$), and (d) working curves of laccase *T.* assay by using ABTS as the substrate at 5 min of oxidation time ($\lambda = 420 \text{ nm}$).

Figure 3 showed the working curves of RBBR and laccase *T.* (ABTS as the substrate) stoichiometrically determined by the spectrophotometry method. As shown in Figure 3b, the linear relationships between optical density (O.D.) value and RBBR concentration can also be obtained at higher spectral positions (i.e., 675 and 695 nm). Therefore, for the determination of high RBBR concentration which may exceed the detection limit of the visible spectrophotometer, a higher spectral position for measurement (e.g., 675 and 695 nm) other than one more step dilution operation at 590 nm of spectrum peak can also be applicable.

In Figure 3c, the O.D. value regarding ABTS oxidation kept increasing as oxidation time increased. Generally, the oxidation of colourless ABTS can undergo a fast one-electron transfer process, and the reaction product ABTS^{•+} is a stable green coloured radical (Pinkernell et al., 2000). According to Fernando Bautista et al. (2010), laccase *T.* possesses higher oxidation capacity because it can catalyze the four 1-electron oxidations of electron-rich compounds with the simultaneous 4-electron reduction of molecular dioxygen to water. Therefore, in terms of laccase *T.* working curve, the ABTS oxidation time was fixed at 5 min, in which the corresponding determination coefficient (R^2) of linear equation fitting and relative error bar of triplicate measurements were 0.997 and below 5%, respectively (Figure 3d). In addition, since the measurement accuracy is highly dependent on the oxidation time, it is also suggested to separately measure the corresponding O.D. value rather than unify the measurements altogether.

Figure 4a showed the schematic diagram of a disposable polystyrene column, in which 2 mL of RBBR suspension can be contained and shaken with laccase@UPA(γ) biocatalyst inside after different time intervals. The sponge support inside the polystyrene column played the role of a holder without obvious RBBR dilution after even up to 5 cycles of dilution (Figure 4b). In Figure 4c, it is worth mentioning that after RBBR dilution, a little amount of RBBR molecules retained but distributed uniformly on the surface of sponge support.

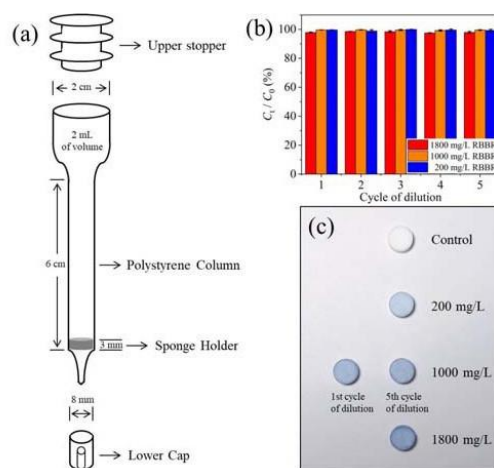


Figure 4: (a) Schematic diagram of disposable 2 mL polystyrene column, (b) residual RBBR (C_t / C_0 , %) in suspension and (c) corresponding photos of sponge supports inside the polystyrene column after different cycles of dilution. $C_{[RBBR]_{initial}} = 200, 1000, \text{ and } 1800 \text{ mg} \cdot \text{L}^{-1}$.

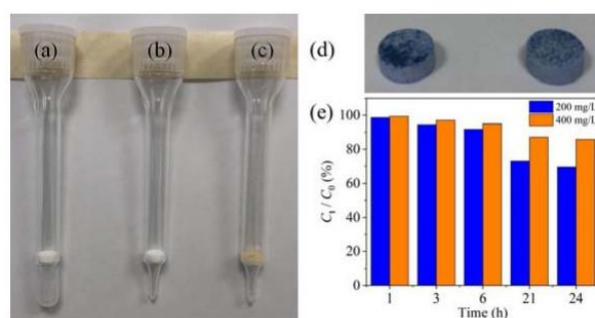


Figure 5: Photos of polystyrene column (a) with and (b) without the lower cap to avoid liquid leakage, (c) photo of sponge support holding laccase@UPA(γ) biocatalyst in polystyrene column, (d) photos of sponge support surface after RBBR dye biodegradation, and (e) residual RBBR (C_t / C_0 , %) after different time intervals of laccase@UPA(γ) biocatalyst treatment in polystyrene column bioreactor at pH = 5.0.

In terms of catalytic performances of obtained laccase@UPA(γ) biocatalyst, three parameters including laccase T . immobilization yield (%), immobilization efficiency (%), and activity recovery (%) were calculated by using ABTS as the substrate (Sheldon and Pelt, 2013). Accordingly, the corresponding results were determined as 90.5%, 19.3%, and 17.5%, respectively. Furthermore, by using glutaraldehyde as the cross-linker, the laccase T . immobilization capacity by UPA(γ) powders was $244.4 \text{ mg} \cdot \text{g}^{-1}$ at pH = 7.5.

As shown in Figure 5d, after corresponding experiments and excluding the suspension by using the upper stopper of the polystyrene column, the surface of sponge support became coarser, and some blue coloured laccase@UPA(γ) samples distributed non-uniformly on its surface as compared with the results discussed above (Figure 4c). By transferring the obtained laccase@UPA(γ) biocatalyst into polystyrene column for RBBR dye biodegradation, approximately 25% and 10% of RBBR with 200 and 400 $\text{mg} \cdot \text{L}^{-1}$ of initial dye concentrations can be degraded with 2 mg of biocatalyst after 24 h of incubation time, respectively (Figure 5e).

4. Conclusions

In the context of green and sustainable chemistry, this communication is devoted to the preliminary experimental results regarding the synthesis of laccase T . immobilized biocatalyst (laccase@UPA(γ)), in which the efficient immobilization capacity of laccase T . by UPA(γ) powders was $244.4 \text{ mg} \cdot \text{g}^{-1}$ at pH = 7.5. The

polystyrene column was applied as a portable and easy-to-carry bioreactor for RBBR dye biodegradation, which can be used as the first prototype of an enzymatic bioreactor for dye treatment in industrial textile effluents. Inspired by these results, the optimization of this process is underway.

Acknowledgments

This research was conducted as a joint collaborative project between Laboratoire des Sciences des Procédés et des Matériaux (LSPM) and EBIInnov, École de Biologie Industrielle (EBI). H. X. thanks the China Scholarship Council for his PhD fellowship, followed by one year of funding source provided by EBI which is also gratefully acknowledged. Authors thank Dr. Brinza for SEM and TEM characterizations.

References

- Bilal M., Asgher M., Parra-Saldivar R., Hu H.-B., Wang W., Zhang X.-H., Iqbal H.M.N., 2017, Immobilized ligninolytic enzymes: An innovative and environmental responsive technology to tackle dye-based industrial pollutants – A review, *Science of the Total Environment*, 576, 646–659.
- Bousslama M., Amamra M.C., Jia Z.-X., Ben Amar M., Chhor K., Brinza O., Abderrabba M., Vignes J.-L., Kanaev A., 2012, Nanoparticulate TiO₂-Al₂O₃ photocatalytic media: Effect of particle size and polymorphism on photocatalytic activity, *ACS Catalysis*, 2, 1884–1892.
- Cicek F., Özer D., Özer A., Özer A., 2007, Low cost removal of reactive dyes using wheat bran, *Journal of Hazardous Materials*, 146, 408–416.
- Fernando Bautista L., Morales G., Sanz R., 2010, Immobilization strategies for laccase from *Trametes versicolor* on mesostructured silica materials and the application to the degradation of naphthalene, *Bioresource Technology*, 101, 8541–8548.
- Gök Ö., Özcan A.S., Özcan A., 2010, Adsorption behavior of a textile dye of Reactive Blue 19 from aqueous solutions onto modified bentonite, *Applied Surface Science*, 256, 5439–5443.
- Hou J.-W., Dong G.-X., Ye Y., Chen V., 2014, Laccase immobilization on titania nanoparticles and titania-functionalized membranes, *Journal of Membrane Science*, 452, 229–240.
- Khodan A., Nguyen T.H.N., Esaulkov M., Kiselev M.R., Amamra M., Vignes J.-L., Kanaev A., 2018, Porous monoliths consisting of aluminum oxyhydroxide nanofibrils: 3D structure, chemical composition, and phase transformations in the temperature range 25–1700 °C, *Journal of Nanoparticle Research*, 20, 1–11.
- Lassouane F., Aït-Amar H., Amrani S., Rodriguez-Couto S., 2019, A promising laccase immobilization approach for Bisphenol A removal from aqueous solutions, *Bioresource Technology*, 271, 360–367.
- Madrakian T., Afkhami A., Jalal N.R., Ahmadi M., 2013, Kinetic and thermodynamic studies of the adsorption of several anionic dyes from water samples on magnetite-modified multi-walled carbon nanotubes, *Separation and Purification Technology*, 48, 2638–2648.
- Moussavi G., and Mahmoudi M., 2009, Removal of azo and anthraquinone reactive dyes from industrial wastewaters using MgO nanoparticles, *Journal of Hazardous Materials*, 168, 806–812.
- Osma J.F., Toca-Herrera J.L., Rodriguez-Couto S., 2010, Transformation pathway of Remazol Brilliant Blue R by immobilised laccase, *Bioresource Technology*, 101, 8509–8514.
- Pinkernell U., Nowack B., Gallard H., von Gunten U., 2000, Methods for the photometric determination of reactive bromine and chlorine species with ABTS, *Water Research*, 34, 4343–4350.
- Routoula E., and Patwardhan S.V., 2020, Degradation of anthraquinone dyes from effluents: A review focusing on enzymatic dye degradation with industrial potential, *Environmental Science & Technology*, 54, 647–664.
- Sheldon R.A., and Pelt S.V., 2013, Enzyme immobilisation in biocatalysis: Why, what and how, *Chemical Society Reviews*, 42, 6223–6235.
- Sheldon R.A., and Woodley J.M., 2018, Role of biocatalysis in sustainable chemistry, *Chemical Reviews*, 118, 801–838.
- Souza Santos P., Souza Santos H., Toledo S.P., 2000, Standard transition aluminas. Electron microscopy studies, *Materials Research*, 3, 104–114.
- Torres-Salas P., del Monte-Martinez A., Cutiño-Avila B., Rodríguez-Colinas B., Alcalde M., Ballesteros A.O., Plou F.J., 2011, Immobilized biocatalysts: Novel approaches and tools for binding enzymes to supports, *Advanced Materials*, 23, 5275–5282.
- Vignes J.-L., Frappart C., Di Costanzo T., Rouchaud J.-C., Mazerolles L., Michel D., 2008, Ultraporos monoliths of alumina prepared at room temperature by aluminium oxidation, *Journal of Materials Science*, 43, 1234–1240.
- Zdarta J., Meyer A.S., Jesionowski T., Pinelo M., 2018, Developments in support materials for immobilization of oxidoreductases: A comprehensive review, *Advances in Colloid and Interface Science*, 258, 1–20.